Louisiana State University
LSU Digital Commons

LSU Doctoral Dissertations | Graduate School

2012

The effects of spatial confinement and oxygen stoichiometry on complex metal oxides

Zhaoliang Liao
Louisiana State University and Agricultural and Mechanical College

Follow this and additional works at: https://digitalcommons.lsu.edu/gradschool_dissertations

Part of the Physical Sciences and Mathematics Commons

Recommended Citation
Liao, Zhaoliang, "The effects of spatial confinement and oxygen stoichiometry on complex metal oxides" (2012). *LSU Doctoral Dissertations*. 873.
https://digitalcommons.lsu.edu/gradschool_dissertations/873

This Dissertation is brought to you for free and open access by the Graduate School at LSU Digital Commons. It has been accepted for inclusion in LSU Doctoral Dissertations by an authorized graduate school editor of LSU Digital Commons. For more information, please contactgradetd@lsu.edu.

THE EFFECTS OF SPATIAL CONFINEMENT AND OXYGEN STOICHIOMETRY ON COMPLEX METAL OXIDES

A Dissertation

Submitted to the Graduate Faculty of the
Louisiana State University and
Agriculture and Mechanical College
in partial fulfillment of the
requirements for the degree of
Doctor of Philosophy

in

The Department of Physics and Astronomy

by
Zhaoliang Liao
B.S., University of Science and Technology of China, China, 2006
Ph.D, Institute of Physics, Chinese Academy of Sciences, China, 2011
December 2012

Acknowledgements

I believe that I am the luckiest student during my Ph.D study. During these 7 years, I have great experience in 4 different places -Institute of Physics of Chinese Academy of Sciences (IOP, CAS), Louisiana State University (LSU), Technical Institute of Physics and Chemistry (TIPC) of CAS and Institute of High Energy Physics (IHEP) of CAS. As a dual degree student between IOP and LSU, I have been incredibly fortunate that I have four best advisors. I have to say that what I has achieved today owes much to their guidance and incredible influence throughout my PhD study.

I am very grateful to Prof. Ward Plummer and Prof. Jiandi Zhang. At the time when I sent out an email to apply for the dual degree program, Ward Plummer directly answered me very soon. He is the one who initiated and promotes this dual degree program through which I can be here to write this thesis. He is not just the best scientist but also a great people with his support of students. Jiandi Zhang gave me a lot of vivid advice in day-to-day research. Every progress I has made was inspired by his insight of science. I must say thank you again for your invaluable guidance and help.

I must thank my advisors in China: Prof. Dongmin Chen and Prof. Li Lu. Dongmin Chen was so busy but he never missed the time to discuss with me about the experiments, data and papers. I never forget how he told me to write a paper and how he revised my first paper word by word. Words are always too few to express how grateful I feel to him for all that he has done to me. I need to thank Li Lu too. He gave me a lot of valuable suggestion and guidance. I appreciate Li Lu for his help in my dual degree program and my dissertation in IOP.

I need to thank my first advisor-Prof. Huanyu Wang. Huanyu Wang was my advisor when I was in IHEP. My last half year of undergraduate study and first year of Ph.D were spent in his space exploration lab where I got a lot of guidance and training. It is his support that I transferred from IHEP to IOP to major in condensed matter physics.

My first experiment on ZnO nanotube after I attended IOP was done in TIPC in Prof. Wensheng Shi's lab. Wensheng Shi was so nice to me during this time and gave me a lot of support. Wensheng Shi, thank you very much for give me a good start.

I would like to thank Dr. Rongying Jin for her help in transport measurement, Dr. Von Braun Nascimento and Diogo D. Reis for the help in LEED theoretical calculation, Dr. Xiaoqing Pan and Xuedong Bai for the help in TEM experiments and Dr. Shane Stadler for his help in XRD test. I also thank Dr. Hongwu Zhao, Xuejin Liang, Ruquan Wang, Baoli Liu, Xinyu Pan in the IOP group for their help and helpful discussion. I need to acknowledge Changzhi Gu, Junjie Li, Qiang Luo, Haifang yang, Wuxia Li for their help in microfabrication.

I feel very grateful to all my colleagues in LSU. They are the ones that make my time on research presented in this dissertation become carefree. Xiaobo He picked me up at the airport when I first arrived here. Guorong Li helped me buy my car with his good insight. It made the long night in the lab bearable that I still could say hello somebody like Biao Hu, Guorong Li, Yiming Xiong until ~11 pm. I also feel lucky to work with Jing Teng, Yi Li, Lina Chen, Junsoo Shin, Gaomin Wang, Jianneng Li, Chen Chen, Fangyang Liu, Mesa Dalgis, Amar Karki, Zhenyu Diao, Fei Fang, Drew Antony. I need to send my thanks to my college in IOP and TICP: Weiwei Cai, Zhengzhong Wang, Fei Pang, Jianlei Gang,

Hongming Zhao, Peng Liu, Yang Meng, Ziyu Liu, Peijian Zhang, Qiang Cao, Xinyu Luo, Lili Yang, Dong Li, Cuicui Sun and other Q01 member. They gave me a lot of help. Peng Gao in SF01 group in IOP is very good at TEM and he is the one we still have collaboration in TEM through these years. Yao Wang and Guangwei She in TICP gave me a lot of help when I was in TICP.

The special acknowledge belongs to my wife Lin Li. It is her support and encourage that allowed me to follow my whims and get over difficulties. I would like to thank her parent too for their support.

The heartfelt acknowledgement must go to my parent and my brothers for their endless support and love. It will be the last piece of works I do as a student. It cannot be imagined how I could go through this 23 years' student life and graduate as a PhD today without them. I would like to dedicate this paper to my father.

Table of Contents

Acknowledgements ii

List of Tables vii

List of Figures viii

Abstract xix

Chapter 1 Introduction and Background 1
1.1 Introduction 1
1.2 Spatial Confinement Effect 3
1.3 Oxygen in Metal Oxides 13

Chapter 2 Experiment Methods 21
2.1 Thin Film Growth 21
2.1.1 Laser Molecular Beam Epitaxy 21
2.1.2 Reflection High Energy Electron Diffraction 23
2.1.3 Back-Biased-Face-Target-Sputtering 25
2.2 Characterization 26
2.2.1 Transmission Electron Microscopy 26
2.2.2 Scanning Tunneling Microscopy 30
2.2.3 X-ray Photoelectron Spectroscopy 31
2.2.4 Low Energy Electron Diffraction 34
2.2.5 Transport Measurement 36
2.3 Device Fabrication Technique 38
2.3.1 Photolithography 38
2.3.2 E-beam Lithography 39
2.3.3 Focused Ion Beam 40

Chapter 3 $SrTiO_3$ Substrate Treatment 41
3.1 Introduction and Motivation 41
3.2 Experiments and Results 42

Chapter 4 Dimensionality and Stoichiometry Effect on $La_{2/3}Sr_{1/3}MnO_3$ 52
4.1 Introduction and Motivation 52
4.2 Growth of $La_{2/3}Sr_{1/3}MnO_3$ Ultrathin Film 56
4.3 Thickness of Dead Layer 59
4.4 Singularity in Critical Thickness 65
4.5 $SrTiO_3$ Capping Effect 70
4.6 Surface Stoichiometry and Structure 73
4.7 Discussion 83

Chapter 5 Controllable Properties in Artificial Columnar Nanocomposite 95
5.1 Introduction and Motivation 95

5.2 Basic Properties of the Raw V_2O_3 and $La_{2/3}Sr_{1/3}MnO_3$ Thin Films 97
5.3 Growth and Structure of V_2O_3-$La_{2/3}Sr_{1/3}MnO_3$ Columnar Nanocomposite 100
5.4. Phase Diagram of The V_2O_3-$La_{2/3}Sr_{1/3}MnO_3$ Columnar Nanocomposite 107

Chapter 6 Resistive Switching in Metal Oxide Thin Films 113
6.1 Introduction and Motivation 113
6.2 Investigation of Resistive Switching in $Pr_{0.7}Ca_{0.3}MnO_3$ Thin Film 120
6.2.1 Categorization of Resistive Switching 120
6.2.2 Mechanism of Resistance Switching 127
6.2.3 Self-limiting of Redox at Reactive-Metal/$Pr_{0.7}Ca_{0.3}MnO_3$ Junction 130
6.2.4 EPIR Performance in Reactive-Metal/$Pr_{0.7}Ca_{0.3}MnO_3$/Pt Devices 137
6.2.5 Dynamic Visualization of Oxygen Migration and Diffusion with *in-situ* TEM 138
6.3 Investigation of Resistance Switching in Single Crystalline CeO_2 Thin Film 149
6.3.1 Improve Resistance Switching Performance of CeO_2 149
6.3.2 *In-situ* TEM Investigation of Resistance Switching in CeO_2 Thin Film 153
6.3.3. Resistive Switching Mechanism in CeO_2 Thin Film Device 157
6.4 Investigation of Resistance Switching in Metal Oxide Heterojunction 159

References 169

Appendix A: Software Interfaces and Codes 181

Appendix B: Letters of Permission 184

Vita 189

List of Tables

Table 1-1: Oxygen mobility and travelling time in a distance of 10 nm for different materials under a electric field of 1 kV/cm. Electron mobility in Si is listed for comparison. 17

Table 4-1: Reported thicknesses of dead layer of LSMO grown on different substrates. ε ≡ (a_{Sub}-a_{LSMO})/a_{LSMO} and a_{LSMO} = 3.8804 Å **[131]**. The superscript NO. is the reference. ..55

Table 4-2: Relative atomic positions of the refined surface structure of 2 u.c. LSMO film on (001) $SrTiO_3$............81

Table 4-3: Relative atomic positions of the refined surface structure of 6 u.c. and 10 u.c. LSMO film on (001) $SrTiO_3$. 82

Table 5-1: Lattice constant of LSMO, V_2O_3 and $LaAlO_3$ and their lattice mismatch.............97

Table 6-1: Examples of metal-oxides which exhibit RS behavior.......................................114

List of Figures

Figure 1–1: (a) Structural model of perovskite; (b) Splitting of d-orbital. 1

Figure 1–2: Schematic view of coupling between different kinds of degrees of freedom in CMOs, which could be tuned by external stimulus, such as pressure, temperature, laser, spatial confinement, electric and magnetic field.. 3

Figure 1–3: Reduced dimensionality induced change of density of States (DOS). 4

Figure 1–4: (a) Phase separation in $La_{0.55}Ca_{0.45}MnO_3$ evolves with temperature imaged by TEM. (b) MFM images of phase separation in $La_{1-x}Pr_xCa_{3/8}MnO_3$ (LPCMO) and its evolution with temperature. Figures adapted from **[19, 20]**. 5

Figure 1–5: Tuning parameters in ultrathin films. 6

Figure 1–6: Left, possible interface combination; Right, possible interface effects. 7

Figure 1–7: Top, structural model for the surface of $BaTiO_3$ showing the polarization direction. Bottom is STEM EELS measurement showing the chemical abrupt interface. Figure adapted from [**35**].. 8

Figure 1–8: Transport properties of (a) $La_{2/3}Ca_{1/3}MnO_3$ and (b) $La_{2/3}Sr_{1/3}MnO_3$ thin films with different thicknesses. Figures adapted from **[38, 39]**. 10

Figure 1–9: Spatial confinement effect on percolation. 11

Figure 1–10: Resistivity in a 10μm LPCMO (x=0.3) wire (black) as a function temperature The red curves are for the thin film. The measurements were made at 1T and the arrows show the heating or cooling cycle. The inset shows a SEM image of the wire. Figure adapted from **[50]**. 13

Figure 1–11: Scheme of mechanism of double exchange. 14

Figure 1–12: (a) Resistance of oxygen deficient $SrTiO_{3-\delta}$ as a function of temperature. (b) Coupling of the magnetism and resistivity with oxygen content in Fe-In_2O_3. (c) The superconductive critical temperature vs. Oxygen vacancy concentration in $YBa_2Cu_3O_{7-\delta}$. (d) The transport properties of $La_{2/3}Sr_{1/3}CoO_3$ thin films with different oxygen vacancy contents. Figures adapted from **[59-61]**. 15

Figure 1–13: Left, Oxygen vacancy in a crystal field; Right, lower down of barrier under electric field. λ is jump distance and Δε is the energy barrier. 17

Figure 1–14: (a) Write a conductive wire at $LaAlO_3/SrTiO_3$ interface with conductive AFM tip by applying a bias to the tip. (b) The conductivity between two electrodes as a function of writing length. It suddenly jumps to high value due to two electrodes connected. (c) Erase metallic 2D-gas locally. (d) Conductivity between electrodes drops due to locally break of conductive wire. Figure adapted from **[72]**....................18

Figure 1–15**:** Direct imaging of oxygen column in $SrTiO_3$ and $YBa_2Cu_3O_7$ with Cs-TEM **[77]**. 19

Figure 2–1: (a) Schematic diagram of Laser-MBE setup; (b) Our integrated Laser-MBE and *in-situ* characterizations system made up of XPS, STM/AFM, LEED....................21

Figure 2–2: Drawing of substrate heater....................22

Figure 2–3: (a) Schematic diagram of a RHEED setup.(b) RHEED patterns for different surface morphology....................23

Figure 2–4: The dynamic process of layer by layer growth monitored with REEED....................24

Figure 2–5: Scheme of a back-biased face target sputtering chamber....................25

Figure 2–6: Left, sketch of first TEM; Right, picture of the first practical TEM. Figure adapted from wikimedia....................26

Figure 2–7: (a) Optical setup for both optical microscopy and TEM. (b) EELS of La M_5 and M_4. (c) A schematic diagram of integrated TEM, EDS, EELS system....................27

Figure 2–8: (a) Integrated SPM-TEM system; (b) Schematic diagram of *in-situ* electrical properties measurement; (c) SPM-TEM sample holder (d) Drawing of the 3D piezo-motor used for SPM; Drawing (e) and real picture (f) of home-made specimen holder....................29

Figure 2–9 (a) Diagram of STM surface imaging. (b) STM image of surface structure of (001) TiO_2....................30

Figure 2–10: (a) Scheme of the photoelectron process, (b) Scheme of a XPS set-up....................31

Figure 2–11: Setup of angle resolved XPS....................33

Figure 2–12: Scheme of LEED setup. Right top, scheme of LEED diffraction process....................34

Figure 2–13: Universal curve for the electron mean free path **[90]**....................35

Figure 2–14: Time-resolved physical properties measurement system....................36

Figure 2–15: Schematic diagram of a standard dry-etch lithography process........................38

Figure 3-1: Surface morphology of $SrTiO_3$ (001) at different treatment condition................43

Figure 3-2: (a) STM image and (b) height profile of as-etched $SrTiO_3$ surface after degassing at 100 ^oC in UHV. (c) STM image and (d) height profile of sample annealed at 900 ^oC for 1 h at 10^{-4} Torr Ozone and (e) its 3D image..43

Figure 3-3: LEED pattern of the sample 1 to sample 4 as mentioned in Figure 3-1. The profiler along the red line is shown near the image in the same panel. 44

Figure 3-4: LEED pattern at 100 eV of surface after 1 h degassing (a) and 10 h degassing (b) at 100 ^oC. (c) The LEED I-V curves of these two surfaces. 45

Figure 3-5: (a) LELD pattern of as-etched $SrTiO_3$ (001) surface at 77 K (b) The comparison between experimental LEED-IV curves at 77 K and theoretical curves. Structure of as-etched $SrTiO_3$ (001) surface (c) and 3D structure model (d). 46

Figure 3-6: (a) Schematic setup of ARXPS. (b) Structure of TiO_2 termination surface. Theoretical calculation result of the emission angle dependent intensity ratio of (c) Ti2p/Sr3p in the case of TiO_2 vs. SrO termination and (d) O1s/Ti2p at different oxygen deficient level at top TiO_2 termination layer..47

Figure 3-7: Emission angle dependent intensity ratios of Ti2p/Sr3p at different treatment conditions. Rectangle: 100 ^oC UHV degassing for 1 h, circular: 500 ^oC 10^{-4}Torr Ozone annealing for 1 h, triangle: 900 ^oC 10^{-4}Torr Ozone annealing for 1 h. The open pentagram is the theoretical simulation result. 48

Figure 3-8: Angle resolved spectrum of C1s peak (a) and F1s peak (b). The intensity ratios of F1s/Sr3p and C1s/Sr3p are shown in (c) and (d), respectively.......................................50

Figure 3-9: (a) The ARXPS of samples at different treatment conditions. All the samples are annealed for 1 h at 10^{-4} Torr Ozone except the one at 100 ^oC degassing in UHV. (b) Zoom-in of the F1s peak..50

Figure 4-1: Crystal structures of Ruddlesden-Popper (RP) serials of $(R, A)_{n+1}M_nO_{3n+1}$. From left to right, it is n=1, n=2, n=∞ respectively..52

Figure 4-2: Thickness of dead layer vs. lattice mismatch. The points with error bar used are according to the **Ref. [129]**...55

Figure 4-3: RHEED diffraction pattern of $SrTiO_3$ substrate (a) and LSMO thin film (b). (c) RHEED intensity monitored during growth at different Ozone pressure........................57

Figure 4-4: STM image of the 10 u.c. LSMO thin film: (a) 2D contour image; (b) 3D image. 58

Figure 4-5: HRTEM image of LSMO (a) and LSMO/$SrTiO_3$ interface (b). (c) FFT pattern of the (b) image. 58

Figure 4-6: Temperature dependent resistivity for LSMO films with different thicknesses grown at (a) 1 μTorr, (b) 8 mTorr, (c) 80 mTorr, (d) 130 mTorr, (e) 180 mTorr Ozone pressure. 60

Figure 4-7: Effect of growth pressure on transport properties. Temperature dependent resistivity for 6 u.c. LSMO (a) and 7 u.c. LSMO (b) grown at different Ozone pressure. 60

Figure 4-8: (a) Metal-insulator transition temperature T_P vs. thickness for films grown at different pressures, inset shows the definition of T_p. For insulating film, the T_P is defined as 0. (b) The thickness of dead layer versus growth pressure 61

Figure 4-9: Evolution of thermal activation energy (ΔE) vs. thickness. (a) Resistivity vs. temperature curves for insulating film grown at 130 mTorr plotted in Ln[ρ]-1000/T scale. The temperature range used here is from 77 K to 350 K. (b) Definition of the Low T and High T range for a film with a insulator-insulator transition. A 5 u.c. film grown at 130 mTorr is used as an example. ΔE vs. thickness for LSMO thin films at (c) 80mTorr, (d) 130 mTorr, (e) 180 mTorr. (f) ΔE at low-T range vs. growth pressure for different thickness. 62

Figure 4-10: Low-T thermal activation energy (ΔE) versus thickness for LSMO films grown at 180 mTorr. 64

Figure 4-11: (a) ρ vs. T for 5 u.c LSMO plotted in Log[ρ]-1/T scale.(b) ρ vs. T for 6 u.c. LSMO plotted in (b) ρ vs. 1/T scale and (c) Log[ρ]-1/T scale. 65

Figure 4-12: (a) Blow-up of the high temperature region of **Figure 4-11(b)**. (b) ρ vs. T around 105 K for 5, 6 and 7 u.c. LSMO grown at 130 mTorr. The resistivity is normalized to plot together for comparison. 66

Figure 4-13: The temperature dependent resistivity curve around 105 K for 6 u.c. LSMO grown at different pressure. The resistivity is normalized to plot together for comparison. 68

Figure 4-14: Robust kind at ~ 105 K under magnetic field. (a)Temperature dependence of resistivity for 6 u.c. LSMO grown at 130 mTorr under various magnetic fields. (b) ZOOM-IN of the 105 K region. The resistivity is normalized to plot together for comparison. 69

Figure 4-15: Temperature dependence of resistivity under various magnetic fields for (a) 7 u.c. (b) 5 u.c. (c) 4 u.c. LSMO grown at 130 mTorr. (d) MR ratio vs. temperature for films with different thickness. 69

Figure 4-16: Effect of capping 2 u.c. $SrTiO_3$ on LSMO thin film. Temperature dependent resistivity for single LSMO thin film and LSMO capped with 2 u.c. STO (a) 3 u.c. LSMO; (b) 5 u.c. LSMO, (c) 6 u.c. LSMO; (d) 7 u.c. LSMO, (e) 5.5 and 6.0 u.c. LSMO capped with 2 u.c. STO. Growth pressure for (a-e) is 130 mTorr. (f) 6 u.c. LSMO grown at 80 mTorr. 71

Figure 4-17: Temperature dependent resistivity for LSMO films capped with 2 u.c. STO at region around 105 K. 72

Figure 4-18: (a) Temperature dependent resistivity under various magnetic fields for 6 u.c. LSMO capped with 2 u.c. STO grown at 130 mTorr. (b) Zoom-in of 105 K region. The resistivity is normalized for convenient comparison. (c) MR ratio for 6 u.c LSMO thin film with and without capping STO. All the films were grown at 130 mTorr. 72

Figure 4-19: XPS of Mn2p core levels for LSMO thin films with different thicknesses grown at same pressure. 73

Figure 4-20: XPS of Mn2p core levels for LSMO thin films of the same thickness grown at different Ozone pressures. 75

Figure 4-21: (a-d) Surface LEED images of the LSMO films grown at different pressures. The white arrows in (a) and (d) indicates the incommensurate spot and (1/2,1/2), respectively. A surface reconstruction pattern based on the LEED pattern in (a) is schematically shown in (e). The un-identified diffraction spots are labeled with green spots. The red spots are the 1x1 spots. Such surface is tentatively called α-structure. 76

Figure 4-22: Surface LEED pattern of 6 u.c. and 7 u.c. LSMO films grown at 130 mTorr. ...76

Figure 4-23: (a) Ion scattering spectrum (ISS) of 2 u.c. LSMO sample grown at 80 mTorr. The red line is the ISS of Sr element. The incident ion beam is 2 keV Ne^+. (b) ISS of 7 u.c. LSMO grown at 130 mTorr with using 1 keV Ne^+. The Sr has a double scattering (DS) peak right at the single scattering (SS) peak. The ISS of 6 u.c., 15 u.c. sample and $La_{2/3}Sr_{1/3}$ (From (110) LSMO surface) reference spectrum with using (c) 1.2 keV Ne^+ and (d) 1.2 keV He^+. 77

Figure 4-24: Evolution of the LEED-IV curves of LSMO films with 7 different thicknesses. The left top corner shows the diffraction beam. The corresponding thickness of the IV curves increases from bottom to the top for all panels. 79

Figure 4-25: The comparison between experimental LEED-IV curves and theoretical curves for 2 u.c. LSMO. 80

Figure 4-26: (a) Structure of 2 u.c. LSMO. (b) 3D structure model. 81

Figure 4-27: Effect of substrate transition on the transport properties. Temperature dependent resistivity under various magnetic field for (a) 6 u.c. LSMO (b) 6 u.c. LSMO capped with 2 u.c. STO. The films were grown at 130 mTorr. The red dash lines are tangent lines at the kink from left and from right. The resistivity is normalized for comparison. 84

Figure 4-28: XRD patterns of $La_{0.67}Sr_{0.33}MnO_{3-\delta}$ on (a) (001) $SrTiO_3$ and (b) (110) NGO. The LSMO 004 (peak) which is the (220) peak when (110) NGO is used as substrate shifts to the left with increasing δ, so the c value becomes bigger with increasing oxygen deficiency. Figure adapted from **[133]**. 87

Figure 4-29: Chemical composition depth profile for different thickness of LSMO calculated by Herger *et al.*. Figure adapted from **[132]**. 88

Figure 4-30: Two transitions in LSMO films with and without capping 2 u.c. STO and change of their T_c under field. 91

Figure 4-31: A comparison between the effect of capping 2 u.c. STO and magnetic field. Temperature dependent resistivity curves for single LSMO film, LSMO capped by 2 u.c. STO film, and single LSMO film under 14 T magnetic field are shown in blue line, red line and black line, respectively. 92

Figure 4-32: (a) Structure model of STO/LSMO/STO; (b) Schematic diagram of interface coupling and spin configuration [140]. 93

Figure 5-1: Schematic model of horizontal structure (left) and vertical structure (right) 95

Figure 5-2: (a) Typical picture of electronic phase separation induced inhomogeneity. Figure adapted from **[9]**. (b) Chemical phase separation in inhomogeneous nanocomposite system. 96

Figure 5-3: (a) XRD pattern of V_2O_3 thin film. (b) TEM image of the cross-section of V_2O_3 thin film and (c) High resolution STEM image of $LaAlO_3/V_2O_3$ interface. (d) Temperature dependence of resistivity of V_2O_3 thin films with different thicknesses and (e) plotted in Ln(R) Vs.1000/T scale. 98

Figure 5-4: (a) Temperature dependence of resistivity for 3D growth LSMO thin films with different thicknesses. (b) Effect of growth modes on transport properties of LSMO thin films. 99

Figure 5-5: Magnetoresistance effect in (a) 2.4 nm LSMO; (b) 32 nm V_2O_3........................100

Figure 5-6: (a) Scheme of growth of nanocomposite with alternate deposition method. (b) Structure models of the LSMO and V_2O_3 and (111) $LaAlO_3$ substrate..........................101

Figure 5-7: RHEED pattern (a) of LAO substrate; (b) after growing LSMO for 22 min on LAO; (c) after growing V_2O_3 for 24 min on LAO; (d) after growing 2.5 min V_2O_3 on LSMO. The note on the top of the pattern indicates the equivalent deposited thickness. 102

Figure 5-8: (a) Dark field image of the cross-section of α ≡ 13/10 nanocomposite. Bright field image (b) and dark field image (c) of the planar structure of same region....................103

Figure 5-9: (a) Planar view of the α ≡ 13/10 nanocomposite. (b) EELS spectrums of selected points in panel (a), P1(blue), P2(red), P3(black). (c)The calculated relative quantification of elements of Mn, V and La. (d) EELS mapping with STEM: <1> mapping area and relative concentration of <2>V, <3>La, and <4>Mn..104

Figure 5-10: (a) High-resolution cross-section image of α ≡ 13/10 nanocomposite via dark field STEM. The FFT of the selected regions in (a) are shown in (b) and (c). (d) HRTEM planar view image and (e) the smooth image of the Morie pattern in (d). (f) The FFT of Morie pattern...105

Figure 5-11: (a) Planar dark view image of the α ≡ 4/10 nanocomposite. High resolution TEM image of the dark island (b) and grey island (c). (d) Region for EELS line mapping. (e) EELS line mapping along the line in (d). 107

Figure 5-12: Dark field TEM planar view images of nanocomposites with different ratios. 107

Figure 5-13: Temperature dependent sheet resistance for nanocomposites with same ratio α but different individual deposition time..108

Figure 5-14: Resistance vs. temperature curves for nanocomposites with different α. Curves for the insulating nanocomposites are shown in (a) and for nanocomposites with metallic phase at high temperature are shown in (b). The resistances are normalized to plot together for comparing...108

Figure 5-15: Sheet resistance vs. temperature curves for (a) 2.4 nm LSMO (black) and α = 0.4 nanocomposite (red); (b) α = 2.0 (black) nanocomposite, α = 4.33 (red) nanocomposite and 5 nm V_2O_3 (blue). 109

Figure 5-16: Temperature dependent sheet resistance under magnetic field for (a) α=0.4, (b) α=1.0, (c) α=1.66. (d) α=1.8 nanocomposite. 110

Figure 5-17: (a) Temperature dependent sheet resistance of nanocomposites with different α values. (b) Phase diagram of V_2O_3-LSMO nanocomposite. 110

Figure 6-1: Left, Metal/Metal-Oxide/Metal sandwiched structure; Right, scheme of writing/erasing and read cycle. 114

Figure 6-2: Typical I-V sweep loop for (a) Unipolar resistive switching (b) Bipolar resistive switching. 115

Figure 6-3: Left, schematic diagram of Electrode/Metal-Oxide/Electrode cross-section structure with a interfacial transition region. The overall resistance of this sandwiched structure is $R_{I1}+R_{MO}+R_{I2}$; Right, scheme of filament model. 116

Figure 6-4: The *I-V* sweep loops for NiO films using Pt (black), Ta (red), and Al (green) top metal electrode, (a) as-fabricated devices (b) after one day. All samples have a Pt bottom electrode. X-ray photoelectron spectra of (c) Ta 4f and (d) Ag 3d. Ta 4f spectrum indicates oxidation of Ta while no oxidized Ag peak appears. Figures adapted from **[196]**. 117

Figure 6-5: Scheme of interfacial oxidation and reduction model. 118

Figure 6-6: Left, XRD pattern of PCMO thin film; Right, TEM image of cross-section of PCMO/Pt and ZOOM-IN of A and B regions. 120

Figure 6-7: (a) Photo of square electrode array on PCMO (b) Schematic diagram of measurement of TE/PCMO/Pt with probe station and inset is the photo of gold-tip contacting electrode 121

Figure 6-8: (a) I-V curve of Pt/PCMO/Pt devices. (b) Statistics of resistance of 100 hundred devices. 121

Figure 6-9: I-V characteristics for (a) Ag, Cu, Au, Pt/PCMO /Pt, (b). Al/PCMO/Pt, (c) Ti/PCMO/Pt, and (d) Ta/PCMO/Pt; The data was taken with bias looped from 0→3 V→-3 V→0. There are 6 consecutive loops for (b), (c) and (d), and label-1 marks the first loop, and 6 is the last. The size of the loop reduces progressively from 1 to 6. Label-F marks the forming process. Inset of (b), (c) or (d) shows the blow up of the hysteresis loop at positive bias. 122

Figure 6-10: (a) Virgin resistance (VR) vs. workfunction. The data of each TE material is an average over 100 devices, and small error bars indicate that these devices are quite uniform. The dash line marks the workfunction of PCMO **[206]**. (b)VR vs. metal-oxide formation free energy taken from Refs.**[207, 208]**. The dash line at -366KJ/mol. indicates the oxidation free energy of PCMO from **[209]**. 123

Figure 6-11: HRTEM images of interfaces between top electrodes and PCMO: (a) Pt/PCMO, (b) Al/PCMO , (c)Ti/PCMO and (d) Ta/PCMO. All figures have the same scale shown in (d). 124

Figure 6-12: Scheme of devices and I-V characteristics for Ag-Paste/PCMO/Pt (a), Ag-tip/PCMO/Pt (b), Ag-film/PCMO/Pt (c). The Cross-section view of Ag-Paste/PCMO is referred from **ref. 212.** 126

Figure 6-13: I-V characteristics for Pt(Ag, Au, W, Ni, Al)-tip/PCMO/Pt devices in (a)-(f). The schematic diagram of measurement with AFM is shown (g). 127

Figure 6-14: Scheme of mechanism of resistance switching in Electrode/PCMO junction. Left, oxygen migration induced interfacial oxidation/reduction. Right, oxygen pileup near non-reactive metal electrode under external electric field. 130

Figure 6-15: RS characteristics of the Al/PCMO/Pt memory devices: (a) The electroforming with different sweep voltages with the inset showing no hysteresis when $V < 1.5$ V; (b) Consecutive *I-V* sweep loops ($0 \rightarrow V_{max} \rightarrow 0$) V_{max}= 3 V; (c) Sequential I-V sweep loops ($0 \rightarrow V_{max} \rightarrow 0$) with V_{max} = 1.8 V (black), 3 V (red), 4 V (green); and (d) *I-V* sweep loop ($0 \rightarrow$ -3V$\rightarrow$3V$\rightarrow$0). Arrows and number indicate sweep direction and sequence. 131

Figure 6-16: (a) Consecutive *I-V* sweeps after electroforming with V_{max} = 3.0 V. Inset shows the zoom-in of the marked region of *I-V* curves of 6-sequencial loops. Label-1 marks the first loop (EF). (b) 6 groups of HRS and LRS are distinguished by the vertical dash line and the corresponding sweep parameter $V^{(-)}{}_{max}/V^{(+)}{}_{max}$ is indicated for each group. Resistance state was read at V_r=- 2.1 V. 132

Figure 6-17: HRTEM images (with the same scale bar) of Al/PCMO/Pt device cross section: (a) 125 nm thick PCMO; (b) 19 nm thick PCMO. (c) HRTEM image of 19 nm thick PCMO without Al layer. (d) XPS spectra of Al 2p core level showing distinct oxidization state. (e) *I-V* characteristics for electroformed Al/PCMO/Pt (black curve) and as fabricated Al/Al_2O_3/PCMO/Pt (red curve) 134

Figure 6-18: (a) Scheme of devices and measurement setup. (b) Resistance switching under pulsed cycles for (b)Ti/PCMO/Pt device and (c) Ta/PCMO/Pt devices 137

Figure 6-19: (a) Draft of SPM inside TEM, (b) TEM specimen holder, (c) Photo of the holder with SPM-tip and TEM specimen, (d) TEM image of Au-tip/Si contact. 139

Figure 6-20: (a)Schematic figure of cross-section specimen. (b) enlarged picture of cross-section structure as indicated in (a). (c) Schematic diagram for W-tip/PCMO Contact. 140

Figure 6-21: I-V characteristics for W-tip/Si/Pt device. Three I-V curves were taken every one minute. The I-V curves show a very excellent repeatability. 140

Figure 6-22: A schematic view of the *in-situ* TEM characterization setup. The W-tip is controlled by a 3D piezomotor and Pt electrode is grounded. The SiO_2/Si substrate is not shown. (b) An *I-V* sweep loop (0→5V→-5V→0) for W-tip/PCMO/Pt device measured inside TEM. The sweep sequence is 1→2→3→4. 141

Figure 6-23: (a) A TEM image of W-tip/PCMO/Pt devices. Inset is the resistance of the device versus time under -5 V bias and the thick solid line curve is used to shows the trend. (b) A zoom-in image of the selected region of the PCMO film marked in (a). (c) A zoom-in and time-dependent image of selected region marked in (b) under the electric field applied through the W-tip. The field intensity is estimated ~ 9×10^6 V m^{-1}. The dot curves sketch the boundary of stripe domain. The white arrows indicate the electric field directions. An electron energy of 200 keV was used for TEM imaging. 142

Figure 6-24: A series of TEM images for the decaying electric-field-induced stripes in a crystalline grain of PCMO film. The evolution started right after the applied electric field (~ 9×10^6 V m^{-1}) was removed. The crystalline orientation of the imaged grain is marked in panel (f). The inset is the corresponding FFT pattern. 144

Figure 6-25: (a) *I-V* hysteresis of Ag-Paint/PCMO/Pt; (b) Resistance relaxation after applying only positive sweep loop; Temperature-dependent *I-V* hysteresis in (c) linear and (d) logarithmic scale 145

Figure 6-26: (a) Zoom-in image of stripes in **Figure 6-23c**, showing a $p(3\times1)$ stripe superstructure along [001] direction; (b) The structural model in $(1\text{-}10)_P$-plane view of primitive lattice in pseudo cubic perovskite (ABO_3) structure; A possible $A_3B_3O_8$ oxygen vacancy model in (c) $(110)_P$- and (d) $(1\text{-}10)_P$-plane view. 147

Figure 6-27: AFM image of CeO_2 surface. 149

Figure 6-28: (a) XRD pattern of single crystalline CeO_2 thin film (b) TEM image of cross-section of CeO_2/NSTO (c) High resolution image of CeO_2 thin film (d) High resolution image of CeO_2/NSTO interface. 150

Figure 6-29: I-V sweep loops of Top-electrode/CeO_2/NSTO with different top-electrodes of Ag, Au, Pt, Al, Ta, Ti 151

Figure 6-30: (a) Consecutive I-V (0→2V→0) sweep loops on Ag/CeO_2/NSTO, (b)Retention behavior of HRS and LRS of Al/CeO_2/NSTO. The resistance was read at 0.3V. 152

Figure 6-31: I-V loop of Au-tip/CeO_2/NSTO inside TEM. Inset is TEM image of Au-Tip/CeO_2/NSTO devices. Figure adapted from **[220]**.. 154

Figure 6-32: (a) High resolution image of CeO_2 film along <110> zone axis and its diffraction pattern and structure model shown in (b) and (c) respectively. After application of 5 V bias, superstructure appeared. The higher resolution image is shown in (d), the diffraction pattern and structure mode are shown in (e) and (f) respectively. Figures adapted from **[220]**. 154

Figure 6-33: (a) Atomic-level TEM image of Ceria single crystal film alone <110> zone axis. Inset: corresponding electron diffraction pattern. (b) EEL spectra of Ce-M edge. (c) 10 V voltage ($E \sim 1.5\times10^8$ *V/m*) was applied between the gold tip and Nb-STO. The gold tip was anode. Superlattice reflections and extra diffraction spots (inset) appeared. (d) A reversal in the intensity of Ce M_{45} was observed; and the shoulder indicated by arrow in (b) disappeared. Figure b and d adpated from **[220]**. 155

Figure 6-34: (a) Structure of a MOH RRAM device. (b) Schematic diagram of working mechanism. 161

Figure 6-35: (a) three types of relation between change of resistance (ΔR) and number of oxygen (ΔN) moving across the MOH interface. (b) Applied bias versus time and corresponding ΔN versus time. (c) Correspond I-V curves for three types of MOH in (a). 163

Figure 6-36: I-V sweep loop (1→2→3→4) of (a) Ta/TaO_x/CeO_2/Nb-STO; (b) Al/Al_2O_3/PCMO/Pt. 164

Figure 6-37: (a): Electron moves via Mn-O-Mn chain and is blocked after that the oxygen ion is removed. (b) Band structures of CeO_2 without oxygen vacancies and with oxygen vacancies. 166

Figure 6-38: (a) Schematic cross-section structure of Pt/CeO_2/PCMO/Pt MOH device. (b) First I-V sweep loop (forming process). Reproducible I-V hysteresis in linear scale (c) and in logarithm scale (d). 166

Abstract

Complex metal oxides, such as transition-metal oxides, appearing with exotic properties and optimal functionalities, present formidable challenges in condensed matter physics, while at the same time, immense opportunities in materials science and engineering. The signature of these materials is the multitude of competing ground states that can be tuned or manipulated by doping, structural modification, strain induction, or the application of external stimulus, such as pressure, electric or magnetic fields, etc. The interest in these materials stems from the richness of their novel properties, the complexity of underlying physics, and the promise of technological applications.

Novel phenomena emerge by spatial confinement. Stoichiometry can have more profound effect on spatially confined materials than on the bulk. The purpose of the thesis is to explore and understand the spatial confinement and oxygen stoichiometry effect on complex metal oxides to pave the way for oxide electronics. To achieve this goal, I first investigate the properties of the $La_{2/3}Sr_{1/3}MnO_3$ (LSMO) thin films of different thicknesses with different oxygen deficient level. Reducing the thickness of the LSMO thin film drives the LSMO to behave far away from its bulk and leads to several new phenomena such as enhanced magnetoresistance at critical thickness, emergent of effect from substrate structure transition and interface coupling. Unlike the bulk, introduction of few oxygen vacancies can strongly affect the properties of LSMO ultrathin film.

Furthermore, I also investigated the epitaxial columnar naoncomposite thin film to study nanoscale inhomogeneity effects on properties of thin films. It is revealed that percolation plays most important role in determining properties. Finally, I also studied the dynamic

effects of the oxygen vacancies in oxide materials thin films under external electric field. I show that the field can control the oxygen stoichiometry via field induced oxygen migration and then control the properties of the complex metal oxide in real time. Due to the strong coupling of oxygen with the complex metal oxides, field induced oxygen migration will cause a colossal change of resistance. As a result, we can engineering complex metal oxides for the technological applications such as non-volatile memory devices.

Chapter 1 Introduction and Background

1.1 Introduction

Transition metal oxides (TMOs), one class of most focused complex metal oxides (CMOs), displays an array of extraordinary phenomena, e.g., high temperature superconductivity **[1]**, multiferroicity **[2]**, ionic conductivity **[3]**, colossal magnetoresistance **[4]**. These materials are of great interest in fundamental physics and have many potential technological applications for energy transfer, superconducting quantum computation, non-volatile memory, gas sensor, electronics, and fuel cell, transistor **[5-7]**. More importantly, the emergent phenomena in these materials present formidable challenges in condensed matter physics as well as materials science.

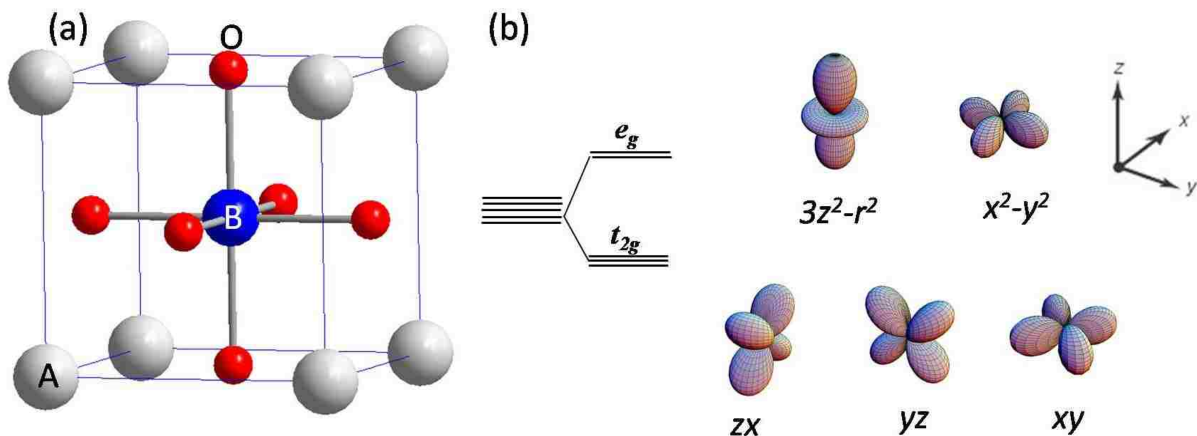

Figure 1–1: (a) Structural model of perovskite; (b) Splitting of d-orbital.

It is becoming increasingly clear that the exotic properties displayed by complex metal oxides, such as cuprates, manganites and heavy-fermion compounds, are intimately related to the coexistence of competing nearly degenerate states which couple simultaneously active degrees of freedom—charge, lattice, orbital, and spin states **[8, 9]**. One example comes from the correlation between lattice and orbital degrees of freedom in perovskite compounds as shown in **Figure 1-1**, a very popular class of TMOs. An ideal perovskite structure is cubic

with an empirical formula ABO_3. The A cations are located on the corners, the B cation generally being a transition metal element is located in body center while the oxygen atoms occupy the face center and form a BO_6 octahedral. Due to the symmetry of the crystal field defined by lattice structure and the configuration of the d-orbital, the d orbitals of B cation are split into e_g ($d_{3z^2-r^2}, d_{x^2-y^2}$) and t_{2g} (d_{xy}, d_{zx}, d_{yz}) with e_g having higher energy level. The e_g electrons are more itinerant and the t_{2g} electrons are more localized generally. The degenerate d-orbital further affects the spin coupling, thus creating a complex system which is more than the sum of its single parts [**9**]. Through varying the ionic size of the A site or doping level of B site, etc., we can introduce the tilting and rotating of oxygen octahedral, thus change the band width and tune the occupation of the d-orbital. As a result, a tremendous and exciting phenomena emerge [**8**]. On the other hand, the striking phenomena associated with these materials are due in large part to spatial electronic inhomogeneity or nanoscale phase separation **[9-11]** because of the nature of competing nearly degenerate states existing in these materials. In many of these hard materials, the functionality is a result of the soft electronic component that leads to self-organization.

The complexity of CMOs is directly responsible for their controllability. The signature of these materials is the multitude of competing ground states that can be tuned or manipulated by doping, structural manipulations, strain induction, and the application of external stimulus, such as pressure, electric/magnetic fields (see **Figure 1-2**). Furthermore, the creating surfaces, interfaces, ultrathin films, and artificial superstructures add the additional twists of 'man-made' dimensions, approaching the quantum phenomena of correlated electron materials with broken symmetry and reduced dimensionality.

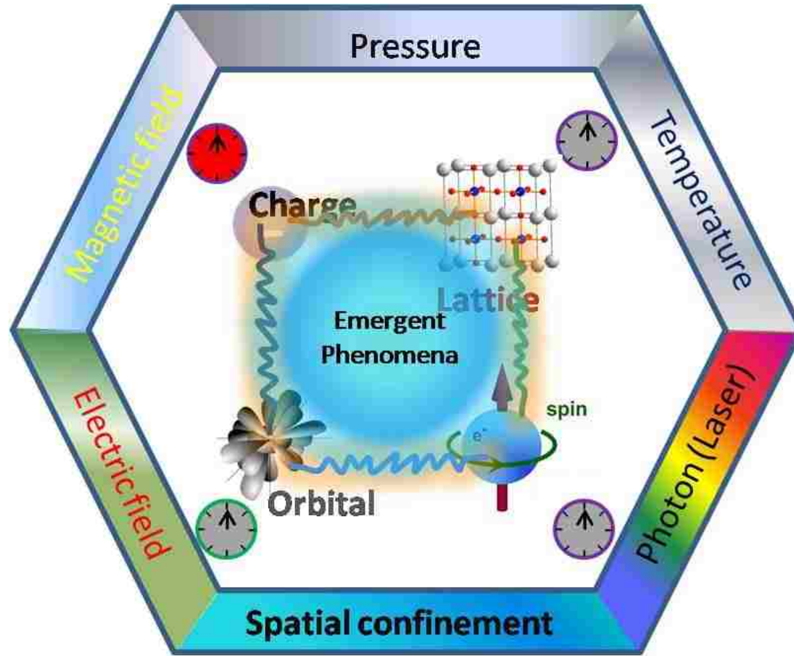

Figure 1–2: Schematic view of coupling between different kinds of degrees of freedom in CMOs, which could be tuned by external stimulus, such as pressure, temperature, laser, spatial confinement, electric and magnetic field.

1.2 Spatial Confinement Effect

Smaller can be different and better. There must be a scale that connects and behaves quite differently from both the classical materials and a localized single atom. Such scale which is expected to have emergent behavior is recognized as NANO now. The unprecedented idea and roadmap of NANO are first inspired by Feynman who imagined a world where objects are composed of a few atoms in his talk on Annual American Physical Society in 1959 **[12]**. Several decades later, the emergent phenomena in nanoscale materials are greatly and comprehensively demonstrated in lots of materials ranging from single element substance such as gold nanodots to compound such as manganite thin films. Nanoparticle, nanowire, and ultrathin film, *etc.*, are typical examples of nanomaterials. Broadly speaking, these nanostructural materials result from spatial confinement, which is of both interest to technology and basic science. Spatial confinement reduces the size of the materials and

typically the dimensionality, for example, confining a bulk material to 2 dimensional (2D) ultra thin film. The most obvious reduced dimensionality effect is the change of density of state (DOS) (see **Figure 1-3**), which is extremely important for almost every aspect of materials' properties. From 3D to 0D, the DOS changes from continuous function (3D) to step function (2D), sawtooth (1D) and δ function (0D). With respect to the band structure, the smaller size the material, the wider band gap we get. These will dramatically vary such as mechanical, thermal, electronic, optic, magnetic properties and even chemical reaction.

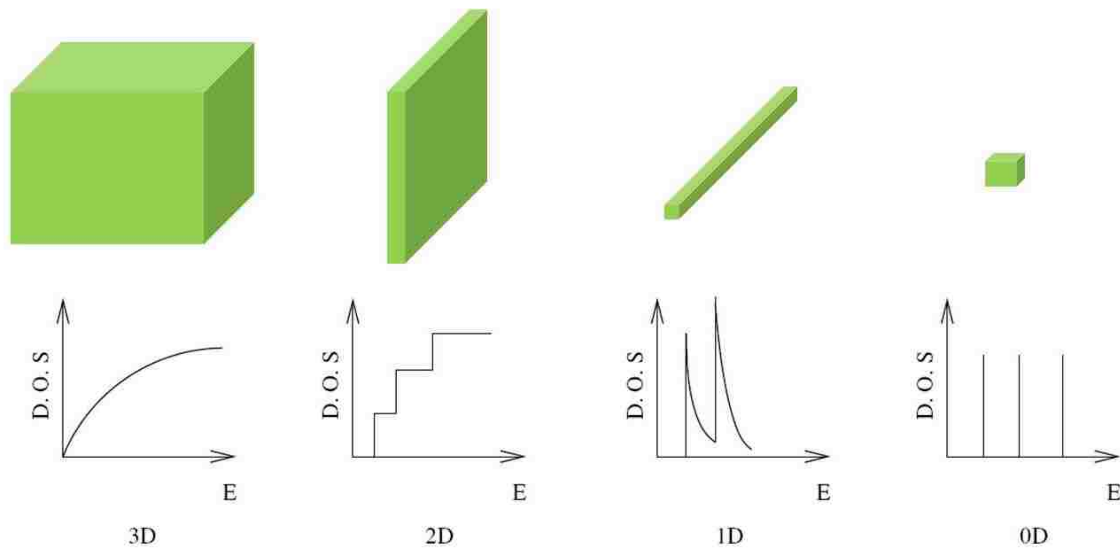

Figure 1–3: Reduced dimensionality induced change of density of States (DOS).

Here we will show some examples of the spatial confinement effect. Gold generally is very inert, but the gold nanodots with the radius of about 3 nanometers can catalyze the oxidation of CO to CO_2 **[13]**. Some non-magnetic materials (e.g. Rh) can become magnetic at nanoscale **[14, 15]**. The reduced dimensionality can control the electronic phase transition in $LaNiO_3/LaAlO_3$ superlattice **[16]**. Quantum well state emerges in ultrathin $SrVO_3$ film **[17]**.

Many materials have some kinds of inherent length scale of interaction, or inhomogeneities (for example, phase separation). These length scales could vary from 1 nm to 1 micrometer. The superconductive coherent length which is the characteristic size of

cooper pair is about 2 nm in $YBa_2Cu_3O_7$ in a-b plane. The Bohr radius of 1s exciton in bulk ZnO is reported to be 2.34nm **[18]**. As shown in **Figure 1-4**, the phase separation domain size in $La_{0.55}Ca_{0.45}MnO_3$ is about 5 nm as revealed by transmission electron microscopy **[19]**. The largest micrometer domain size is reported in $La_{1-x}Pr_xCa_{3/8}MnO_3$ (LPCMO) which is directly confirmed by AFM image (see **Figure 1-4**) **[20]**.

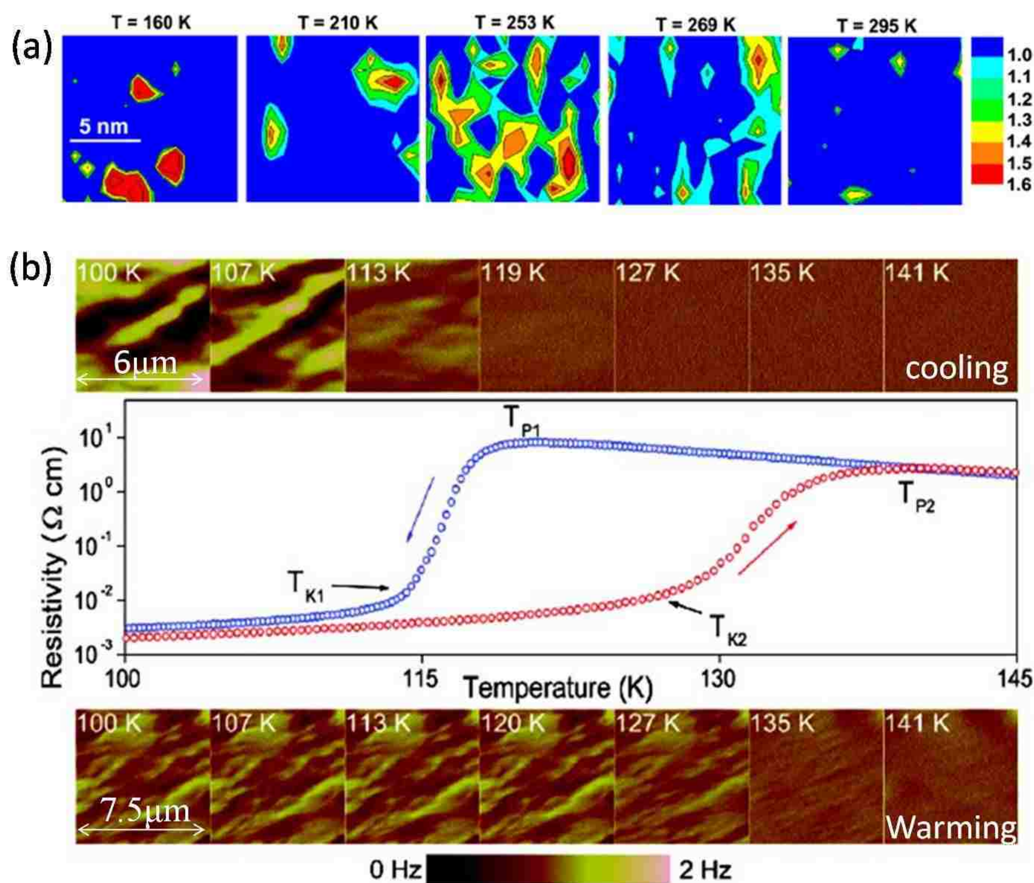

Figure 1–4: (a) Phase separation in $La_{0.55}Ca_{0.45}MnO_3$ evolves with temperature imaged by TEM. (b) MFM images of phase separation in $La_{1-x}Pr_xCa_{3/8}MnO_3$ (LPCMO) and its evolution with temperature. Figures adapted from **[19, 20]**.

Novel phenomena will emerge when the a material is confined to a scale which is comparable with the inherent length scale in the bulk. If the radius of a semiconductor quantum dot is smaller than its Bohr radius, the band gap then will increase. As a result, its absorption and emission wavelengths will have a blue shift **[21]**. The quantum dots provide a less costly avenue to adjust the band gap. Quite different from bulk where the shape has

almost no effect on properties, the shape of quantum dots can control the electron wave functions. For example, the wave-functions in rectangular dots are more s-type than p-type, while in pyramid-shaped dot, the wave-functions are mixed with s-type and p-type due to asymmetry **[22]**. With respect to the complex metal oxides, the spatial confinement will strongly affect the co-existent and competing coupling among the spin, lattice, charge and orbita, thus it is another key control parameter to tune the properties. A good example comes from the achievement of high superconducting critical temperature (T_C) in two dimensional $HgBa_2Ca_2Cu_3O_8$ **[23]**. The conductive CuO_2 plane in $HgBa_2Ca_2Cu_3O_8$ which is sandwiched by insulating layer forms a 2D correlated electron system which greatly affects the interaction among the spin, charge, lattice and orbital, and somehow leads to a higher T_C.

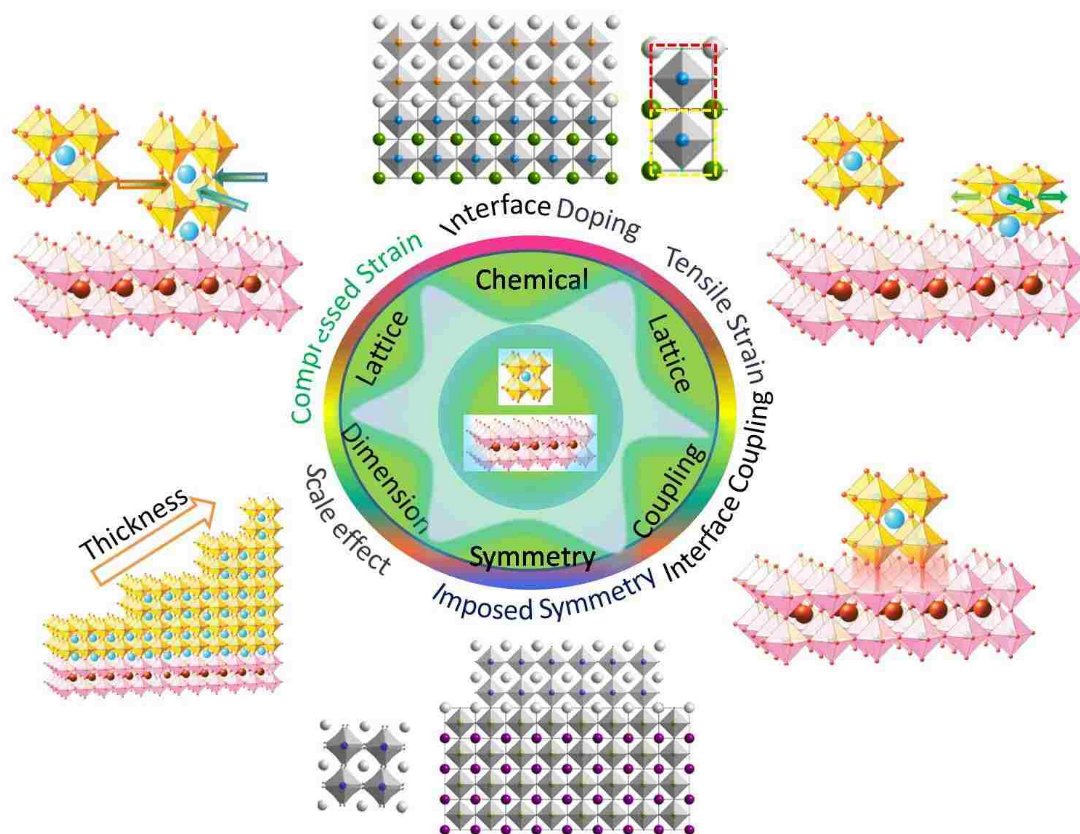

Figure 1–5: Tuning parameters in ultrathin films.

Motivated by expected exotic phenomena in low dimensional complex metal oxides, people have been making a great effort to grow and investigate artificial low dimensional

oxides during past decades. Among a lot of kinds of nanostructural oxides, a supported complex oxide grown on a substrate is attracting much more interest not just because of their immense potential technological application bust also of their emergent new physics. The supported nanostructural will have considerable interface and surface effect **[24]**, as well as the strain effect **[25]** coming the substrate besides the spatial confinement forced on out-of plane direction. It can be expected that the interface or surface will have almost the equal role to inner part in a ultrathin film with only a few layers. The strain can lock the lattice parameter of epitaxial thin film to that of a substrate up to a scale of a few nanometers **[26]**, although it is quickly released after this scale [**27]**. A schematic diagram of the possible effect appearing in the ultrathin film system is summarized in **Figure 1-5**.

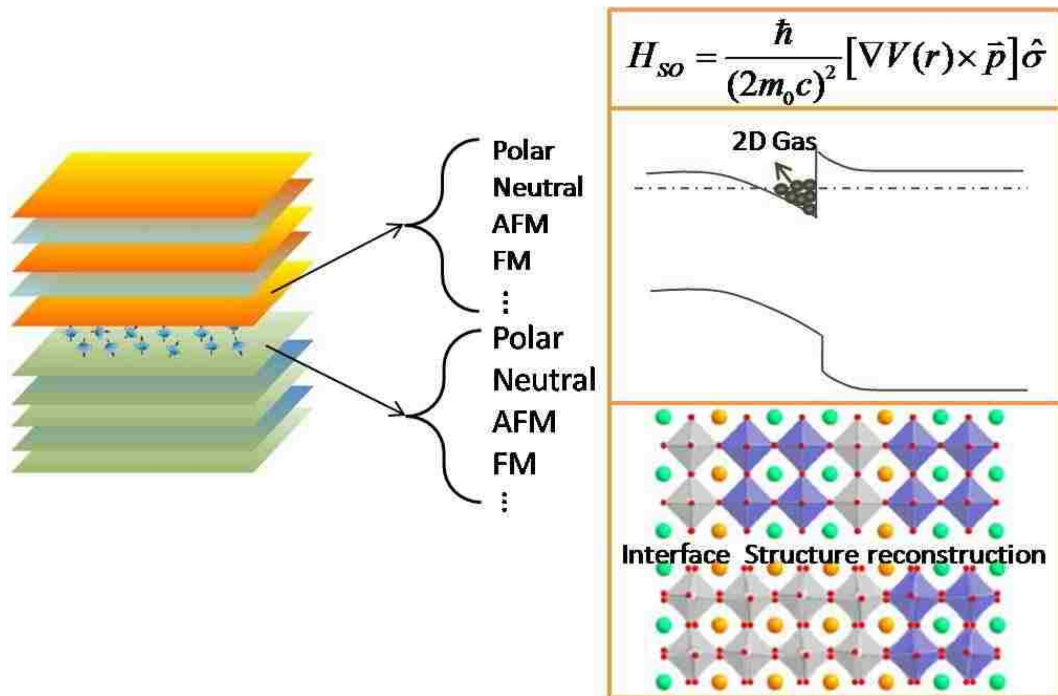

Figure 1–6: Left, possible interface combination; Right, possible interface effects.

There are several kinds of interfaces, e.g., polar-polar interface, FM-AFM interface, polar-neutral interface as shown in **Figure 1-6**. The interface may have strong spin-orbital coupling due to the abrupt change of lattice field appearing at interface, or built-in electric

field caused by electron re-distribution as well as structural reconstruction. For example, the polar (001) $LaAlO_3$ grown on non-polar (001) $SrTiO_3$ could drive the electron to interface, thus inducing a 2D free electron gas at the interface **[28]**. More surprisingly, this 2D electron gas becomes superconductive at low temperature of below ~300 mK **[29].** The interface charge transfer in La_2CuO_4 and $(La,Sr)_2CuO_4$ interface changes the doping level of each material, causing the bulk to become non-superconductor while the interface is still superconductive [**30, 31**]. Another example of the interface effect is the spin reconstruction due to interface coupling. The interface of $LaFeO_3$ with $LaCrO_3$ surprisingly becomes ferromagnetic though both the $LaFeO_3$ and $LaCrO_3$ are antiferromagnetic [**32**]. Such emergent ferromagnetic property has been explained by superexchange coupling of Fe^{3+}-O-Cr^{3+} which is originally proposed by Anderson **[33]** and Goodenough [**34**].

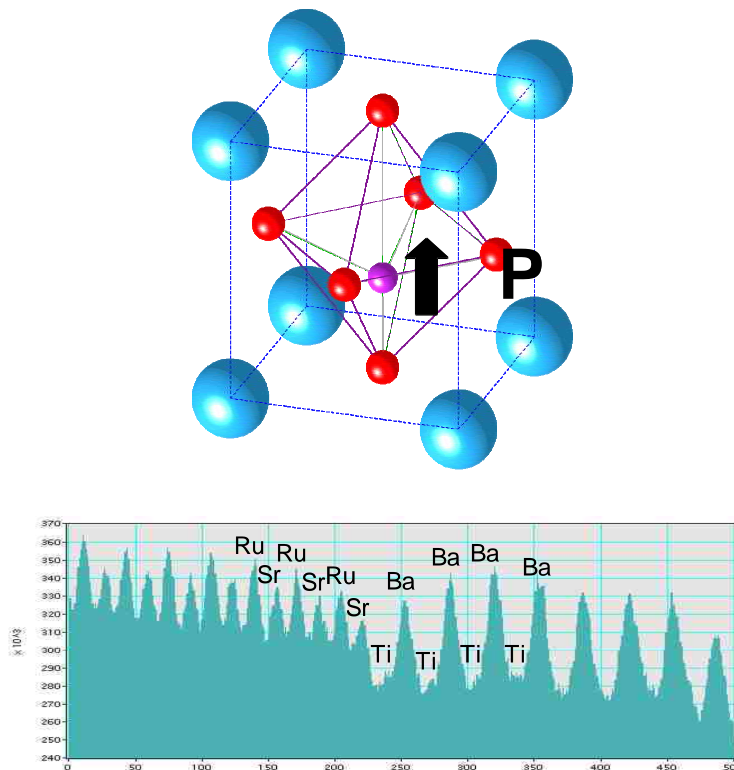

Figure 1–7: Top, structural model for the surface of $BaTiO_3$ showing the polarization direction. Bottom is STEM EELS measurement showing the chemical abrupt interface. Figure adapted from [**35**].

Sometimes interface coupling will have long-range effect, completely changing the whole thin film's properties. One example is the polar distortion of ultrathin $BaTiO_3$ film, a classical ferroelectric material. Fully strained epitaxial $BaTiO_3$/$SrRuO_3$ (BTO/SRO) bilayer were grown on (001)-oriented TiO_2-terminated $SrTiO_3$. A 15-nm-thick SrO-terminated SRO film with an atomically flat surface was deposited as a bottom electrode followed by the growth of ultrathin BTO films (4 and 10 unit cell) [**35**]. The surprising result for both 4 and 10 unit cell thick films was that the surface BaO layer was polarization dead but the second TiO_2 layer is vertically polarized with the polarization pointing out of the surface. The film has a monodomain of vertical polarization shown schematically in **Figure 1-7**, which is attributed to the intrinsic asymmetry (SRO/BTO/vacuum) and the stability of a polarized phase to compensation of depolarizing charges by dipoles induced by surface stress [**36**]. The bottom of **Figure 1-7** shows the STEM-EELS data across the BTO/SRO interface revealing an ordered and chemically abrupt interface.

There could be a cross-over transition due to the reduced dimensionality. The bulk $SrVO_3$ is correlated metal. With the thickness of the $SrVO_3$ thin film being reduced, the ultrathin film of 1 unit cell is a Mott insulator and the film of 2-3 unit cell thick has the metal-to-insulator transition; the bulk like properties start to develop at about 6 unit cell **[37]**. This dimensionality driven MIT is thought to arise from the reduced bandwidth with decreasing thickness and a conversion of 3D band structure into 2D. The dimensionality driven transition of a thin film from bulk to non-bulk properties is commonly observed in other complex metal oxides. A critical thickness responsible for this transition is called deal layer generally. Either the magnetic or electric dead layers have been reported in

$La_{2/3}Ca_{1/3}MnO_3$ **[38]** and $La_{2/3}Sr_{1/3}MnO_3$ **[39, 40]** thin films. The transport properties as a function of thickness of $La_{2/3}Ca_{1/3}MnO_3$ and $La_{2/3}Sr_{1/3}MnO_3$ are shown in **Figure 1-8**, which shows that the films become insulator below certain thickness for both optimized doping $La_{2/3}Ca_{1/3}MnO_3$ and $La_{2/3}Sr_{1/3}MnO_3$. It is generally accepted that the reduced dimensionality will indeed cause a dead layer. However, some other ingredients such as strain **[39-43]**, non-stoichiometry **[44-45]** and interface coupling **[24, 46]** should also contribute to the observed thickness of dead layer. For example, the dead layer of $La_{2/3}Sr_{1/3}MnO_3$ on $NdGaO_3$ is reported to be ~3 nm while on the $LaAlO_3$ which has more compressed strain is about 5 nm. The built-in electric field at electric contact region may also affect the thickness of the dead layer. Liang *et al.* shows that the dead layer of $La_{2/3}Ca_{1/3}MnO_3$ on conductive Nb-$SrTiO_3$ substrate is 4.4 nm, much less than that (= 13 nm) of the case on insulating $SrTiO_3$ substrate **[38]**. As a result, the sole reduced dimensionality induced exact thickness of dead layer still remain mysterious.

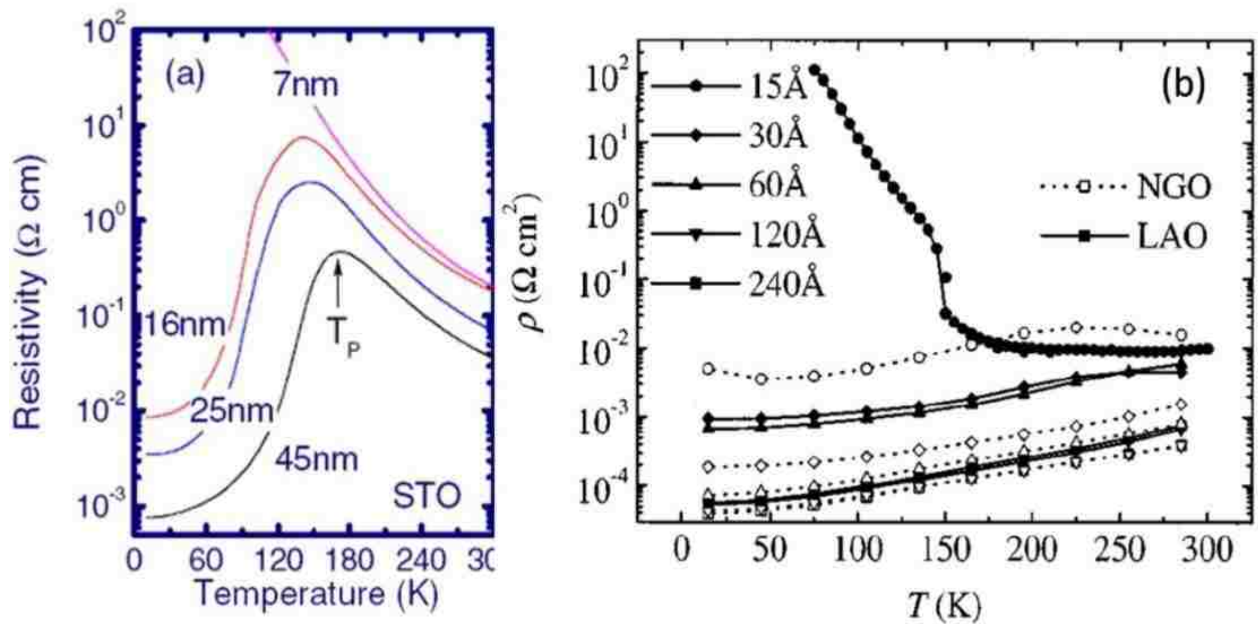

Figure 1–8: Transport properties of (a) $La_{2/3}Ca_{1/3}MnO_3$ and (b) $La_{2/3}Sr_{1/3}MnO_3$ thin films with different thicknesses. Figures adapted from **[38, 39]**.

Another scale typically existing in correlated electron materials is the size of the inhomogeneity [**9, 10**]. The relative size of a material to its inside domain size of individual phase critically affects the properties. Although the direct cause of the inhomogeneity still remains mysterious, it is generally thought to be either chemical disorder or spontaneous electronic phase separation leading to the inhomogeneity. The phase separation will occur in almost any strongly correlated electron system near a bi-critical or multi-critical point which is precisely where these studies will be conducted. Any small fluctuation close to the critical region caused by such as thermal or chemical disorder will lead to the "Butterfly Effect". For example, change of A site radius $<r_A>$ by 0.002% in $La_{5/8-y}Pr_yCa_{3/8}MnO_3$ will induce a huge change of their transport properties [**47, 48**]. There will always be a length scale for domain size of separated phase in these materials. When the materials has reached that scale, one would expect a fundamental change of the properties.

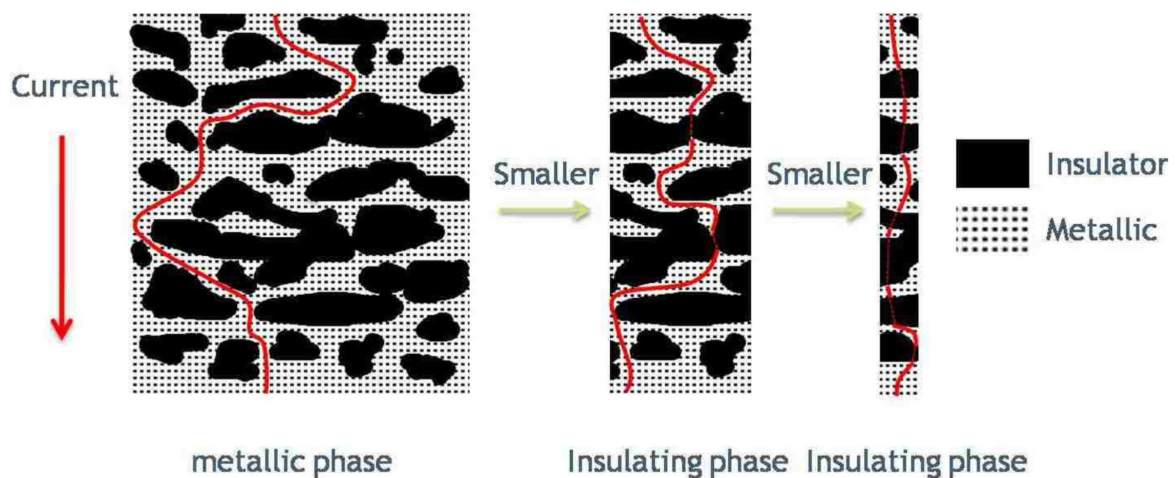

Figure 1–9: Spatial confinement effect on percolation.

Although we don’t know exactly whether and how the spatial confinement would affect the coupling, its effect on transport properties in a phase separated materials could be expected. In a system where metal and insulator phases coexist, electrons will prefer the lowest resistivity region to flow through and bypass the high resistance area. In bulk, the

individual domain will be hidden in domain sea. As shown the **Figure 1-9**, if the size of a material is much bigger than its characteristic domain size, the percolation would more easily occur than the case that the scale of the material is comparable with its domain size. If a wire could be fabricated with a width on the same scale or smaller than scale expected for the electronic phase separation in the CMOs, one would expect quite dramatic changes in functionality and the emergence of new phenomena. The challenge is that the expected length scale is in the order of nanometers, which makes fabrication very difficult. Fortunately, submicrometer scale of phase separation has been observed in the $La_{1-x}Pr_xCa_{3/8}MnO_3$ (LPCMO) system where ferromagnetic metallic and charge order insulating domains of ~ micrometer coexist **[47]**. This large scale phase coexistence makes the LPCMO an ideal model system for fabrication, because wires of micrometer wide can easily be achieved by using conventional lithographic fabrication processes. The scientists in Oak Ridge National Lab realized the unique characteristics of the domain size in LPCMO and they confined LPCMO into submicrometer wires [**49, 50**]. The LPCMO thin films were first epitaxially grown on single crystal substrates using Laser Molecular Beam Epitaxy. Wires were fabricated from the epitaxial thin films using conventional wet-etch optical lithography [**49**]. **Figure 1-10** illustrates the dramatic changes in transport behavior that spatial confinement can cause on CMOs. The thin film (red) shows a metal-insulator transition (MIT) at ~ 180 K just like that in the bulk. The wire exhibits a MIT at a slightly lower temperature (~ 150 K) than that in the film, but after entering a region of metallicity (~125 K), the resistivity rebounds and forms a second MIT--a reemergent MIT. This behavior was found to be tunable through the balancing of strains induced by the substrate and doping composition [**50**].

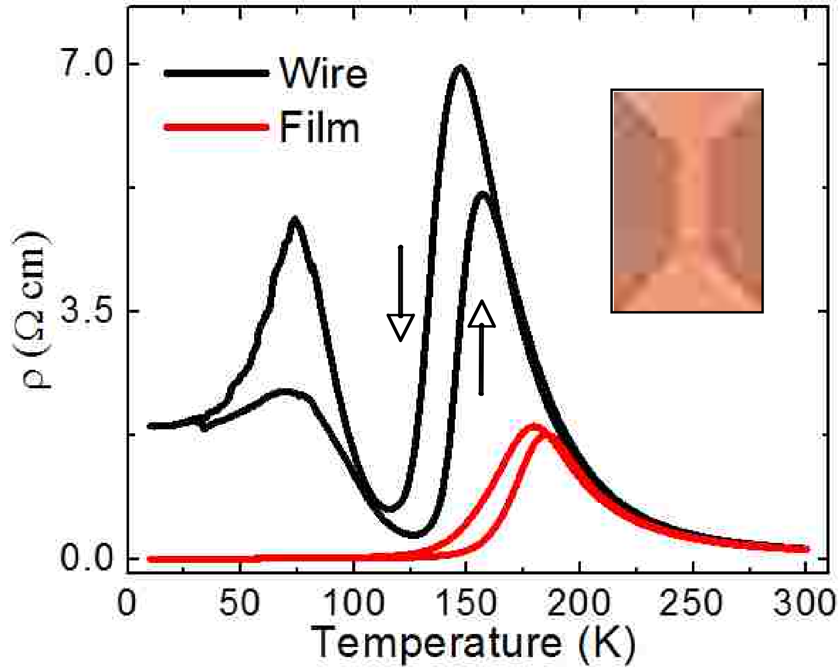

Figure 1–10: Resistivity in a 10μm LPCMO (x=0.3) wire (black) as a function temperature The red curves are for the thin film. The measurements were made at 1T and the arrows show the heating or cooling cycle. The inset shows a SEM image of the wire. Figure adapted from **[50]**.

1.3 Oxygen in Metal Oxides

Oxygen atom with non-magnetic 2p-electron outside has very high electron affinity. The 2p electron plays an important role in orbital hybridization and formation of crystal. Oxygen in metal oxide will pull valence electrons away from metal cations, resulting in strong interatomic electric fields, which will generate correlated interaction. In ferroelectrics materials, using $BaTiO_3$ as an example, hybridization of d orbitals with occupied p orbitals of the octahedrally coordinated oxygen ions can induce long range polarization **[51]**. The 2p electron in oxygen atom can be an intermediate for electron wandering through double exchange [**52]**. The double exchange mechanism is schematically shown in **Figure 1-11**. We choose Mn-O-Mn chain as an example to illustrate the double exchange. As a spin up electron of O 2p could jump to empty e_g orbital of Mn^{4+}, and the spin up e_g electron in Mn^{3+} jumps to O 2p, the e_g electron can wander from one Mn^{3+} to neighbor Mn^{4+}, creating a

conductive channel. The double exchange will induce a ferromagnetic coupling between two neighbor Mn atoms, resulting in the coupling between electrical phase and magnetic properties as broadly observed in many manganites **[53]**. In high temperature superconductive cuprates, such as $YBa_2Cu_3O_{7-x}$, the special strong interaction between electron and the two dimensional Cu-O plane is thought to be the reason of making cooper pair more tightly bonding. Oxygen orbital is one of the important issues in the Cu-O plane **[54]**.

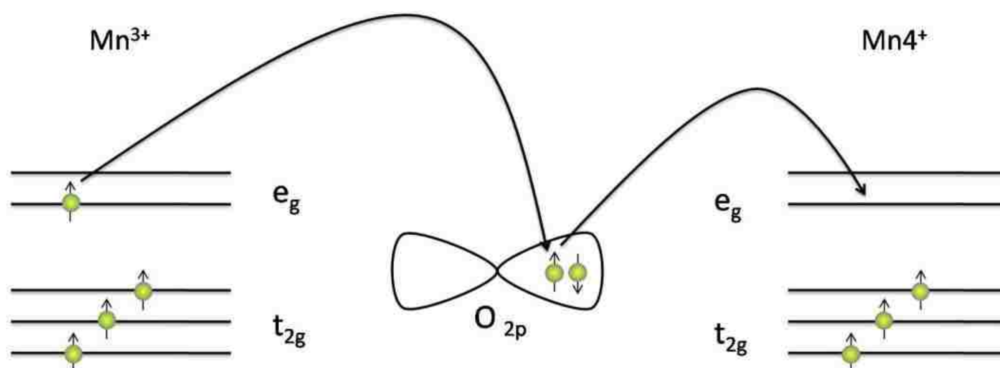

Figure 1–11: Scheme of mechanism of double exchange.

The importance of the oxygen is also reflected in the role of oxygen vacancies in metal oxides. Due to the nature of oxygen of gas state, oxygen vacancies are easily introduced through decreasing oxygen partial pressure during growth of a crystal or post-annealing in vacuum. More than a solely doping effect, like defects in a simple semiconductor, oxygen vacancy can strongly change the correlation effects especially in transition metal oxides. The oxygen vacancy can change structure; dope with electron/hole; vary valence of cation; induce local strain and change local electron density finally changing the magnetic, dielectric properties and transport properties of complex metal oxides. In high temperature superconductive cuprates, the occupancy of oxygen vacancy at particular crystal sites and its concentration both are very important for superconductive critical temperature **[54-57]**. The

oxygen vacancies can change the ferroelectricity of $Bi_4Ti_3O_{12}$ **[58]**; tune the ferromagnetism of Fe doped In_2O_3 **[59]**; control the metal-to-insulator transition temperature in $La_{2/3}Sr_{1/3}CoO_3$ **[60]**; switch insulating $SrTiO_3$ to superconductor/metal [**61**]. **Figure 1-12** sketches several examples of the oxygen deficiency effect on the complex metal oxides.

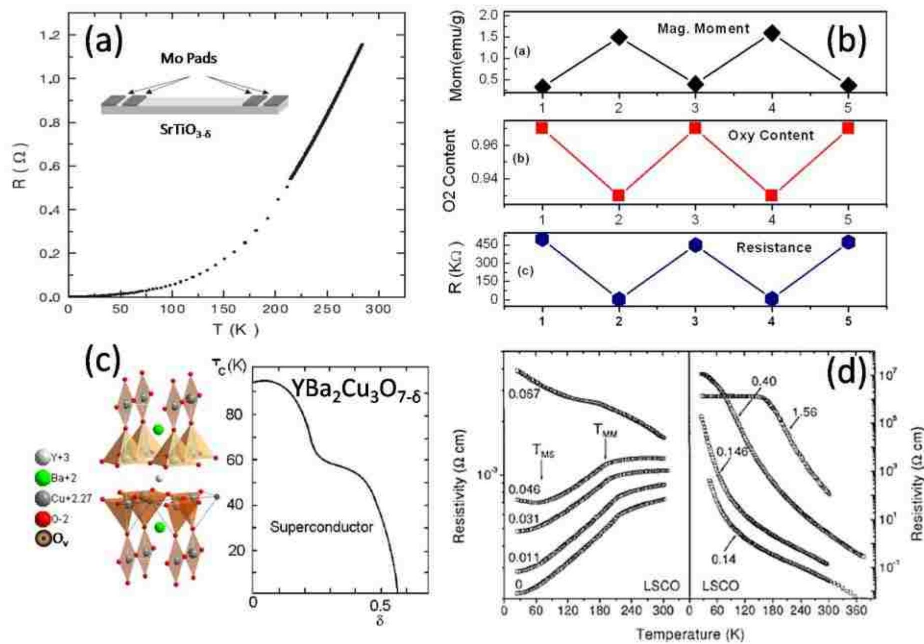

Figure 1–12: (a) Resistance of oxygen deficient $SrTiO_{3-\delta}$ as a function of temperature. (b) Coupling of the magnetism and resistivity with oxygen content in Fe-In_2O_3. (c) The superconductive critical temperature vs. Oxygen vacancy concentration in $YBa_2Cu_3O_{7-\delta}$. (d) The transport properties of $La_{2/3}Sr_{1/3}CoO_3$ thin films with different oxygen vacancy contents. Figures adapted from **[59-61]**.

In perovskite $SrTiO_3$, the oxygen captures two electrons and forms O^{2-}. After removing a oxygen to create a vacancy, two electrons then are released. As a result, the oxygen vacancy acts like a double electron donor [**62**]. Doping electron is just one aspect of the roles that oxygen vacancies play. It is reported in 2005 that introduction of the oxygen vacancies by Ar^+ irradiation will make $SrTiO_3$ shine blue light and even enhance the bandgap energy emission but at the same time we have to notice that the $SrTiO_3$ is an indirect semiconductor [**63, 64**].

Oxygen adds another degree of freedom allowing us to tune the properties of complex metal oxides. We may ask questions such that how the oxygen vacancies affect the properties

of nanostructural complex metal oxides and is it different from that in bulk. To date, very few researches directly compare the oxygen defects in nanostructure with those in bulk. There is one report by Kotomin *et al.* on such issue accomplished by first-principle calculations of oxygen vacancies in ultrathin $SrTiO_3$ thin film **[65]**. They show that surface plane defect properties differ from the bulk. Formation energy of oxygen vacancies (V_O) at the surface dramatically decreases by 1 eV and the defect energy level locates much deeper in the band gap. The behavior of Ti-V_O-Ti complex differs with different orientations (parallel or perpendicular to the surface). Oxygen defects (e.g., vacancies) could have much more different effect in the nanostructural complex metal oxides than in the their counterpart of bulk.

Generally, the oxygen content can be controlled during the growth by controlling oxygen partial pressure, after growth by annealing and quenching in specific atmosphere. The Ar^+ irradiation as mentioned above is another example to manipulate the oxygen. All these methods can be categorized into "static control". In contrast to this “static” control, dynamic control could be accessed too due to mobility of oxygen in many metal oxides. The field can move the oxygen, so it could be an ideal way to dynamically control the oxygen vacancies. In other words, a real time control of the properties of metal oxides can be achieved dynamically. Such possibility is promoted in nanoscale materials where ultra strong electric field (> MV/m) could be easily accessed. At low electric field, the drift velocity of oxygen is proportional to the external electric field so that the mobility ($\mu = v_d/E$) is a constant. Unfortunately, the mobility is relatively low for most of the metal oxides. **Table 1-1** lists the mobility of several metal oxides **[66-71]**. Taking example of $BaTiO_3$, it is just 10^{-14} $cm^2 s^{-1} \cdot V^{-1}$ at room

temperature **[68]**, which will cost the oxygen to take nearly 4 months to travel through 10 nm under 1 kV/cm electric field.

Table 1-1: Oxygen mobility and travelling time in a distance of 10 nm for different materials under a electric field of 1 kV/cm. Electron mobility in Si is listed for comparison.

Material	μ ($cm^2.s^{-1}.V^{-1}$)	(E=1kV/cm) V_d ($cm.s^{-1}$)	(*l*=10 nm) τ (s)
$Pr_{0.7}Ca_{0.3}MnO_3$[66]	3.8×10^{-12}	3.8×10^{-9}	260
$SrTiO_3$[67]	10^{-13}	10^{-10}	1000
$BaTiO_3$[68]	10^{-14}	10^{-11}	10000
TiO_2[69, 70]	4×10^{-17}	4×10^{-14}	2.5×10^{7}
Electron in Si[71]	1000	10^{6}	10^{-12}

However, ultra strong electric field can exponentially enhance the mobility. As shown in **Figure 1-13**, the presence of external electric field decreases the energy barrier for oxygen neighbor jumping.

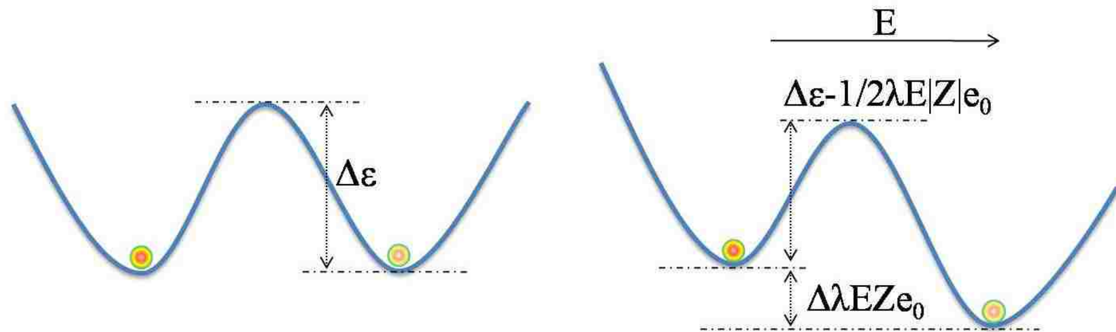

Figure 1–13: Left, Oxygen vacancy in a crystal field; Right, lower down of barrier under electric field. λ is jump distance and Δε is the energy barrier.

Considering this, the drift velocity is then described by the followed item

$$v_d = \upsilon\lambda e^{-\frac{\Delta\varepsilon}{k_B T}}\left(e^{\frac{\lambda E|Z|e_0}{2k_B T}} - e^{-\frac{\lambda E|Z|e_0}{2k_B T}}\right)$$

υ is the attempt frequency, and λ is jump distance, Δε is potential barrier, E is electric field intensity. The mobility can be derived

$$\mu = \frac{v_d}{E} = \frac{\upsilon\lambda}{E} e^{-\frac{\Delta\varepsilon}{k_B T}}\left(e^{\frac{\lambda E|Z|e_0}{2k_B T}} - e^{-\frac{\lambda E|Z|e_0}{2k_B T}}\right)$$

At the low field, the drift velocity is linearly proportional to electric field

$$v_d = E\frac{\upsilon\lambda^2|Z|e_0}{k_B T}e^{-\frac{\Delta\varepsilon}{k_B T}}$$

And so the mobility just depends on temperature. However, at high field where the $\lambda E|Z|e_0$ is comparable with thermal energy ($k_B T$), then the drift velocity can be approximately estimated by

$$v_d = \upsilon\lambda e^{-\frac{\Delta\varepsilon}{k_B T}}e^{\frac{\lambda E|Z|e_0}{2k_B T}}$$

Therefore the drift velocity will increase exponentially with field. If λ=4 Å, E=10^9 V/m, and |Z|=2, at room temperature, $e^{\frac{\lambda E|Z|e_0}{2k_B T}} = 5 \times 10^6$, v_d(E=10^9 V/m)/v_d(E= 10 V/m) = 10^{13}, the strong electric field will gigantically boost the motion of oxygen.

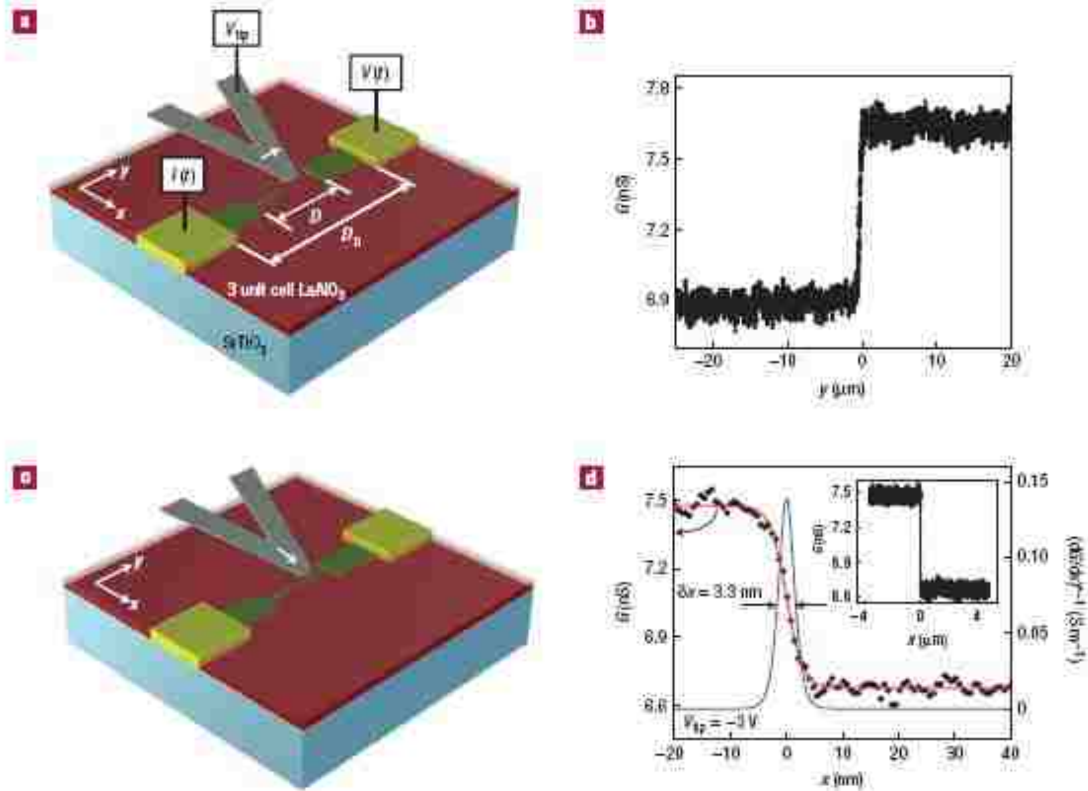

Figure 1–14: (a) Write a conductive wire at $LaAlO_3/SrTiO_3$ interface with conductive AFM tip by applying a bias to the tip. (b) The conductivity between two electrodes as a function of writing length. It suddenly jumps to high value due to two electrodes connected. (c) Erase metallic 2D-gas locally. (d) Conductivity between electrodes drops due to locally break of conductive wire. Figure adapted from **[72]**.

In 2008, Cen *et al.* successfully used electric field from conductive a AFM tip to control $LaAlO_3/SrTiO_3$ interface oxygen vacancies and achieved the nanoscale control of

metal-insulator transition at $LaAlO_3/SrTiO_3$ interface [**72**]. They could even use AFM tip to write a metallic nanowire by scanning AFM tip (see **Figure 1-14**). The local strong electric filed can also induce local oxygen vacancies migration in $SrTiO_3$ single crystal which then leads to a resistance switching [**73**]. It is extensively reported in metal/meta-oxide/metal sandwiched structure that an electric field can induce a large and permanent but still reversible change of resistance **[73-76]**. The oxygen migration is thought to be a key mechanism responsible for the resistive switching in many kinds of such sandwiched structure [**74, 75**]. The resistive switching phenomenon can be applied for resistance random access memory. The dynamic control of oxygen vacancies will be significant for oxide nanoelectronics.

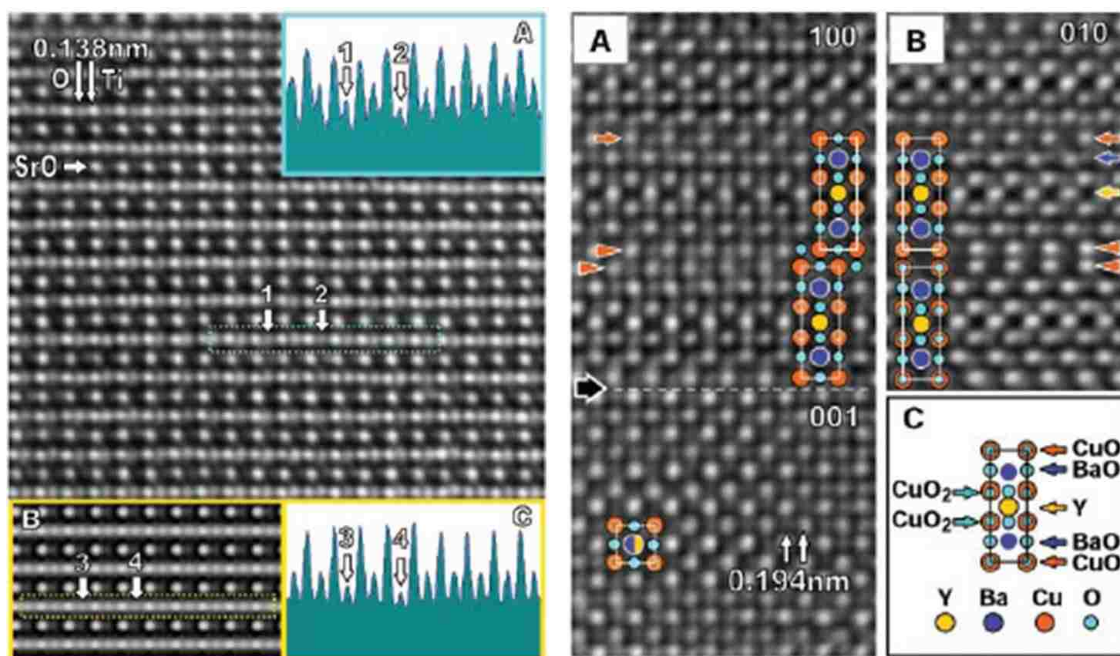

Figure 1–15**:** Direct imaging of oxygen column in $SrTiO_3$ and $YBa_2Cu_3O_7$ with Cs-TEM **[77]**.

Nevertheless, understanding at the atomic level of the nature of the oxygen and its vacancies remains limited. Directly imaging oxygen atom inside a crystal is very difficult because of its weak scattering to electron and very small size (~0.1 nm). Development of

aberration-corrected TEM (Cs-TEM) makes the imaging of oxygen atom possible. Through properly adjusting the spherical aberration coefficient to a negative value, Jia *et al*. **[77]** first directly imaged the strings of oxygen atoms in $SrTiO_3$ and $YBa_2Cu_3O_7$ (see **Figure 1-15**). Such technique of allowing us to determine oxygen position and content will hold the key to research of physics in oxide, especially the oxidation/reduction process, relation between oxygen vacancies and physical properties.

Chapter 2 Experiment Methods

2.1 Thin Film Growth

2.1.1 Laser Molecular Beam Epitaxy

A Laser Molecular Beam Epitaxy (Laser-MBE) system is made up of a KrF excimer laser; a rotational multiple-target assembly; a gas flow nozzle; substrate heater and a Reflection High Energy Electron Diffraction (RHEED) (see **Figure 2-1a**). The KrF excimer laser which we use was provided by Lambda Physik Co.. It has a wavelength of 248 nm and pulse duration of 30 ns. The laser energy of each pulse can reach up to ~1.0 J. Dynamic growth process can be monitored by RHEED. In order to be compatible with high growth pressure, RHEED usually uses a double-stage differentially pumping system to keep pressure inside the RHEED very low. A multi-target holder is necessary for growing multilayer. Our multi-target holder has a target rotating motor to switch the targets and a spinning motor to spin the targets . Our setup enables us to install 6 targets at the same time.

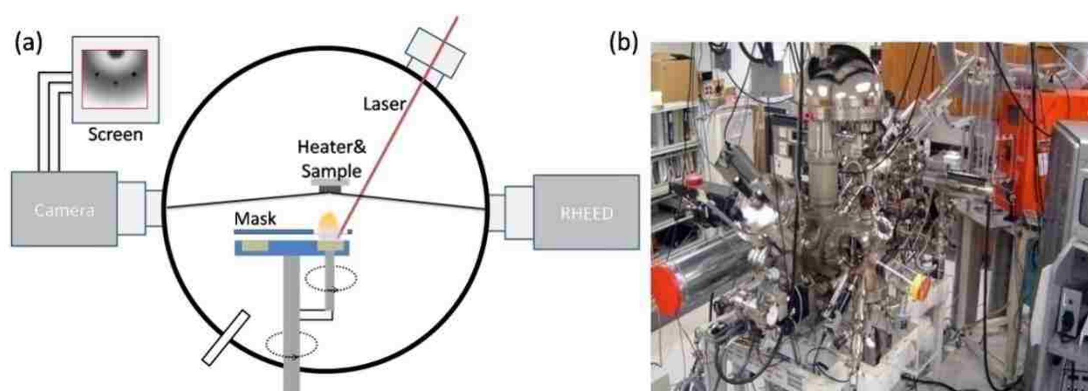

Figure 2–1: (a) Schematic diagram of Laser-MBE setup; (b) Our integrated Laser-MBE and *in-situ* characterizations system made up of XPS, STM/AFM, LEED.

To deposite the material of a target on a substrate, a pulsed-laser beam with a spot size in the order of magnitude of 1 mm^2 is required to bombard a target and cause a rapid removal of the material and formation of an energetic plasma plume. The plume travels through vacuum

and then condenses back to solid state onto a substrate. The plume always contains a combination of ions, electrons and neutral particles. Generally, a target which can be either ceramic or single crystal is shaped into a disk. In the process of laser ablation, the photons are first converted into electronic excitations and then into thermal, chemical and mechanical energy, resulting in rapid removal of the material from the target surface. The density and mean free path of the plasma plume are determined by both the chamber pressure and the incident laser energy. Different from thermal evaporation deposition where evaporated atoms have very low kinetic energy, the particles in the plasma plume have very high kinetic energy on the order of magnitude of 50 eV, which results in much longer mean free path even at high pressure. As a result, the Laser-MBE has a very big gas pressure window ranging from ~1.0 Torr to ultra high vacuum (UHV). With this capability, the stoichiometry can be easily controlled. Laser-MBE is good for growing metal oxides with admittable and exhaustible oxygen gas. The quality of the thin film also relies on the substrate structure and temperature.

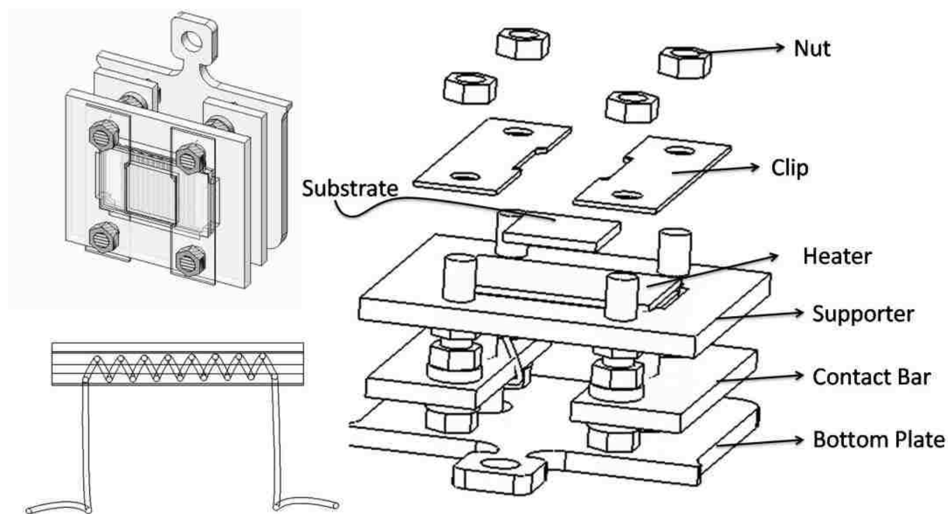

Figure 2–2: Drawing of substrate heater.

Our Laser-MBE setup is connected to our comprehensive *in-situ* characterization system comprised of LEED, STM/AFM, XPS as shown in **Figure 2-1b**. To transfer the as-grown

sample to the *in-situ* characterization chamber, a special mobile substrate heater was designed. **Figure 2-2** displays the drawing of the heater. With this special design, most of the heating power is localized to the heating part as shown in the left corner of **Figure 2-2** so as to keep the other parts of the heater frame at much lower temperature. The filament can be made of either inertia metals such as Pt or other refractory metals such as W, Ta, Mo, depending on the specific application. The heater if made of inertia filament such as Pt wire can be used both in reactive gas and ultra high vacuum. If a filament has very high melting point such as W and Ta, the heater can provide as high as 1300 Celsius degree but be only used in vacuum condition or relative low pressure of reactive gas.

2.1.2 Reflection High Energy Electron Diffraction

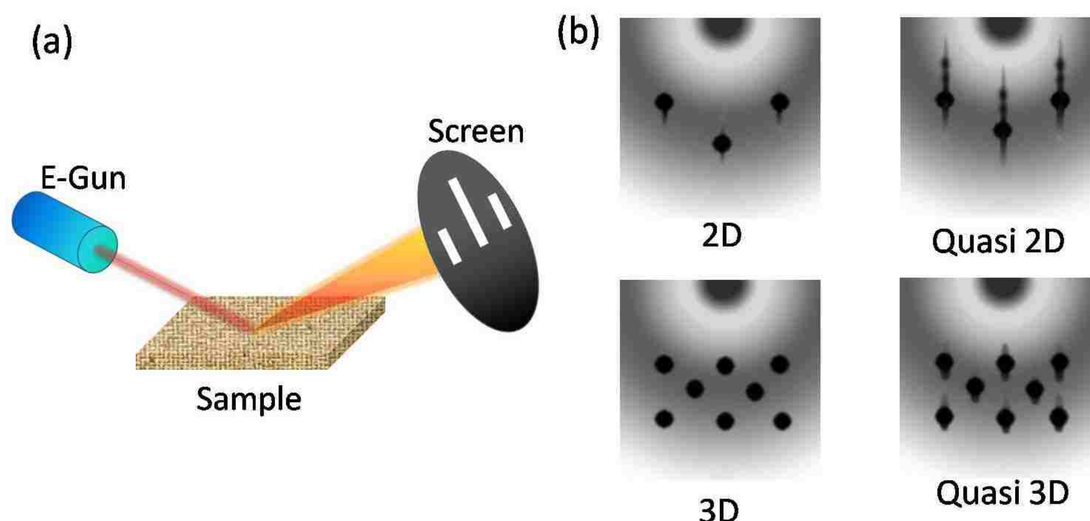

Figure 2–3: (a) Schematic diagram of a RHEED setup.(b) RHEED patterns for different surface morphology.

Reflection High Energy Electron Diffraction (RHEED) is a surface sensitive technique to probe surface topography and monitor dynamic growth process. The RHEED setup is schematically shown in **Figure 2-3a**. It is made up of an electron gun and a phosphor screen to record the pattern. High energy electron beam approaches a sample surface at a very small grazing angle θ ($<5^{o}$) and is reflected off the surface. Some of the diffracted electrons reach a

phosphor screen and form a RHEED diffraction pattern which strongly depends not only on the surface symmetry but also surface topography. The relation between surface topography and RHEED pattern is shown in **Figure 2-3b**. A real time record of RHEED evolution could be used to monitor the growth of a thin film. A RHEED pattern can tell us the growth mode-2D or 3D. The tracking of the intensity of a specific spot can be used to monitor layer-by-layer growth. For a 100% coverage 2D surface, the RHEED intensity is strongest; after growing some, for example half unit cell equally, the intensity will become weakest; the intensity can recover after a full one unit cell grown. **Figure 2-4** shows a typical layer by layer growth process and corresponding oscillation curve. One period represents one layer. The oscillation can tell us growth rate and number of grown layers. To collect a RHEED pattern, a camera is used to collect the image from a phosphor screen; images will be processed in a computer where the intensity of a specific spot could be traced.

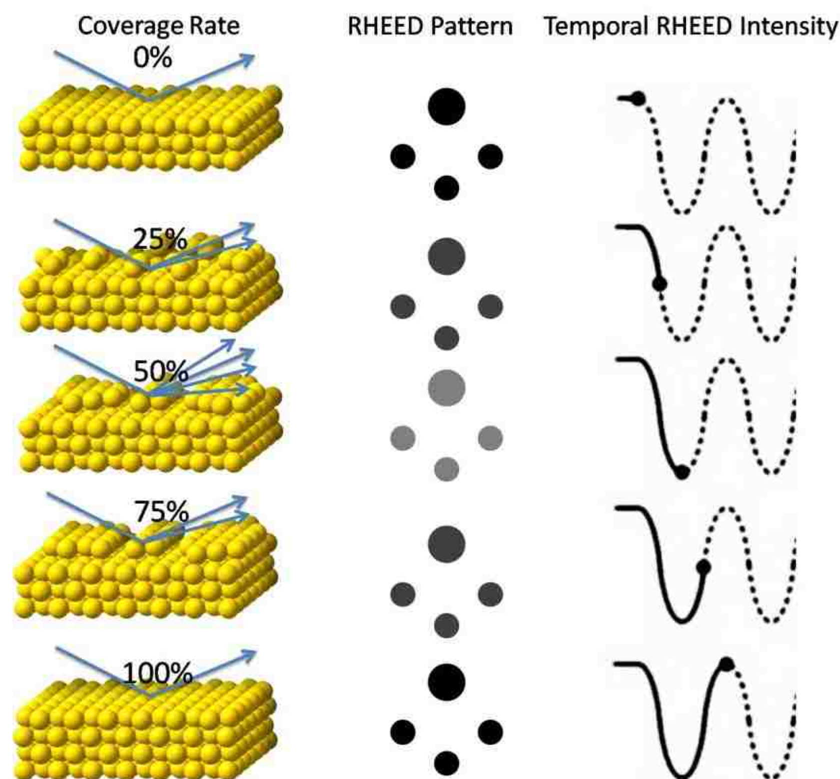

Figure 2–4: The dynamic process of layer by layer growth monitored with REEED.

In a RHEED setup, only atoms at a sample surface contribute to the RHEED pattern. The diffraction pattern on a screen is a function of surface structure. The pattern depends on the spacing of periodic atoms at the surface and the wavelength of the incident electron beam. Two types of diffraction will happen. Some of electrons are elastically scattered at crystal surface, that is, kinematic scattering. Some will undergo multiple scattering and lose some of their energy, called dynamic scattering. The kinetic scattered electrons account for the high intensity spots or rings. Generally, we use kinetic diffraction pattern in thin film growth to monitor surface morphology and growth process.

2.1.3 Back-Biased-Face-Target-Sputtering

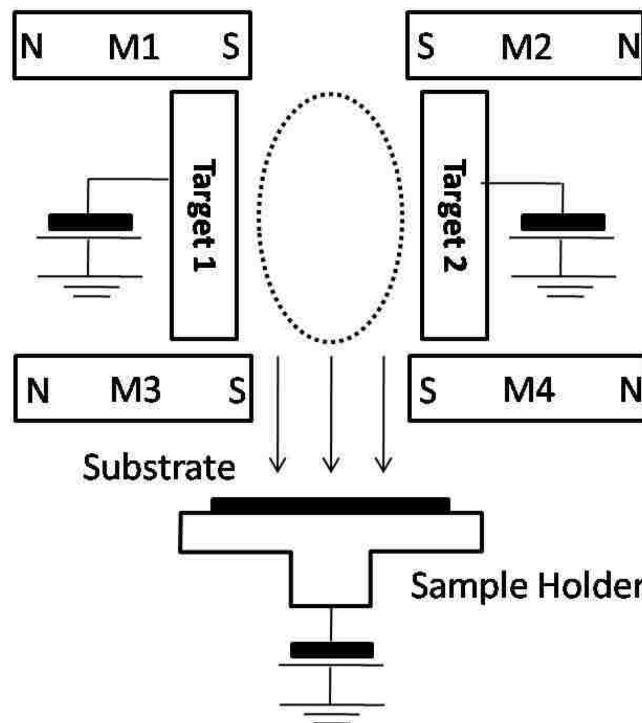

Figure 2–5: Scheme of a back-biased face target sputtering chamber.

Back-Biased-Face-Target-Sputtering (BBFTS) **[78]** is a well developed technique for growing a metal oxide thin film compatible with complementary metal oxide semiconductor (CMOS) process. A metal oxide thin film can be grown at low temperature (< 400 ^{o}C) with this technique. The structure of a facing targets sputtering device is schematically shown in

Figure 2-5. A pair of target plates are placed at opposite ends of chamber respectively so as to face each other and form a plasma region there between. Magnet poles of different polarities face each other across plasma region so as to establish magnetic field to help formation of plasma region between target plates. With the help of Ar^+ sputtering and a magnetic field, a region of plasma composed of materials of targets is formed between the target plates. A substrate, which maintains at low temperature, is placed close, but out of this plasma region. The substrate is back-biased with another voltage source which attracts the plasma to the substrate, resulting in growth of target material on top of the substrate. With gas (inert or active) admittable and exhaustible, the stoichiometry such as oxygen content of a grown thin film can be controlled.

2.2 Characterization

2.2.1 Transmission Electron Microscopy

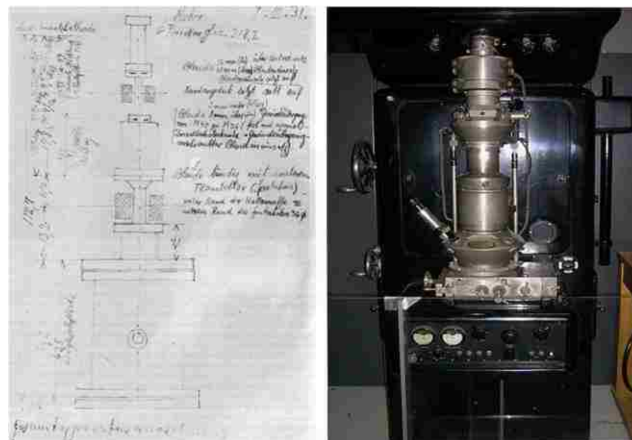

Figure 2–6: Left, sketch of first TEM; Right, picture of the first practical TEM. Figure adapted from wikimedia.

Transmission Electron Microscopy (TEM) has become a very popular and powerful tool for both the materials science community and industry to reveal microscopic structure with ultrahigh resolution of sub-Ångström. The history of TEM is traced back to early 1920s. The

resolution of a microscopy is limited by the wavelength of an incident beam. Traditional optical microscopy has confronted a bottleneck due to its big wavelength or otherwise expensive quartz optical components for UV or X-ray of smaller wavelength. New method was required. In 1925, Louis de Broglie proposed the concept of matter wave that the wavelength of a particle is determined by an equation as followed

$$\lambda = \frac{h}{p}$$

A wavelength of a 100 keV electron is 3.7 pm and such high energy electron if can be used to image must be able to provide much higher spatial resolution than that of an optical microscopy. The electron microscopy was indeed realized in 1931. Max Knoll and Ernst Ruska created the first electron microscope which already showed better resolution than optical microcopy at that time and later in 1939 they developed first commercial TEM (see **Figure 2-6**).

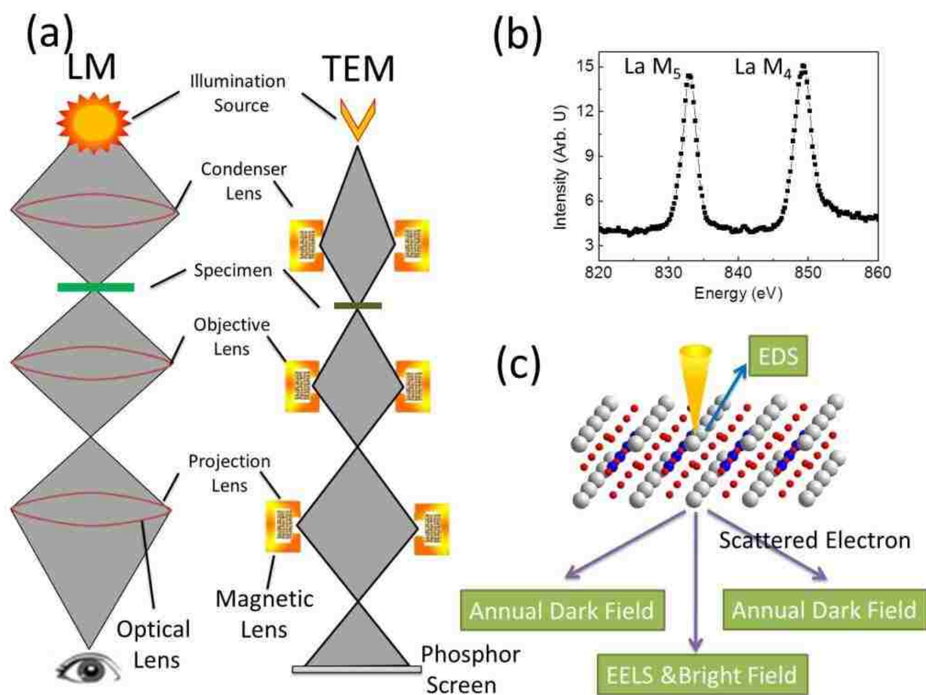

Figure 2–7: (a) Optical setup for both optical microscopy and TEM. (b) EELS of La M_5 and M_4. (c) A schematic diagram of integrated TEM, EDS, EELS system

The working mechanism of a TEM is quite similar with optical microscopy. Two big differences are that TEM uses magnetic lens and electron beam as light source. **Figure 2-7** shows the optical paths for both optical microscopy and TEM. When aTEM electron beam is focused to ultra narrow spot (~1 nm) and scanned over a TEM specimen in a raster, the resulted mapping is called scanning TEM (STEM) image. STEM can provide better spatial resolution of ~1 Å.

Besides a function of structure imaging, the nature of electron allows TEM to probe chemical information and electron structure. When an electron travels through a specimen, it will be either elastically or inelastically scattered by the specimen. Elastic scattered electron can be used to form diffraction pattern, which can provide the information of the lattice structure of the specimen including symmetry. Inelastic scattered electron includes some other interesting information, for example, chemical composition, electron bonding. Inelastic scattered electron could yield Electron Energy Loss Spectrum (EELS). The amount of energy loss of an inelastic scattered electron can be measured via an electron spectrometer. Inelastic interactions include phonon excitations, inter and intra band transitions, plasmon excitations, inner shell ionizations, and Čerenkov radiation. The energy loss due to inner-shell ionizations (a core level transited into outer empty states) is a fingerprint of element, so it could be used to detect elemental components of a material. The inner-shell ionization features "absorption edges" in EELS. One example of adsorption edges is shown in **Figure 2-7b**. The absorption edges can reflect information of local density of empty states, oxidation state, local coordination of a respective atom, etc.. The Energy Dispersive X-ray Spectroscopy (EDS) which uses the electron beam to activate the emission of X-ray from a TEM specimen is a

complementary elemental analysis tool to EELS. **Figure 2-7c** shows an example of integrated functions of a STEM which includes EELS, and EDX. Such set-up is useful for structure analysis, elemental identification, quantification and mapping.

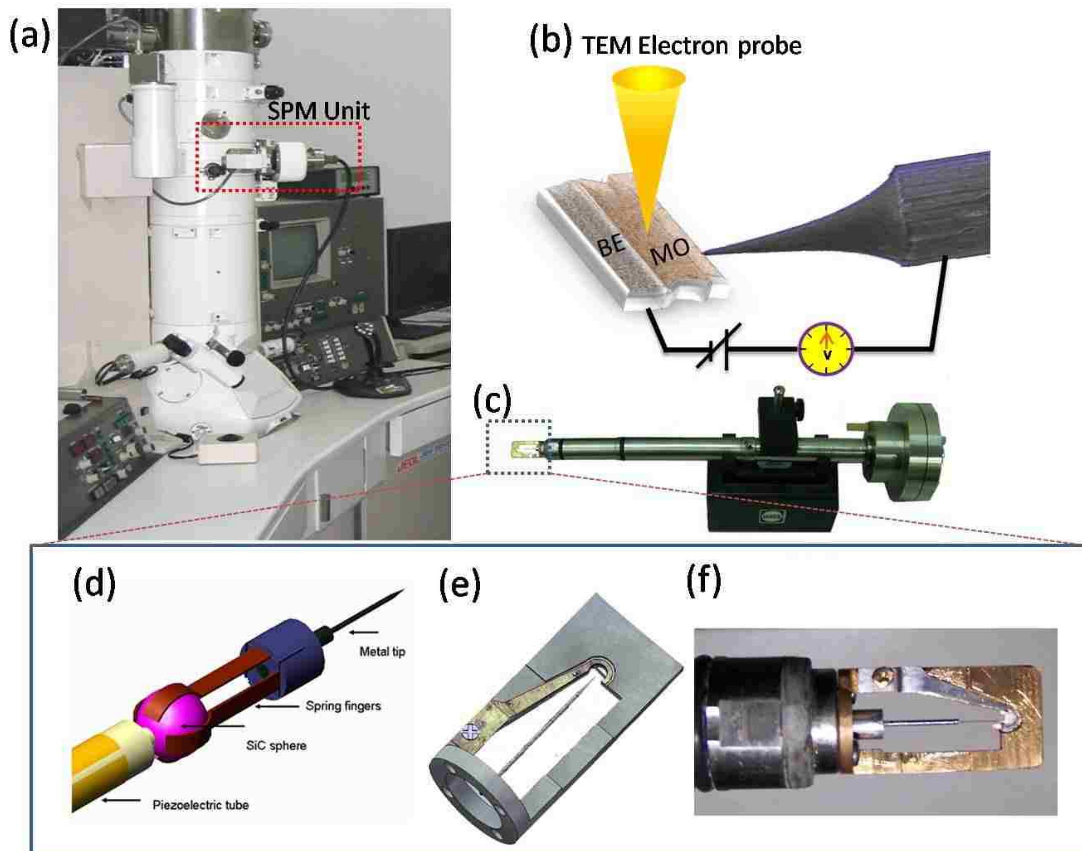

Figure 2–8: (a) Integrated SPM-TEM system; (b) Schematic diagram of *in-situ* electrical properties measurement; (c) SPM-TEM sample holder (d) Drawing of the 3D piezo-motor used for SPM; Drawing (e) and real picture (f) of home-made specimen holder.

Another advantage of TEM is the capability that external stimulus can be applied inside it with simultaneous *in-situ* characterization with TEM. External stimulus can be temperature **[79-81]**, electric field **[82-85]**, mechanical stress **[86]**. X. D. Bai' group in institute of physics, Chinese academy of science, cooperating with our group, has developed a scanning probe microscopy SPM-TEM system **[87-88]** whereby the SPM tip navigated by TEM can approach to the TEM specimen to act as an electrode. SPM tip can provide very local electric field. **Figure 2-8** shows the picture of this setup. A SPM unit is integrated with the TEM

sample holder. The process of transport measurement and simultaneous investigation with TEM is schematically shown in **Figure 2-8b.** To conveniently measure the electrical properties of a TEM specimen, a special TEM specimen holder with a open window for the SPM tip to approach the specimen was designed (see **Figure 2-8e**).

2.2.2 Scanning Tunneling Microscopy

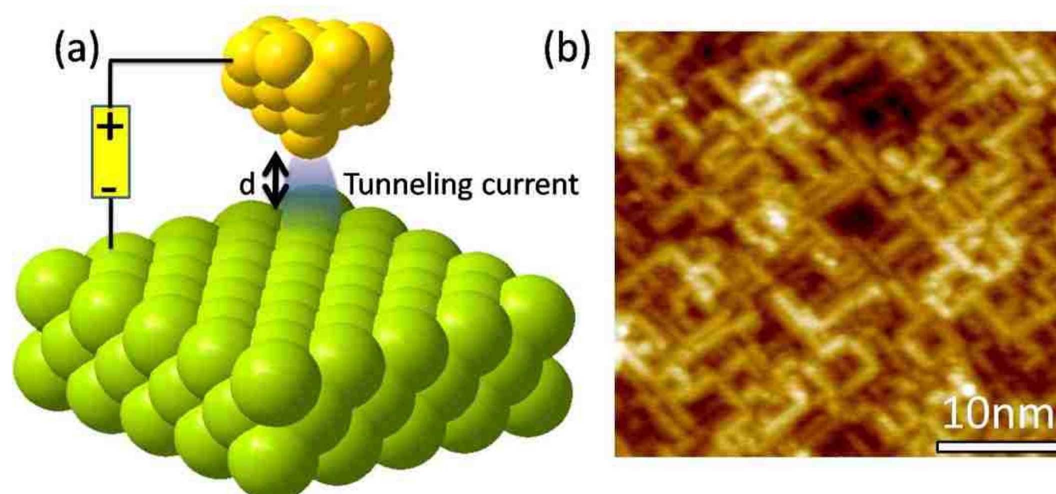

Figure 2–9 (a) Diagram of STM surface imaging. (b) STM image of surface structure of (001) TiO_2.

Scanning Tunneling Microscopy (STM) is one of the few inventions that took just 5 years after its invention to win the Nobel Prize. It was developed by Binig and Rohrer at IBM in 1981 and proved to be a powerful tool for surface science **[89]**. STM is famous in public for its ability of "seeing" atoms, but much beyond this, STM can probe surface electron' density of state (DOS). The working mechanism of a STM is schematically shown in **Figure 2-9a** and **Figure 2-9b** is structure of (001) TiO_2 surface imaged by our Omicron STM system. A sharp tip finely controlled by a 3D piezo motor biased a voltage stands above but very close to the surface. Generally, a STM tip and sample surface are spaced by *d (*1 Å < d < 10 Å*)*. A tunneling current goes from the tip to sample. The tunneling current strongly depends on DOS of a specific sample and tip as well as the tunneling gap as revealed by the

following equation:

$$I \approx \frac{4\pi e}{\hbar} e^{-d\sqrt{\frac{8m\varphi}{\hbar^2}}} \rho_t(0) \int_{-eV}^{0} \rho_s(\varepsilon) d\varepsilon$$

The differential of tunneling current over bias gives rise to information of DOS

$$\frac{dI}{dV} \propto DOS(eV)$$

The tunneling current will choose the most near atom to sample surface. A very sharp tip is critical for topographic imaging. The tip can be platinum, tungsten, gold. Tungsten tip is more popular since it is much more easily to be obtained through electrochemical etching.

2.2.3 X-ray Photoelectron Spectroscopy

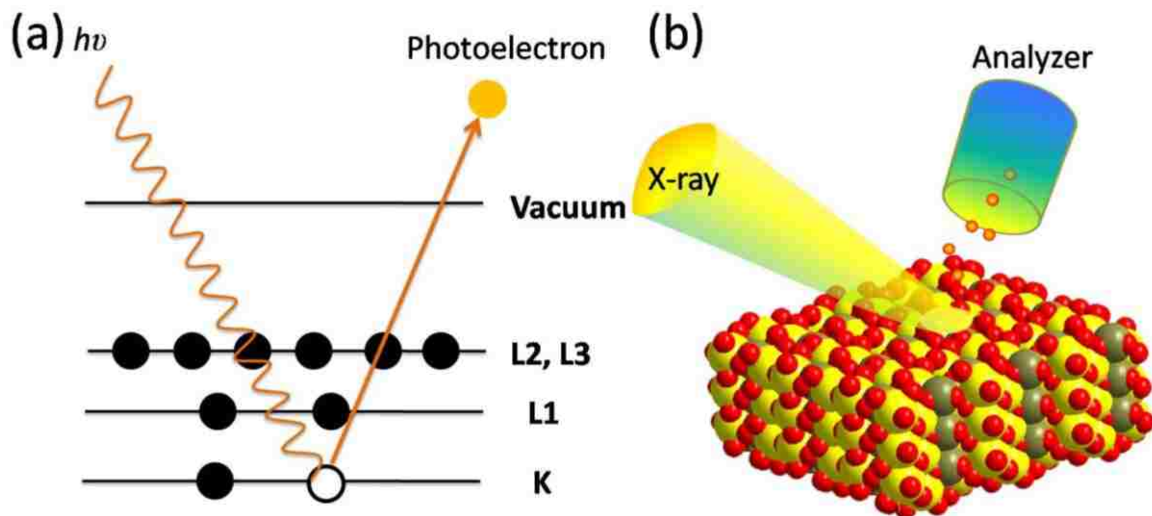

Figure 2–10: (a) Scheme of the photoelectron process, (b) Scheme of a XPS set-up.

X-ray Photoelectron Spectroscopy (XPS) is an instrument widely integrated in UHV system. It is an important technique to obtain chemical composition, impurity, chemical valence and bonding environment. As shown in **Figure 2-10a**, the incident X-ray will ionize atom/molecular with generation of a photoelectron. According to energy conversation law, we have

$$E_f\text{-}E_i = h\upsilon\text{-}E_k$$

Here, E_f is the total energy of final state (after ionization), and E_i is total energy of initial

state (neutral state). The binding energy E_B is formally defined as the difference between the E_f and E_i.

$$E_B = E_f - E_i.$$

Suggestion from above equations, the E_B can be measured by measuring kinetic energy of photoelectron. Right of **Figure 2-10** shows the process of measuring E_B. First, photoelectron is generated by X-ray irradiation; then collected by an electron energy analyzer; the kinetic energy of the photoelectron is measured by the analyzer finally. The sample is short-connected with the analyzer and so they have same Fermi energy level. People usually use Fermi level of analyzer as reference energy and thus the E_B is rewritten as

$$E_B = h\upsilon - E_k - \Phi$$

Φ is the work function of the analyzer. Recording the number of electrons as a function of binding energy yields the spectrum. Different elements have quite different energy of orbitals and electron population, as a result the peak (corresponding to E_B) in XPS spectrum can serve as a fingerprint of an element, making it a useful tool to analyze chemical composition. Since the electron population, chemical environment, bonding and electron-electron correlation can affect the E_f and E_i, the shift of the peak from core levels can provide information on chemical composition and chemical valence and the satellite spectra in XPS offers the information on electron-electron correlations.

The kinetic energy of a photoelectron is relative low (~1 KeV generally), so only a number of electrons which escape from the top 1 to 10 nm of a material are analyzed. XPS is surface sensitive technique and requires ultra high vacuum (UHV) condition.

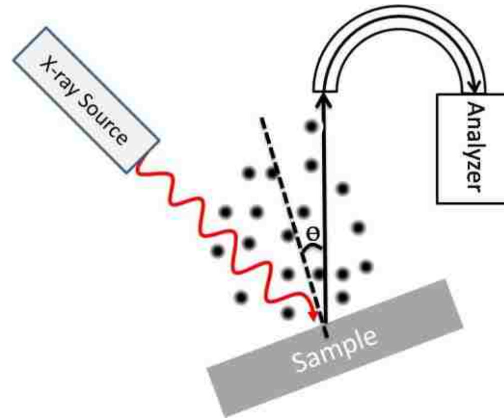

Figure 2–11: Setup of angle resolved XPS.

By collecting the off-normal photoelectron as shown in **Figure 2-11**, angle resolved XPS (ARXPS) can be used to perform depth profile analysis. The photoelectron of certain kinetic energy will have a limited inelastic mean free path (IMFP) which is an index of how far an electron can move in a solid before losing energy. The kinetic energy of a photoelectron generally ranges from several hundreds of eV to about one thousand eV. In this energy range, the IMFP is about 1-3 nm. The off-normal photoelectron will have much of its component from the surface. For a layer material, the intensity ratio between two elements (A and B) as a function of off-normal angle can be written as

$$\frac{I_A(\theta)}{I_B(\theta)} = \frac{\sum_j n_A e^{-jd/\lambda_A(E)Cos(\theta)}}{\sum_j n_B e^{-jd/\lambda_B(E)Cos(\theta)}} \cdot \frac{\sigma_A}{\sigma_B}$$

Here, j means the *jth* atomic layer, and θ is the off-normal angle, λ is the IMFP of electron with certain kinetic energy (E), and d is the space between closest neighbor layer, n is the atom concentration in *jth* layer, σ is the photoelectron cross-section. Take λ = 2 nm as an example, the $\lambda\ Cos(85^o)$ is equal to 0.17 nm and generally the d is ~0.2 nm, so the photoelectron from the layer just underneath top surface atomic layer will strongly be decayed by a factor of 0.3 compare to the top surface. The intensity of surface XPS information will increase with increasing off-normal angle. The ARXPS is a powerful method to get the surface XPS information as well as depth profile.

2.2.4 Low Energy Electron Diffraction

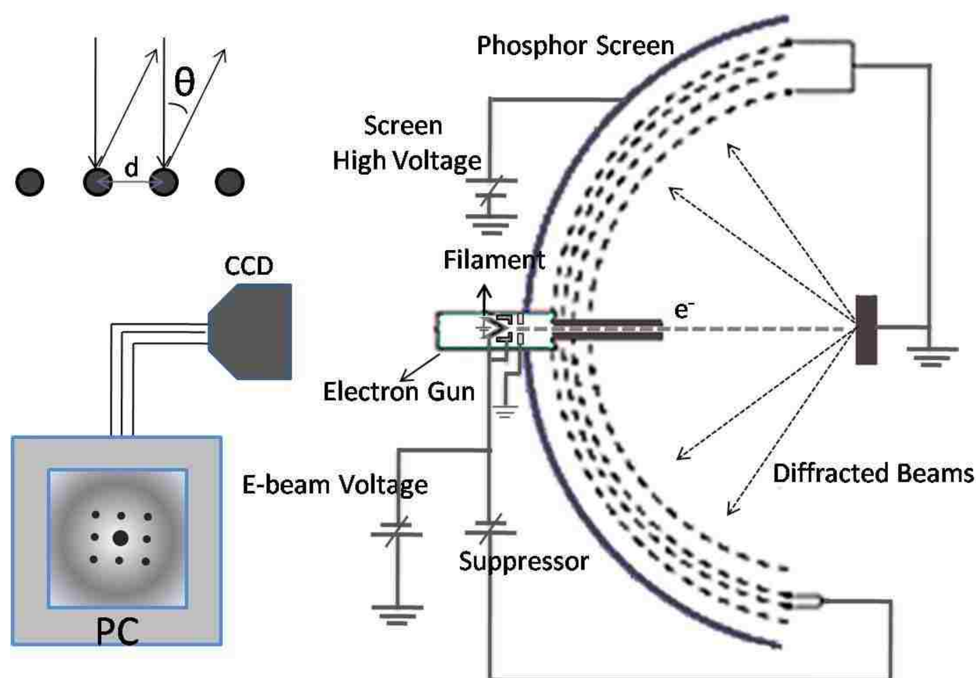

Figure 2–12: Scheme of LEED setup. Right top, scheme of LEED diffraction process.

Low Energy Electron Diffraction (LEED) is a surface sensitive technique used to determine surface structure. **Figure 2-12** schematically illustrates a typical setup of LEED experiment. A monochromatic electron beam generated by an electron gun with energy variable (range: 20 eV-300 eV typically) is normally incident on a surface; the backscattered electrons then will form specific pattern on a phosphor screen. To get enough intensity on the phosphor screen, a high voltage is biased on the screen to accelerate the electrons so that high energy electron can lighten the screen. A suppressor voltage (0-3 V) is used to filter unexpected low energy electrons to reduce noise. The sample must be conductive and grounded in case of charging. LEED pattern is usually recorded with a CCD and processed in a computer.

A LEED pattern in principle is reciprocal space of a sample surface. Spots are formed due to Bragg law. From the right-top panel of the schematic illustrate of Bragg diffraction, we

can derive that

$$dsin(\theta)=n\lambda$$

where λ is wavelength of an incident electron. According to De Broglie relation, the wavelength of an electron is given by

$$\lambda=h/p=h/(2mE)^{1/2}=(150.4eV/E)^{1/2}\ (\text{Å})$$

Here, *e* is the electron charge and *m* is the mass of electron, *E* is energy of electron beam. The typical energy range of an electron beam is from 20 eV to 300 eV, correspondingly, the λ ranges from 2.74 Å (20 eV) to 0.7 Å (300 eV). As a result, the λ is smaller than lattice constant in most cases.

LEED is surface sensitive technique. According to the mean free path vs. electron energy curve in **Figure 2-13**,, a minimum value (~5 Å) exhibits at the energy range from 50-100 eV, hence we can conclude that only a few atomic layers on top of the sample surface contribute to the LEED pattern and intensity.

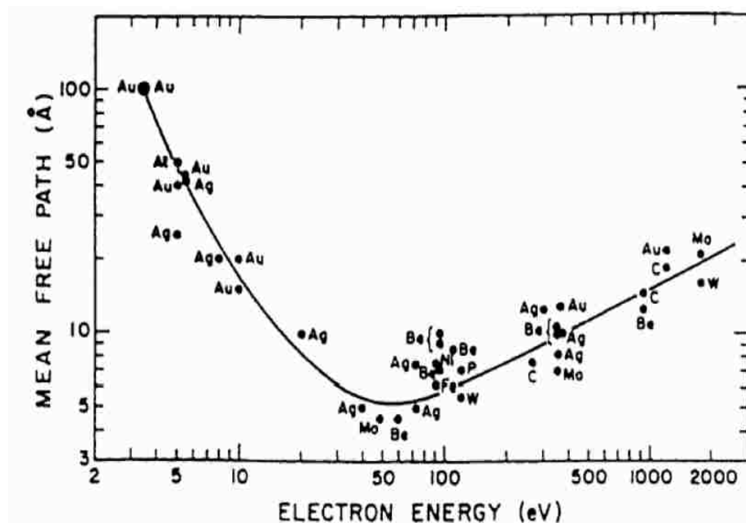

Figure 2–13: Universal curve for the electron mean free path **[90]**.

Besides rough estimation of surface symmetric and surface structure, LEED can be used to determine accurate positions of surface atoms in a way that recording the intensity of a

diffraction spot as a function of incident electron beam energy (I-V curves) and performing theoretical calculation of I-V curves. The LEED I-V curves depend on both the surface structure and chemical composition. A theoretic model will be proposed to generate theoretic I-V curves. Theoretic curves will be used to compare with the experimental LEED IV curves. Some methods are used to determine whether the theoretic curves are a good fit of experimental data, such as Pendry R-factor (R_p) **[91]**. The smaller R_p means more reliable structure refinement. A small R_p of less than 0.3 is generally thought to be a good fit and then the proposal structure model is thought to be reliable.

2.2.5 Transport Measurement

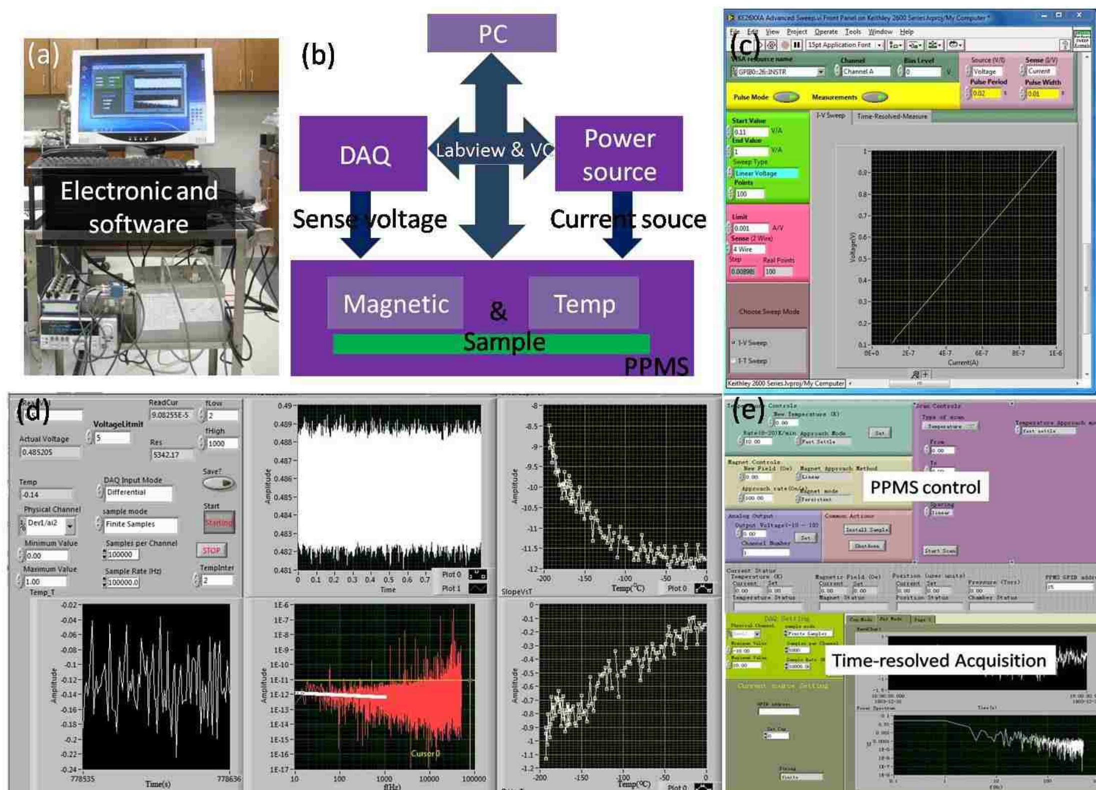

Figure 2–14: Time-resolved physical properties measurement system. (a) Real photo of electronic test devices and computer. (b) Schematic picture of the system setup. All measurement will be automatically finished by friendly software written by Labview. (c) current-voltage (I-V) test software. (d) Temperature-dependent resistance and noise measurement. The software will automatically calculate the power spectrum density and fit spectrum with 1/f noise parameters, then plot these parameters versus temperature. (e) PPMS control interface integrated with our home made test system.

The Current-Voltage (I-V) test is a fundamental electrical characterization of materials, especially a junction where a current rectification exists. The resistance could be measured via I-V measurement. To measurement the resistivity of a material, there are two approaches. One is two-termination measurement and another is four-termination measurement. We usually has a contact resistance between electrode and material, so simple two-termination could involve a contact resistance error and it is not good for accurate measurement. In contrast, four-termination measurement could exclude contact resistance. To perform a I-V test and resistivity measurement, we developed a home-made electrical measurement system as shown in **Figure 2-14.** The Keithley sourcemeter (2601 & 2400) can provide wide range current & voltage source and precisely measure current & voltage as well. With Labview language programming, we can easily developed customized functions. Some functions such as I-V sweep, time resolved transport are shown in **Figure 2-14**. To extend our research capability, we developed a temperature dependence noise and electrical transport measurement system. A liquid nitrogen cooling system is used to vary temperature. The sample is put in a copper case which can be cooled down by liquid nitrogen. During cooling down and naturally heating up, we are able to measure electrical transport property of a sample at varying temperature. Such simple setup enables us to measure *T*-dependence transport.

The fluctuation of transport properties (e.g., time resolved resistance record) can reflect some intrinsic fluctuation in materials. There are some papers using resistance fluctuation to research phase separation and domain wall motion **[92-94]**. The measurement is performed by using to provide low noise constant current and high speed NI data acquisition card to

acquire voltage. Current from Keithley 2601 ranges from 1 nA to 1 A. The data acquisition rate can reach 1 MS/Hz, giving us a time resolution of 1 μs. Such capability endows us to measure large resistance range from 1 Ω to 100 MΩ with time resolution of 1 μs.

The Quantum Design PPMS can only measure samples with not too big resistance (<10 MΩ), which will limit some measurements. To use PPMS to measurement big resistance, we developed an interface changer, through which we can connect our home-made electronic setup to PPMS. Beyond the resistance range, our external electronic setup can be used to measure resistance fluctuation and I-V curve in PPMS with access to its low temperature and strong magnetic environments.

2.3 Device Fabrication Technique

2.3.1 Photolithography

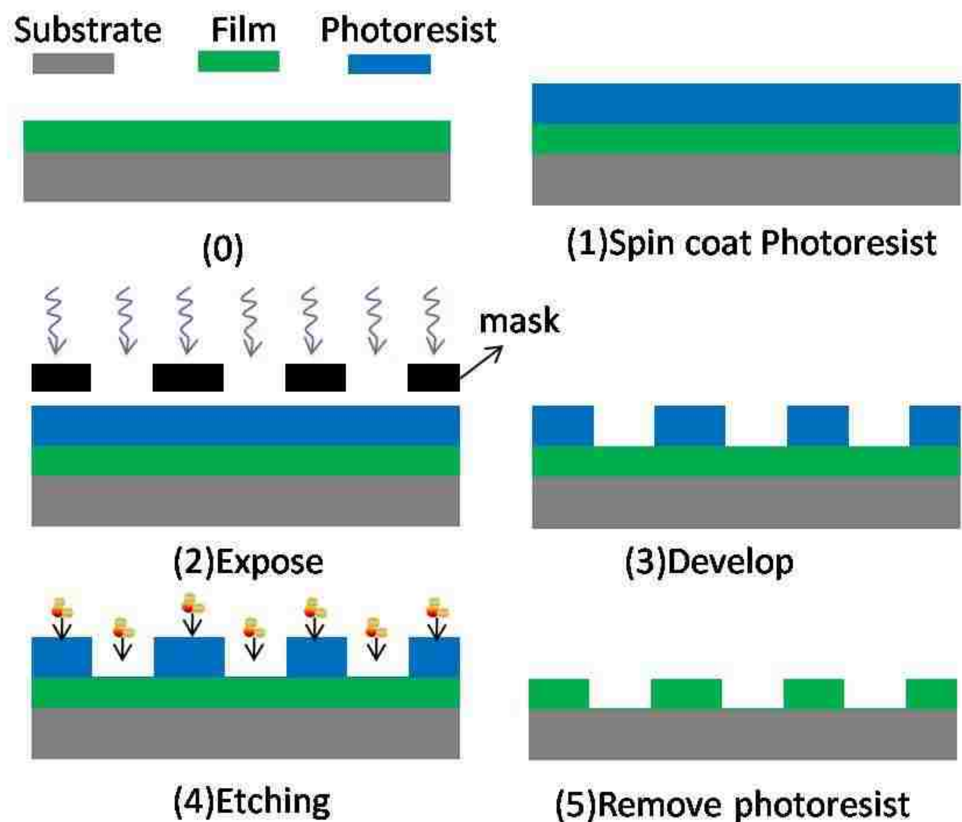

Figure 2–15: Schematic diagram of a standard dry-etch lithography process.

Photolithography is fast and convenient way to create nano/microstructure. Combining with etching and deposition, we can fabricate complex structure, such as field effect transistor (FET) devices, array of nanostructures. A procedure as shown in **Figure 2-15** is used to illustrate how the photolithography works. At first, photoresist is spin-coated on a thin film uniformly, and then is exposed to a light with a mask. The photoresist which is exposed to light will become soluble in a development solution and after development these areas will be removed. The residual photoresist with pattern same as the mask plays a role of mask for reactive ion etching process. After a subsequent process of reaction ion etching and removing the photoresist by such as acetone, we finally transfer a pattern from the mask to the film. If we deposite metal thin film instead of etching, then we get patterned metal thin film on the substrate. Photolithography is a process that transfers geometric pattern from a photo mask to a substrate. The exposure of photolithography is very fast that it takes just about 30 seconds and can has a big exposure area (for example, 4 inch wafer), enabling us to create billions of structure at a short time. Photolithography is so a low cost and fast microfabrication technique that it is widely used in semiconductor industry.

2.3.2 E-beam Lithography

E-beam lithography which uses electron-beam of ~10 KeV as "light source" works similar with photolithography, but it does not need a mask, instead E-beam lithography uses a small electron beam to directly write a pattern like drawing picture with a pencil. The smallest line width of lithography is related to wavelength of the "light" or diameter of light beam. In principle, smaller wavelength or smaller-beam-size generates smaller line width. The limit factor for E-beam lithography is the beam size rather than the wavelength of a

E-beam (12 pm for a 10 keV electron). The smaller beam size can produce smaller line width. Ideally, the E-beam lithography can produce line width on the order of 10 nm or smaller. The development process of E-beam lithography has to take very long time since that the scanning speed of E-beam is low. To create an area of 100 μm×100 μm, it needs to take several minutes. E beam lithography is used for creating smaller structure usually.

2.3.3 Focused Ion Beam

Focus Ion Beam (FIB) is very similar with E-beam lithography, but the nature of ion beam makes FIB much like a direct machining rather than lithography. Focused ion beam uses relative heavy Ga^+ ion, so it will directly sputter the sample surface in an imaging mode or directly cut specific region with ion beam focused. In another word, it can directly write patterned structure by scanning sample surface with focused beam. The high energy Ga^+ can decompose some gases, so we can directly deposite metal such as platinum with precursor gas of trimethyl platinum.

Chapter 3 $SrTiO_3$ Substrate Treatment

3.1 Introduction and Motivation

$SrTiO_3$ is of cubic perovskite structure and an insulator with a band gap of 3.2 eV. Self doping with oxygen vacancies or external element doping by Nb or La will result in a n-type semiconductor. More and more interest in $SrTiO_3$ has been stimulated by its exotic properties at not only its bare surface but also its interface with other metal oxides.

(001) $SrTiO_3$ surface itself exhibits numerous interesting properties. $SrTiO_3$ plays an important role in surface reactions and catalysis **[95, 96]**. The angle resolved photoemission spectrum (APRES) reveals the existence of universal free electron gas at surface which can be controlled by ultraviolet illumination **[97, 98]**. First principle pseudopotential method also indicates that reduced surface becomes metallic **[99]**.

(001) $SrTiO_3$ is one of the most important substrate for epitaxial growth with easy control of termination layer (TiO_2 vs. SrO). An flat TiO_2 terminated surface (TiO_2-(001)) can be easily obtained by buffer oxide HF solution etching and *in-situ* annealing **[100]**; while SrO termination surface (SrO-(001)) is obtained by high temperature annealing **[101]** or depositing a SrO layer on TiO_2-(001) **[102]**. Various surface reconstructions (1x2, 2x2, 4x2, C(2x2), C(4x2), c(6x2), c(√5x√5), etc.) have been reported **[103-108]**, and two structures of surface reconstruction (2x1 **[106]**, 4x2 **[107]**) have been solved. The surface reconstruction can even affect the growth and properties of epitaxial thin films **[109, 110]**.

Besides a role as a substrate, the (001) $SrTiO_3$ plays an important role in interface properties. When interfacing with other oxides, $SrTiO_3$ exhibits surprising behavior. At the $LaAlO_3/SrTiO_3$ interface where both $LaAlO_3$ and $SrTiO_3$ are wide band gap band insulators,

unexpected quasi two dimensional high-mobility free electron gas emerges **[28]**. This interface can be superconductive at low temperature **[29]**. Superconductivity behavior was also reported at $LaTiO_3/SrTiO_3$ interface **[111]**. Another amazing phenomenon is termination (TiO_2 vs. SrO) tuning interface properties. Take the $LaAlO_3/SrTiO_3$ interface for example, the interface maintains insulating when the termination layer is SrO; only TiO_2 termination layer provides possibility of creating free electron gas **[28]**. A theoretic calculation suggests that the termination layer of $SrTiO_3$ can vary the electronic and magnetic properties of $SrTiO_3/La_{2/3}Sr_{1/3}MnO_3$ interface **[112]**. With respect to interface electronic heterojunction (e.g., schottky junction), it is reported that junction with SrO termination has larger Schottky barrier than that with TiO_2 termination **[113]**.

The surface defects, polarity, reconstruction and termination layer can so strongly affect properties that we really need to know what is the surface structure. Although many surface structure models have been proposed, but there are still some contradictions. The most basic issue is what is the termination layer. Recent reports seem to be inconsistent. Liang, *et al.* have shown that the annealing in UHV above 1000 ^oC will give rise to SrO rich surface, because sublimation rate of Ti is higher than that of Sr **[114, 115]**. However, Szot *et al.* reported that the UHV annealing results in TiO_x rich surface **[116]**. It seems like that there are some controversial findings. In this chapter, we will introduce the treatment of $SrTiO_3$ and investigate its surface chemistry and structure by using STM, LEED and XPS.

3.2 Experiments and Results

The 0.1 wt% (001) Nb-$SrTiO_3$ single crystal substrates were provided by CrysTec Co.. To perform wet-etching, a substrate was first sonicated in (1) Acetone for 5 min; (2) Ethanol

for 5 min (3) Milli-Q water for 5min; (4) then put in buffer oxide HF solution (from Alfa Co.) for 30s. After wet-etching, we used ultrapure N_2 gas to blow it to dry, and then mounted it onto a home-made sample holder (see Chapter 2), and finally put it into UHV system with a base pressure: 10^{-10} Torr.

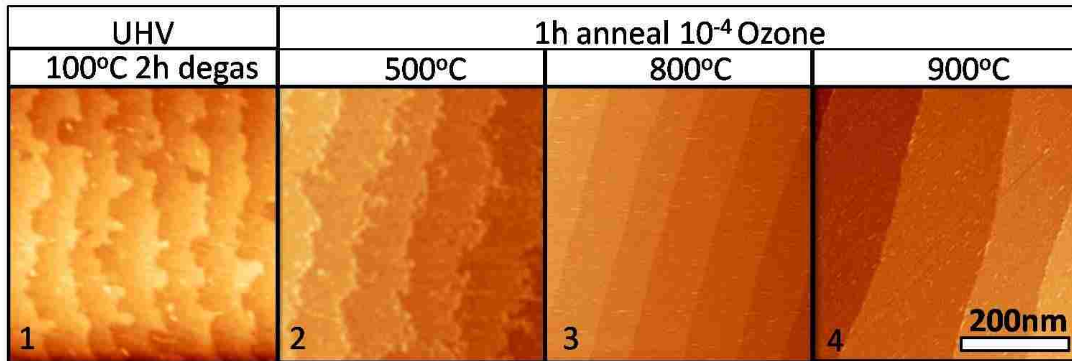

Figure 3-1: Surface morphology of $SrTiO_3$ (001) at different treatment condition.

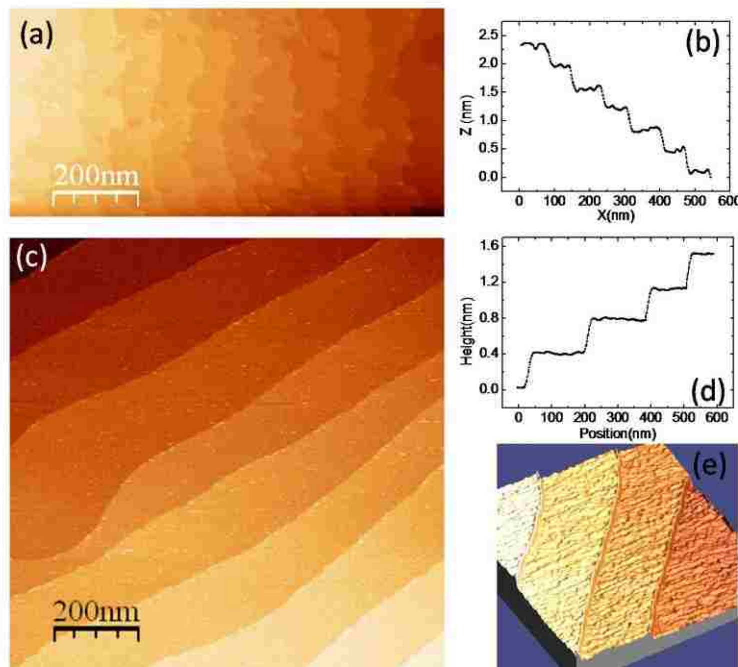

Figure 3-2: (a) STM image and (b) height profile of as-etched $SrTiO_3$ surface after degassing at 100 °C in UHV. (c) STM image and (d) height profile of sample annealed at 900 °C for 1 h at 10^{-4} Torr Ozone and (e) its 3D image.

The surface morphology under different annealing condition was imaged with STM. As shown in **Figure 3-1**, the surface of the as-etched sample (sample-1) has relative narrow terraces of about 40 nm wide and the step edges are a little winding. After annealing at 500

^{o}C for 1 h (sample-2), step edge still looks a little winding. The step edge will be straightened out at higher annealing temperature as the samples annealed at 800 ^{o}C (sample-3) and 900 ^{o}C (sample-4) as examples. The large scale STM images of sample-1 and sample-4 are displayed in **Figure 3-2**. The height profile of sample-1 surface shows that step height is ~0.39 nm, suggesting a single termination surface of the as-etched sample. After annealing at 10^{-4} Torr Ozone at 900 ^{o}C for 1 h, the surface morphology changes, but the step height is still 0.39 nm, indicating that the surface still has a single termination. Generally, an atomically flat substrate will favor 2D growth and is good for the quality of a thin film. With respect to a ultrathin film especially in the case that the interface coupling cannot be ignored, a single termination and atomically flat surface is usually necessary. Through buffer oxide HF solution etching and high temperature annealing, we can obtain a good substrate morphology for epitaxial growth.

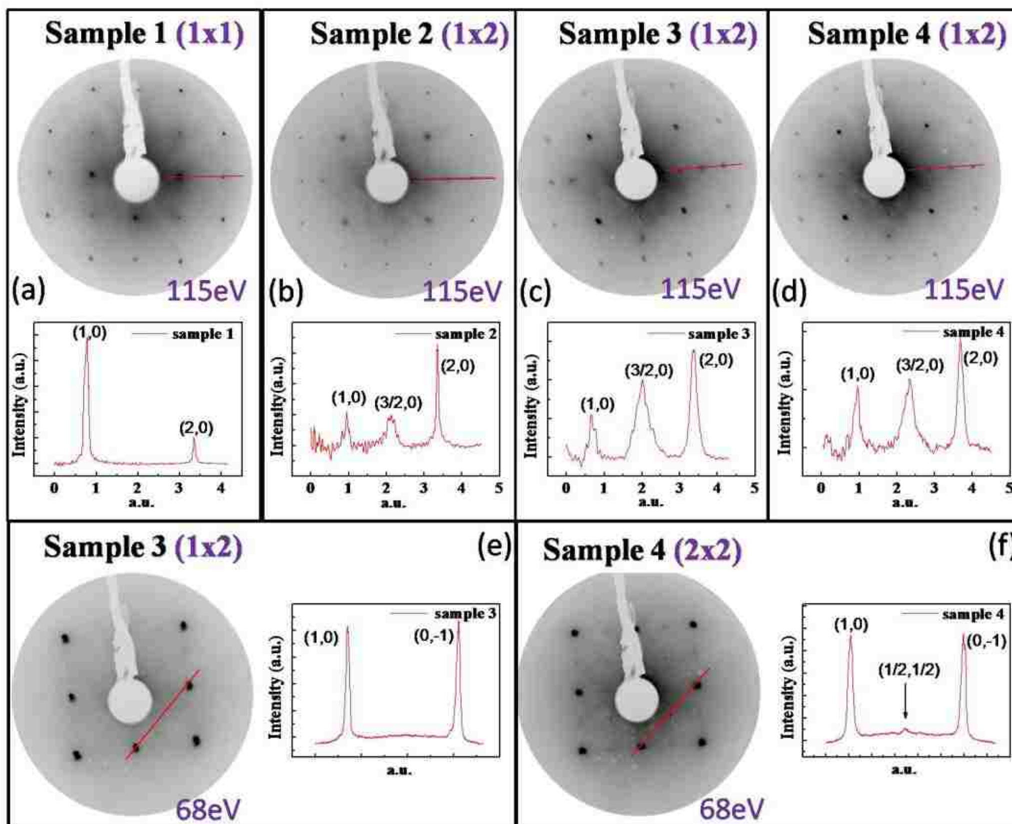

Figure 3-3: LEED pattern of the sample 1 to sample 4 as mentioned in Figure 3-1. The profiler along the red line is shown near the image in the same panel.

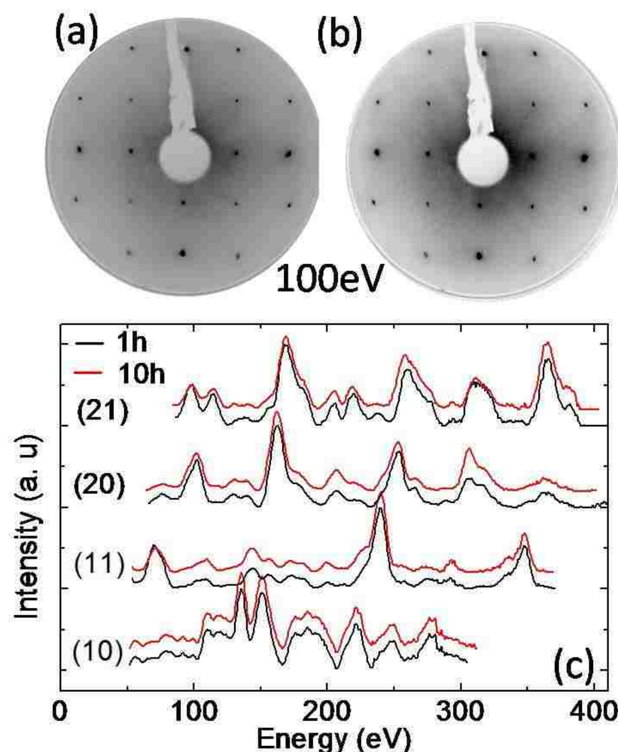

Figure 3-4: LEED pattern at 100 eV of surface after 1 h degassing (a) and 10 h degassing (b) at 100 ^{o}C. (c) The LEED I-V curves of these two surfaces.

The surface structures of sample 1-4 under four different preparation conditions as shown in **Figure 3-1** were further investigated by LEED. Both the surface of as-etched sample (data not shown) and the *in-situ* 100 ^{o}C degassing sample show 1x1 LEED pattern (see **Figure 3-3a**). The 1x1 surface of (001) $SrTiO_3$ is not stable against high temperature. The sample-2 which was annealed at 500 ^{o}C already shows some weak 1x2 reconstruction pattern. After annealing at higher temperature, the intensity of the fractional spot of 1x2 reconstruction increases as the profile curves right below the pattern image revealing (see **Figure 3-3(b-d)**). If the annealing temperature is 900 ^{o}C, some weak central spots (e.g., (1/2, 1/2)) appear and the intensity of the central spots is much weaker than the integral spot as shown in **Figure 3-3f**. The surface reconstruction of sample-4 may be mixed with 1x2 and 2x2. We also check the LEED pattern of sample annealed at higher Ozone pressure such as 100 mTorr. The surface 1x1 will collapse into reconstruction of ($\sqrt{2}\times\sqrt{2}$) at such high

oxidation atmosphere. Our results indicate that the 1x1 is not stable during the high temperature treatment.

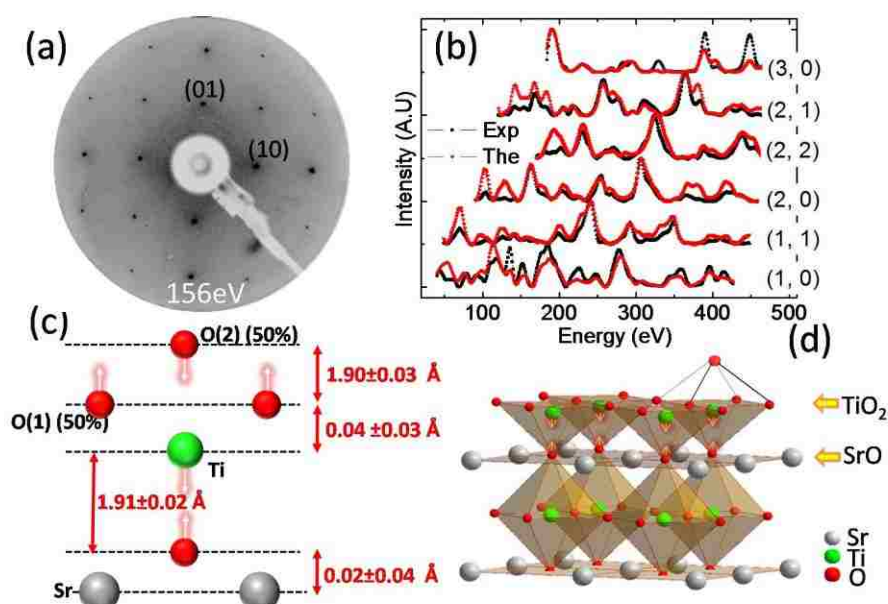

Figure 3-5: (a) LELD pattern of as-etched $SrTiO_3$ (001) surface at 77 K (b) The comparison between experimental LEED-IV curves at 77 K and theoretical curves. Structure of as-etched $SrTiO_3$ (001) surface (c) and 3D structure model (d).

The 1x1 surface which is obtained after etching is stable at low treatment temperature. A comparison of LEED results between two samples of degassing for 1 h and for 10 h at same temperature of 100 ^{o}C is shown in **Figure 3-4**. Both the surfaces of 1 h degassing and 10 h degassing samples are 1x1. The background of the LEED is a little different that the 1 h degassing sample has much lower background intensity than the 10 h sample. However, their LEED I-V curves show very small or no difference, indicating that they have the same surface structure. To figure out the structure of 1x1, a LEED IV of a sample cooled down to 77 K was acquired. The structure refinement of LEED I-V was performed and the possible structure model is figured out as shown in **Figure 3-5**. The R_p is 0.24. The surface is TiO_2 termination which is consistent with the results from **Ref. [100]**. However, there are two other features which are worth noticing [see **Figure 3-5**]. One is that there is ~50% O(2) randomly

atop Ti and ~50% of O(1) in the TiO_2 plane is missing. Another feature is the buckling that Ti moves down by ~0.02 Å and the oxygen right down the Ti moves up by 0.02 Å relative to its bulk coordination. Both the TiO_x plane plus the O(2) and the SrO plane become polarized with same polarization direction pointing inside, so we obtain a polar surface. As a result, buffer oxide HF solution etching causes a high oxygen deficient polar STO surface.

Because of such high oxygen deficient polar character, this surface is instable to high temperature treatment. The appearance of surface reconstruction as shown in **Figure 3-3** may be partly induced by such unique surface structure. Indeed, our experiments show that the 1x2 easily forms when the as-etched surface is annealed at above 500 ^oC in both UHV and oxygen atmosphere of even up to 100 mTorr. The sample annealed in oxygen flow in a tube furnace is pure 1x1, indicating that a very high oxygen pressure is required during annealing to get a pure 1x1 surface structure.

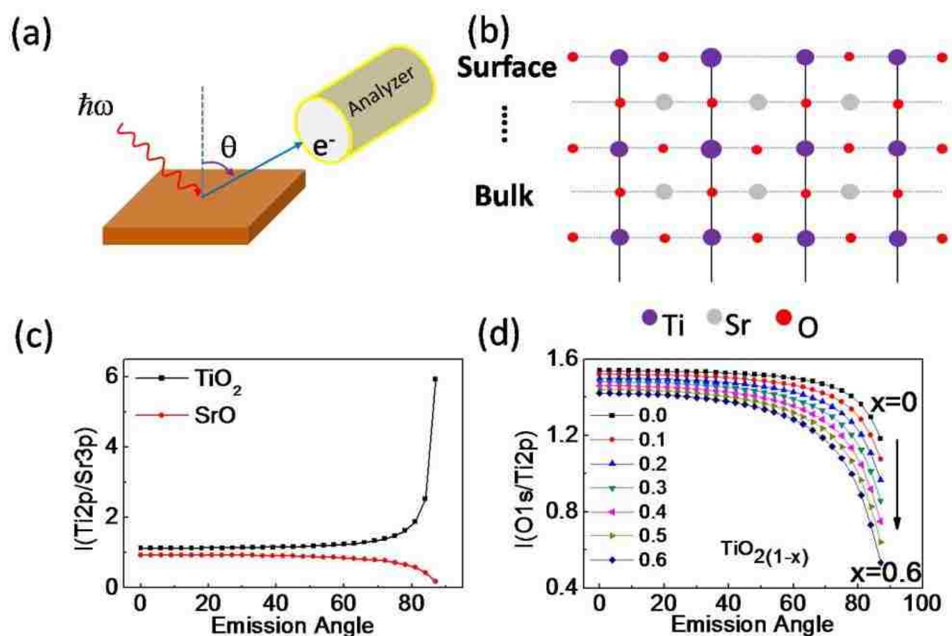

Figure 3-6: (a) Schematic setup of ARXPS. (b) Structure of TiO_2 termination surface. Theoretical calculation result of the emission angle dependent intensity ratio of (c) Ti2p/Sr3p in the case of TiO_2 vs. SrO termination and (d) O1s/Ti2p at different oxygen deficient level at top TiO_2 termination layer.

The chemical composition of the surface is investigated by using angle resolved XPS (ARXPS). With the equation about ARXPS described in **2.2.3**, we can theoretically calculate the ratio of different element (peak) as a function of off-normal emission angle. The ARXPS setup and theoretical results are shown in **Figure 3-6**. With knowledge of structure and chemical composition distribution, element peak intensity ratio can be figured out theoretically. The structure and distribution of chemical composition in each layer for the TiO_2 termination STO is shown in **Figure 3-6b**, while the SrO termination case can be obtained by removing the top TiO_2 layer. According to the theoretical results as shown in **Figure 3-6c**, the Ti2p/Sr3p ratio will increase/decrease intensively at high emission angle (see **Figure 3-6c**) if the surface terminates with TiO_2/SrO. Assuming that the introduction of the oxygen vacancies doesn't affect the IMFP and photoemission cross-section, we can calculate the intensity ratio of O1s/Ti2p at different oxygen deficient level at TiO_2 termination layer as shown in **Figure 3-6d**. The introduction of oxygen vacancies at the surface will decrease the O1s/Ti2p ratio.

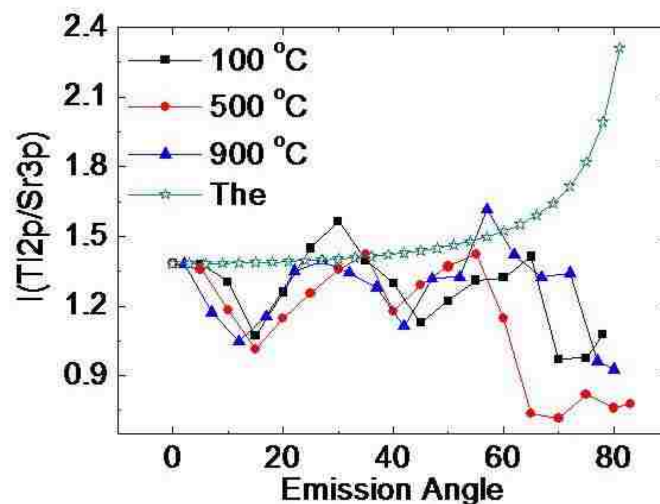

Figure 3-7: Emission angle dependent intensity ratios of Ti2p/Sr3p at different treatment conditions. Rectangle: 100 °C UHV degassing for 1 h, circular: 500 °C 10^{-4}Torr Ozone annealing for 1 h, triangle: 900 °C 10^{-4}Torr Ozone annealing for 1 h. The open pentagram is the theoretical simulation result.

Let us turn to the experimental result of ARXPS of (001) $SrTiO_3$ (see **Figure 3-7**). The experimental curves of samples at different treatment conditions show some kinds of similar oscillation but don't have a monotonic increase/decrease as expected. Since the photoelectrons will be forwardly scattered in s single crystal sample, the diffraction of the photoelectron will modulate the spatial distribution of the photoelectron intensity and induce a holograph **[117]**. The holography induced intensity modulation results in the oscillation as observed in **Figure 3-7**. The photoelectron holography phenomenon in another way brings us trouble to understand the ARXPS data. It is difficult to determine the surface chemical composition due to the disappearance of the monotonic change of intensity ratio. Furthermore, the surface absorption, surface reconstruction and non-stoichiometry will affect the IMFP and thus affect the peak ratio. It is expected to have a great change of peak intensity ratio at high angle up to 85°, but it cannot be reached experimentally. The step edge emission and a little roughness will cause the ARXPS curves deviate much from ideal 2D surface model at very high angle. These effects will change the contribution of surface XPS from the idea consideration. The idea theoretic calculation cannot be over-used to interpret the ARXPS data and a modified calculation should be developed.

The surface absorption and contamination can be easily accessed by high off-normal emission angle XPS. As shown in **Figure 3-8**, the as-etched sample has certain amounts of Carbon and Fluorine at the surface as revealed by the ARXPS. F1s and C1s peaks increase with increasing emission angle and the peak intensity ratios of the F1s and C1s to Sr3p increase too. The F1s/Sr3p ratio can go even up to 0.5. It can be concluded that there are a lot of Fluorine and Carbon at the surface of as-etched sample.

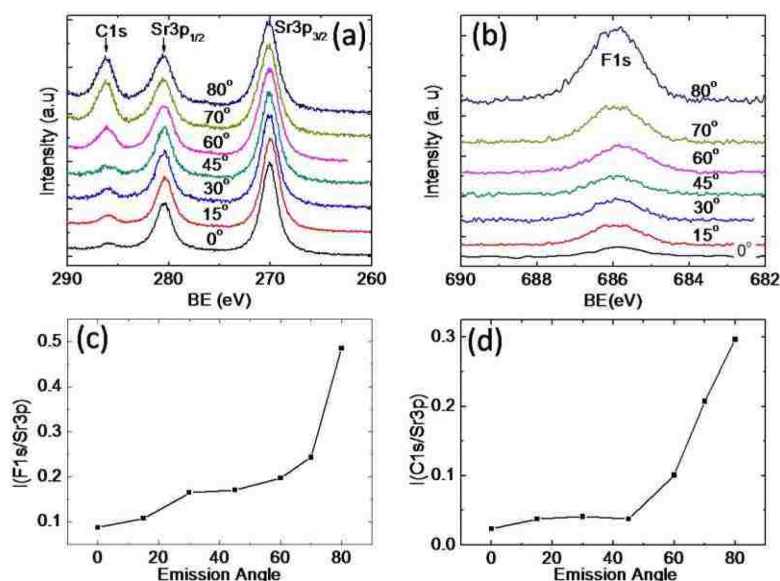

Figure 3-8: Angle resolved spectrum of C1s peak (a) and F1s peak (b). The intensity ratios of F1s/Sr3p and C1s/Sr3p are shown in (c) and (d), respectively.

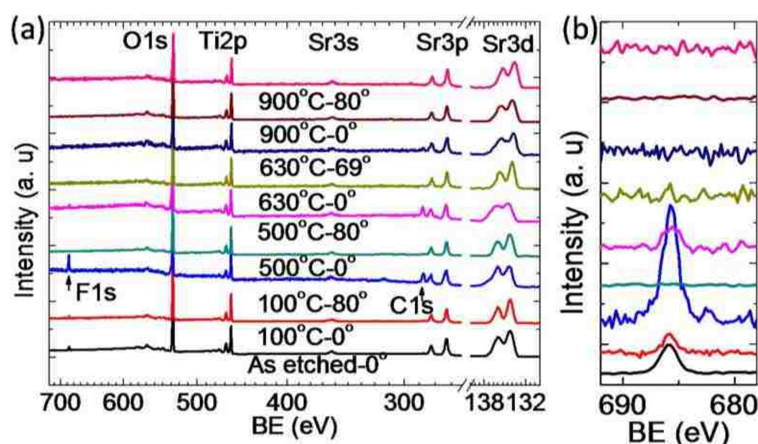

Figure 3-9: (a) The ARXPS of samples at different treatment conditions. All the samples are annealed for 1 h at 10^{-4} Torr Ozone except the one at 100 ^{o}C degassing in UHV. (b) Zoom-in of the F1s peak.

The way of how to clean the surface was explored. ARXPSs for different treatment conditions are shown in **Figure 3-9**. It is found that 100 ^{o}C is not high enough to remove the Fluorine. A strong F1s peak can still be observed at 80° spectrum of 100 ^{o}C degassing sample. The Fluorine peak starts to disappear under 500 ^{o}C annealing that the F1s peak is already very weak even in 80° spectrum. Higher annealing temperature of 650 ^{o}C and 900 ^{o}C can completely remove the Fluorine. The surface contamination by Carbon can also be eliminated by annealing at and above 650 ^{o}C.

In summary, we investigated the surface of HF etched (001) $SrTiO_3$ substrate. It is found that the HF buffer solution etching induces a polarized and oxygen deficient TiO_2 termination surface. This surface is not stable against the high temperature treatment and its initial 1×1 surface easily collapses into reconstruction when the annealing temperature is above 500 ^{o}C. However, the surface can become atomically flat after high temperature annealing. It is found that the (001) $SrTiO_3$ annealed in oxygen flow can sustain its 1×1 structure, so a highly oxidized atmosphere is required to get 1x1 surface. It seems very difficult to obtain a stoichiometric and atomically flat substrate at the same time. With respect to the surface contamination, our experimental results show that a relative high temperature of above 650 ^{o}C is enough to get a clean substrate for epitaxial growth.

Chapter 4 Dimensionality and Stoichiometry Effect on $La_{2/3}Sr_{1/3}MnO_3$

4.1 Introduction and Motivation

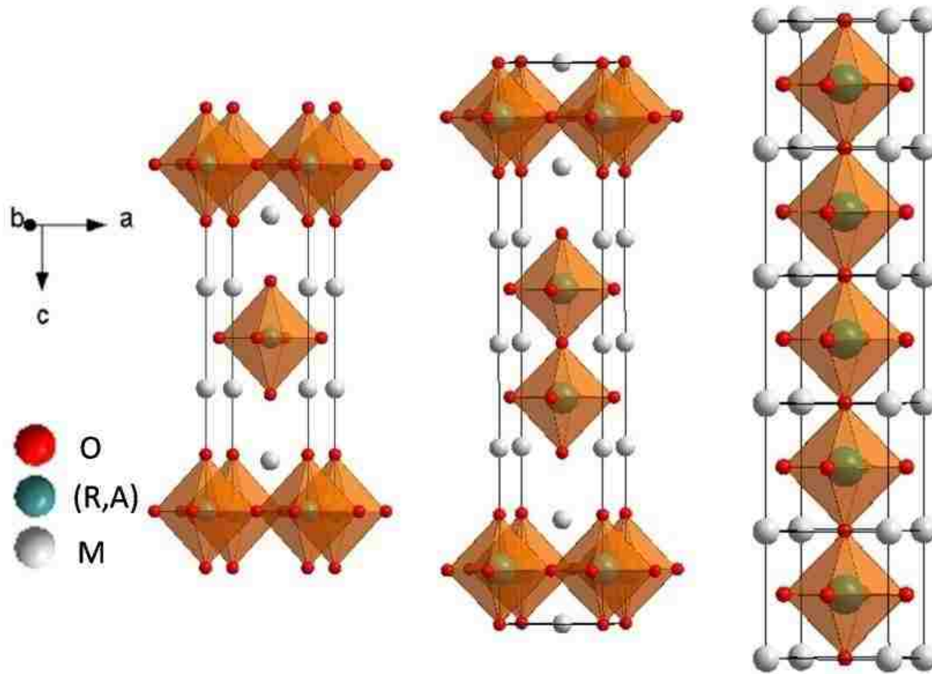

Figure 4-1: Crystal structures of Ruddlesden-Popper (RP) serials of (R, A)$_{n+1}$M$_n$O$_{3n+1}$. From left to right, it is n = 1, n = 2, n = ∞ respectively.

Dimensionality driven transition has been extensively observed in many correlated materials such as transition metal oxides. The reduced dimensionality will drive the metal oxides into a phase far away from its counterpart of bulk, for example, a metallic phase is switched into insulating phase when reducing the dimensionality. The dimensionality effect has been extensively observed in nanomaterials. However, it is not an exclusive phenomenon in nanomaterials such as artificial ultrathin film or quantum dot but also illustrated in layer structural materials such as Ruddlesden-Popper serials (R, A)$_{n+1}$M$_n$O$_{3n+1}$ as shown in **Figure 4-1**. A unique feature for this layer compound is that *n* layers of (R, A)MnO_3 unit cell are sandwiched between two insulating (R,A)O layers along c axis, so it equivalently reates an ultrathin n layers (R, A)MnO_3. The general 3D perovskite structure is the $n = \infty$ case with infinite layers of (R, A)MnO_3. With reducing the *n* so as to reduce the dimensionality, the

properties change. For example, the double layer (n = 2) $La_{1.2}Sr_{1.8}Mn_2O_7$ has a curie temperature of ~100 K **[118]** which is much lower than that of the 3D $La_{0.6}Sr_{0.4}MnO_3$ ($n = \infty$) of ~ 350 K **[119]**. The lower curie temperature results much from the reduced dimensionality effect.

Although Ruddlesden-Popper serials demonstrate the dimensionality effect, but these quasi 2D structures could not be an idea 2D since that the interlayer coupling still exist and some degree of 3D behavior still survives **[120]**. Further, it is extremely difficult to grow a single crystal of Ruddlesden-Popper structure with $n \geq 3$, so it is impossible to investigate how the properties evolve with changing the thickness of (R, A)MnO_3 one layer by one layer through Ruddlesden-Popper crystal.

Artificial ultrathin film is another good and better way to explore the dimensionality effect. The current Laser-MBE/MBE techniques allow us to easily and precisely grow (R, A)MnO_3 layer by layer, so an arbitrary n layers (R, A)MnO_3 materials can be created. Further, the interlayer coupling will disappear in an ultrathin film. As a result, artificial ultrathin film, which allows us to investigate the evolution of properties with gradual change of thickness one unit cell (u.c.) by one unit cell., provides us with a great opportunity to look into the dimensionality effect.

It is supposed to obtain a sole dimensionality effect in artificial thin film, but the presence of the substrate will introduce such as strain, interface coupling and interface disorder, *etc.*. It is unfortunate that we cannot get rid of the substrate, but it could be a good opportunity in another way allowing us to investigate how the low dimensional materials response to the external stimulus such as interface coupling, defect and strain.

In this chapter, we use $La_{2/3}Sr_{1/3}MnO_3$ (LSMO) ultrathin film to illustrate the dimensionality and the stoichiometry effect. 33% doping LSMO is most itinerant ferromagnetic metal with the highest curie temperature of ~370 K **[119]** among manganites. LSMO has nominal 100% spin polarized electrons **[121]**, so it is extensively used for spintronics devices **[122-124]**. However, the electronic and magnetic properties of LSMO will be greatly degraded when its thickness is down to several nanometers. The critical thickness where the properties of LSMO are deteriorated **[39, 40, 125-130]** is called dead layer. The dead layer will depolarize the spin current at the interface of magnetic tunnel junctions. The scalability of a spintronics device will also be limited, since a film thicker than dead layer must be used.

Although a great effort has been paid to understand the origin of the dead layer in LSMO thin film, its origin is still a unsolved mystery. According to the facts that the magnetic dead layer is thinner than electric dead layer and that magnetic moment of films with thickness less than electric dead layer is much smaller than the bulk, a phase separation has been proposed to explain the electric dead layer **[125]**. However, the mechanism of the suppressed ferromagnetism is still unknown. Interface induced modification of orbital has been proposed to be the cause of dead layer **[129, 130]**. Both Tebano *et al.* **[129]** and Lepetit *et al.***[130]** suggested that the occupation of $3z^2 - r^2$ against $x^2 - y^2$ orbital at interface/surface according to the measurement of linear dichroism of the X-ray absorption spectroscopy (LD-XAS) and related theoretical calculation, resulting in a C-type antiferromagnetic (C-AF) ordering phase which is insulating, causes the dead layer. However, Huijben *et al.*, who reduced thickness of the electrical dead layer to 8 u.c., found that the preferential occupation

of the in-plane $x^2 - y^2$ orbital survives down to 5 u.c. **[125]**. They also concluded that there is no orbital reconstruction at interface for all layer thicknesses. This contradicted discovery makes the debate intense. What is more, there is no conclusion about the exact thickness of the electric dead layer. The thicknesses of electric dead layer on different substrates reported by different group are listed in **Table 4-1**. For the same substrate, for example, the $SrTiO_3$, different thicknesses (4.0 nm **[126]**, 3.1 nm **[125]**, 2.7 nm **[129]**) of dead layer are reported. The reported thicknesses of dead layer on $LaAlO_3$ substrate even have a big gap (5 nm **[39]** vs. 12 nm **[129]**). There must be some extrinsic ingredients causing the dead layer. They could be chemically or structurally altered film-substrate interface **[126]**, surface roughness **[40]**, oxygen deficiency **[44, 45]**, surface Sr segregation **[132]**, etc..

Table 4-1: Reported thicknesses of dead layer of LSMO grown on different substrates. $\varepsilon \equiv (a_{Sub}-a_{LSMO})/a_{LSMO}$ and a_{LSMO} = 3.8804 Å **[131]**. The superscript NO. is the reference.

Sub	$LaAlO_3$	$NdGaO_3$	LSAT	$SrTiO_3$	MgO
a(Å)	3.78	3.86	3.868	3.904	4.212
ε	-2.6%	-0.5%	-0.05%	0.6%	8.5%
Thickness of Dead Layer	12 nm[127] 5 nm[39]	3.0 nm[39] 2.7 nm[129]	3.1 nm[128]	4.0 nm[126] 3.1 nm[125] 2.7 nm[129]	4 nm[40]

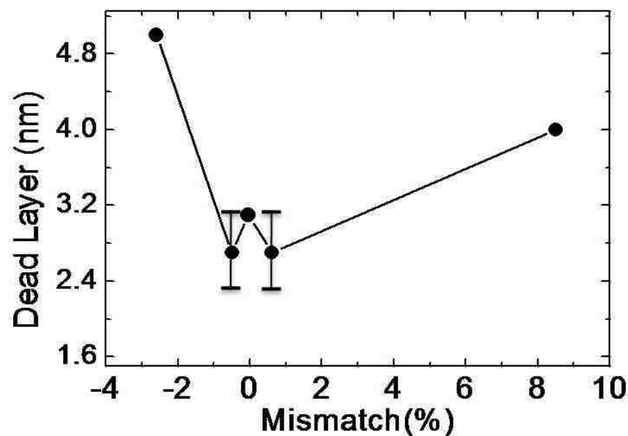

Figure 4-2: Thickness of dead layer vs. lattice mismatch. The points with error bar used are according to the **Ref. [129]**.

Using the thinnest dead layer in **Table 4-1**, the thickness of dead layer versus lattice mismatch is drawn in **Figure 4-2**. The dead layers on $NdGaO_3$, $(La_{0.18}Sr_{0.82})(Al_{0.59}Ta_{0.41})O_3$ (LAST) and $SrTiO_3$ have almost the same thickness, so it can be concluded that small lattice mismatch does not affect the thickness of dead layer a lot. Since the thinnest dead layers for $NdGaO_3$ and $SrTiO_3$ substrates from **Ref. 129** have one u.c. error, we conservatively choose the up-limit and extrapolate that the reported thinnest dead layer is ~8 u.c. (= 3.1 nm) at the low lattice mismatch region. However, the dead layer can be thinner, since some extrinsic effects induced additional thickness of dead layer may still exist in previous reported films.

To reveal the origin of dead layer, we need to exclude the extrinsic factors and find out the intrinsic dead layer or at least get close to it as much as we can. The discrepancy of the thickness of the dead layer may arise from different growth condition, typically the oxygen growth pressure **[125, 126, 129]**. The oxygen stoichiometry should be much more cared since tiny off-stoichiometry may cause big change of the properties of an ultrathin film. In this chapter, we try to reveal the optimal condition to minimize the oxygen off-stoichiometry to get closer to the intrinsic dead layer as well as the nature of the dead layer. Both the dimensionality and oxygen stoichiometry effect on the LSMO ultrathin films will be the main focus.

4.2 Growth of $La_{2/3}Sr_{1/3}MnO_3$ Ultrathin Film

The atomically flat (001) $SrTiO_3$ (STO) substrates were used to epitaxially grow LSMO thin films. STO was first etched by buffer oxide HF solution for 30 s and then annealed at 900 ^{o}C for 2 hours in oxygen flow. Atomically flat TiO_2 termination surface was obtained. Detail of the substrate treatment can be found in **Chapter 3**.

The LSMO thin films were epitaxially deposited on STO by using our Laser-MBE system from a stoichiometric $La_{2/3}Sr_{1/3}MnO_3$ target. A KrF excimer laser (λ = 248 nm) at a repetition rate of 3 Hz and a laser fluence of ~2.3 J/cm^2 was used. The spot size of the laser beam was ~ 0.021 cm^2. During the growth, an Ozone gas atmosphere was employed. The Ozone source was created from a Azcozon HTU500-G2 OZONE GENERATOR. The Ozone output was 25 μg O_3 per millilitre O_2 (25 μg/mL). Ozone gas was injected into the growth chamber through a nozzle and the gas pressure in the chamber could be regulated with a leak valve. The substrates were maintained at a certain temperature during the growth. To obtain a layer-by-layer growth for all Ozone pressure (called growth pressure hereafter) ranging from 10^{-6} Torr to 180 mTorr, an optimized growth temperature window was explored and it was found to be ~ 680 ^{o}C-720 ^{o}C. The RHEED oscillation could not sustain for too long time in the case of using higher temperature (800 ^{o}C for example). Lower temperature (500 ^{o}C for example) will favor 3 D growth and cause poor crystal quality. All the samples mentioned below were grown at 700 ^{o}C.

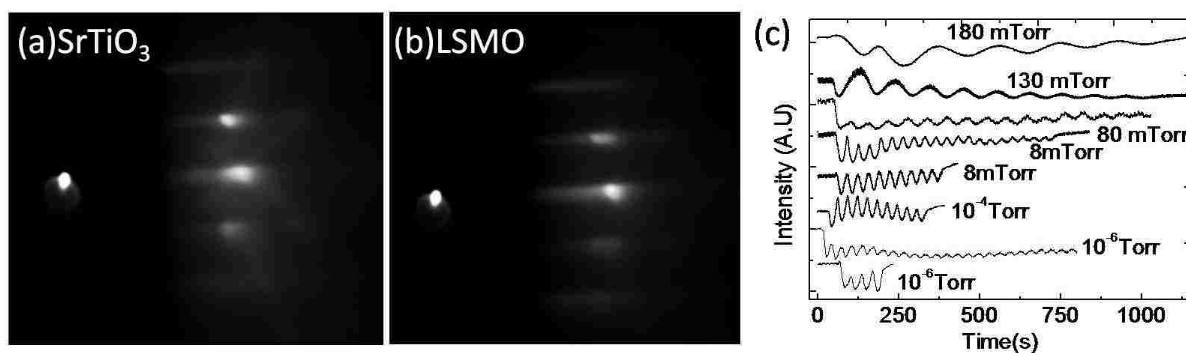

Figure 4-3: RHEED diffraction pattern of $SrTiO_3$ substrate (a) and LSMO thin film (b). (c) RHEED intensity monitored during growth at different Ozone pressure.

With the optimized growth condition mentioned above, an atomically smooth surface of LSMO was obtained. **Figure 4-3** shows the 2D RHEED diffraction pattern for STO substrate and 60 u.c. thick LSMO thin film grown at 8 mTorr. The LSMO maintained 2D flat during

growth. A layer by layer growth mode was obtained for all growth pressure ranging from high vacuum of 10^{-6} Torr to high pressure of 180 mTorr as the RHEED intensity oscillation in **Figure 4-3c** showing. According to **Figure 4-3c**, higher growth pressure results in lower growth rate. The growth pressure of higher than 180 mTorr was also tried, but it was found to favor a 3D growth.

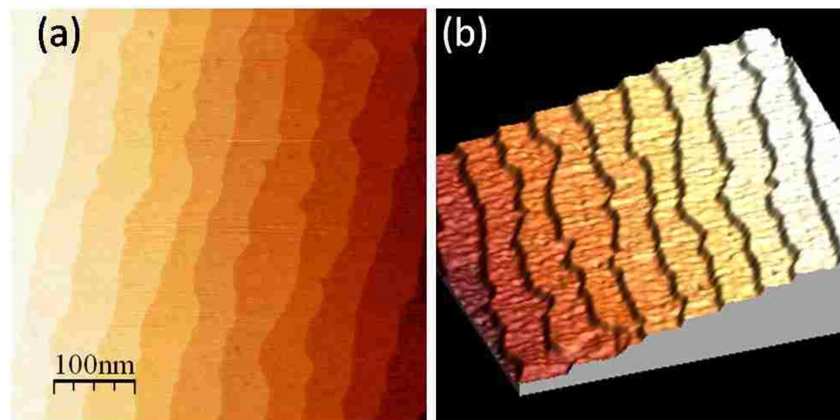

Figure 4-4: STM image of the 10 u.c. LSMO thin film: (a) 2D contour image; (b) 3D image.

The surface morphology of the LSMO thin film was investigated by STM. To perform the STM scanning, a conductive 0.1wt% Nb doped $SrTiO_3$ (NSTO) substrate rather than pure STO was used. **Figure 4-4** shows the surface morphology of a 10 u.c. LSMO ultrathin film. Nice terrace with a width of about 50 nanometers is observed. A single step height of ~0.39 nm can be found in our STM image, indicating a single termination surface.

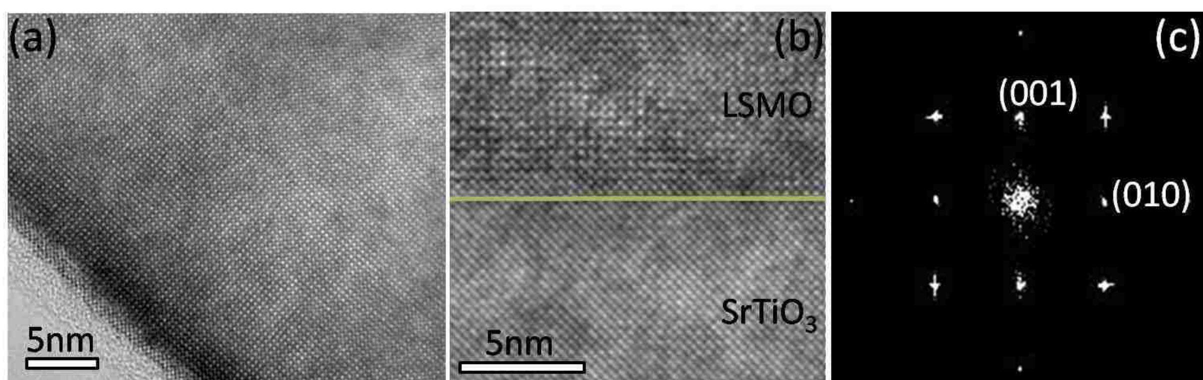

Figure 4-5: HRTEM image of LSMO (a) and LSMO/$SrTiO_3$ interface (b). (c) FFT pattern of the (b) image.

The microscopic structure was further investigated by TEM. **Figure 4-5** shows the high resolution TEM image of the cross-section structure of LSMO and its interface with STO. The film was well crystalline and the LSMO/STO interface was very sharp. The fast Fourier transform (FFT) of the region around the interface doesn't show any obvious split of the peaks due to very small mismatch, indicating that the LSMO film was epitaxially grown.

4.3 Thickness of Dead Layer

The properties of the LSMO thin films with thicknesses ranging from 2 u.c. to 120 u.c. were investigated. The transport properties of the LSMO thin films of different thicknesses and grown at different pressures are displayed in **Figure 4-6**. The transport properties strongly depend on the growth pressure and thickness. For a film grown at certain pressure, it will become less metallic with decreasing thickness. Below certain critical thickness (t_c), LSMO becomes insulator. A cross-over metal-to-insulator transition with metallic ground state can be observed for the films with thickness bigger than t_c. For example, the LSMO film grown at 1 μTorr has a critical thickness of 14 u.c. and the critical thickness for that grown at 80 mTorr is 6 u.c.. The critical thickness decays with increasing growth pressure but stops at 6 u.c. when the growth pressure is ≥ 80 mTorr. Higher Ozone growth pressure will enhance the conductivity and favor a metallic ground state.

The transport properties of 6 u.c. and 7 u.c. samples grown at different pressures are shown in **Figure 4-7a** and **Figure 4-7b**, respectively. For the 6 u.c. LSMO thin films grown at different pressures, all are insulating at low temperature but the resistivity dramatically decreases with increasing pressure. For the 7 u.c. samples, the ground state becomes metallic at a growth pressure of ≥ 80 mTorr. Higher Ozone pressure will oxidize the film more

completely, thus reduce the oxygen deficiency. It can be concluded that oxygen deficiency will drive the films to be more insulating.

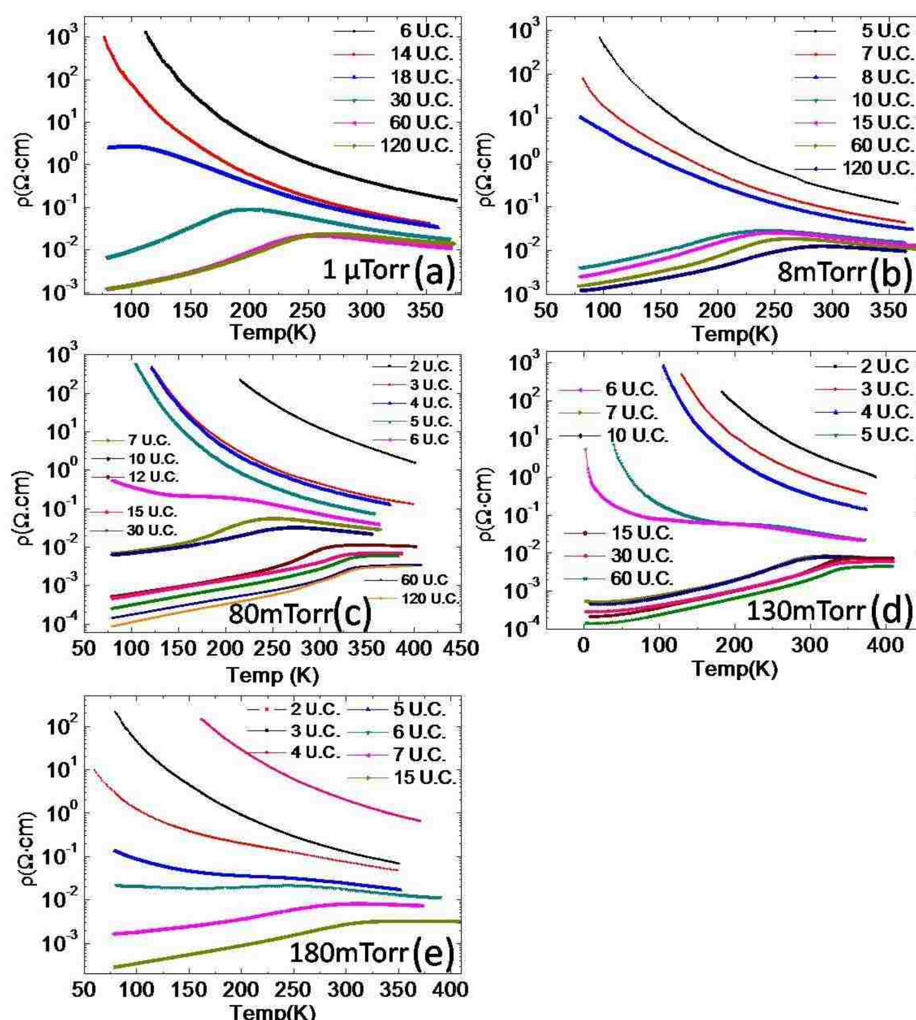

Figure 4-6: Temperature dependent resistivity for LSMO films with different thicknesses grown at (a) 1 μTorr, (b) 8 mTorr, (c) 80 mTorr, (d) 130 mTorr, (e) 180 mTorr Ozone pressure.

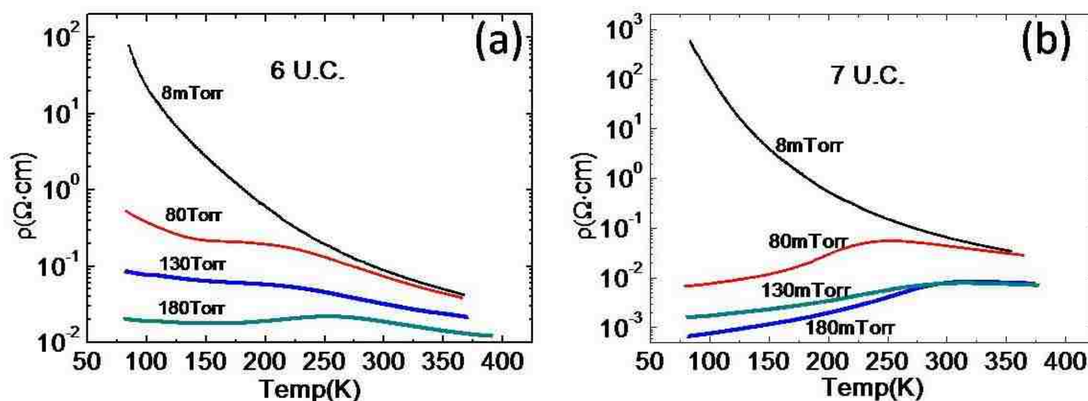

Figure 4-7: Effect of growth pressure on transport properties. Temperature dependent resistivity for 6 u.c. LSMO (a) and 7 u.c. LSMO (b) grown at different Ozone pressure.

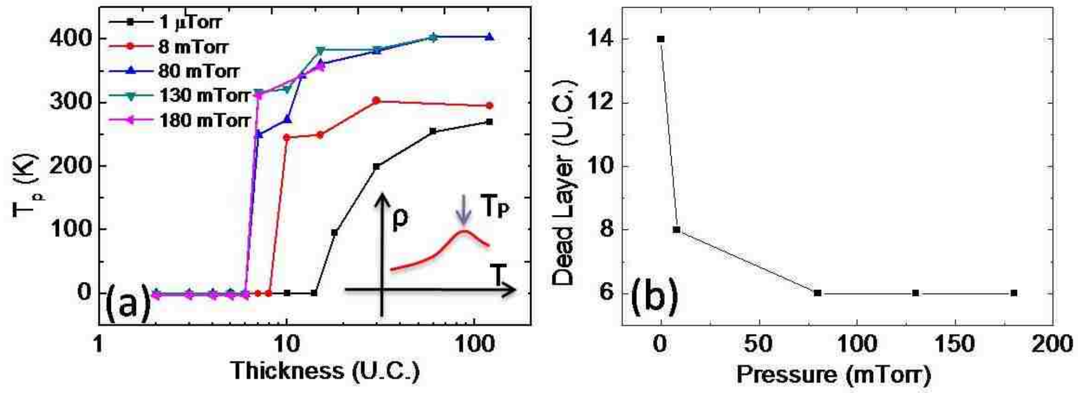

Figure 4-8: (a) Metal-insulator transition temperature T_P vs. thickness for films grown at different pressures, inset shows the definition of T_p. For insulating film, the T_P is defined as 0. (b) The thickness of dead layer versus growth pressure

The bulk LSMO is ferromagnetic metal below the curie temperature of ~370 K and above the 370 K, it is paramagnetic poor metal. The properties of ultrathin film may deviate from the bulk that the film exhibits a lower transition temperature than the bulk **[125]** with transition temperature strongly depending on the growth condition. Both the off-stoichiometry and reduced thickness will reduce the transition temperature (T_P) as shown in **Figure 4-8**. For all specific growth pressure, the T_P will saturate at a thick enough thin film. A critical Ozone pressure is required to push the saturated T_P value to close to that of the bulk. With using our growth condition, a 80 mTorr Ozone pressure is enough to make a thick film behave like the bulk LSMO. In the case of using relatively low growth pressure, for example 8 mTorr, the 120 u.c. thick film which can be considered to be a bulk, has a T_P (295 K) much lower than that of the bulk. Lower T_P should result from oxygen deficiency. The thickest insulating film is generally called as electronic dead layer. The thicknesses of dead layers for the films grown at 1 μTorr and 8 mTorr are 14 u.c. and 8 u.c. respectively. With increasing the growth pressure to be ≥ 80 mTorr, the thickness of dead layer decays to a minimum value of 6 u.c. Although we cannot guarantee that there is no oxygen deficiency in our LSMO samples of our highest growth pressure of 180 mTorr, but the trend from **Figure 4-8b** could enable us

to extrapolate that the 6 u.c. is true critical thickness for the onset of metallic ground state for a stoichiometric film. Actually, the resistivity for the thicker samples grown at ≥ 80 mTorr is quite close to or already equal that of the bulk. For example, the 60 u.c. LSMO grown at 130 mTorr has a resistivity of 100 μΩ·cm at 2 K, which is equal to that of bulk **[119]**. Based on these facts, The contribution of increasing thickness of the dead layer due to oxygen deficiency could be excluded from our films grown at high Ozone pressure such as 180 mTorr.

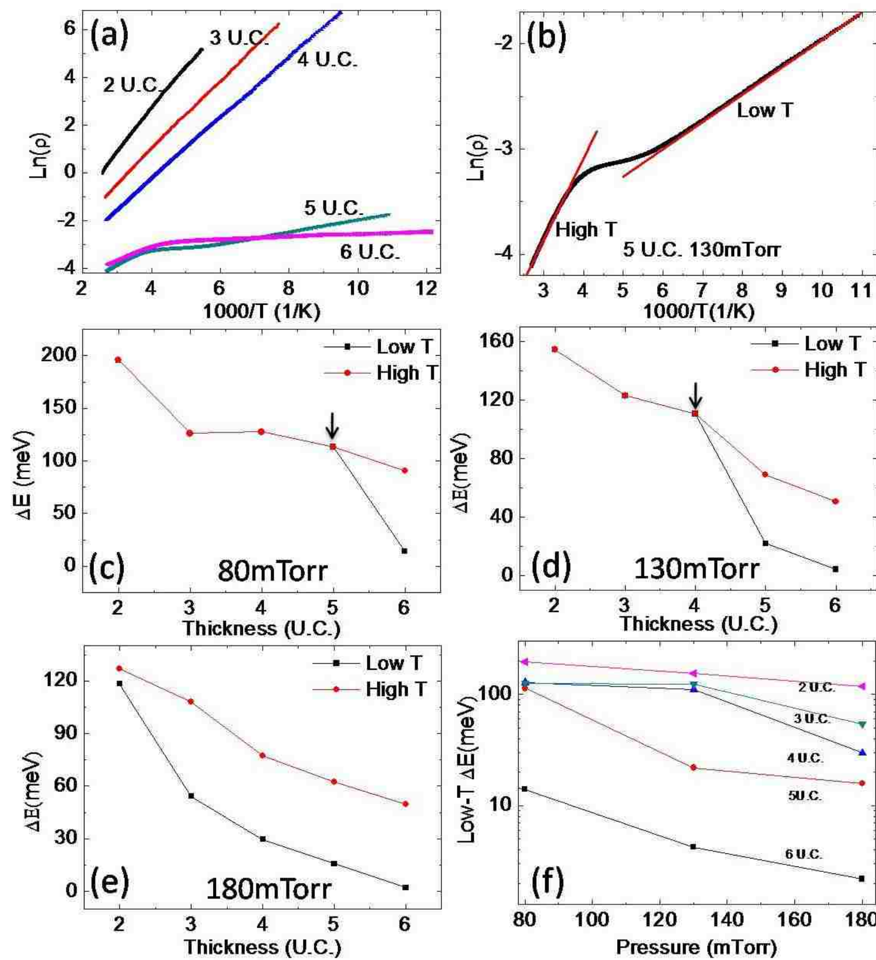

Figure 4-9: Evolution of thermal activation energy (ΔE) vs. thickness. (a) Resistivity vs. temperature curves for insulating film grown at 130 mTorr plotted in Ln[ρ]-1000/T scale. The temperature range used here is from 77 K to 350 K. (b) Definition of the Low T and High T range for a film with a insulator-insulator transition. A 5 u.c. film grown at 130 mTorr is used as an example. ΔE vs. thickness for LSMO thin films at (c) 80mTorr, (d) 130 mTorr, (e) 180 mTorr. (f) ΔE at low-T range vs. growth pressure for different thickness.

Dimensionality driven metal to insulator transition seems to be a cross-over like. The thermal activation energy (ΔE) obtained by fitting with Arrhenius equation ($\rho = \rho_0 e^{\Delta E/KT}$) for LSMO of different thickness grown at different pressure is shown in **Figure 4-9**. Since an insulator-insulator transition would occur for certain thickness of thin film at certain pressure, we separately fit the curve at low temperature (low-T) range and high temperature (high-T) range as an example in the **Figure 4-9b** showing. For the 80 mTorr growth pressure, the low-T ΔE starts to deviate from high-T ΔE at 5 u.c., indicating the presence of the insulator-to-insulator transition. The critical thickness for the occurrence of the insulator-to-insulator transition decreases with increasing growth Ozone pressure. If the growth pressure is 130 mTorr, the deviation starts at 4 u.c.. For 180 mTorr, it is suggested to start from 1 u.c. according to **Figure 4-9e**. As a result, the stoichiometric ultrathin insulating LSMO film on (001) $SrTiO_3$ has an insulator-to-insulator transition down to 1 u.c.. The ΔE, no matter at low temperature range or high temperature range decreases with increasing thickness. However, the low-T ΔE gets very close to 0 at 6 u.c. thick LSMO, while the high-T ΔE still maintains a relative big value, indicating the ground state becomes less and less insulating with increasing thickness.

If we still use the Arrhenius equation to fit the temperature dependent resistive curve for metallic phase, we can obtain a negative thermal activation energy. The ΔE for 7 u.c. LSMO grown at 180 mTorr is ~ -6.77 meV. **Figure 4-10** displays the ΔE vs. thickness for LSMO grown at 180 mTorr. The ~ 0 meV thermal activation energy in 6 u.c. LSMO suggests that 6 u.c. is a cross-over transition thickness. Low-T ΔE gradually decreases to 0 with increasing thickness until 6 u.c. and after 6 u.c. the LSMO film becomes more and more metallic.

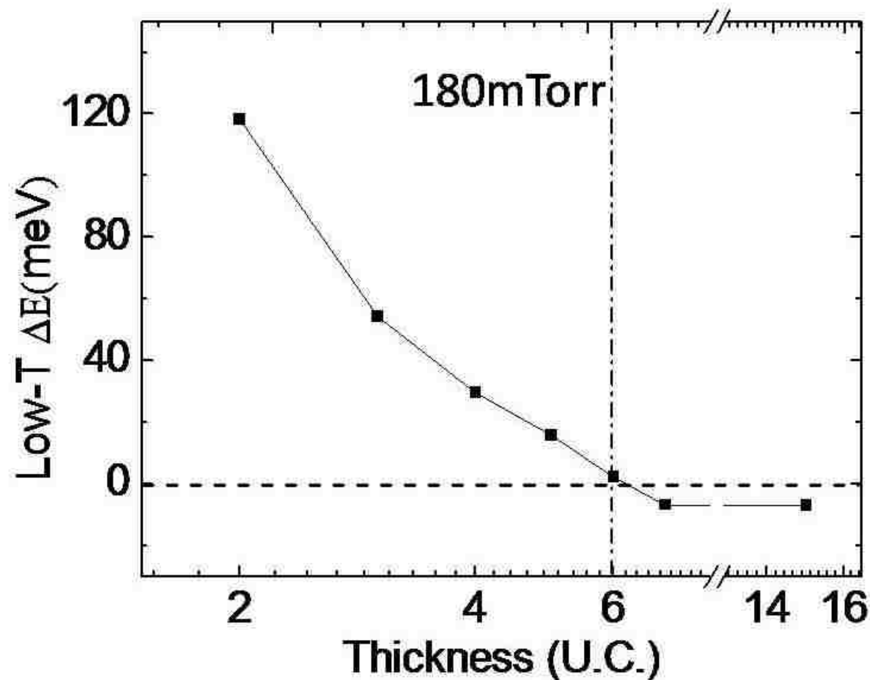

Figure 4-10: Low-T thermal activation energy (ΔE) versus thickness for LSMO films grown at 180 mTorr.

According to **Figure 4-9f**, it could be further concluded that the 6 u.c. could be the thinnest dead layer that we can approach. The ΔE of the 5 u.c. LSMO maintains a finite and relative big value. There is no trend for the ΔE of 5 u.c. LSMO to get close to 0 with increasing Ozone pressure. Although the film can become less insulating with less off-stoichiometry according to the trend as illustrated in **Figure 4-9f**, but there is no sign that the 6 u.c. thick film can become metallic. The ground state of the more stoichiometric 6 u.c. LSMO grown at 180 mTorr is still insulating, although it has a insulator-to-metal transition at 244 K upon cooling (see **Figure 4-7a**). The perfect 6 u.c. LSMO film has few possibility to becomes metallic at low temperature. It can be concluded that the dead layer cannot be less than 5 u.c. and should be 6 u.c..

We should notice that ultrathin film is more sensitive to oxygen deficiency than thicker film. This has been ignored before. A lot of films which have been investigated before have

been claimed to have correct stoichiometry but a systematical investigation of growth partial pressure was missed. It is hard to keep exactly same growth condition to grow LSMO layer by layer at different pressure, so the sole off-stoichiometry effect cannot be probed. The critical growth condition that we discovered enables us to clearly reveal the oxygen stoichiometry effect on ultrathin films. The evolution of thermal activation at different growth pressure does illustrate that very few oxygen vacancies can induce large thermal activation energy. It should be extremely careful of oxygen deficiency in ultrathin films.

4.4 Singularity in Critical Thickness

In correlated electron materials, any perturbation will induce a big change especially when the materials are close to a critical region where the competing couplings between spin, lattice, charge and orbital are nearly even. The typical correlated LSMO is very sensitive to external magnetic field **[119]** as well as the oxygen deficiency [**44, 45, 133]** and dimensionality as discussed in section **4.3**. The critical thickness of 6 u.c. which is the onset of metallic ground state should be located at a critical region with comparable co-existent competitions.

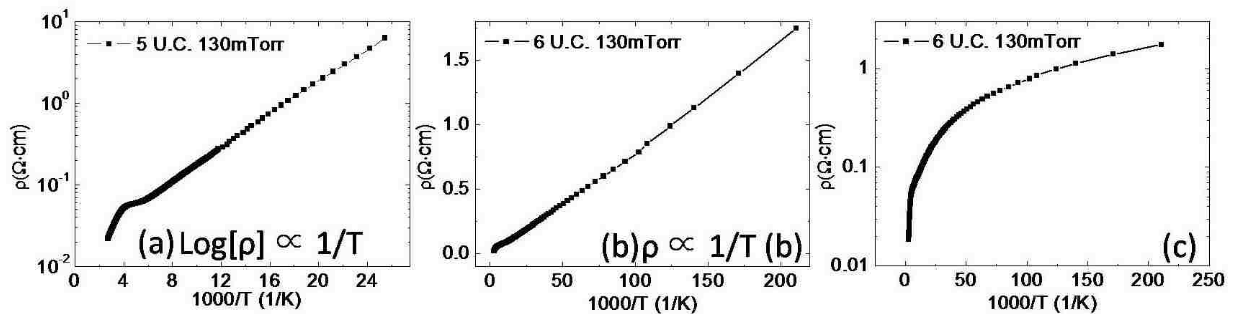

Figure 4-11: (a) ρ vs. T for 5 u.c LSMO plotted in Log[ρ]-1/T scale.(b) ρ vs. T for 6 u.c. LSMO plotted in (b) ρ vs. 1/T scale and (c) Log[ρ]-1/T scale.

One of the singular behaviors of the 6 u.c. LSMO is revealed in **Figure 4-11**. The LSMO ultrathin films of thickness less than 6 u.c. obey the Arrhenius equation at low temperature

and so it is $\rho = \rho_0 e^{\Delta E/KT}$, hence the 5 u.c. or thinner LSMO films have an energy gap for the activation of carriers. Quite differently, resistivity for 6 u.c. LSMO is inversely proportional to temperature at low temperature, so $\rho \propto 1/T$. It is still an insulator because of the fact that the resistivity will go to infinite value at 0 K. The carries in 6 u.c. LSMO cannot be characterized by simple energy gap theory. As shown in **Figure 4-11c**, the slop of curve monotonically decreases and approaches to 0 when T is close to 0 K, indicating that the thermal activation will become zero at 0 K. Such exotic transport properties suggest some critical behavior in 6 u.c. LSMO ultrathin film. Since $\rho = \rho_0 e^{\Delta E/KT}$, so, $\Delta E = K\frac{\ln\rho}{d(1/T)}$, and if $\rho = Const \times \frac{1}{T}$, then we have $\Delta E = K\frac{\ln\rho}{d(1/T)} = KT$. As a result, the $\Delta E = 0$ when $T = 0$ K. On the other hand, if ΔE is extremely small and so is $\frac{\Delta E}{KT}$, then we can get 1/T behavior too, since $\rho_0 e^{\Delta E/KT} = \rho_0 \frac{\Delta E}{KT}$ in this case. No matter what, the 1/T behavior should result from the zero thermal activation energy, further indicating that the 6 u.c. film is a critical thickness for the onset of metallic behavior.

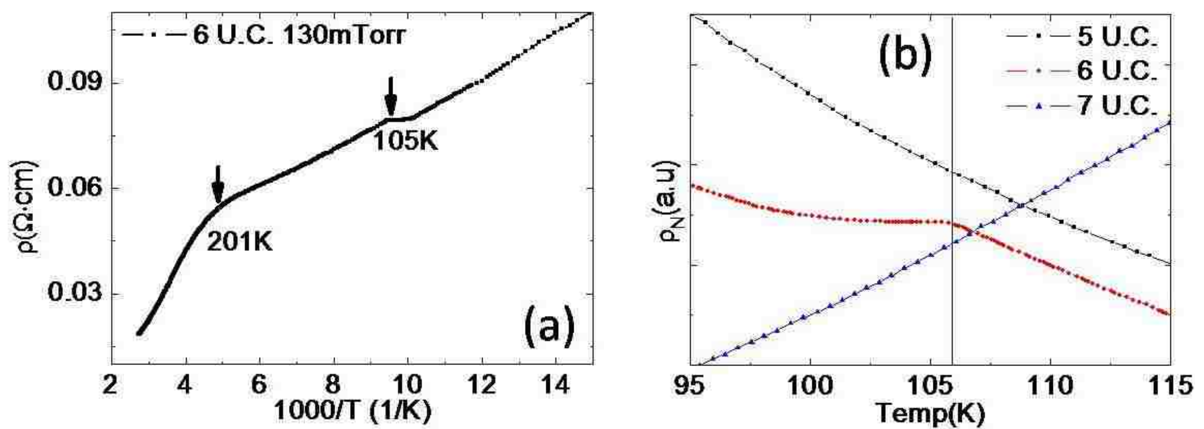

Figure 4-12: (a) Blow-up of the high temperature region of **Figure 4-11(b)**. (b) ρ vs. T around 105 K for 5, 6 and 7 u.c. LSMO grown at 130 mTorr. The resistivity is normalized to plot together for comparison.

The singular behavior in 6 u.c. LSMO is further reflected from its unique response to substrate structure transition. If we take a close look near the region around 105 K as shown in **Figure 4-12a**, a kink appears at ~105 K besides a normal insulator to insulator transition at ~ 201 K as discussed in **4.3**. However, the evident kink at 105 K only shows up in 6 u.c. LSMO film as shown in **Figure 4-12b**. This kink should be directly related to the $SrTiO_3$ structure transition **[134]**. The $SrTiO_3$ undergoes a structure transition from cubic to tetragonal phase at 105 K upon cooling down. A little change of the transition temperature at the surface may happen **[135, 136]**. The a-b plane lattice constant is reduced from 3.905 Å to 3.894 Å during the transition. Since the surface of the (001) $SrTiO_3$ at tetragonal phase maintains a 4 fold symmetry, same as the cubic phase, hence the symmetry of substrate surface doesn't change. Actually we could not observe any in-plane anisotropic behavior. The 105 K kink should be related to the change of lattice constant. The transition from cubic phase to tetragonal phase reduces the lattice mismatch between LSMO and STO from 0.63% to 0.35%. Since the reduced tensile strain will reduce the resistivity of LSMO film **[137]**, resistivity of LSMO film should decrease during the STO substrate transition under cooling down. The **Figure 4-12b** shows that the resistivity really decreases at the transition, further supporting that kink is cause by change of strain. It is surprising that only 0.3% change of lattice constant of STO substrate can cause an evident kink in 6 u.c. LSMO thin film. Further, the emergent kink only appears in 6 u.c. LSMO thin film. Such unique property in 6 u.c. implies that LSMO of critical thickness is very sensitive to external stimulus.

The evident kink at the 6 u.c. film is also very sensitive to the oxygen pressure during the growth of the film. As shown in **Figure 4-13**, the 6 u.c. LSMO grown at 8 mTorr and 80

mTorr don't show any evident signal of kink, but it appears at growth pressure of 130 mTorr and 180 mTorr. The kink in 180 mTorr grown sample is more pronounced than that in 130 mTorr grown sample. Although 6 u.c. is also the critical thickness for the films grown at 80 mTorr, but it doesn't show evident kink. It is concluded that introduction of oxygen vacancies will suppress the kink. In an another word, a perfect LSMO thin film without oxygen deficiency is more sensitive to strain. The resistive behavior of LSMO has been extensively investigated, but there are no reports on such kink at 105 K in the critical thickness. **Figure 4-13** strongly indicates that the kink at 105 K which has not been found is due to the off-stoichiometry although it is very small.

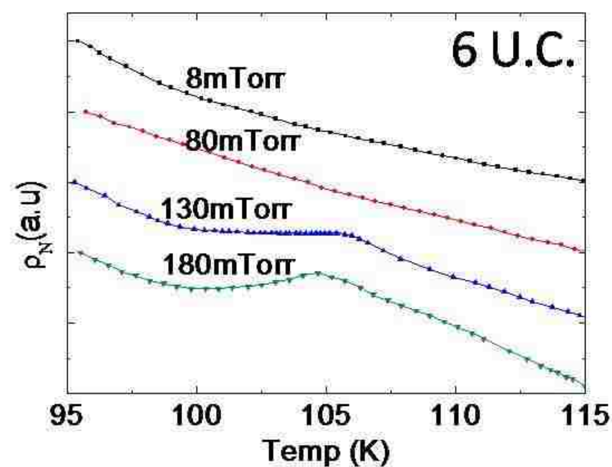

Figure 4-13: The temperature dependent resistivity curve around 105 K for 6 u.c. LSMO grown at different pressure. The resistivity is normalized to plot together for comparison.

The kink is robust against the magnetic field. **Figure 4-14** shows the transport properties under magnetic field. The field reduces the resistivity but the kink at ~105K sustains up at all magnetic field. For example, the 6 u.c. LSMO grown at 130 mTorr is insulating at zero field and it becomes metallic under 14 T magnetic field in the intermediate temperature range (130 K - 275 K), but the kink can still be observed. The response of the stoichiometric 6 u.c. LSMO to substrate transition is not affected by the spin state of the LSMO.

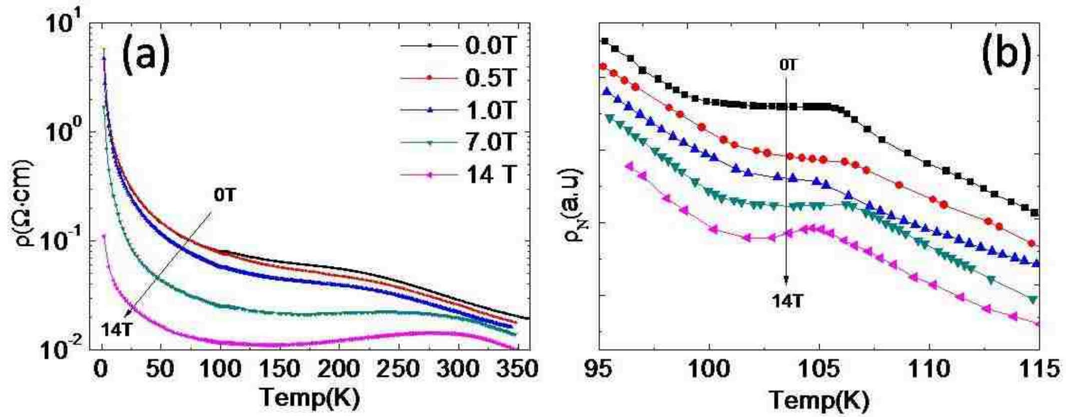

Figure 4-14: Robust kind at ~ 105 K under magnetic field. (a)Temperature dependence of resistivity for 6 u.c. LSMO grown at 130 mTorr under various magnetic fields. (b) ZOOM-IN of the 105 K region. The resistivity is normalized to plot together for comparison.

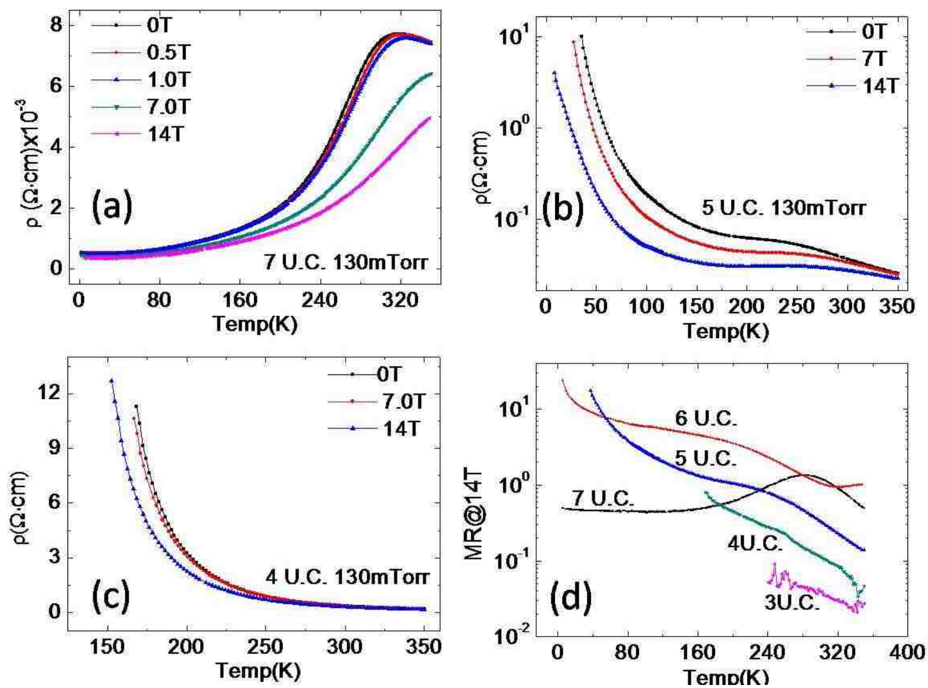

Figure 4-15: Temperature dependence of resistivity under various magnetic fields for (a) 7 u.c. (b) 5 u.c. (c) 4 u.c. LSMO grown at 130 mTorr. (d) MR ratio vs. temperature for films with different thickness.

Although the kink is not sensitive to the external magnetic field, the overall resistivity of the 6 u.c. film shows large field dependency, e.g., large MR effect. The stoichiometric 6 u.c. LSMO is more sensitive to magnetic field than other thickness of LSMO. **Figure 4-15** plots the temperature dependent resistivity under various magnetic fields for LSMO with different

thickness. Colossal magnetoresistance (MR) is observed for all thin films but the MR ratio varies with different thickness. The MR ratio is defined by the followed formula

$$MR(B,T)=\frac{R(B,T)-R(0,T)}{R(B,T)}\times 100\%$$

The MR ratio for different thickness is shown in **Figure 4-15d**. Interestingly, the 6 u.c. film has largest. The most insulating 3 u.c. LSMO has the smallest MR. The thicker one of 7 u.c. which has ferromagnetic ground state has a smaller MR than the film of 6 u.c. Such as non monotonic MR effect with thickness indicates a critical behavior at 6 u.c. LSMO film.

4.5 $SrTiO_3$ Capping Effect

The [$LSMO_M/STO_N$] superlattice exhibits distinct properties from single LSMO thin film on $SrTiO_3$ **[138-140]**. Generally, the interlayer coupling in superlattice is proposed to be the main reason to tune the properties **[138-140]**. Recently, Bruno *et al.* found that the interfacial Mn and Ti atom can antiferromagnetically couple together, which enhances the interlayer coupling **[140]**. Such coupling is also found at $LaMnO_3/SrTiO_3$ interface **[141]**. For a single LSMO thin film, there is no interlayer coupling and generally the interface effect is thought to cause the dead layer. To further investigate how the LSMO/$SrTiO_3$ interface and LSMO/air interface affect the transport properties of LSMO thin film, we *in-situ* subsequently deposited 2 u.c. $SrTiO_3$ on LSMO right after the growth of LSMO to make the LSMO sandwiched between two $SrTiO_3$. The growth condition for $SrTiO_3$ was same with that for LSMO and a layer by layer growth was obtained too. With $SrTiO_3$/LSMO/$SrTiO_3$ sandwiched structure, the top LSMO surface is not exposed to air/vacuum now instead facing with $SrTiO_3$ thus creating two LSMO/$SrTiO_3$ interfaces, enabling us to amplify effect from LSMO/$SrTiO_3$ interface.

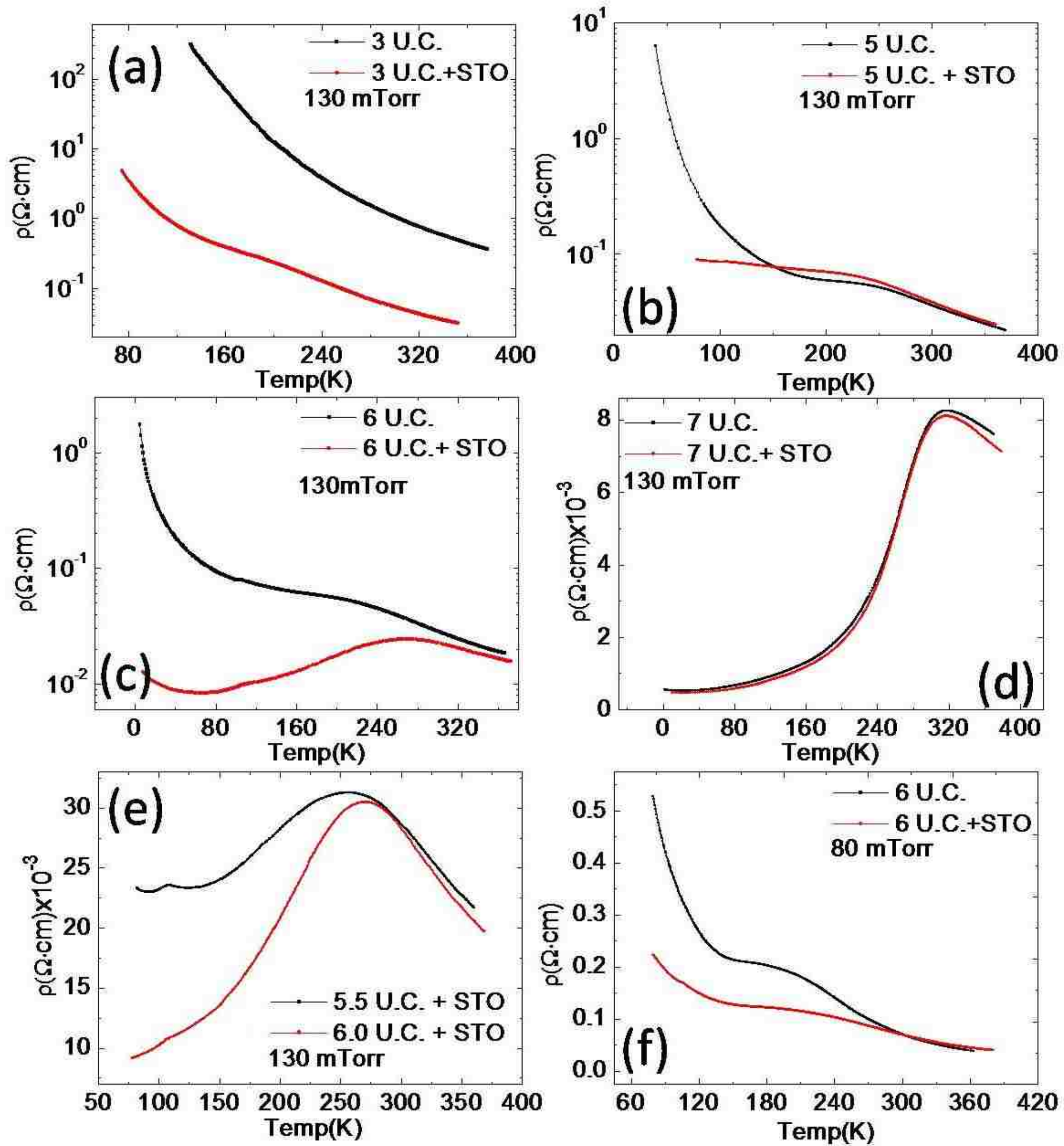

Figure 4-16: Effect of capping 2 u.c. $SrTiO_3$ on LSMO thin film. Temperature dependent resistivity for single LSMO thin film and LSMO capped with 2 u.c. STO (a) 3 u.c. LSMO; (b) 5 u.c. LSMO, (c) 6 u.c. LSMO; (d) 7 u.c. LSMO, (e) 5.5 and 6.0 u.c. LSMO capped with 2 u.c. STO. Growth pressure for (a-e) is 130 mTorr. (f) 6 u.c. LSMO grown at 80 mTorr.

The effect of capping 2 u.c. $SrTiO_3$ is summarized in **Figure 4-16**. It has a very strong effect on the insulating films that makes them less insulating, but weakly affect the metallic film (see **Figure 4-16(a-d)**). Such effect can also be found in 6 u.c. LSMO grown at 80 mTorr. This result contradicts to some previous reports which claimed that the capping of STO has no effect **[129,142]**. Surprisingly, an insulating 6 u.c. LSMO becomes metallic after capping

2 u.c. STO. Actually, a 5.5 u.c. LSMO film can also be converted into metallic phase after capping. Although the 6 u.c. is the critical thickness for 80 mTorr growth pressure as well, but capping 2 u.c. STO cannot switch it into metallic state as shown in **Figure 4-16f**. This fact suggests that the sample grown at 80 mTorr still has certain amount of oxygen vacancies which interferes with the capping effect.

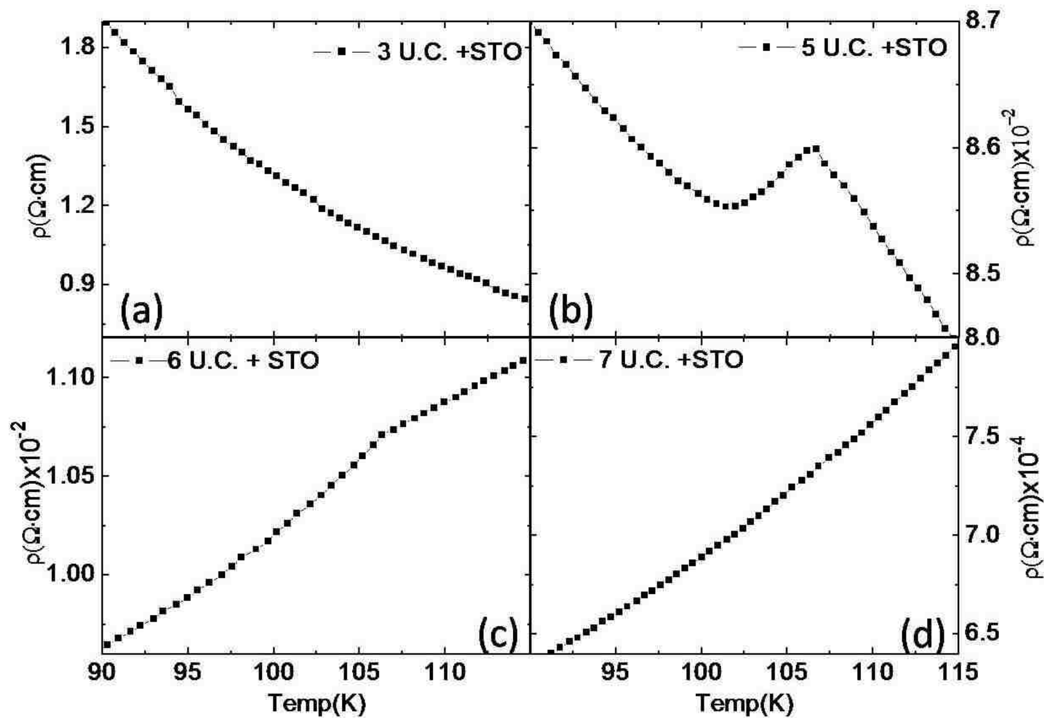

Figure 4-17: Temperature dependent resistivity for LSMO films capped with 2 u.c. STO at region around 105 K.

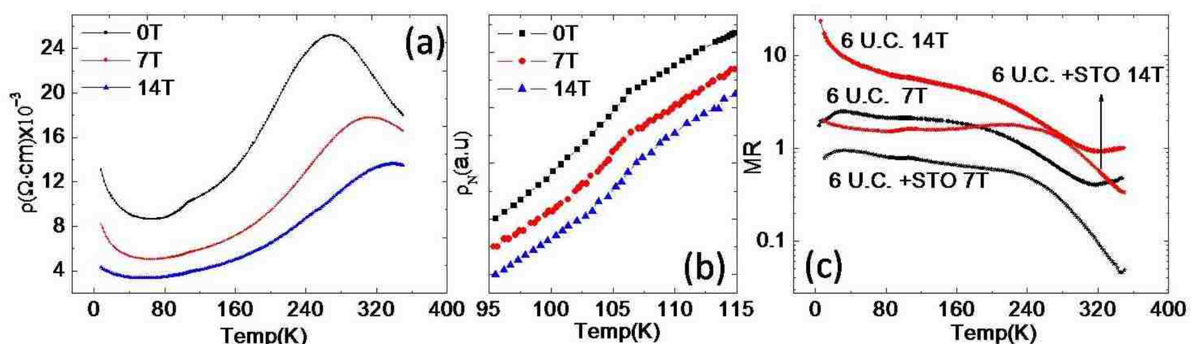

Figure 4-18: (a) Temperature dependent resistivity under various magnetic fields for 6 u.c. LSMO capped with 2 u.c. STO grown at 130 mTorr. (b) Zoom-in of 105 K region. The resistivity is normalized for convenient comparison. (c) MR ratio for 6 u.c LSMO thin film with and without capping STO. All the films were grown at 130 mTorr.

The capping also affects the kink at 105 K. **Figure 4-17** shows that capping STO makes the kink appear in 5 u.c. thin film. The kink at 6 u.c. LSMO capped by STO can still be observed, but suppressed. As mentioned above, the 6 u.c. LSMO capped with STO is metallic, so the kink is not strongly correlated to insulating state. The 7 u.c. capped with STO doesn't have evident kink.

Effect of capping STO on MR effect is displayed in **Figure. 4-18a**. Colossal negative MR effect can be still observed in 6 u.c. LSMO capped with 2 u.c. STO. The kink in $SrTiO_3$ capped LSMO thin film is robust against the magnetic field too (see **Figure 4-18b**). After capping $SrTiO_3$, the MR decreases as comparing with the film without capping $SrTiO_3$. Such reduced MR effect in STO capped LSMO may have some relation to the suppressed kink in STO capped LSMO.

4.6 Surface Stoichiometry and Structure

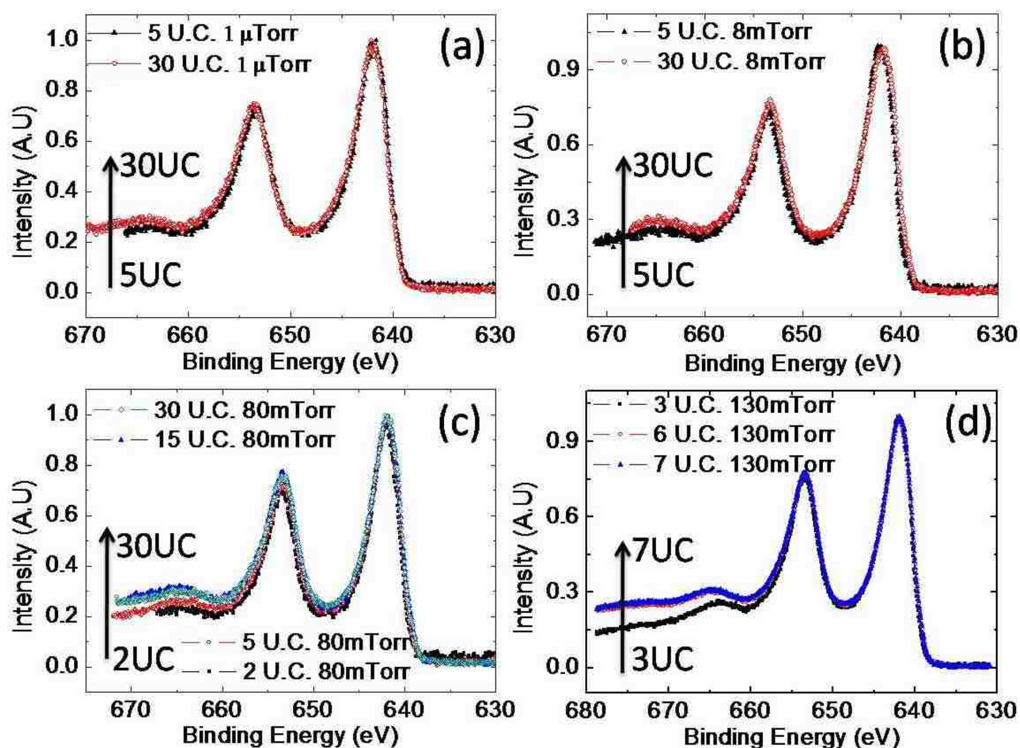

Figure 4-19: XPS of Mn2p core levels for LSMO thin films with different thicknesses grown at same pressure.

There are several possible reasons which can change the properties of LSMO thin films. They are oxygen deficiency, strain, interface effect and Sr segregation. The intrinsic dead layer on (001) $SrTiO_3$ should solely be caused the strain, interface coupling, and dimensionality. The Sr segregation and oxygen deficiency which vary the stoichiometry should be considered as extrinsic effect and should be eliminated.

By choosing more reactive Ozone gas of high enough pressure as growth atmosphere, the oxygen deficiency was minimized to a level that it didn't affect the intrinsic thickness of dead layer. The chemical stoichiometry was first characterized by XPS. **Figure 4-19** displays the XPS data for LSMO thin films grown at different pressure. To avoid the charging, conductive Nb-doped STO substrates were used. For the LSMO thin films grown at same pressure, the shape and the peak position of Mn2p core level do not show evident difference, but the satellite peak in thicker films moves upward and saturates at certain thickness. Take the films grown at 80 mTorr for example, the main peaks of 2 u.c., 5 u.c., 15 u.c. and 30 u.c. thin films locate at the same position, but the satellite peak of thicker film moves to higher intensity. It saturates at the 15 u.c. and 30 u.c. thin films. This can also be found in 130 mTorr grown LSMO thin films. It is very clear that the 6 u.c. and 7 u.c. have exactly same shape of Mn2p peak. Their satellite peaks are above that of 3 u.c. film. The upturn of the satellite peak in thicker film possibly arises from its more metallic behavior. The metallicity will enhance the secondary electron scattering, so the background at high binding energy part will increase, resulting an upturn. However, this mechanism may not fully be accounted for the upturn, since the satellite peak position in thicker film shifts a little bit to higher energy. Other unknown effect may have an impact on the satellite peak. Regardless of the satellite peak, the

overlap of the main peak suggests that the thickness doesn't affect the stoichiometry within the probe precision of XPS. The XPS of same thickness but different growth pressure is shown in **Figure 4-20**. The Mn2p core levels of films with same thickness do not show difference. The films grown at different Ozone pressure show distinct properties, so the certain variation of stoichiometry should exist. The XPS results then indicates that the variation of the stoichiometry is too small to be detected by XPS within its resolution.

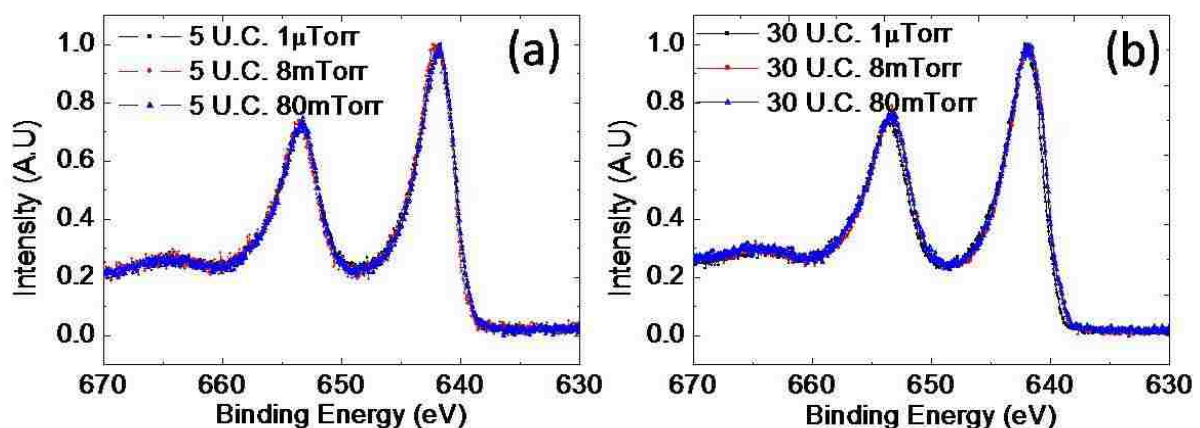

Figure 4-20: XPS of Mn2p core levels for LSMO thin films of the same thickness grown at different Ozone pressures.

LEED appears to be a more powerful tool to detect such tiny difference. The LEED images of LSMO grown at different pressure are shown in **Figure 4-21**. The surface structure changes with different growth pressure. If the growth pressure is very low, for example, 10^{-6} Torr, our results show that the surface of LSMO film has some incommensurate diffraction spots besides the integral spots. The intensity of the incommensurate spot is comparable with the integral spot. Such un-identified surface reconstruction is tentatively called α-structure for convenient description. With increasing Ozone growth pressure, the α-structure is suppressed and the surface is driven into 1x1 with certain amount of the $\sqrt{2}\times\sqrt{2}$ domain. The surface LEED images taken at 70 eV of 6 u.c. and 7 u.c. LSMO grown at 130 mTorr display a more

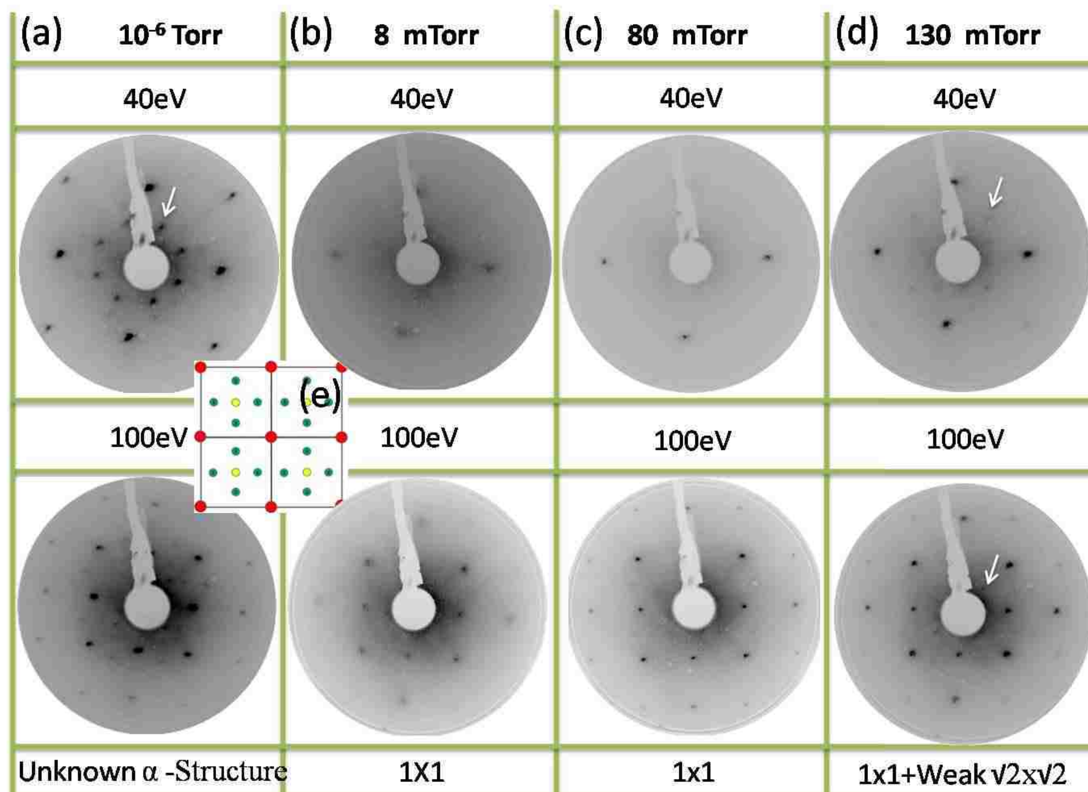

Figure 4-21: (a-d) Surface LEED images of the LSMO films grown at different pressures. The white arrows in (a) and (d) indicates the incommensurate spot and (1/2,1/2), respectively. A surface reconstruction pattern based on the LEED pattern in (a) is schematically shown in (e). The un-identified diffraction spots are labeled with green spots. The red spots are the 1x1 spots. Such surface is tentatively called α-structure.

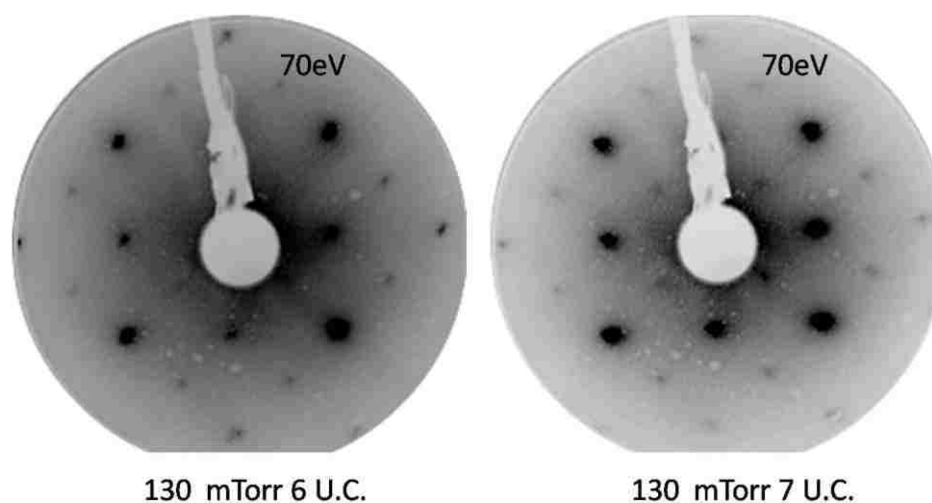

Figure 4-22: Surface LEED pattern of 6 u.c. and 7 u.c. LSMO films grown at 130 mTorr.

clear √2×√2 reconstruction (**see Figure 4-22**). We also tested the sample of post-annealing at high Ozone pressure and found that the high Ozone pressure annealing can make the fraction spot of √2×√2 brighter and annealing in UHV can reduce the intensity of the fractional spot.

As a result, the √2×√2 should be oxygen abundant surface. Although we could not obtain exact same intensity of the fractional spot in √2×√2 surface LEED image of different batch of samples grown at same condition, but we didn't observe evident change of the transport properties. Since the post-annealing in Ozone will enhance the fractional spot of √2×√2 surface and it is hard to maintain exactly the same growth condition such as same post treatment process, the change the domain area of the √2×√2 of films of different batches then can be due to a little vary of growth condition including post-treatment. The appearance of oxygen abundant surface suggests that our as-grown LSMO at above 130 mTorr is much more oxygen stoichiometric.

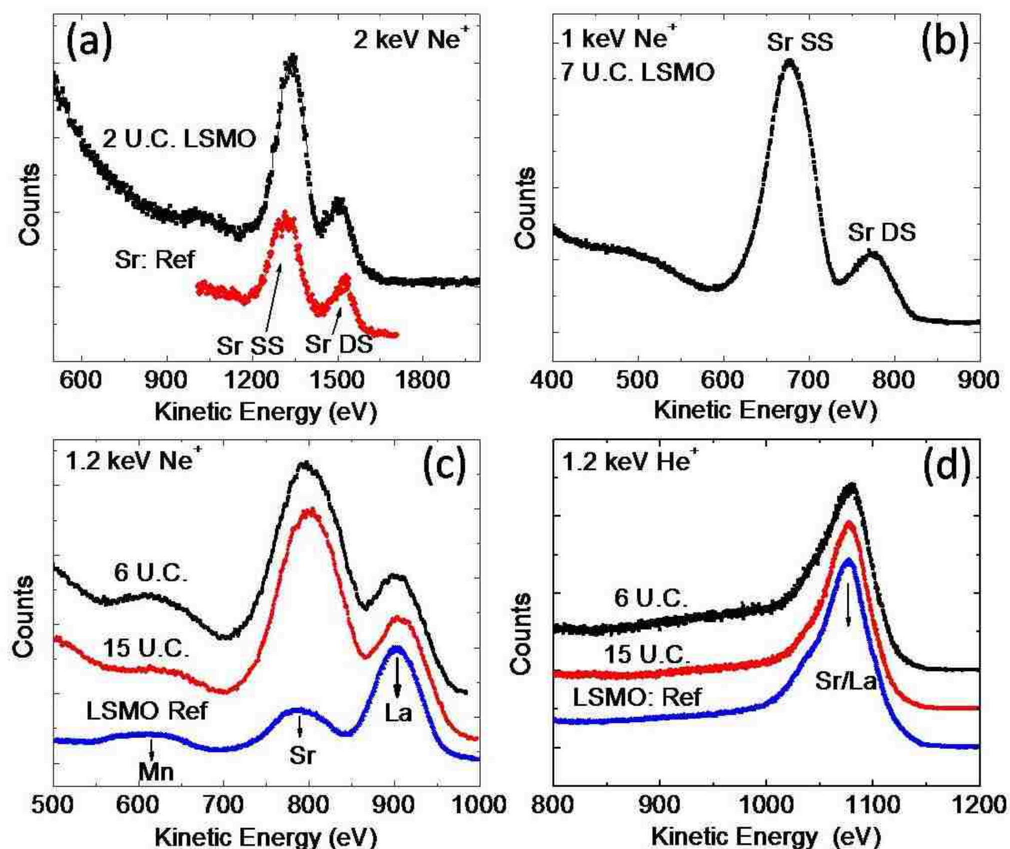

Figure 4-23: (a) Ion scattering spectrum (ISS) of 2 u.c. LSMO sample grown at 80 mTorr. The red line is the ISS of Sr element. The incident ion beam is 2 keV Ne^+. (b) ISS of 7 u.c. LSMO grown at 130 mTorr with using 1 keV Ne^+. The Sr has a double scattering (DS) peak right at the single scattering (SS) peak. The ISS of 6 u.c., 15 u.c. sample and $La_{2/3}Sr_{1/3}$ (From (110) LSMO surface) reference spectrum with using (c) 1.2 keV Ne^+ and (d) 1.2 keV He^+.

The surface Sr segregation is reported to be the another possible reason causing the dead layer **[132]**. To determine surface chemical composition of our LSMO thin film, low energy ion-scattering spectra (LE-ISS) of LSMO thin films was measured. The ISS only probes the chemical composition of topmost atomic layer. The ISS of 2 u.c. LSMO sample grown at 80 mTorr is shown in **Figure 4-23a**. Comparing the spectrum with the Sr reference spectrum, it could be concluded that the topmost layer of 2 u.c. LSMO film is dominated by Sr without La or just with very few La, so do the 6 u.c., 7 u.c. and 15 u.c. LSMO samples as illustrated in **Figure 4-23(b-c)**. The ISS with using He^+ ion beam has also been checked. However, the peak of the La and Sr with using He^+ is much closer than that with using Ne^+ , so He^+ ISS cannot distinguish the La and Sr very clearly as shown in **Figure 4-23d**. This is due to the light mass of He^+ which has a relative low mass resolution. It is generally expected that the LSMO terminates with MnO_2 at layer by layer grown mode with using TiO_2 termination $SrTiO_3$ (001) substrate. The appearance of the topmost SrO layer on MnO_2 should result from the Sr segregation as reported by Herger *et al.* **[132]**. According to **Ref. 132**, the Sr segregation will occur for all kinds of thickness. Our ISS results show a same tendency for the Sr segregation behavior. Since the x=1/3 is the optimal doping level for $La_{1-x}Sr_xMnO_3$ and both the $SrMnO_3$ and $LaMnO_3$ are insulator, deviation of 1/3 doping level will weaken its metallicity at least at the surface. It then could be expected that the Sr segregation will suppress metallicity in the LSMO ultrathin film.

To understand the origin of the dead layer, we further used LEED-IV refinement to determine the surface structure and chemical composition. Conductive Nb-STO substrates were used for LEED experiment. After the growth of LSMO at optimized Ozone pressure

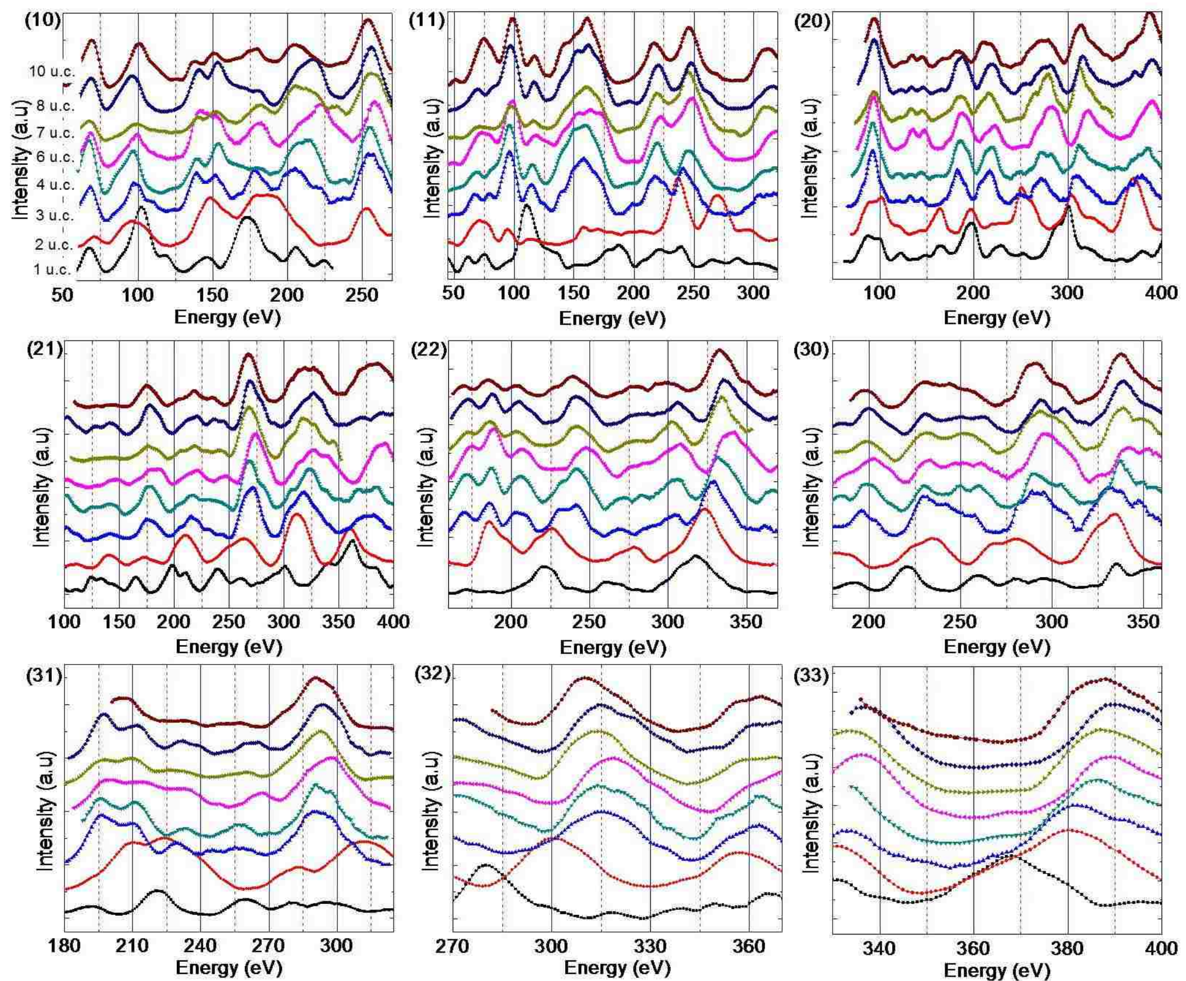

Figure 4-24: Evolution of the LEED-IV curves of LSMO films with 7 different thicknesses. The left top corner shows the diffraction beam. The corresponding thickness of the IV curves increases from bottom to the top for all panels.

($\geq$ 80 mTorr), the film was *in-situ* transferred into LEED chamber and a LEED-IV was taken at room temperature at ultra high vacuum of pressure of ~ 4×10^{-10} Torr. The surface structure is p(1x1) as the LEED pattern illustrated. An evolution of the LEED-IV curves of different thickness will help us roughly know how the structure changes with thickness. The LEED-IV curves of 7 different thickness is shown in **Figure 4-24**. For the 1 u.c. LSMO ultrathin film, the substrate will contribute certain LEED intensity, so it is expected to have quite different LEED-IV curves from other thicker films. As a result, the LEED-IV curves of 1 u.c. LSMO film cannot be directly used to compare with other thicker films. In contrast to the 1 u.c.

sample, the 2 u.c. film with 4 monolayer of atoms is thick enough to completely dominate the LEED intensity. The LSMO films with thickness of bigger than 2 u.c. can be directly used for comparing structure and performing LEED-IV refinement. The LSMO films with thickness ≥ 3 u.c. looks similar that they have same peak features but a little shift of the peak position. In contrast to the a dimensionality driven metal-to-insulator transition across 6 u.c. there is no strong surface structure change across the critical thickness of 6 u.c..

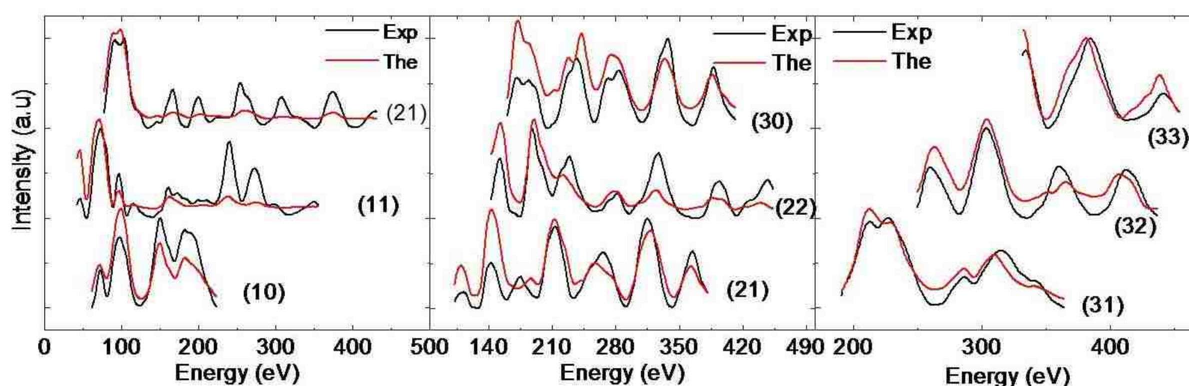

Figure 4-25: The comparison between experimental LEED-IV curves and theoretical curves for 2 u.c. LSMO.

To know details of the structures and their evolutions with thickness, the LEED-IV structure refinements were performed. Results of structure refinement of 2 u.c. LSMO sample are shown in **Figure 4-25**. An outstanding R_p factor of 0.16 is obtained, indicating that the surface structure refinement is very reliable. Relative atomic positions of the refined surface structure is shown in **Table 4-2** and structure model is shown in **Figure 4-26**. The LEED-IV refinement shows that the topmost atomic layer is SrO, which is consistent with the ISS result. Since LEED is not sensitive to the level of the underneath second (La, Sr)O layer, the exact La to Sr ratio at inner layer is unknown. All the atoms at top most layer move down especially the Sr which moves down by 0.2952 Å. The Mn in the topmost layer is not at the center of the unit cell, instead, it moves toward the surface. The out of plane lattice constant

(c) of topmost unit cell is compressed by 0.27 Å and the bottom unit cell is compressed by 0.09 Å. The averaged lattice constant for 2 u.c. LSMO sample is ~ 3.7 Å. The LEED-IV refinement also indicates that there is no oxygen deficiency.

Table 4-2: Relative atomic positions of the refined surface structure of 2 u.c. LSMO film on (001) $SrTiO_3$.

Layer	Atom	Bulk Position (Å)	Surface Position (Å)	ΔZ (Å)	Error (Å)
1	Sr	0.0000	0.2952	+0.2952	±0.03
1	O	0.0000	0.0685	+0.0685	±0.03
2	O	1.9467	2.0289	+0.0822	±0.04
2	O	1.9467	2.0289	+0.0822	±0.04
2	Mn	1.9467	1.9579	+0.0112	±0.01
3	La /Sr	3.8933	3.9232	+0.0299	±0.04
3	O	3.8933	3.9348	+0.0415	±0.05
4	O	5.8400	5.9313	+0.0913	±0.12
4	O	5.8400	5.9313	+0.0913	±0.12
4	Mn	5.8400	5.8269	-0.0131	±0.01
5	La / Sr	7.7867	7.7279	-0.0588	±0.07
5	O	7.7867	7.7336	-0.0531	±0.27

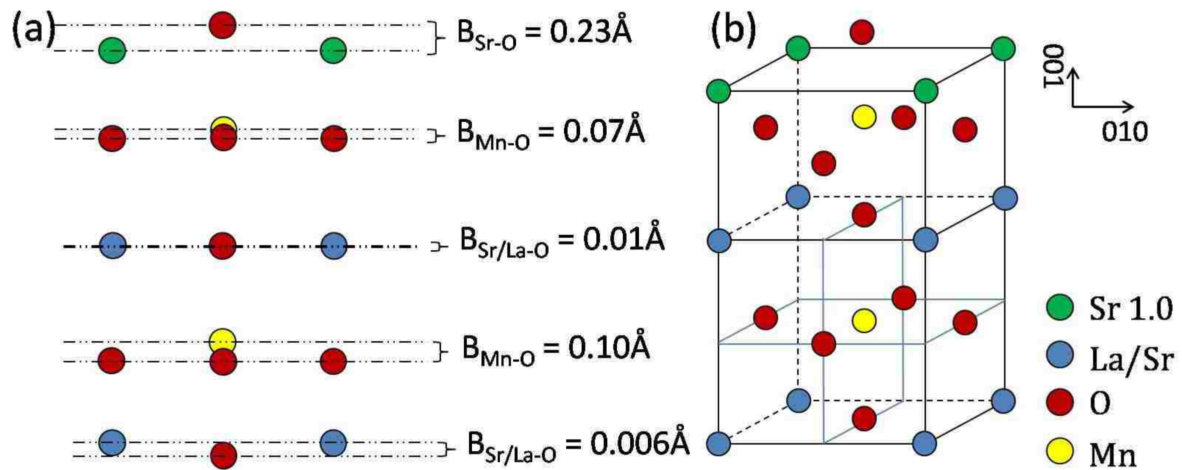

Figure 4-26: (a) Structure of 2 u.c. LSMO. (b) 3D structure model.

Table 4-3: Relative atomic positions of the refined surface structure of 6 u.c. and 10 u.c. LSMO film on (001) $SrTiO_3$.

Layer	Atom	Position (Bulk) (Å)	Positions (6 u.c.) (Å)	Positions (10 u.c.) (Å)
1	La / Sr	0.0000	0.5836	0.4041
1	O	0.0000	0.1149	0.0955
2	O	1.9467	2.2120	2.2415
2	O	1.9467	2.2120	2.2415
2	Mn	1.9467	2.0472	2.0067
3	La /Sr	3.8933	3.7456	3.8835
3	O	3.8933	3.9050	3.9593
4	O	5.8400	5.8909	5.6348
4	O	5.8400	5.8909	5.6348
4	Mn	5.8400	5.7781	5.7984
5	La / Sr	7.7867	7.5902	7.6912
5	O	7.7867	7.7637	7.8046

The preliminary results of LEED-IV structure refinements of 6 u.c. and 10 u.c. thin films are shown in **Table 4-3**. The R_p for 6 u.c. and 10 u.c. are 0.3125 and 0.3155 respectively. According to the current results, both the surfaces of the 6 u.c. and 10 u.c. films terminate with SrO. For the 6 u.c. LSMO, the topmost surface unit cell is compressed by 0.73 Å which is much bigger than that (0.27 Å) of 2 u.c. film. The second unit cell is compressed by 0.05 Å, which is a little smaller than that (0.09 Å) in 2 u.c. For the 10 u.c. LSMO which has properties very close to the bulk, LEED-IV refinement shows that the topmost layer is compressed by 0.41 Å and the underneath second layer is compressed by 0.08 Å. From 2 u.c. to 10 u.c., both the top two layers are compressed. The fact that the top one is compressed a lot than the underneath second one could be due to the Sr segregation at the topmost surface and broken symmetry. The inner LSMO can have correct stoichiometry **[132]**. For such

ultrathin film, the inner LSMO part should be fully strained. As a result, the underneath vertically compressed layer is caused by the in-plane tensile strain. If keeping the volume of the strained LSMO film same with the bulk and the in-plane lattice constant same with the substrate, then the expected compressed value of c is 0.02 Å. Our LEED-IV refinement results show that the underneath layer is compressed in the same order of magnitude but a little bigger (for example, 0.05 Å for 6 u.c. LSMO) than the expected value.

LEED-IV evolution as shown in **Figure 4-24** and structure refinement of 2 u.c., 6 u.c. and 10 u.c. indicate that the LSMO thin films of different thicknesses have similar surface structure and chemical composition. Since the LSMO part underneath the second layer will gradually affect the structure of the second layer, so such common surface structure will reflect the similar structure of underneath inner LSMO.

4.7 Discussion

With these oxygen stoichiometric LSMO thin films, we can discuss the origin of the dead layer more clearly. First, let us take a look at the strain effect. The lattice mismatch between LSMO and STO is ~0.6% and it is tensile strain. The effect of the tensile strain can be reflected by the kink at 105 K. As shown in **Figure 4-27**, the structure of STO substrate at 105 K during cooling reduces the resistivity no matter whether the film is metallic or insulating. The lattice mismatch below 105 K is ~0.35% which is ~50% smaller that above 105 K, hence it is concluded that the tensile strain suppresses the conductivity. This could be the most reliable conclusion about strain effect so far since nothing else changes. The strain effect is generally extrapolated by comparing properties of LSMO films on different substrates with different lattice mismatch. However, the growth of LSMO itself on different

substrates will introduce some extrinsic effects. As a result some other extrinsic effects will change the properties of LSMO besides the strain, thus pure strain effect cannot be obtained. We really don't know how the properties of a stoichiometric film changes if the strain goes to zero. According to **Table 4-1** and **Figure 4-2**, it seems like that the ±0.6% strain effect no matter tensile or compressed doesn't affect the thickness of dead layer beyond 1 u.c. The substrate structure transition can induce a insulator to metal transition upon cooling as shown in **Figure 4-16e** and **Figure 4-17b**, but later it reenters insulating phase again. The insulating ground state is robust in 6 u.c. stoichiometric LSMO thin film. Based on these discussions, the dead layer for a film without any strain is expected be ≥5 u.c and is quite possibly equal to 6 u.c..

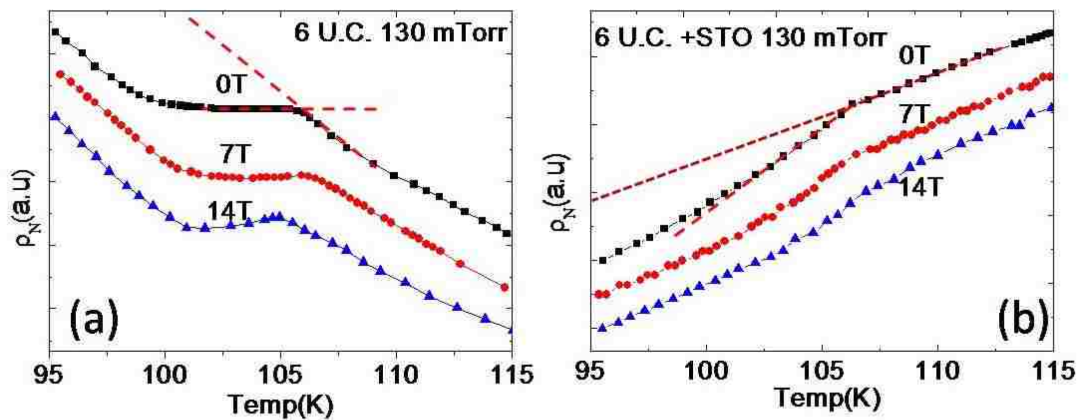

Figure 4-27: Effect of substrate transition on the transport properties. Temperature dependent resistivity under various magnetic field for (a) 6 u.c. LSMO (b) 6 u.c. LSMO capped with 2 u.c. STO. The films were grown at 130 mTorr. The red dash lines are tangent lines at the kink from left and from right. The resistivity is normalized for comparison.

The LSMO/STO interface affects the LSMO film properties by reducing the thickness of the dead layer. The STO/LSMO/STO has a dead layer of 5 u.c.. The STO/LSMO/STO with LSMO of 7 u.c. thick shows very small difference from 7 u.c. LSMO on STO. Due to the fact that the 10 u.c. LSMO also has small difference from 7 u.c. LSMO (see **Figure 4-6**), therefore, it can be expected that the capping of 2 u.c. STO on 7 u.c. LSMO should not give

rise to big change. The capping effect on 7 u.c. LSMO also indicates that the metallicity of the 7 u.c. LSMO is intrinsic rather than caused by interface coupling at that occurs in STO capped 6 u.c. LSMO.

Orbital reconstruction is another possible reason. It was proposed by Tebano *et al.* **[129]** that the broken symmetry at the interface which results in a preferential occupation of $3z^2$-r^2 orbital against the in-plane x^2-y^2 orbital causes the dead layer. The absence of x^2-y^2 orbital suppresses the double exchange and occupation of $3z^2$-r^2 orbital leads to C-type antiferromagnetic insulator. This scenario of orbital reconstruction near the interface is supported by linear dichroism in X-ray absorption spectrum (LD-XAS). Similar conclusion is made by Lepetit *et al.* **[130]** but the explanation is different. Lepetit *et al.* measured the lattice constant of <c> of films of different thickness and found that the <c> monotonically increases with decreasing thickness. Down to 3 u.c., the c/a is bigger than 1 and then the occupation of $3z^2$-r^2 orbital dominates. Thicker than 3 u.c., the film gradually relaxes. The evolution of the c parameter is thought to arise from interface through-bridge delocalization mechanism **[130]** that $3z^2$-r^2 orbital orientation in Mn at interface will lead to larger transfer integral between Mn and Ti atoms. However, this model contradicts to the argument in **Ref. [129]** where they found that the interface doesn't affect the properties. Our result also strongly suggests that the interface plays minus role in adding the dead layer, instead, the interface tries to reduce the thickness of the dead layer. Even the model of orbital reconstruction driven by broken symmetry could be denounced. Some contradicted experimental discoveries of the orbital reconstruction are reported by Huijben *et al.***[125]**. They also used LD-XAS measurement like what Tebano *et al.* did to detect the $3z^2$-r^2 and x^2-y^2 orbital, but they found

that the x^2-y^2 orbital is preferred in all layer thickness and no orbital reconstruction happens at interface. In the case of our 2 u.c. thin film, the average <c> is about ~3.7 Å, so the c/a = 0.94, as a result, the e_g electron will prefer x^2-y^2 orbital rather than $3z^2$-r^2 orbital which is consistent with the observation reported by Huijben *et al.* **[125]** as mentioned above. Our LEED-IV refinements also show that the thick films (6 u.c. and 10 u.c.) are compressed too and so c/a is smaller than 1, as a result the $3z^2$-r^2 orbital ordering won't occur. It is then concluded that the $3z^2$-r^2 orbital ordering is not the reason that causes dead layer in our LSMO thin films.

The origin of the dead layer then puzzles us more due to these contradicted experimental results. The contradiction may arise from the existence of extrinsic effects, for example, the non-stoichiometry. The films which Tebano *et al.***[129]** and Lepetit *et al.* **[130]** used to illustrate the origin of dead layer were grown at ~1 mTorr Ozone and ~0.3 mTorr oxygen, respectively. A much higher pressure of 200 mTorr was used by Huijiben *et al.* **[125]**. All the films were expected to be stoichiometric, but the claim of correct stoichiometry should be much more careful according to our results. Very few oxygen deficiency can increase the thickness of the dead layer, so some extrinsic signal caused by oxygen deficiency, especially in the ultrathin film which is much more sensitive to oxygen deficiency than the bulk, is detected. Effect of a considerable oxygen vacancy concentration has be investigated before **[44, 45, 133]**. Oxygen vacancies will reduce the curie temperature and the conductivity. With reducing the amount of oxygen vacancies, the dead layer is reduced from 14 u.c. to 8 u.c. and finally to stop at 6 u.c. as demonstrated in our experiments. The reported dead layer (see **Table 4-1**) of thicker than 6 u.c. should still a relative considerable amount of oxygen vacancies. It is reported that the c value of LSMO thin film becomes bigger and bigger due to

the increasing oxygen vacancies no matter it is under tensile or compressive strain (see **Figure 4-28** from **Ref. [133]**). Since the in-plane a and b lattice constant will be locked to substrate in ultrathin film **[143]**, the elongation of the c due to oxygen deficiency then will lower down the energy level of $3z^2$-r^2 orbital and result in increased occupation of $3z^2$-r^2 orbital, thus an oxygen deficiency induced orbital reconstruction is probed. LSMO grown by Huijben *et al.* at 200 mTorr oxygen pressure should have less deficiency and so the $3z^2$-r^2 orbital reconstruction doesn't occur. Besides the effect on the structure, oxygen vacancies can directly affect the double exchange which need oxygen to bridge the Mn. As a result, oxygen vacancies induced insulating region may coexist with metallic region, creating a phase separation **[45]**. With oxygen vacancy concentration reduced to certain value, the stretch of the out of plane lattice constant can be eliminated, thus the orbital reconstruction disappears. However, the residual vacancies still have negative effect on LSMO's properties. It thus can be concluded that the some contradicted discoveries arise from oxygen vacancies.

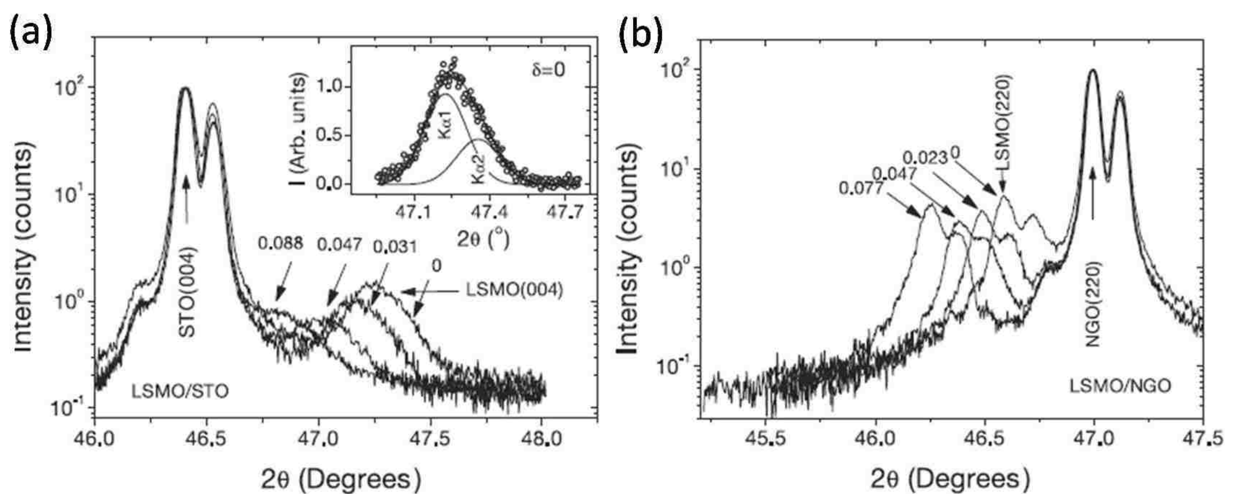

Figure 4-28: XRD patterns of $La_{0.67}Sr_{0.33}MnO_{3-\delta}$ on (a) (001) $SrTiO_3$ and (b) (110) NGO. The LSMO 004 (peak) which is the (220) peak when (110) NGO is used as substrate shifts to the left with increasing δ, so the c value becomes bigger with increasing oxygen deficiency. Figure adapted from **[133]**.

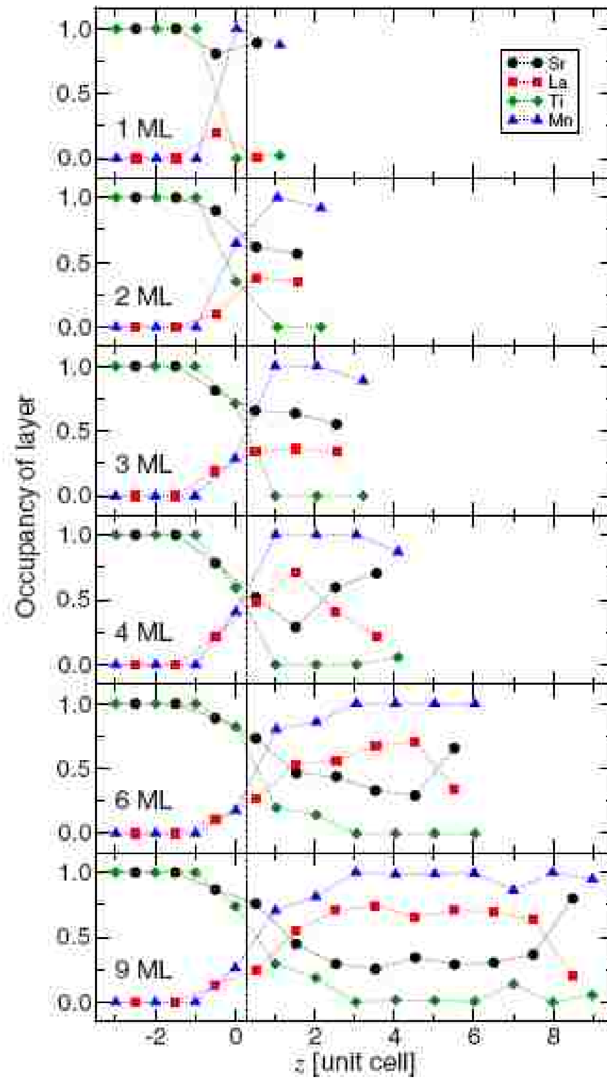

Figure 4-29: Chemical composition depth profile for different thickness of LSMO calculated by Herger *et al.*. Figure adapted from **[132]**.

Another non-stoichiometry effect of Sr segregation has to be considered. As our ISS spectrum and LEED-IV refinement indicating, all the films of different thicknesses have surface Sr segregation that the topmost layer is dominated by SrO. According to **Ref. 132**, the Sr will be rich in both the surface and LSMO/STO interface. Our LEED-IV refinement suggests that the topmost atomic layer of 2 u.c. LSMO is SrO. In this case, even the second (La, Sr)O is LaO without any Sr, it still cannot account for the mol ratio of La to Sr of 2:1 in LSMO. As a result, some La atoms should diffuse into STO part. The interface diffusion and surface segregation both cause the doping level to be changed. In this situation, only inner

part of the film can have correct doping level at a thick enough film as **Figure 4-29** showing **[132]**. According to **Figure 4-29**, their 6 u.c. film starts to have correct La and Sr stoichiometry in their ~ 3 u.c. thick inner part. However, the dead layer of the LSMO films at their growth condition is at least 9 u.c. **[132]**. It should be noticed that the oxygen growth partial pressure which they used was 10^{-4} Torr. We also expects to have a electric dead layer of ~ 9 u.c. at that growth pressure according to our phase diagram as shown **Figure 4-8**. The dead layer with thickness bigger than 6 u.c. should be caused by the oxygen deficiency. The elongation of the out of plane lattice constant of their films then may be due to the oxygen deficiency as discussed above. Since the inner past has a correct stoichiometry, the Sr segregation cannot fully account for the dead layer.

Back to our films, we also have surface Sr segregation but at the same time a much correct oxygen stoichiometry. Removing the layers which are rich of Sr due to Sr segregation, considering all the effects from substrate and according to the previous reports, the residual dead layer without oxygen vacancies, strain and interface coupling, is estimated to be ~3 u.c., which then will be assigned to dimensionality effect as that occurring in $SrVO_3$ and $LaNiO_3$ thin films which are discussed in **Chapter 1**. The $(La, Sr)_{n+1}Mn_nO_{3n+1}$ could be a referred system to illustrate the dimensionality effect. The fact that double layer $La_{1.2}Sr_{1.8}Mn_2O_7$ has a curie temperature of ~100 K much lower than that of the 3D $La_{0.6}Sr_{0.4}MnO_3$ of ~ 350 K implies that reduced dimensionality drives the film to be more insulating and non-magnetic. The LSMO thin film could be a similar case with the multilayer $(La, Sr)_{n+1}Mn_nO_{3n+1}$ that it has a inner part with a correct stoichiometry sandwiched between two insulator layers (Top most layer and interface). The inner part can be driven into insulating phase due to reduced

dimensionality. Different from $(La, Sr)_{n+1}Mn_nO_{3n+1}$ where small interlayer coupling still exist, the spatial confinement LSMO ultrathin film doesn't have interlayer coupling, so the n layer LSMO ultrathin film could be more insulating than n layer LSMO in $(La, Sr)_{n+1}Mn_nO_{3n+1}$.

The reduced dimensionality effect and the intrinsic double exchange coupling between neighbor Mn will compete. As discussed in **4.3**, the dimensionality driven metal-to-insulator transition seems much like a cross-over transition with 6 u.c. as its critical thickness. With decreasing the thickness, the strength of coupling responsible for the dead layer becomes stronger and exceeds the double exchange coupling below certain thickness, resulting in the a dimensionality metal-to-insulator transition. Such scenario is further supported by the fact that the thermal activation energy increases with decreasing thickness. The competing effect could be found in **Figure 4-30**. The 6 u.c. LSMO film grown at 180 mTorr has two transitions besides the kink at 105 K. It is insulating above T_{C2}. The film becomes metallic below T_{C2}, but reenters insulating ground state at T_{C1}. T_{C2} increases with magnetic field while the T_{C1} does a reverse way. The 6 u.c. LSMO grown at 130 mTorr doesn't exhibit an evident metal-to-insulator transition at T_{C2} at zero field, but it emerges again with applying magnetic field. The presence of oxygen vacancies smears the metal-to-insulator transition. For the metallic ground state, a small upturn of the resistivity at low temperature still can be observed as shown in **Figure 4-30(c-d)**. The T_{C2} as a signature of inherent properties of LSMO as mentioned before is related to paramagnetic poor metal/insulator to ferromagnetic metal transition. It goes higher under magnetic field due to the coupling between metallicity and ferromagnetism. The T_{C1}, signature of emergent dimensionality effect, is reduced by magnetic field due to the enhanced magnetism under magnetic field.

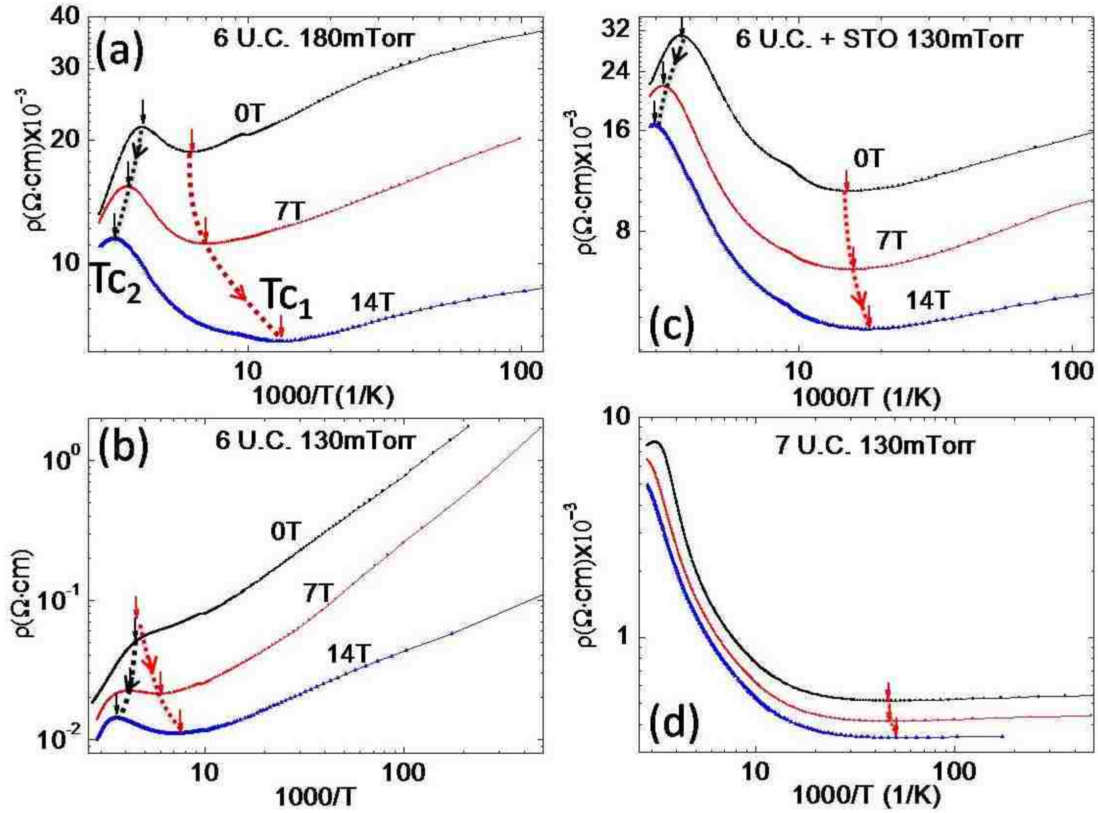

Figure 4-30: Two transitions in LSMO films with and without capping 2 u.c. STO and change of their T_c under field.

The singularity in 6 u.c. thin film could be explained by the two competing coupling as mentioned above. The thermal activation energy at 6 u.c. thin film is very close to zero. As a result, 6 u.c. is the critical thickness that the dimensionality effect completes with double exchange coupling at a nearly balanced point. The 1/T resistivity behavior results from this balance. A little change of the thickness breaks the balance, thus switches the film to metallic (thicker film) / insulating (thinner film) phase. The film at such critical status is very sensitive to external stimulus. Although the lattice constant of STO substrate is changes only by 0.2% during the structure transition at 105 K, but its effect can emerge in LSMO of this critical thickness. The missing of signal of substrate transition in other thicknesses could be due to the their bluntness to external stimulus. For example, the MR at 6 u.c. critical thickness is 10 times bigger than other thickness of films.

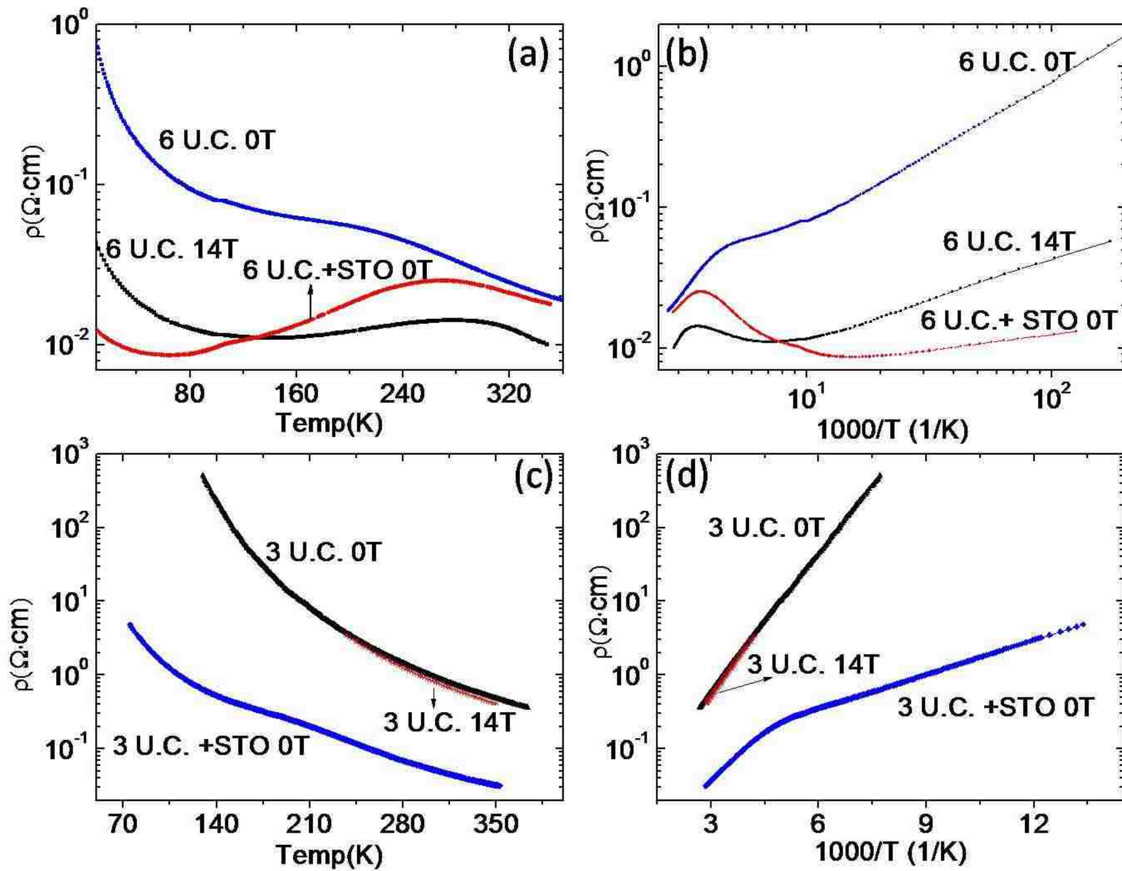

Figure 4-31: A comparison between the effect of capping 2 u.c. STO and magnetic field. Temperature dependent resistivity curves for single LSMO film, LSMO capped by 2 u.c. STO film, and single LSMO film under 14 T magnetic field are shown in blue line, red line and black line, respectively.

As we know, the magnetic dead layer is thinner than electronic dead layer **[125]**, that is, the ferromagnetic state exists in insulating film of LSMO. However, the ferromagnetism in electronics dead layer is much weaker than the bulk according to all the reports by different groups on LSMO ultrathin films **[125, 127, 128].** A phase separation with ferromagnetic domain coexisting with non-magnetic domain is proposed to explain this phenomenon **[125]**. Spontaneous electronic phase separation is thought to arise from coexisting competing coupling. In complex metal oxides of bulk form, simultaneously active but close strength of couplings among spin, lattice, charge and orbital are thought to be the main reason causing the phase separation. When the complex metal oxide becomes smaller, the dimensionality,

another degree of freedom, then participates in these couplings, thus driving the ultrathin film to reenter a phase separation scenario. The thickness dependent MR effect as discussed in section **4.4** further supports the phase separation scenario.

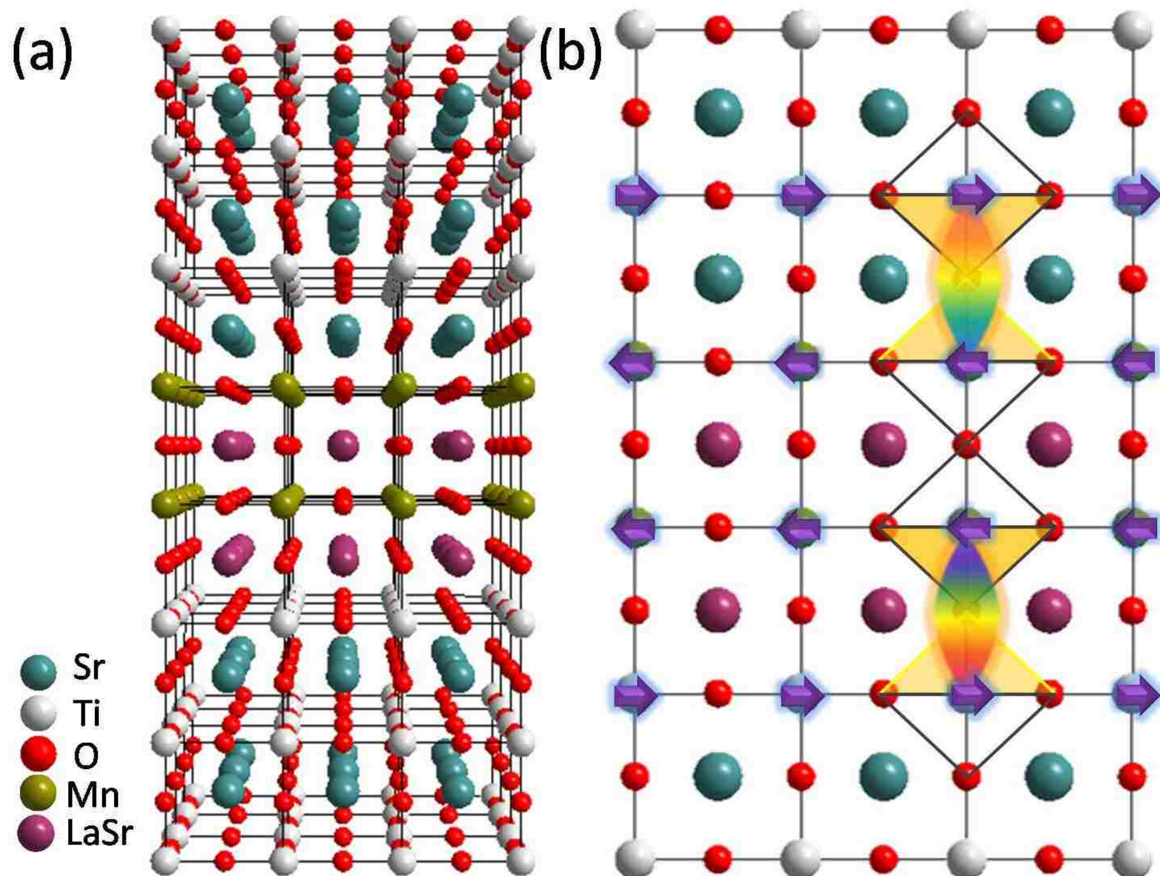

Figure 4-32: (a) Structure model of STO/LSMO/STO; (b) Schematic diagram of interface coupling and spin configuration [140].

A comparison between magnetic field effect and capping STO effect may help us understand the role of STO/LSMO interface. The capping effect has a very similar effect to applying magnetic field like 14 T strong magnetic field (see **Figure 4-31**). It could be extrapolated that the STO tries to align the spin of LSMO. In 2011, Bruno *et al.* discovered the interface antiferromagnetic coupling between interfacial Mn and Ti atoms in ($LSMO_M/STO_2$) superlattice **[140]**. The interface coupling can also be found when STO is thicker than 2 u.c.. A superlattice structure is not essential for occurrence of interface

coupling **[140]**. The enhanced conductivity in our STO/LSMO/STO further supports this issue. **Figure 4-32a** shows the 3D structure model of STO/LSMO/STO and the interface spin alignment is shown in **Figure 4-32b**. The interface antiferromagnetic coupling between Mn and Ti through the shared oxygen between makes the spin of Mn in LSMO layer parallel to each other, similar to strong magnetic field, drives the LSMO to be more metallic. According to the fact that capping STO has stronger effect on LSMO than applying 14 T magnetic field in the 3 u.c. LSMO, the interface coupling should be very strong.

Chapter 5 Controllable Properties in Artificial Columnar Nanocomposite

5.1 Introduction and Motivation

Epitaxial thin films on a substrate generally can be categorized into horizontal structure (e.g., multilayer) and vertical nanocomposite as shown in **Figure 5-1**. The horizontal structure such as layer by layer epitaxial films and heterostructure has been highly focused on in past decades due to their novel properties especially the unexpected interface properties **[24]**. However, the nanocomposite **[144]**, by assembling different nanostructures to composite form and providing a new avenue to develop new controllable functionality, has drawn a lot of interest recently. It is found that not only the multifunctionality can be realized but also the enhancement of single functionality can be obtained in a nanocomposite **[145-149]**. For example, multiferroic functionality can be created by embedding $CoFe_2O_4$ nanopillars into $BaTiO_3$ matrix **[146]**. The First vertical nanocomposite was realized in $La_{0.67}Ca_{0.33}MnO_3$-MgO **[150]** where properties of $La_{0.67}Ca_{0.33}MnO_3$ can be controlled by tensile strain induced by MgO.

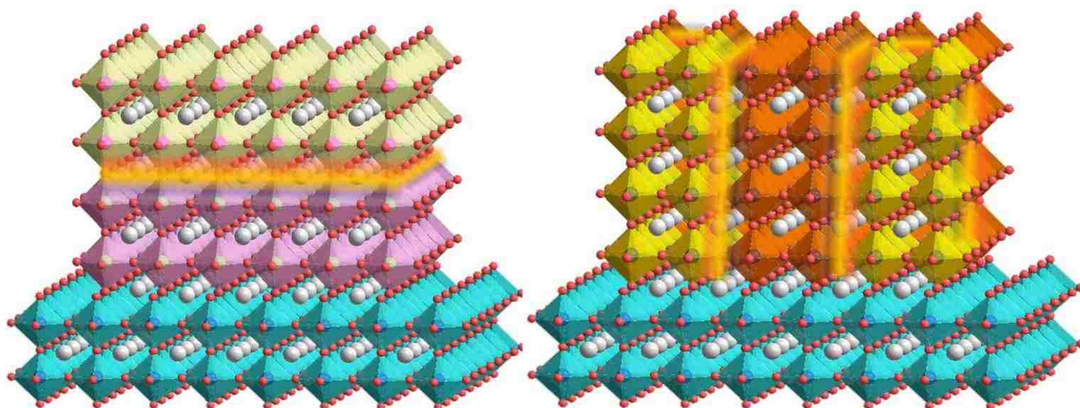

Figure 5-1: Schematic model of horizontal structure (left) and vertical structure (right)

The nanoscale inhomogeneity ranging from chemical disorder to spontaneous electronic phase separation has been proved to have strong effect on physics properties **[151, 152]**. **Figure 5-2a** displays an electronic phase separation with co-existence of ferromagnetic and

anti-ferromagnetic phase in a correlated material. The chemical phase nanoscale inhomogeneity is also great signature of nanocomposite as the **Figure 5-2b** showing, so we would expect some emergent properties in a nanocomposite. With respect to transport property in an inhomogeneous system, the percolation as that discussed in many correlated electron materials **[151, 152]** could be one of the central characteristics of a nanocomposite. The relative ratio between different phase determines the specific percolation situation and then affects overall transport property. The nanocomposite enables us to tune the percolation network in another way. Since phase ratio can be artificially controlled by tuning growth parameter and condition, we could expect a controllable transport property. Furthermore, the out-of-plane strain and interface induced novel properties will have unexpected effect on in-plane transport properties which will be quite different from the in-plane strain and interface effect as discussed in **Ref. 144**.

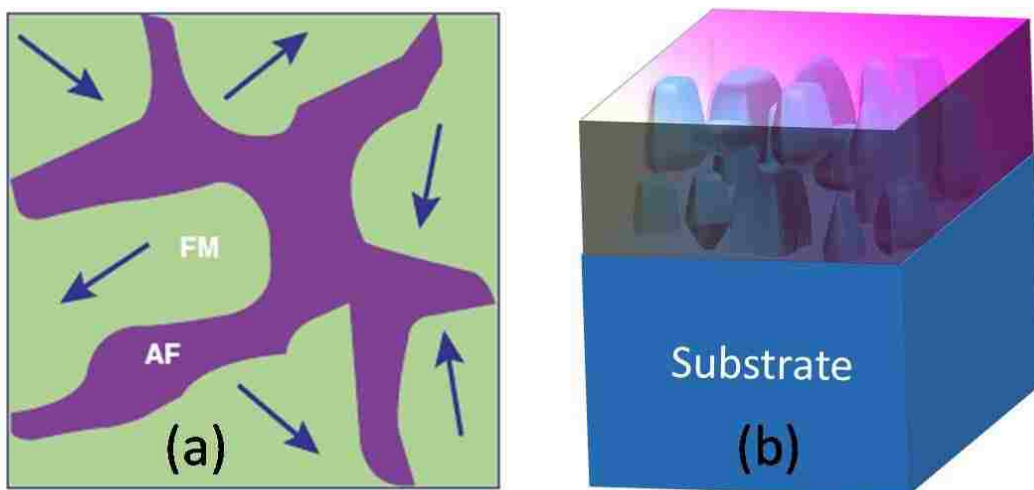

Figure 5-2: (a) Typical picture of electronic phase separation induced inhomogeneity. Figure adapted from **[9]**. (b) Chemical phase separation in inhomogeneous nanocomposite system.

Strain in a nanocomposite will be more profound. In a horizontal thin film, strain has been proved to dramatically change the properties of a thin film. However, the in-plane strain effect can only lock the lattice parameter to substrate only in a limited thickness, generally on

the order of a few nanometers and then quickly relax. In contrast, the vertical strain effect could affect across the whole thin film. The profound vertical strain effect is reported in $La_{0.7}Ca_{0.3}MnO_3$-MgO **[150]** and $BiFeO_3$-Sm_2O_3. **[153]**

In this chapter, we introduce a method of alternate deposition to grow nanocomposite and used two raw materials of V_2O_3 and $La_{2/3}Sr_{1/3}MnO_3$ (LSMO) to demonstrate a nanocomposite with structure and properties controlled by tuning the deposition time ratio.

5.2 Basic Properties of the Raw V_2O_3 and $La_{2/3}Sr_{1/3}MnO_3$ Thin Films

Table 5-1: Lattice constant of LSMO, V_2O_3 and $LaAlO_3$ and their lattice mismatch

	$La_{2/3}Sr_{1/3}MnO_3$	$LaAlO_3$	Mismatch
a(Å)	5.505	5.357	2.6%
b(Å)	5.502	5.357	2.6%
c(Å)	13.34	13.086	2%
	$La_{2/3}Sr_{1/3}MnO_3$	V_2O_3	Mismatch
a(Å)	5.505	4.9	11%
b(Å)	5.505	4.9	11%
c(Å)	13.14	13.96	4%

Both the LSMO and V_2O_3 are rhombohedral structure and their lattice constants are shown in **Table 5-1**. (111) $LaAlO_3$ (LAO) substrates were used for epitaxial growth. LSMO has very small lattice mismatch with LAO substrate (2%). The lattice mismatch between V_2O_3 and LSMO is very large (11% in a-b plane). The V_2O_3 also has big lattice mismatch with LAO (8% in a-b plane). Such lattices mismatch configuration will result in a nanocomposite when growing V_2O_3 and LSMO together on LAO with alternate deposition method as described in the next section. Here, we would like to introduce the properties of raw V_2O_3 and LSMO thin films first.

LSMO and V_2O_3 thin films were grown via pulsed laser deposition (PLD) on (111) LAO substrates at the same condition. The Ozone ambient during deposition was 1.3×10^{-7} Torr. The as-received LAO substrates were directly used for epitaxial growth without any pre-treatment. The substrate temperature was maintained at 600 ^{o}C. A KrF excimer laser (λ = 248 nm) was used for growing at a repetition rate of 3 Hz. Under this condition, both the growth modes of V_2O_3 and LSMO are 3D. The deposition fluxed was calibrated by TEM. The average deposition fluxes for LSMO and V_2O_3 are 2 Å/min and 1.3 Å/min respectively .

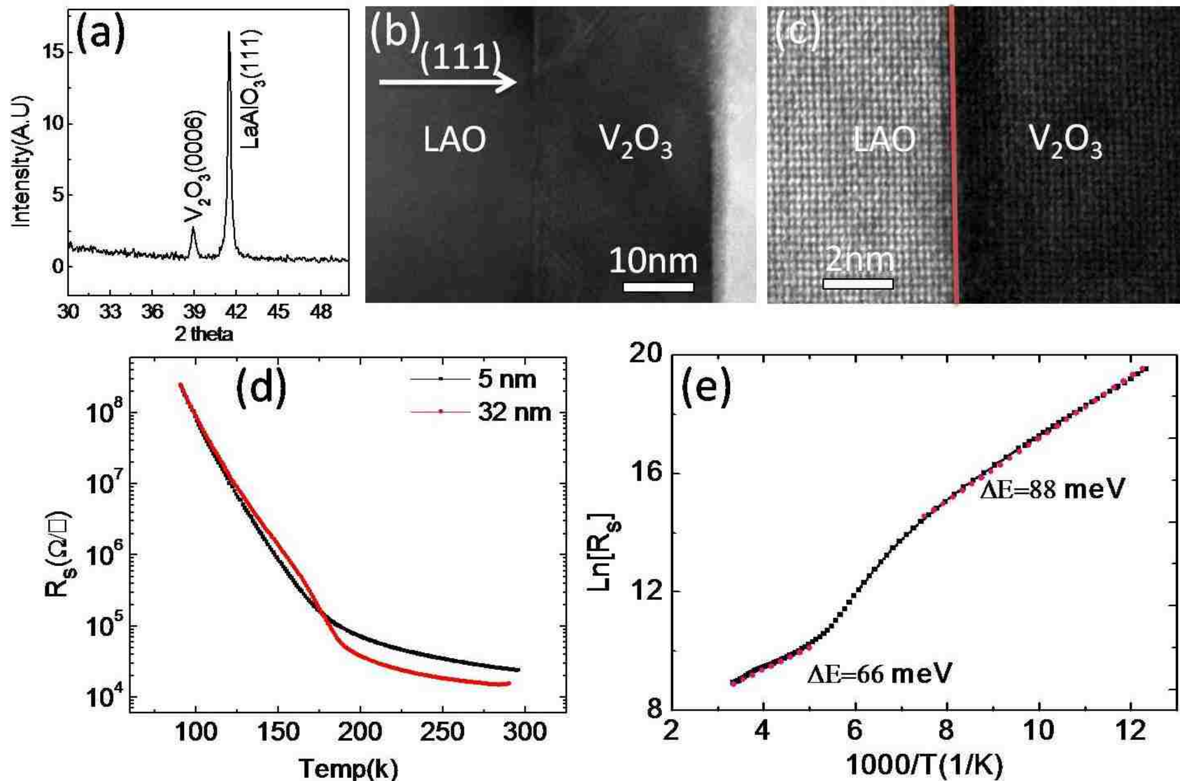

Figure 5-3: (a) XRD pattern of V_2O_3 thin film. (b) TEM image of the cross-section of V_2O_3 thin film and (c) High resolution STEM image of $LaAlO_3/V_2O_3$ interface. (d) Temperature dependence of resistivity of V_2O_3 thin films with different thicknesses and (e) plotted in Ln(R) Vs.1000/T scale.

Bulk V_2O_3 is a prototype Mott insulator. During cooling down, V_2O_3 undergoes a transition from rhombohedral paramagnetic metal to monoclinic antiferromagnetic insulator at the transition temperature of 160 K, with a jump in resistivity of about seven orders of

magnitude. However, the thin film of V_2O_3 on (111) LAO shows a different transition behavior. The structure and transport property of V_2O_3 thin film on LAO are shown in **Figure 5-3**. The X-ray diffraction pattern of V_2O_3 thin film indicates that the growth direction is [0001] and high resolution image indicates that the film is well crystalline. The film undergoes a semiconductor to semiconductor "transition" from thermal activation of ~ 66 meV to ~ 88 meV during cooling down as shown in **Figure 5-3e**. The films with different thicknesses exhibit similar transport properties. In contrast to sharp transition the bulk, the broad transition region may be due to the strain and oxygen deficiency.

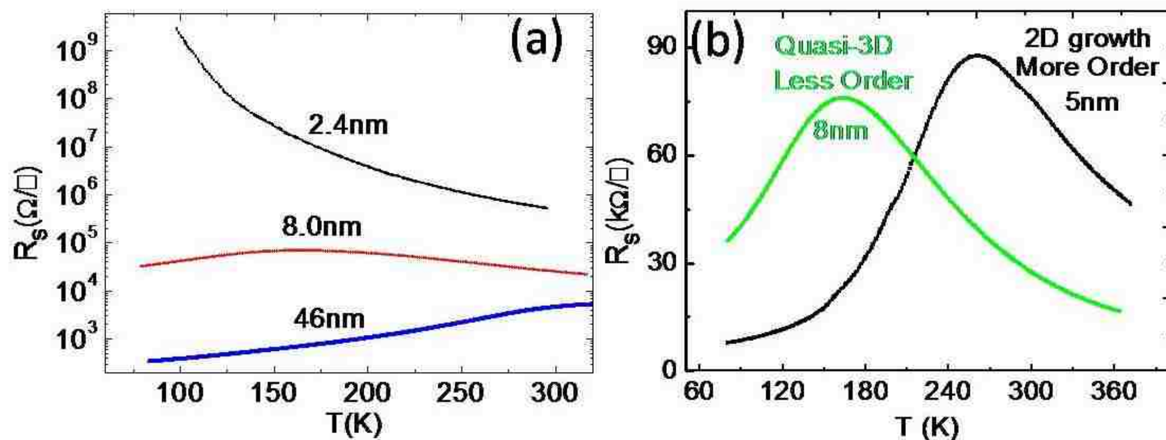

Figure 5-4: (a) Temperature dependence of resistivity for 3D growth LSMO thin films with different thicknesses. (b) Effect of growth modes on transport properties of LSMO thin films.

The transport properties of LSMO thin films on (111) LAO substrate are shown in **Figure 5-4**. The cross-over metal to insulator transition temperature T_C is strongly dependent on the thickness of LSMO. The 2.4 nm thick LSMO film is insulator. The 8.0 nm thick film has a cross-over metal-to-insulator transition with T_P of 165 K. The T_P is promoted to 350 K when the thickness increases to 46 nm. The insulating behavior and lower T_P than bulk should be caused by the strain, oxygen deficiency and existence of dead layers as discussion the **Chapter 4**. Furthermore, the disorder can suppress the metallicity of LSMO thin film. By using a 2D flat LAO substrate which had been annealed at 900 °C for 2 hours in oxygen flow

before growing, a 2D growth of LSMO was obtained. The 5 nm thick LSMO thin film with 2D growth on 2D flat LAO substrate has a higher T_P than that of the 8 nm thick LSMO with 3D growth (see **Figure 5-4b**)

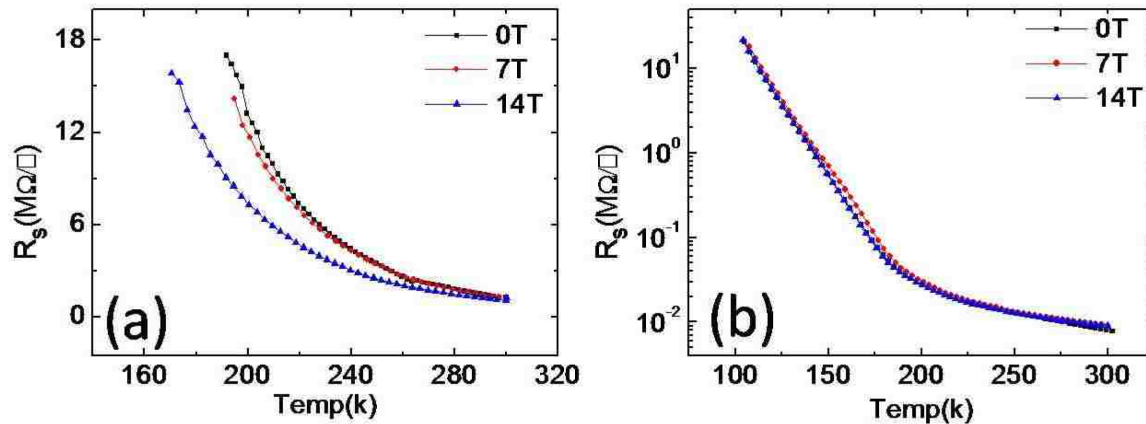

Figure 5-5: Magnetoresistance effect in (a) 2.4 nm LSMO; (b) 32 nm V_2O_3.

The magnetoresistance (MR) effects in LSMO and V_2O_3 thin films are shown in **Figure 5-5**. Very weak or almost no MR is observed in the V_2O_3 thin film while the LSMO of 2.4 nm exhibits large negative MR effect at low temperature range. LSMO and V_2O_3 thin films exhibit dramatically different transport properties.

5.3 Growth and Structure of V_2O_3-$La_{2/3}Sr_{1/3}MnO_3$ Columnar Nanocomposite

Self-assemble effect is broadly employed to synthesize the oxide nanocomposite **[144]**. A major challenge is how to control a self-assembled nanocomposite thin film to tailor properties. Traditionally, the nanocomposite is grown via mixed target growth where two materials are uniformly mixed together in certain chemical ratio and pressed into one target, and then the chemical ratio can only be tuned via making a new target **[144-148]**. Another possible way is to grow a nanocomposite film by depositing such as two different metal oxides together alternately with each for specific time. In general, such alternate deposition will result in a horizontal layer structure when the deposited materials and substrate have a

small lattice mismatch between each other, and a large lattice mismatch may favor a formation of a self-assembled nanocomposite as that occurring in mixed target growth **[144-148]**. If the alternate deposition can give rise to a nanocomposite by exploiting the lattice mismatch, the chemical ratio and structure then could be easily tuned by controlling the deposition time ratio. As a result, an artificially tailored nanocomposite with desired properties can be achieved in a more flexible way.

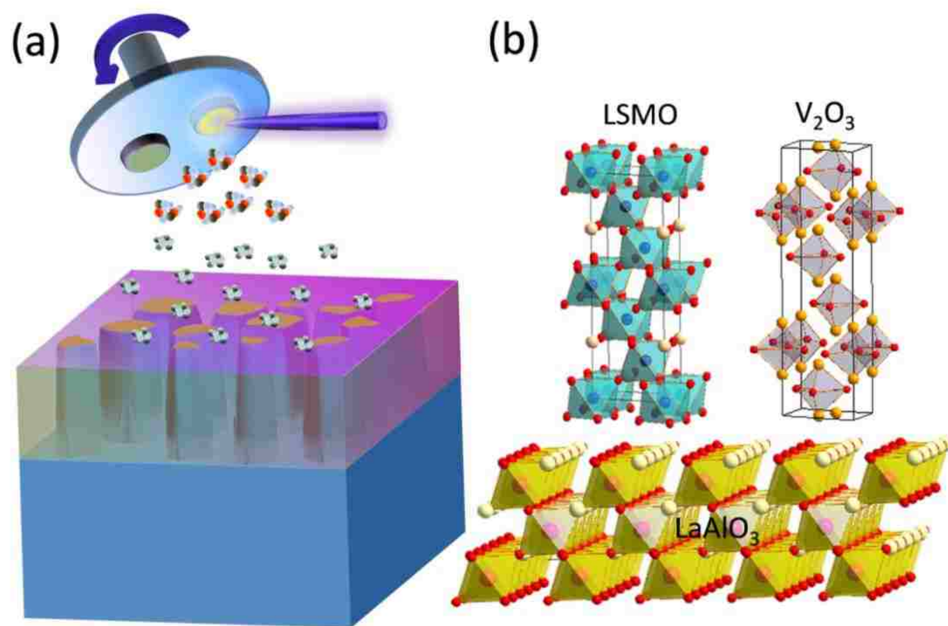

Figure 5-6: (a) Scheme of growth of nanocomposite with alternate deposition method. (b) Structure models of the LSMO and V_2O_3 and (111) $LaAlO_3$ substrate

We have grown V_2O_3 and LSMO together via alternate deposition with using PLD in order to get a nanocomposite and explore the in-plane transport properties. The schematic alternate deposition method is shown in **Figure 5-6a**. Two targets of single raw materials are used and they are alternately deposited on a substrate with each one grown for specific time individually. Such alternate deposition could end up with a nanocomposite rather than a multilayer superlattice due to strain and self-assemble effect. Both the LSMO and V_2O_3 in the bulk have rhombohedral structure and their structure models are shown in **Figure 5-6b**. As

shown in **Table 5-1**, LSMO has very small lattice mismatch with LAO substrate (2%), while the V_2O_3 has large lattice mismatch in a-b plane with both the LSMO (11%) and LAO (8%).

V_2O_3-LSMO nanocomposite was grown via depositing V_2O_3 and LSMO alternately from their single phase targets. V_2O_3 and LSMO were deposited alternately for specific time with LSMO grown first and the deposition sequence was $[(V_2O_3)_{t_1}/(LSMO)_{t_2})]_n$/LAO. Here t_1 and t_2 (in unit of minute) were individual deposition time of V_2O_3 and LSMO in one cycle respectively. The total time $(t_1+t_2) \times n$ was about 80 min. For convenient, the nanocomposite is labeled with t_1/t_2 which is defined as $\alpha \equiv t_1/t_2$ hereafter.

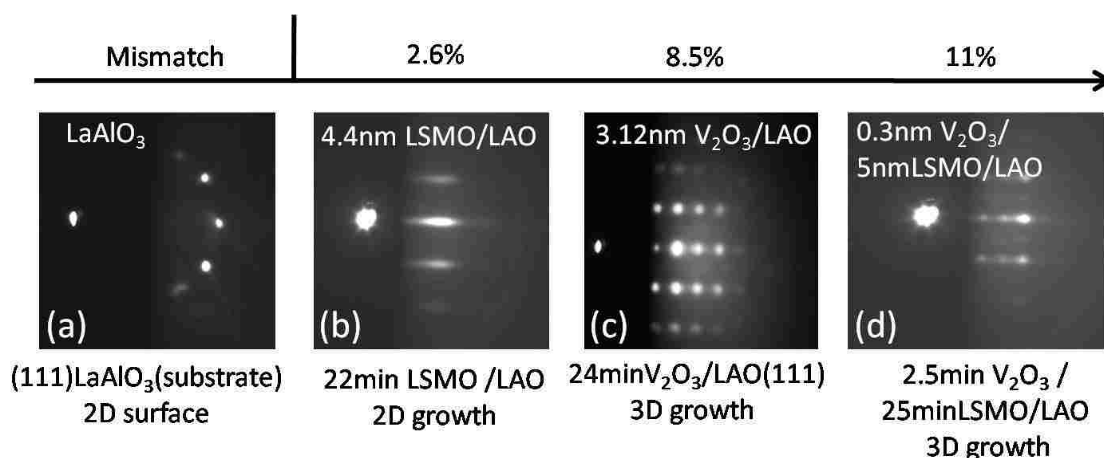

Figure 5-7: RHEED pattern (a) of LAO substrate; (b) after growing LSMO for 22 min on LAO; (c) after growing V_2O_3 for 24 min on LAO; (d) after growing 2.5 min V_2O_3 on LSMO. The note on the top of the pattern indicates the equivalent deposited thickness.

The growth modes of V_2O_3 and LSMO and their mixed deposition on a 2D flat LAO substrate are shown in **Figure 5-7**. The 2D flat LAO substrate as indicated by its RHEED pattern in **Figure 5-7a** was obtained by annealing the as-received LAO substrate at 900 ^oC for 2 hours in oxygen flow. The LSMO which has a small lattice mismatch with LAO substrate exhibits a 2D growth mode. After depositing LSMO for 22 min, which is equivalent to 4.4 nm, the RHEED sustains 2D pattern. The growth of V_2O_3 on LAO is 3D and the RHEED becomes 3D after the deposition of V_2O_3, so is its growth on LSMO. The large

lattice mismatch will favor a 3D growth and then the formation of a nanocomposite. To suppress the 2D growth of LSMO to obtain a nanocomposite during alternate deposition, we directly used the as-received LAO substrates with relatively rough 3D surface for growth.

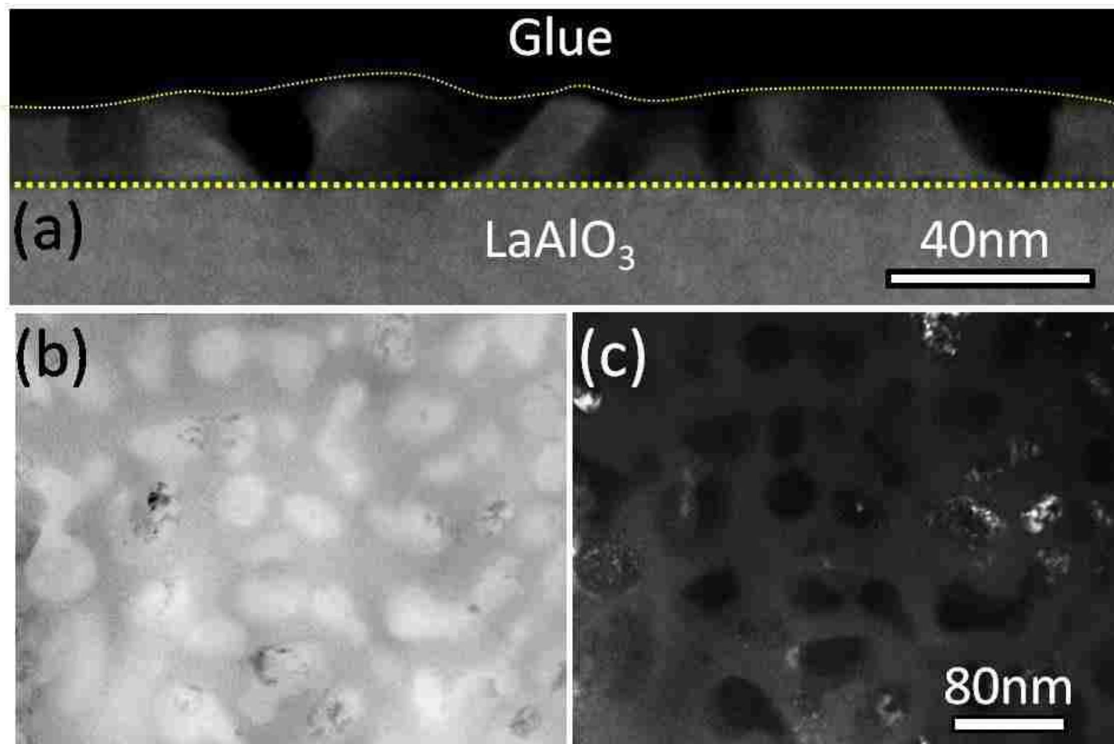

Figure 5-8: (a) Dark field image of the cross-section of $\alpha \equiv 13/10$ nanocomposite. Bright field image (b) and dark field image (c) of the planar structure of same region.

The structure of the V_2O_3-LSMO nanocomposite was revealed by TEM. **Figure 5-8** summarizes the cross-section and planar structures of $\alpha \equiv 13/10$ nanocomposite. The cross-section view (as shown in **Figure 5-8a**) shows that there are some quasi vertical dark columns embedded in the bright film. An evident scenario of the chemical phase separation can be found in planar view image as shown in **Figure 5-8(b-c)**. Take the bright field image of planar view for example, there are isolated dark islands embedded in a matrix and separated by a space of ~ 25 nm. According to the planar view, a typical scale for these islands is ~ 30 nm. Based on **Figure 5-8(a-c)**, it is concluded that the alternate deposition of V_2O_3 and LSMO gives rise to an oxide nanocomposite.

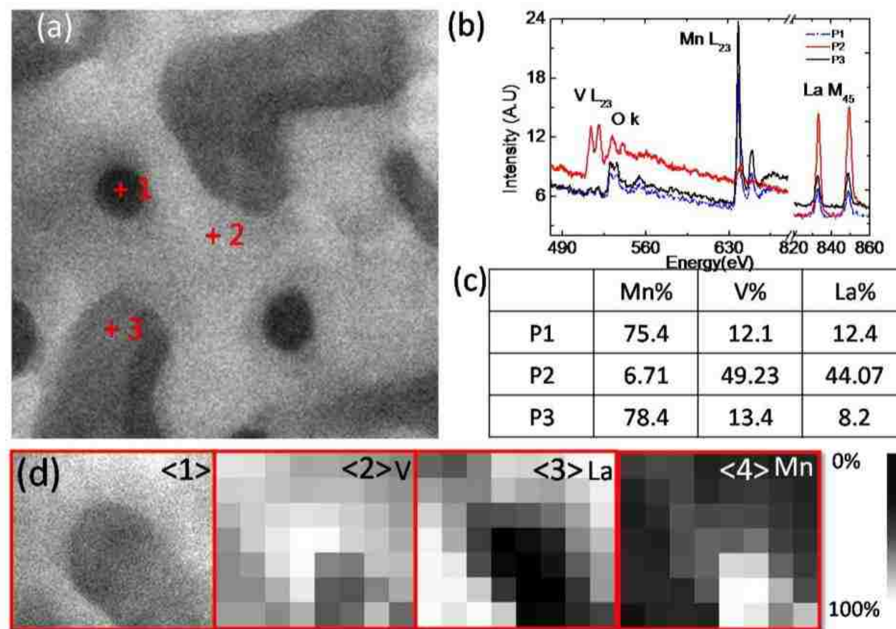

	Mn%	V%	La%
P1	75.4	12.1	12.4
P2	6.71	49.23	44.07
P3	78.4	13.4	8.2

Figure 5-9: (a) Planar view of the $\alpha \equiv 13/10$ nanocomposite. (b) EELS spectrums of selected points in panel (a), P1(blue), P2(red), P3(black). (c)The calculated relative quantification of elements of Mn, V and La. (d) EELS mapping with STEM: <1> mapping area and relative concentration of <2>V, <3>La, and <4>Mn.

To identify the chemical phase of the bright matrix and the dark columns, a EELS mapping via scanning TEM (STEM) which has a spatial resolution of ~ 1 nm was performed. ELL spectra of three typical points at three regions of different contrast as marked in the **Figure 5-9a** are displayed in **Figure 5-9b**. By quantifying the EEL spectrum, the relative chemical concentration is obtained as shown in **Figure 5-9**c. The darker region (Point-1) was dominated by Mn with less V and La, while the bright region (Point-2) is dominated by V and almost same level of La with few Mn. The Point-3 at grey region still has a lot Mn with few V and La. A much clear distribution of the elements is obtained by EELS chemical mapping. The relative chemical concentration mappings of V and La and Mn of region as shown in panel-1 of **Figure 5-9d** are displayed in panel-2, panel-3 and panel-4, respectively. Panel-1 of **Figure 5-9d** is the dark field planar view TEM image in which the grey island at right-bottom corner corresponds to the dark islands in **Figure 5-9a**. It is clearly that the bright region

around the island is dominated by La and V but almost no Mn while the grey region is dominated by Mn. As a result, The chemical compositions of these two distinct phases of materials in the film are completely different from the raw compounds, neither V_2O_3 nor LSMO. The bright regions are composed of La, V and certain oxygen while the gray are mainly Mn and oxygen.

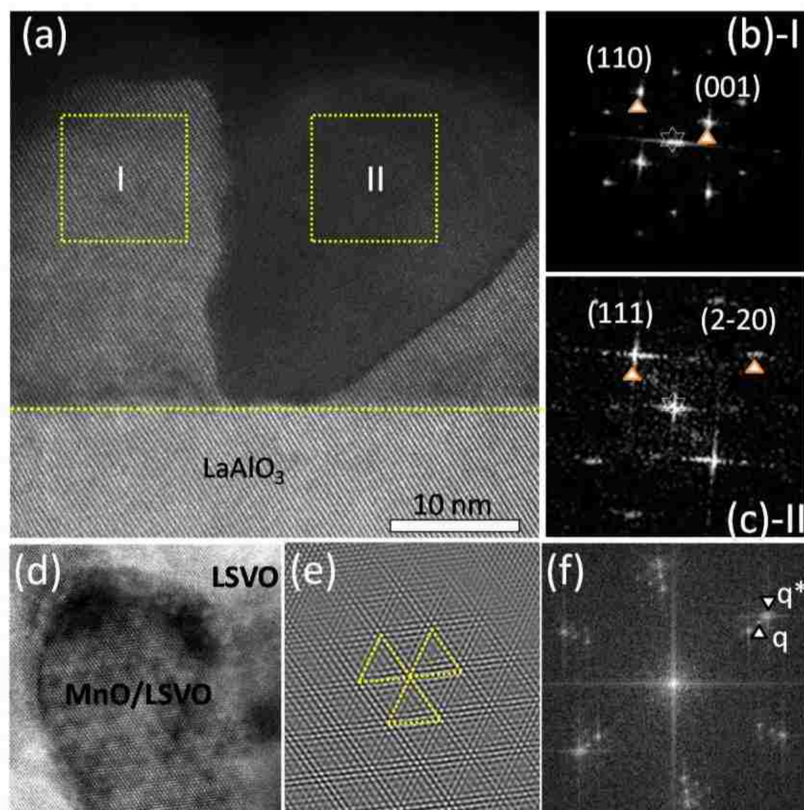

Figure 5-10: (a) High-resolution cross-section image of α ≡ 13/10 nanocomposite via dark field STEM. The FFT of the selected regions in (a) are shown in (b) and (c). (d) HRTEM planar view image and (e) the smooth image of the Morie pattern in (d). (f) The FFT of Morie pattern.

To further figure out the chemical phase, lattice constant is measured by performing the fast Fourier transform (FFT) of high resolution TEM cross-section image in **Figure 5-10**. The FFTs of the region I and region II show that the bright region is $La_{1-x}Sr_xVO_3$ (LSVO) and dark column is MnO. Such conclusion is further supported by the appearance of the Morie pattern (see **Figure 5-10d**). The ratio of the k-space (q) of the main peak to the satellite peak

(q*) is q/q*=7.53. Since a_{Mno}=4.443 Å and a_{LSVO}=3.89 Å, the theoretic q/q* is 7.53.

$$\frac{q}{q*} = \frac{a_{LSVO} \times a_{MnO} / (a_{LSVO} - a_{MnO})}{(a_{LSVO} + a_{MnO})/2} = 7.53$$

It is equal to the observed value, further supporting that the dark grey region is MnO.

EELS and HRTEM image both indicate that the two raw materials of LSMO and V_2O_3 react with each other, resulting in a formation of new MnO and LSVO materials. A few V_2O_3 columns which does not react with the LSMO could be found.

The chemistry and structure of $\alpha \equiv 4/10$ nanocomposite are revealed as well with STEM and EELS mapping. It is found that the LSMO dominates the $\alpha \equiv 4/10$ nanocomposite and forms a percolated matrix (bright region in **Figure 5-11**) with embedded nanocolumn defects. According to the EELS mapping, the dark circular like island is dominated by V and O while the grey one is dominated by Mn and O. The bright region is confirmed to mainly consist of the LSMO and have with few LSVO due to the low V_2O_3 to LSMO chemical ratio.

The structures and chemistries of the other nanocomposites with different combination of t_1 and t_2 have been also figured out by STEM and EELS. A summary of the structure evolution with increasing ratio is shown in **Figure 5-12**. It is found that the value of the ratio α determines properties as discussed later, so we use α value to mark specific nanocomposite thin films hereafter. The nanocolumns could be found for all kinds of nanocomposites of different ratios but the chemical phase of the matrix and columns changes with increasing ratio as shown in **Figure 5-12**. With small α value, the LSMO will dominate as the $\alpha = 0.4$ nanocomposite showing. With respect to the $\alpha = 1.3$ nanocomposite, the LSVO forms a percolated matrix. With increasing α, the percolation of LSVO will be diminished. Take $\alpha = 4.33$ for example as shown in **Figure 5-12c**, the dark region forming a percolated matrix with

isolated bright islands embedded in. The bright region in α = 4.33 nanocomposite thin film is LSVO while the dark region is dominated by V_2O_3 with some MnO nanocolumns. It is concluded that the percolation network can be tuned via controlling the deposition time ratio.

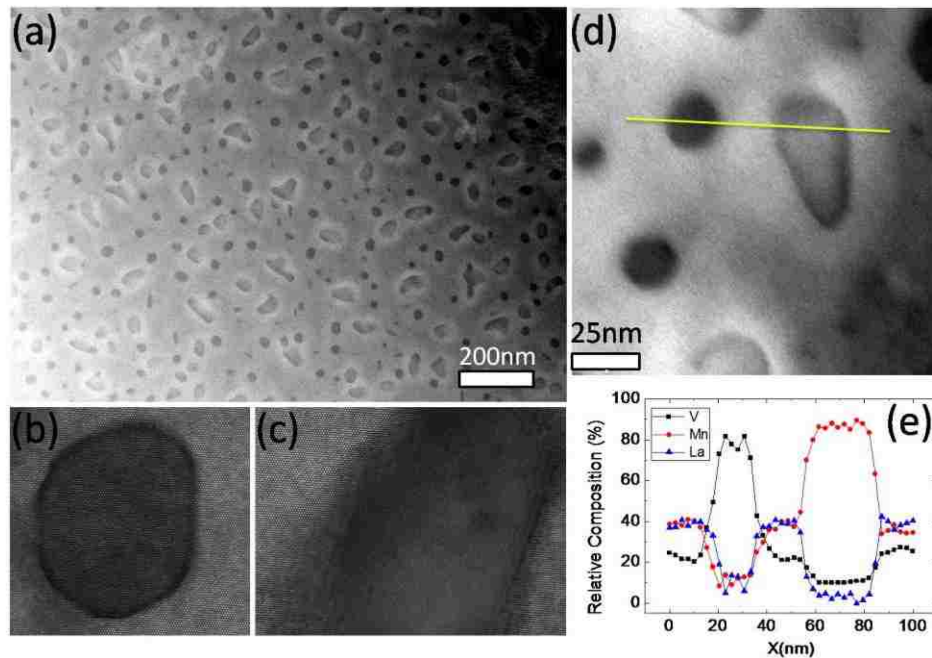

Figure 5-11: (a) Planar dark view image of the α ≡ 4/10 nanocomposite. High resolution TEM image of the dark island (b) and grey island (c). (d) Region for EELS line mapping. (e) EELS line mapping along the line in (d).

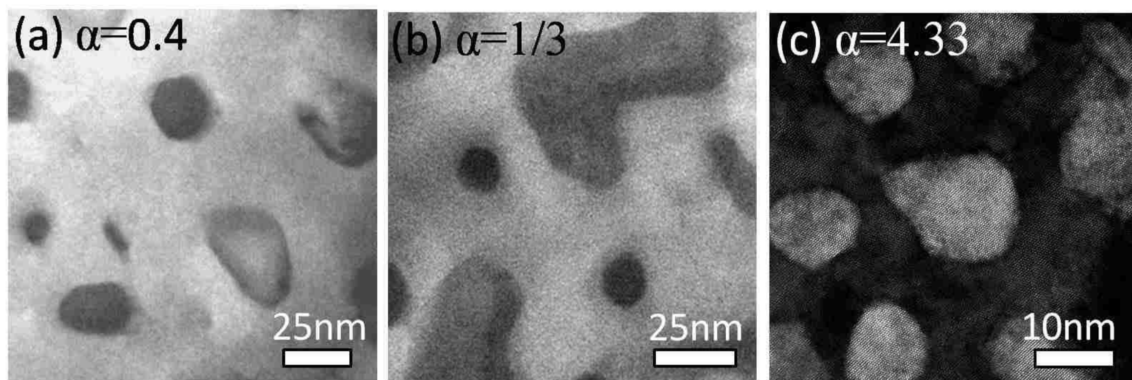

Figure 5-12: Dark field TEM planar view images of nanocomposites with different ratios.

5.4. Phase Diagram of The V_2O_3-$La_{2/3}Sr_{1/3}MnO_3$ Columnar Nanocomposite

Not surprisingly, the transport properties are also a function of t_1/t_2. As shown in **Figure 5-13**, if we keep t_2 = 10 min, the α ≡ 6/10 nanocomposite is insulating, while both the α ≡ 10/10 and α ≡ 16.6/10 samples exhibit a cross-over transition where the high temperature

phase is metallic. The cross over temperature is defined by T_c (defined as $\left.\frac{dR_s}{dT}\right|_{T=T_c}=0$). We should further notice that the samples with same α ratio but different individual t_1 and t_2 value show very similar transport properties (**Figure 5-13**). It is the deposition time ratio α determining the properties rather than the individual t_1 or t_2.

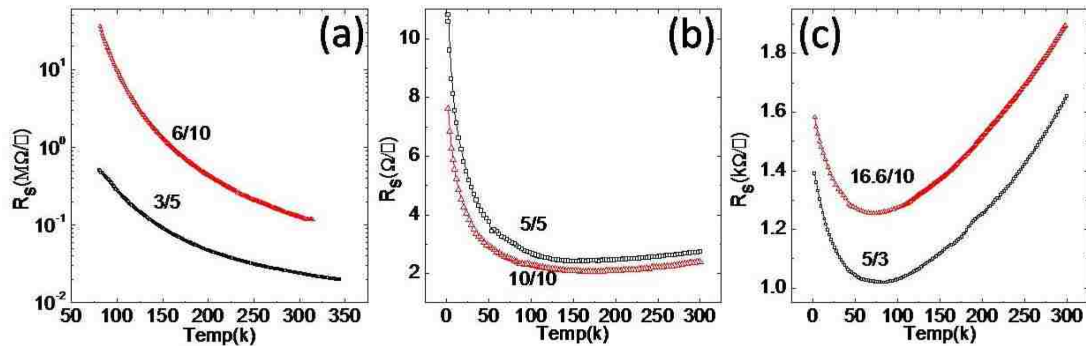

Figure 5-13: Temperature dependent sheet resistance for nanocomposites with same ratio α but different individual deposition time.

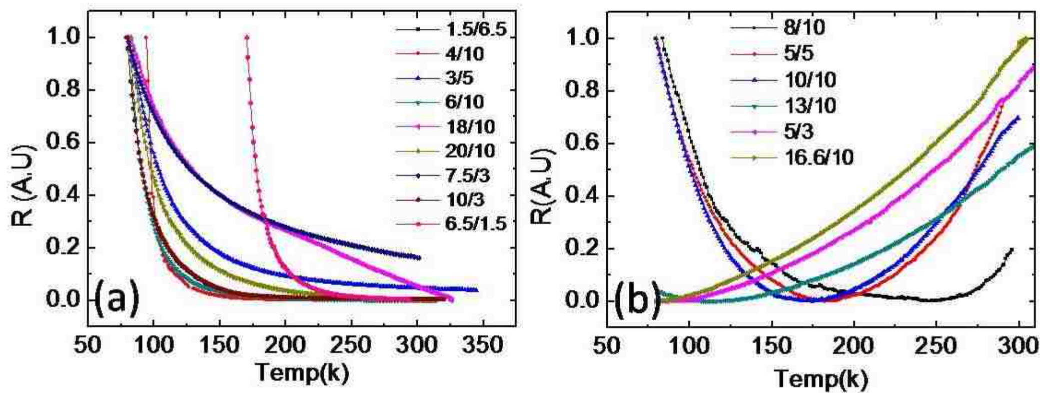

Figure 5-14: Resistance vs. temperature curves for nanocomposites with different α. Curves for the insulating nanocomposites are shown in (a) and for nanocomposites with metallic phase at high temperature are shown in (b). The resistances are normalized to plot together for comparing.

The systematical evolution of the properties with α are shown in **Figure 5-14**. The nanocomposites with different kinds of t_1 and t_2 combination but $\alpha < 0.8$ and $\alpha > 1.66$ are insulating. The nanocomposites exhibit a cross-over transition with metallic phase at high temperature and a upturn of resistivity at low temperature in the range of $0.8 \leq \alpha \leq 1.66$. The transition temperature (T_c) decreases with increasing α.

The temperature dependent sheet resistance of the α = 0.4 nanocomposite is shown in **Figure 5-15a**. It has very similar transport property curve with pure 2.4 nm thick LSMO thin film on the (111) LAO. The thermal activation energy of α = 0.4 nanocomposite obtained by fitting resistivity curve with Arrhenius equation is 100 meV which is a little bigger than that for the pure 2.4 nm LSMO thin film of 70 meV. The insulating behavior of 2.4 nm LSMO could arise from existing dead layer **[125]** and oxygen deficiency **[44, 45]**. The higher thermal activation energy of α = 0.4 nanocomposite than LSMO thin film may be due to the disorder in the nanocomposite. In the range of α > 1.66, the nanocomposite is in insulating phase again. With bigger α, the properties are close to the pure V_2O_3 thin film. As shown in **Figure 5-15b**, the α = 4.33 sample displays a turn over at about 180 K. Such characteristic is very close to that of pure 5 nm thick V_2O_3 thin film grown on LAO(111) and to that of V_2O_3 grown on sapphire **[154]**.

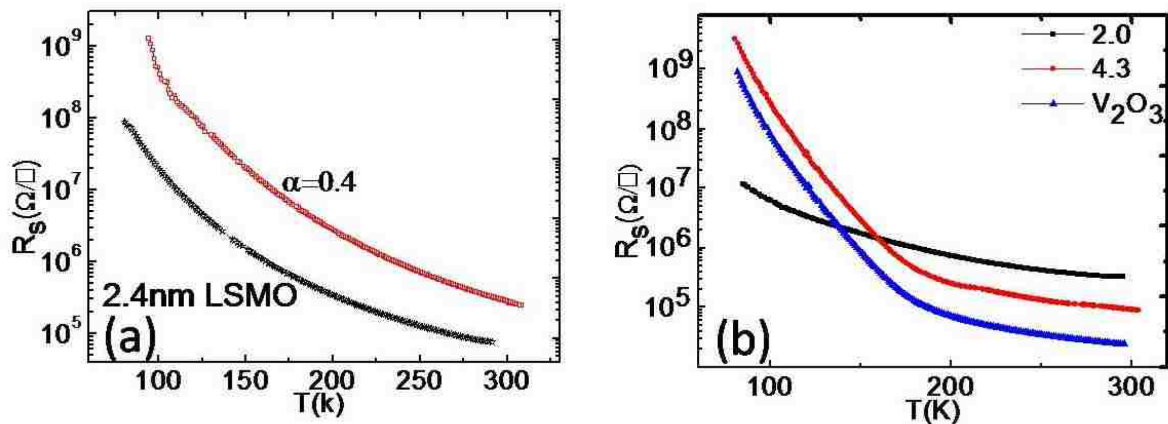

Figure 5-15: Sheet resistance vs. temperature curves for (a) 2.4 nm LSMO (black) and α = 0.4 nanocomposite (red); (b) α = 2.0 (black) nanocomposite, α = 4.33 (red) nanocomposite and 5 nm V_2O_3 (blue).

Further, the magnetic field dependent transport properties of the films with different α values are displayed in **Figure 5-16**. The colossal magnetoresistance (MR) effect can be only observed with smaller α value of less than 0.8. Take the α = 0.4 nanocomposite for example, a

98% negative MR (defined as (R(B)-R(0))/R(0)×100%) effect at 146K was observed in the α = 0.4 nanocomposite, further indicating that the films resembles the films of LSMO. The nanocomposites of α > 0.8 don't have or just have very weak MR effect as the **Figure 5-16(b-d)** showing.

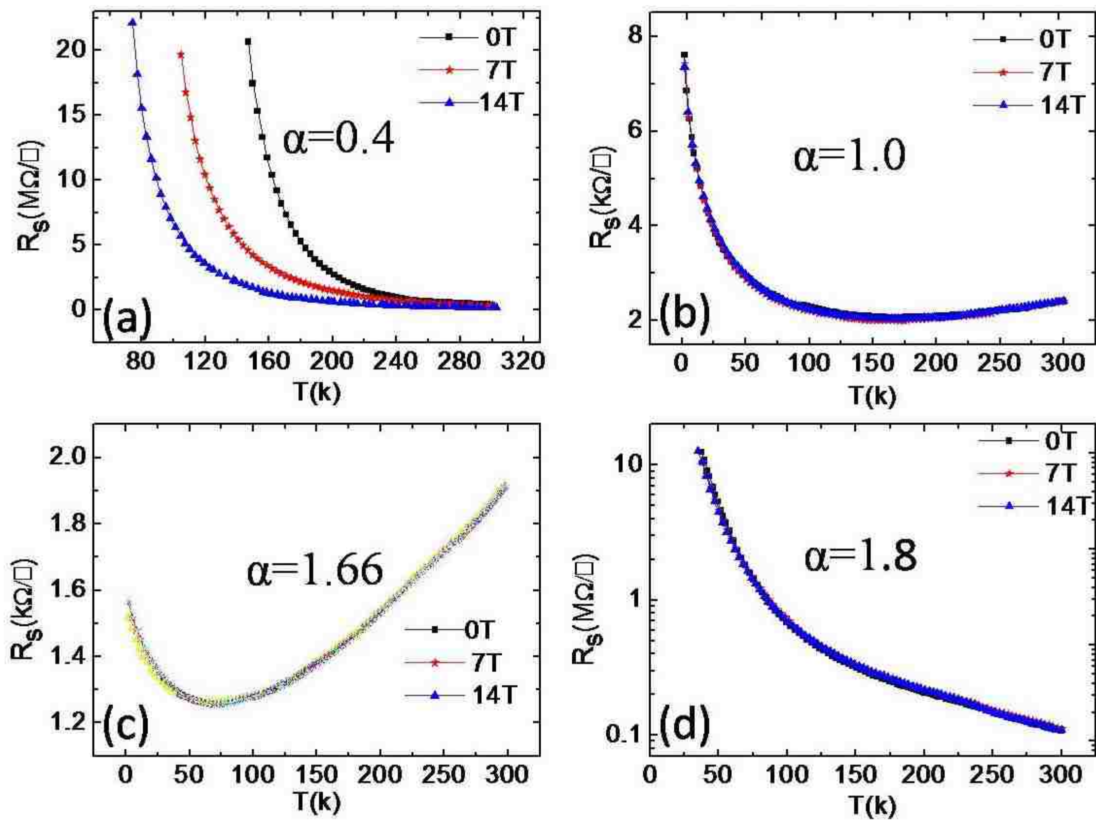

Figure 5-16: Temperature dependent sheet resistance under magnetic field for (a) α=0.4, (b) α=1.0, (c) α=1.66. (d) α=1.8 nanocomposite.

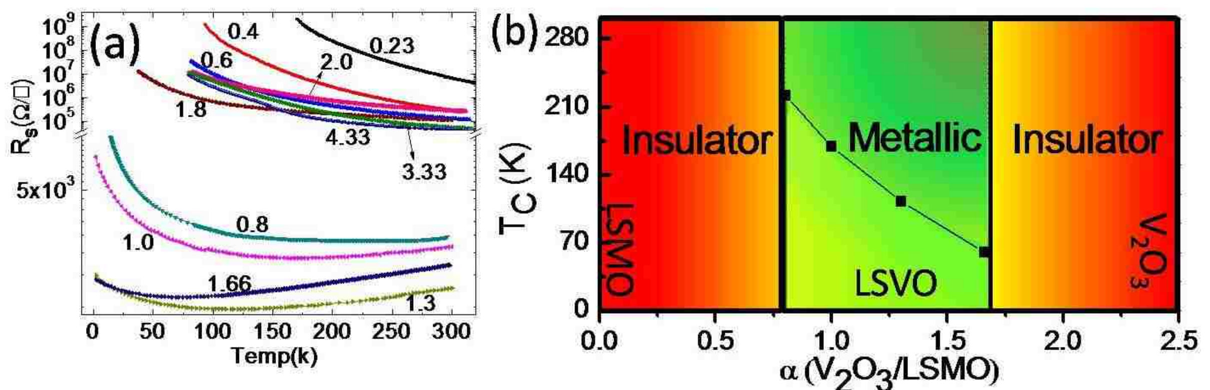

Figure 5-17: (a) Temperature dependent sheet resistance of nanocomposites with different α values. (b) Phase diagram of V_2O_3-LSMO nanocomposite.

A summary of the transport properties of nanocomposites with different α values is shown in Figure **5-17a**. According to the transport properties of nanocomposites with different α values and the above discussion, a phase diagram can be roughly constructed as shown in **Figure 5-17b**. At the left side of phase diagram, with decreasing α the nanocomposite tends to be dominated by excess LSMO and has colossal MR effect. It is consistent with its structure that the LSMO forms a percolation network as mention above in **Figure 5-12a**. In the intermediate region ($0.8 \leq \alpha \leq 1.66$), the new forming LSVO connects together and then the LSVO percolates and dominates the transport properties. In the bulk the $La_{1-x}Sr_xVO_3$ has a metal-to-insulator (MIT) transition with transition temperature (T_c) depending on the doping level **[155]**. In the case of x > 0.176, it is metallic and has a upturn of resistivity at low temperature. The relative content of LSVO in the nanocomposite is determined by the α, which affects the percolation network. Furthermore, the out of plane tensile strain coming from columnar defects also affect the properties of LSVO. Both the percolation and strain effect will change the T_c of the nanocomposite. At the chemical ratio of $\alpha = 1.66$, the T_c goes down to the lowest temperature of 60 K. At the right side of the phase diagram, the increasing amount of V_2O_3 induced excess V_2O_3 dominates as planar view image in **Figure 5-12c** showing, so the properties of V_2O_3 emerge.

The nanoscale inhomogeneity is a focused issue in complex metal oxides due to which a varieties of phenomena emerge, e.g., colossal magnetoresistance. The percolative transport is a result of nanoscale inhomogeneity. A critical ratio of certain phase is required to favor the occurring of percolation. Generally we can use external magnetic field, temperature, pressure to affect the percolation. Here, we demonstrated a new way of alternate deposition to create

nanoscale inhomogeneity and then control the percolation by tuning the ratio between different phases. The interface between the columnar defects and matrix materials may bring some new effect, so a thorough microscopic study is required to reveal the such as strain and detail chemical distribution at grain boundary in the future to clarify interface effect.

In summary, we demonstrated nanocomposites with alternate deposition method and explored the in-plane transport properties. The raw V_2O_3 and LSMO will self-assemble into a columnar nanocomposite. A chemical reaction between V_2O_3 and LSMO leads to the formation of LSVO and MnO. The relative ratio of different phases evolve with change of chemical ratio of V_2O_3 to LSMO, as a result the nature of the percolation changes. At low α value, the LSMO properties emerge and in the intermediate range ($0.8 \leq \alpha \leq 1.66$) the LSVO forms a percolated network and a controllable cross-over transition can be tuned via change the α. With higher α, the nanocomposite is going to be insulator again and tends to be close to V_2O_3.

Chapter 6 Resistive Switching in Metal Oxide Thin Films[1]

6.1 Introduction and Motivation

In simple Metal/Metal-oxide/Metal sandwiched thin films structure, it is found that electric field can vary its resistance persistently but still reversibly with proper applied voltages or currents, that is, electric field induced resistive switching (RS) effect (see **Figure 6-1**). We may have more than two resistance states but two in most cases which can be reversibly switched. Generally speaking, the RS does not include phenomena caused by Joule heating. The accompanied Joule heating may have effect on RS, but it is just assistance or parasite rather than a driving mechanism. The discovery of resistive switching effect in metal oxide thin films can be traced back to 1962 when Hickmott found negative differential resistance effect in several Al/Insulator/Al devices where the insulators were binary metal oxides (Al_2O_3, ZrO_2, TiO_2, SiO, TaO_2) **[76]**. Later in 1960s, more distinct RS effect was revealed in some other metal oxides [**156-158**]. The significance of the RS effect had not been realized until the scientists in University of Houston demonstrated a reversible electric pulse induced resistance (EPIR) and prototype of non-volatile resistance random access memory (NV-RRAM) by using $Pr_{0.7}Ca_{0.3}MnO_3$ (PCMO) thin film in 2000 **[159]**. In the same year, IBM discovered RS effect in $SrTiO_3$ **[160]** and $SrZrO_3$ **[161]**. Like bamboo shoots after a spring shower, the RRAM began to attract a great deal of interest and be quickly developed. In 2002, Sharp Corporation and University of Houston together proposed PCMO based RRAM and another big earthquake shaking both industry and academy is that Sharp

[1] This chapter first appears as Solid-State Electronics 72, 4 (2012), Appl. Phys. Lett. 94, 253503 (2009), Appl. Phys. Lett. 98, 203108 (2011) and J. Appl. Phys. 111, 114506 (2012). Reprinted by permissions of Elsevier and American Institute of Physics.

Corporation developed a first PCMO based RRAM capable of programming data at rates about 100 times faster than flash memory **[162]**. RRAM has much simpler unit cell architecture that it could be 1R1D (one resistor, one diode) or 1R1T (one resistor, one transistor), dramatically increasing memory density and data programming speed. The programming and read voltage could be ~1 V and current is in the range of micro-ampere, so the power is much lower than flash memory. The advantages of high speed, high density, and low power consumption make RRAM to be as a very promising next generation non-volatile memory.

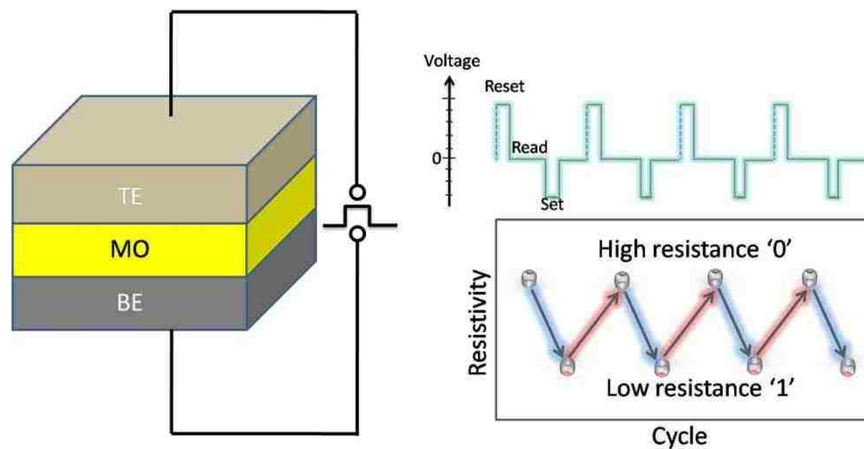

Figure 6-1: Left, Metal/Metal-Oxide/Metal sandwiched structure; Right, scheme of writing/erasing and read cycle.

Table 6-1: Examples of metal-oxides which exhibit RS behavior

Binary	TiO_2, ZrO, NiO, Cu_xO, MoO_x, ZnO, CeO_2, CoO, Fe_2O_3,SiO_2, WO_3, MnO_2,Ta_2O_5, HfO_2, MgO, Cr_2O_3, VO_2, Sm_2O_3
Poly	$SrTiO_3$, $SrZrO_3$, $Pb(Zr_xTi_{1-x})O_3$, $La_{1-x}Sr_xFeO_3$, $La_{1-x}Sr_xCoO_3$,$(Ba,Sr)TiO_3$, $Pr_{1-x}Ca_xMnO_3$, $La_{1-x}Ca_xMnO_3$, $La_{1-x}Sr_xMnO_3$, $BiFeO_3$, $LaCuO_4$

RS has been extensively discovered in a lot of metal oxides from binary compounds to polycompounds (see the **Table 6-1** as examples) **[76, 156-184]**. It seems to be a universal phenomenon in metal oxides thin films, but they may occupy quite different mechanisms. The RS could be categorized into two types (see **Figure 6-2**). One is unipolar RS (URS),

whereby SET, switching from a high resistance state (HRS) to a low resistance state (LRS), and RESET, switching from LHS to HRS, occur at different biases of the same polarity, either positive or negative. Typical unipolar RS devices include binary transition metal oxides such as NiO **[164]** and TiO_2 **[165]**. The other type of RS is bipolar, whereby SET and RESET occur at the opposite bias polarity. Some perovskite materials sandwiched between two metal electrodes are good examples of this second type **[159-163]**.

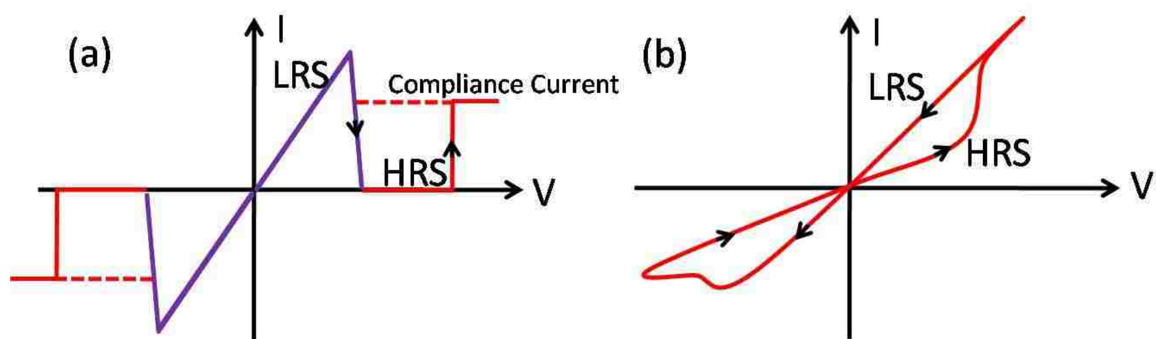

Figure 6-2: Typical I-V sweep loop for (a) Unipolar resistive switching (b) Bipolar resistive switching.

Although a great effort has been paid to find out the mechanism of RS, the underlying physics is still under controversy. This debate is exacerbated by the great difficulty in characterizing the physical changes responsible for the RS because the active regions of RS are extremely small (in nanoscale) and sandwiched between two metal electrodes. At the early stage, different models have been suggested to explain the mechanism of RS effect, including a conducting filament creation or destruction **[165]**, Schottky barrier behavior at the interface **[75, 185]**, Mott transition **[186]**, charge trapping or detrapping **[187]**, polaron melting and ordering **[188]**, oxygen vacancy migration **[66, 189-193]** and interface redox **[171, 194]**.

If we take a look at such sandwiched devices, the resistance that we measure is not just the resistance of metal oxide, but also interface resistance between the electrode and metal

oxide since in the most cases the interface resistance cannot be ignored. The actual resistance should be $R_{I1}+R_{MO}+R_{I2}$ as shown in **Figure 6-3**. The resistance change could arise from interface or bulk of metal oxide. No matter where the change comes from, we still can phenomenologically use filament model to describe resistance change in a way that conductive path is created at low resistance state and destructed at high resistance state. This picture is schematically shown in right panel of **Figure 6-3**. The filament can be either at interface or in metal oxide, thus we can have a commonly description of resistive switching with filament model. Precisely speaking, filament in metal oxide layer is called bulk filament, and interface conductive channel is called interface filament. Such phenomenological model can explain the RS well, but it cannot tell us the microscopic mechanism.

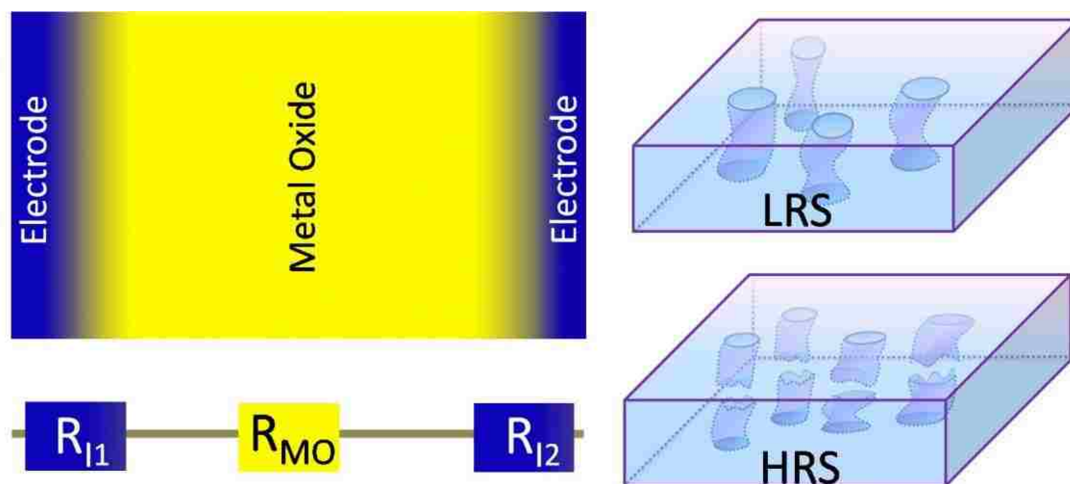

Figure 6-3: Left, schematic diagram of Electrode/Metal-Oxide/Electrode cross-section structure with a interfacial transition region. The overall resistance of this sandwiched structure is $R_{I1}+R_{MO}+R_{I2}$; Right, scheme of filament model.

Electric field induced filament formation and rupture by Joule heating is thought to be the most likely explanation for the URS. The bipolar RS (BRS), which breaks the space inversion symmetry, more related to an electric field direction and the microscopic structure of device, is hard to be understood. The origin of BRS remains elusive, despite of a significant increase in experimental findings in the past year. More and more experimental

results suggest that the region near electrode plays a very important role in BRS, despite of different possible mechanisms **[195-198]**. Such results which in most cases are based on investigation of the effect of different electrodes indicate that different electrodes lead to different RS behavior even in URS case. Lee *et al.***[196]** found that RS behavior of (Ta, or Al)/NiO/Pt is quite different from Pt/NiO/Pt that (Ta, or Al)/NiO/Pt would degenerate one day after fabrication of devices. Their X-ray spectroscopy indicates that the Ta top electrode was oxidized, which would fail the oxidation of filament, as a result the devices maintained in low resistance state (see **Figure 6-4**). The role of interface region is further realized after more and more experimental results from electrode effect and the effort to improve performance of devices in many other kinds of materials **[195-198]**.

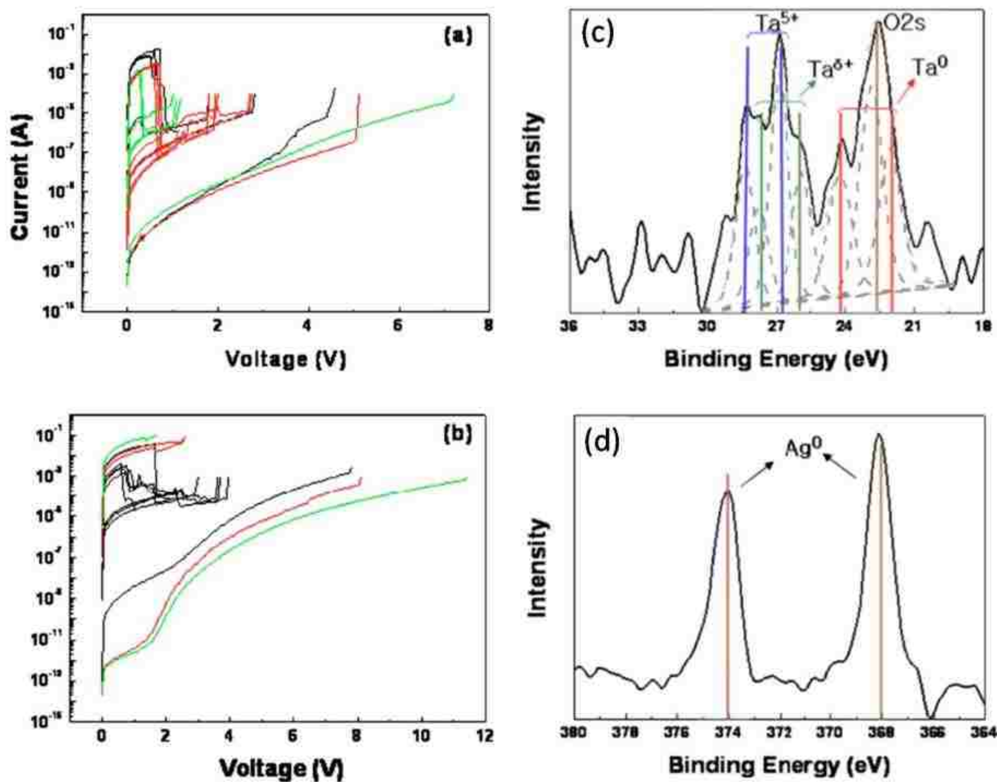

Figure 6-4: The *I-V* sweep loops for NiO films using Pt (black), Ta (red), and Al (green) top metal electrode, (a) as-fabricated devices (b) after one day. All samples have a Pt bottom electrode. X-ray photoelectron spectra of (c) Ta 4f and (d) Ag 3d. Ta 4f spectrum indicates oxidation of Ta while no oxidized Ag peak appears. Figures adapted from **[196]**.

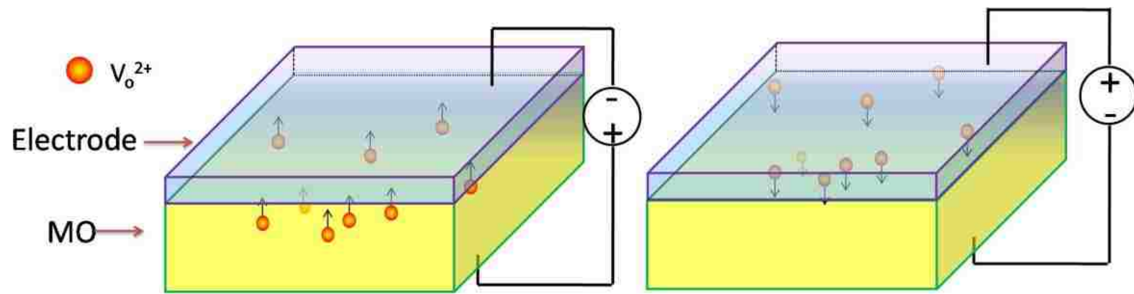

Figure 6-5: Scheme of interfacial oxidation and reduction model.

Metal electrodes affect the RS since the electrode material can participate in oxidation/reduction process **[196, 199, 200],** or in trapping and de-trapping of the oxygen vacancies **[201]**. Typically when the electrode is reactive and then could be easily oxidized, the electric field can drive the oxygen to move in/out of electrode to oxidize/reduce it (see **Figure 6-5**). The role played by metal contacts in these devices goes beyond the Schottky contacts as that in typical semiconductor devices, and may very well hold the key to the successful engineering of practical devices.

Since the RS is a universal phenomenon in metal oxides, a reasonable deduction is that oxygen ions/vacancies will be a center issue in RS. Many transition metal oxides are 'self-doped' by native oxygen vacancies. Some of these point defects are trap-centers and some are electron/hole doping. The mechanism for RS may be the coupling of electronic and ionic phenomena **[74]**.

To date, the underlying physics of the key behavior of RRAM of electroforming (EF) and endurance is still not well understood. In some cases, varying EF process can significantly affect the characteristic of RS. Jeong *et al.* showed that the different histories of electroforming processes can result in very different RS behaviors-unipolar RS or bipolar RS **[202]**. While in other cases, e.g., TO/CMO binary metal oxide structure where TO is tunnel oxide and CMO is conductive metal oxide, EF process is not required **[203]**. The endurance,

one of the critical attributes for practical application of RRAM, is yet to be improved in many of M/MO/M devices. The role of the chemical reactivity of the electrodes is an important aspect of the working mechanism in these devices. It has been reported that for some MO materials, such as (Ba,Sr)TiO_3**[173]**, CuO_x**[204]**, $La_{0.7}Ca_{0.3}MnO_3$**[205]**, the endurance of a device with reactive-metal (RM) top electrode (TE) and a non-reactive metal (NRM) bottom electrode (BE), RM/MO/NRM, is quite different from that with NRM TE, NRM/MO/NRM. In these materials, the NRM/MO/BE devices were easy to fatigue in atmosphere, while weaker fatigue or no fatigue could be obtained in RM/MO/BE **[173, 204, 205].** Loss of oxygen into atmosphere in the NRM/MO/BE system is proposed to be the main reason leading to degradation of RS, while RM can prevent loss of oxygen into atmosphere **[173]**. RM electrode appears to improve the endurance.

The understanding of the physics of metal/metal-oxide junction and role of oxygen will be significant for us to finally hold the key to know the mechanism of RS. To do so, we comprehensively characterized RS in M/MO/M and found that the Gibbs free energy for oxidation of electrodes plays an important role in electrode effect. Our results suggest that the electrodes could be divided into two groups: reactive-metal vs. non-reactive-metal, where reactive-metal electrode has a lower Gibbs free energy for oxidation than metal-oxide, and non-reactive-metal electrode has a bigger Gibbs free energy for oxidation than the metal oxide. With microscopic probe of M/MO interface, we found that oxygen migration near interface is the central role in RS. In RM/MO interface, oxygen migration assistant oxidation/reduction is the main reason driving resistive switching, while oxygen vacancies redistribution in metal oxide plays an important role in NRM/MO junction. The enhancement

of resistive switching performance from reactive metal electrode is due to self limiting behavior of electrochemical redox.

6.2 Investigation of Resistive Switching in $Pr_{0.7}Ca_{0.3}MnO_3$ Thin Film

6.2.1 Categorization of Resistive Switching

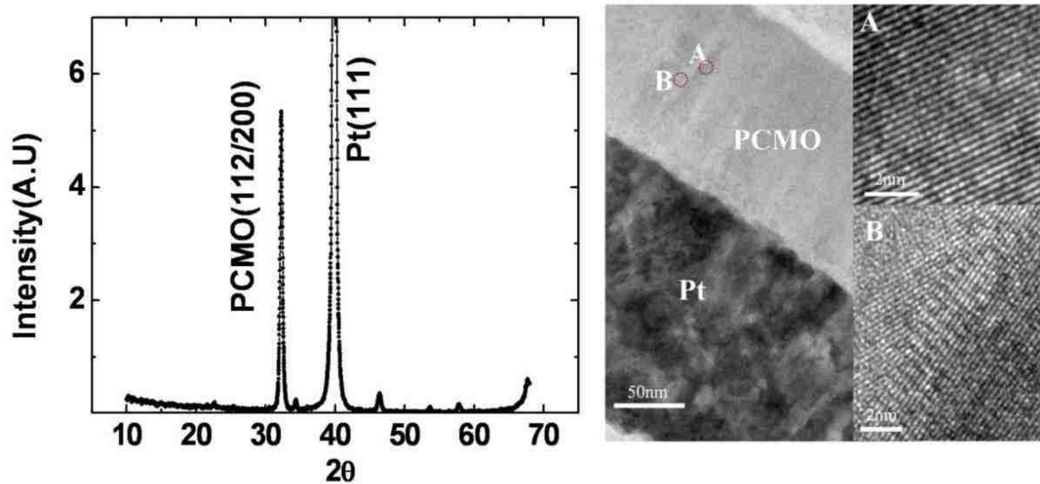

Figure 6-6: Left, XRD pattern of PCMO thin film; Right, TEM image of cross-section of PCMO/Pt and ZOOM-IN of A and B regions.

The PCMO film was fabricated on a 170 nm (111) orientated Pt buffer layer on a silicon wafer by a special low temperature (<400 ^{o}C) back-biased face-target-sputtering process which is compatible with CMOS process by 4DS company in Silicon Valley in USA **[78]**. X-ray Diffraction (XRD) θ-2θ profile of the film as shown in **Figure 6-6** confirms that the PCMO film was c-axis oriented, and HRTEM images revealed that the PCMO film was polycrystalline. Our experiment results show that the thickness of PCMO has less effect on resistive switching behavior and here we used 125 nm thick thin film as an illustration of resistive switching in PCMO.

The uniformity of devices was characterized by measuring hundreds of different devices on a same wafer. An array of electrodes as shown in **Figure 6-7a** was fabricated through standard lithography process. The I-V characteristics were measured on a probe station (see

Figure 6-7b). With our probe-station, we could easily switch the gold-tip from one device to another and effectively measure lots of devices quickly. The I-V sweep of Pt/PCMO/Pt devices and statistics of resistance of 100 different Pt/PCMO/Pt devices are shown in **Figure 6-8**. The I-V curve of Pt/PCMO/Pt is linear, indicating the Pt/PCMO contact is Ohmic. The mean resistance of Pt/PCMO/Pt devices is 43 Ω and its *Var root* is 10.3 Ω. Note that the resistance of Pt/PCMO/Pt device is only 43 Ω, indicating very low Pt/PCMO contact and PCMO bulk resistance. Based on this result, we can distinguish the role of TE/PCMO interface from bottom Pt/PCMO interface and individually investigate top interface.

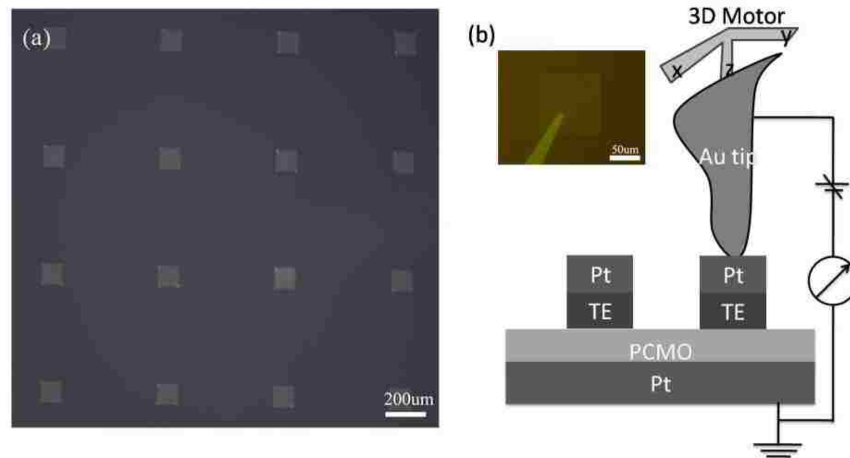

Figure 6-7: (a) Photo of square electrode array on PCMO (b) Schematic diagram of measurement of TE/PCMO/Pt with probe station and inset is the photo of gold-tip contacting electrode

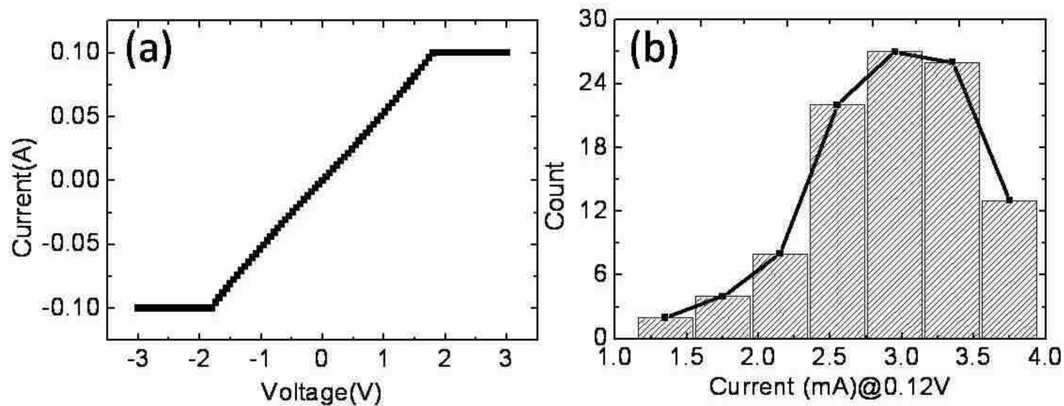

Figure 6-8: (a) I-V curve of Pt/PCMO/Pt devices. (b) Statistics of resistance of 100 hundred devices.

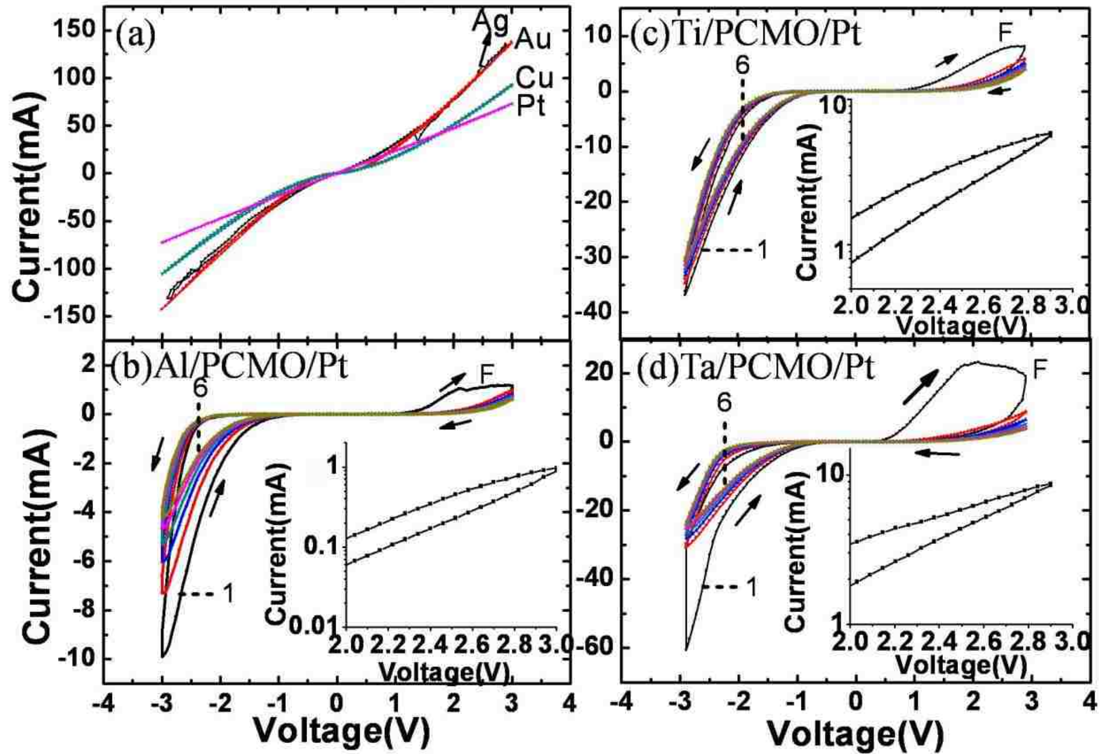

Figure 6-9: I-V characteristics for (a) Ag, Cu, Au, Pt/PCMO /Pt, (b). Al/PCMO/Pt, (c) Ti/PCMO/Pt, and (d) Ta/PCMO/Pt; The data was taken with bias looped from 0→3 V→-3 V→0. There are 6 consecutive loops for (b), (c) and (d), and label-1 marks the first loop, and 6 is the last. The size of the loop reduces progressively from 1 to 6. Label-F marks the forming process. Inset of (b), (c) or (d) shows the blow up of the hysteresis loop at positive bias.

Then we measure devices with different kinds of TEs. **Figure 6-9** shows the I-V characteristics of 7 different TEs on PCMO/Pt. Quite noticeably, large hysteresis loops at negative bias were present for Al/PCMO/Pt (**Figure 6-9b**), Ti/PCMO/Pt (**Figure 6-9c**), and Ta/PCMO/Pt(**Figure 6-9d**), while almost no hysteresis was observed in Ag (Pt, Au, Cu)/PCMO/Pt devices(**Figure 6-9a**). The I-V loop labeled "F" in **Figure 6-9(b-d)** is the "forming process", i.e. when a voltage is applied to the virgin state of a device and ramped above a threshold (1.8-2.5 V), resulting in a new physical state that exhibits hysteresis subsequently. There are 6 consecutive loops for each specimen (**Figure 6-9(b-d)**) and some degrees of fatigue of the size of the hysteresis loop (reducing from #1 towards #6) can be seen. However, after multiple bias sweeps, the I-V characteristics and the hysteresis become

repeatable. Quite interestingly, all devices made with non-reactive metal (Pt, Ag, Au, Cu) TEs do not display a similar "forming" and hysteresis characteristics. Note that the resistance of Pt/PCMO/Pt device is only 43 Ω, indicating very low Pt/PCMO contact and PCMO bulk resistance. In addition, the Pt/PCMO/Pt device does not show RS under I-V sweep up to ±3 V. Thus, the Pt BE should have a negligent effect on the overall measurement and data taken from devices made with other TEs should primarily reflect the effect of the TE materials.

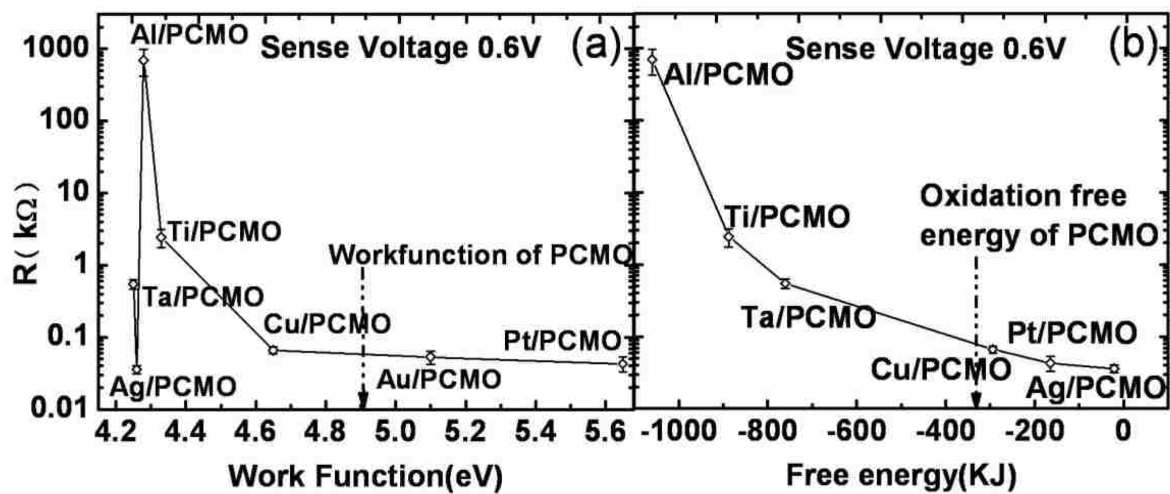

Figure 6-10: (a) Virgin resistance (VR) vs. workfunction. The data of each TE material is an average over 100 devices, and small error bars indicate that these devices are quite uniform. The dash line marks the workfunction of PCMO **[206]**. (b)VR vs. metal-oxide formation free energy taken from Refs.**[207, 208]**. The dash line at -366KJ/mol. indicates the oxidation free energy of PCMO from **[209]**.

Prior to the "forming process", the I-V characteristics in a small bias region below the threshold of all the devices are reversible regardless the TE material. The virgin resistance (VR) is a good measure of the contact resistance between the TE and PCMO. **Figure 6-10a** plots the VR against the workfunction of the TE material where the workfunction of PCMO (4.89 eV) is also marked **[206]**. Note that there is essentially no direct correlation between TE's workfunction and VR. On the other hand, VR for non-reactive-metal/PCMO/Pt is much less than VR of (Al, Ti, Ta)/PCMO/Pt. These observations suggest that the interface is not a

typical Schottky barrier formed by charge redistribution at the interface. For example, there is a large workfunction difference between Ag and PCMO (4.26 eV vs. 4.89 eV), but Ag/PCMO/Pt has a very low VR and linear I-V.

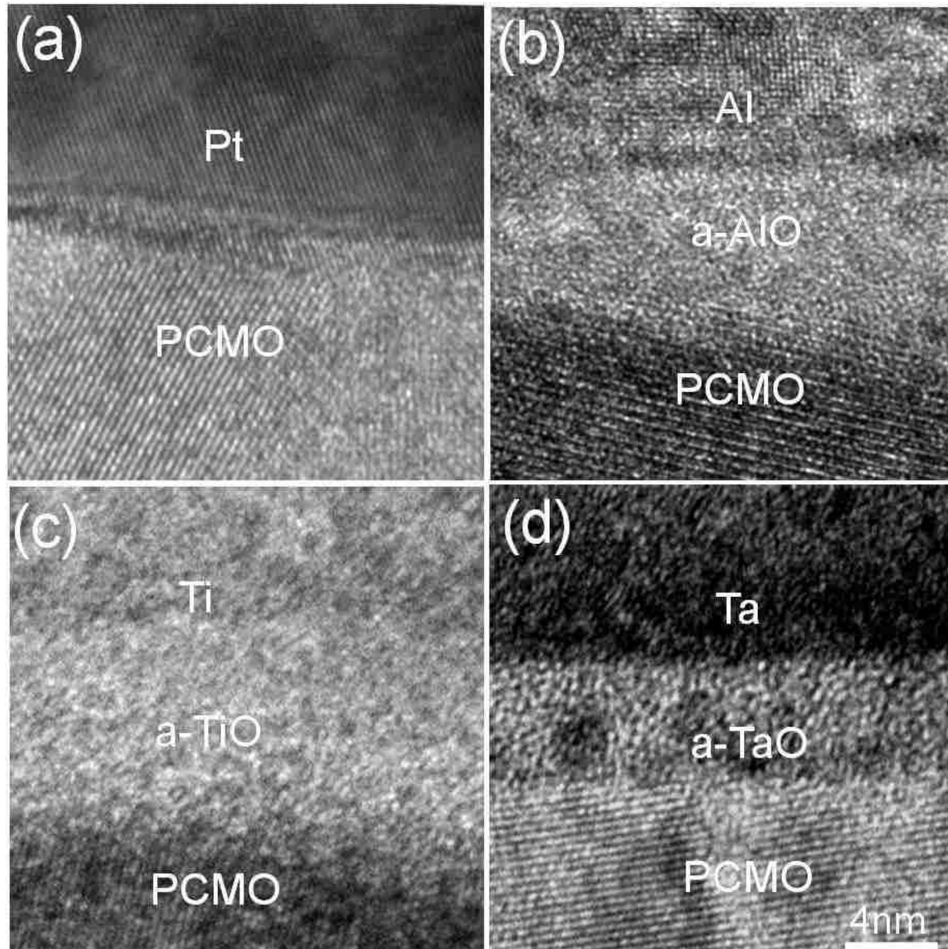

Figure 6-11: HRTEM images of interfaces between top electrodes and PCMO: (a) Pt/PCMO, (b) Al/PCMO , (c)Ti/PCMO and (d) Ta/PCMO. All figures have the same scale shown in (d).

To elucidate the above observations, HRTEM images of top interfaces of as-prepared samples of (Pt, Al, Ti, Ta)/PCMO were taken and are shown in **Figure 6-11(a-d)**. An amorphous layer was found in between (Al, Ti, Ta) and PCMO, but not in Pt /PCMO interface, or (Ag, Au, Cu)/PCMO interface (images not shown). Amorphous oxide layers at (Ta, Ti)/PCMO interfaces have also been confirmed using electron energy loss spectroscopy in two recent reports **[199, 200]**. The relative high VR is somehow associated with the presence of the interfacial metal oxide. **Figure 6-10b** plots VR vs. the oxidation free energy

of the TE material. It shows that the VR decreases with increasing oxidation free energies of TEs. Note that the oxidation free energy of PCMO falls between these two groups. Thus upon deposition, oxidation of the TE and reduction of PCMO at the interface will occur spontaneously for the active metal group (Al, Ti, Ta), but not for the non-reactive metal group (Pt, Ag, Au or Cu), resulting in dramatically different interfaces for the two groups.

To date, experimental findings on how various metal contacts on PCMO affect RS in a sandwiched-structure have yet to converge. Tsubouchi *et al.* **[198]** have surveyed a combination of TE/PCMO/BE where TE, BE are Mg, Ag, Al, Ti, Au, Ni, Pt, and concluded that only electrode pairs including at least one Al showed RS. Kawano et al. **[199]** and Shono *et al.*,**[200]** however, have found that both Ta/PCMO/Pt and Ti/PCMO/Pt exhibit bipolar RS with the former switching faster due to a thinner oxide layer. Sawa *et al.***[185]** studied TE/PCMO/$SrRuO_3$ devices (TE being Pt, Au, Ag and Ti) and found that only device with Ti electrode shows RS.

Combining these reports and the present results, we found quite remarkably that the TEs of the PCMO devices can be categorized into two groups, the non-reactive metal group vs. the reactive metal group, simply based on the relative oxidation free energy with respect to PCMO. They show dramatically different I-V and RS characteristics. It should be noted that there are reports that show RS in NRM/PCMO/Pt devices but with a reversed polarity of SET and RESET voltage compared with devices of reactive metal TE **[210, 211]** and hence do not contradict to the above categorization.

The inconsistent RS characteristics in NRM/PCMO/Pt may arise from a little variation of oxygen vacancies concentration and different electrode morphology. In fact, our experimental

results demonstrated that the electrode morphology can affect the RS. Take Ag/PCMO/Pt as an example in **Figure 6-12**, the Ag-film/PCMO/Pt, Ag-tip/PCMO/Pt and Ag-paste/PCMO/Pt have quite different characteristics of I-V sweep loops.

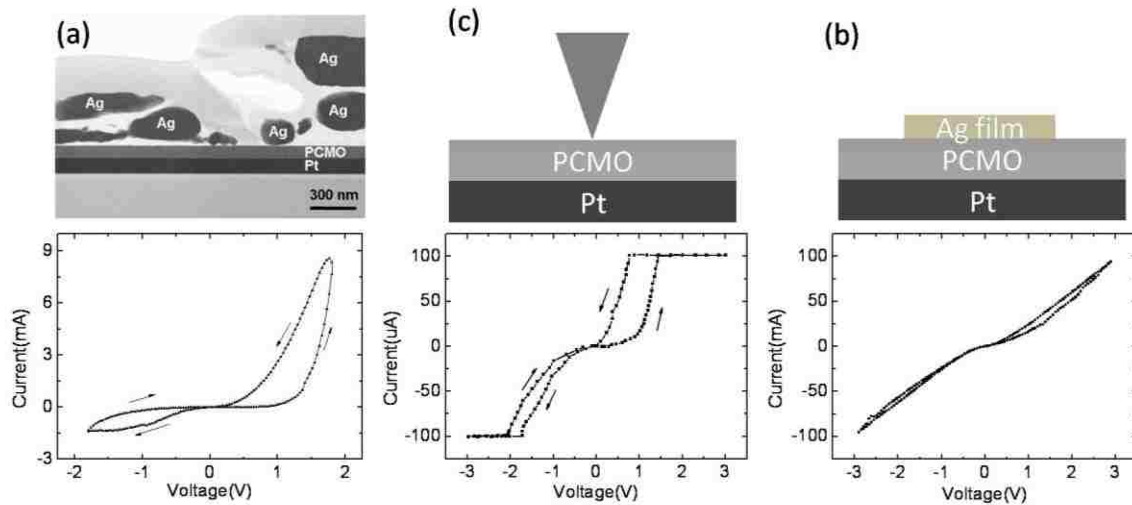

Figure 6-12: Scheme of devices and I-V characteristics for Ag-Paste/PCMO/Pt (a), Ag-tip/PCMO/Pt (b), Ag-film/PCMO/Pt (c). The Cross-section view of Ag-Paste/PCMO is referred from **ref. 212.**

In our experiments, both Ag-Paste/PCMO/Pt and Ag-tip/PCMO/Pt devices exhibit very strong RS behavior while Ag-film/PCMO/Pt devices show very weak hysteresis. The common feature of Ag-Paste/PCMO/Pt and Ag-tip/PCMO/Pt is that the electrode/PCMO actually is point contact. The Ag-Paste/PCMO/Pt cross-section revealed by TEM **[212]** is shown on top of **Figure 6-12a**, the Ag nanoparticles with diameters of 100 nm have a much smaller contact area with PCMO than Ag-film/PCMO. Ag-tip/PCMO was measured with conductive-AFM (the detail of measure with Ag-tip is described below). The Ag-film electrode with size of 100 μm × 100 μm was deposited on PCMO via magnetron sputtering, so it has atomically level good and large contact area. RS is possibly induced by local changes of oxygen vacancy concentration with electric field **[66, 213]**. As discussed in **Ref. [66]**, the oxygen concentration in PCMO can affect RS characteristics in Ag/PCMO/Pt. It can

also affect the sensitivity of migration to external electric field. No matter what, a strong electric field can more easily move the oxygen and cause resistance switching.

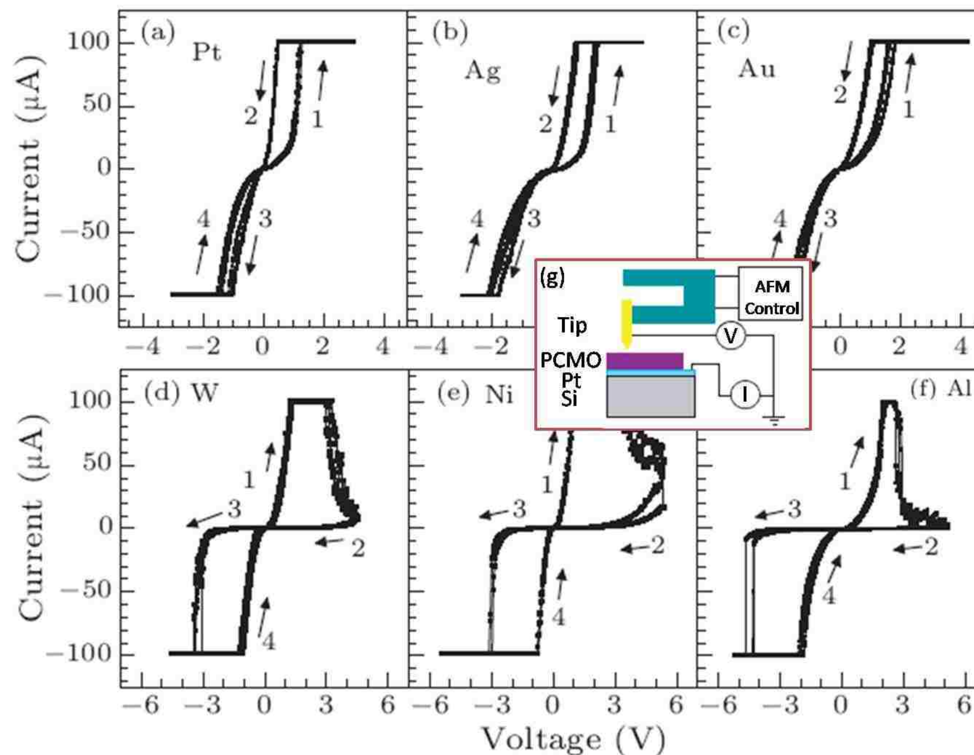

Figure 6-13: I-V characteristics for Pt(Ag, Au, W, Ni, Al)-tip/PCMO/Pt devices in (a)-(f). The schematic diagram of measurement with AFM is shown (g).

The RS mechanism of NRM/PCMO/Pt and RM/PCMO/Pt is likely different. With conductive AFM-tip, we could mount different kinds of tips and approach the tip to point contact with PCMO surface and then perform I-V sweep. **Figure 6-13** shows that the Pt (Ag, Au)-tip/PCMO/Pt share the same resistance switching direction (HRS->LRS under positive bias), and W (Ni, Al) has reversed direction (LRS->HRS under positive bias), further confirm the nature of categorization of RS in TE/PCMO/Pt revealed above.

6.2.2 Mechanism of Resistance Switching

Binary TMO sandwiched between two metal electrodes typically displays URS **[164, 165]**. More recently, Jeong *et al.* have discovered BRS for a Pt/TiO_2/Pt device by using a forming process at a lower current compliance (<0.1 mA), and attributed this BRS to an

electrochemical reaction mechanism in contrast to the filamentary model for the URS **[202]**. For TE/PCMO/Pt devices where the TE is a metal in the reactive group, only BRS has been reported to date, suggesting that the oxide layer and the oxygen deficient PCMO region both play the critical roles. Resistivity for bulk PCMO is 10^{-1} to 10^{-2} Ω cm **[214]** at room temperature while that for a thin film PCMO is 10^{3} to 10^{4} Ω cm due to lower oxygen concentration **[185]**. Our Pt/PCMO/Pt device has a resistivity of ~$3.4x10^{2}$ Ω cm. The resistivity of the LRS of the devices with reactive group TEs is also on the same order (see **Figure 6-9**). This implies that the resistance of the oxide layer at LRS is rather small, but becomes dominant at HRS. Oxygen vacancies in TiO_2 are known to be n-type dopants, V_O^{2+}, which transform a stoichiometric TiO_2 from insulating into semiconducting **[215].** The as-fabricated device has abundant V_O^{2+} in the TiO_{2-x} layer at the Ti/PCMO interface (**Figure 6-11c**) and hence its VR is in LRS. A positive voltage applied to the TE will drive the V_O^{2+} in the Ti-oxide toward PCMO layer and oxidation of Ti-oxide region causes the switching to HRS. When a negative bias is applied to TE, most of the applied voltage will then drop across the oxide layer resulting in a large local electrical field which attracts V_O^{2+} from PCMO towards Ti-oxide, and the reduction of the Ti oxide layer causes a switching back to the LRS. The fatigue on the hysteresis loops shown in **Figure6-9(b-d)** hence reflects the imbalance between oxidation and reduction during the initial cycles of switching.

The above model can be extended to devices made with other TEs in the reactive metal group. While these TEs can be readily oxidized at room temperature (RT) as long as the oxygen ion migration is facilitated by the electrical field, reduction of TEs at RT, however, may need further assistance of local Joule heating to overcome the energy barrier for

disassociation. For a given SET voltage, the degrees of reduction of the TEs are inversely scaled to the Gibbs free energy. During the SET and RESET, the oxygen deficient region of the PCMO acts as a reservoir for storing and supplying oxygen ions. Although the resistivity of PCMO also changes as the oxygen concentration varies, it is much smaller than the change of resistance in the oxide layer. For devices made with TE in the non-reactive metal group, the absence of the metal oxide layer can explain why no appreciable I-V hysteresis was observed, even though oxygen vacancies may still be shuffled between TE and BE and some degrees of oxidation/reduction at the opposite side of the PCMO may still occur. Sawa *et al.* have proposed that SET and RESET create two levels of defect states at the interface which trap different amount of charges and hence create two types of Schottky barriers **[185]**. The draw-back of this model is its inability to naturally account for the categorization of the electrode materials shown above.

We have shown that the contacting material of the TE in a TE/PCMO/Pt thin-film device plays a critical role in determining the device's I-V characteristics. In particular, we have found that metal-PCMO-Pt devices can be categorized into two groups based on whether the Gibbs free energy for oxidation of the TE is greater or less than PCMO oxidation free energy. Our result suggests that interface redox based RS phenomena has less relation with work function, but much determined by Gibbs free energy of oxidation. Herein, We can get a universal physics model for RS in TE/PCMO/Pt as shown in **Figure 6-14**. For RM/PCMO, the actual structure will be RMO/PCMO/Pt. Oxygen migration assistant oxidation/reduction under external electric field is the origin of RS observed in RMO/PCMO/Pt, while pileup of oxygen vacancies near NRM electrode causes the RS in NRM/PCMO/Pt.

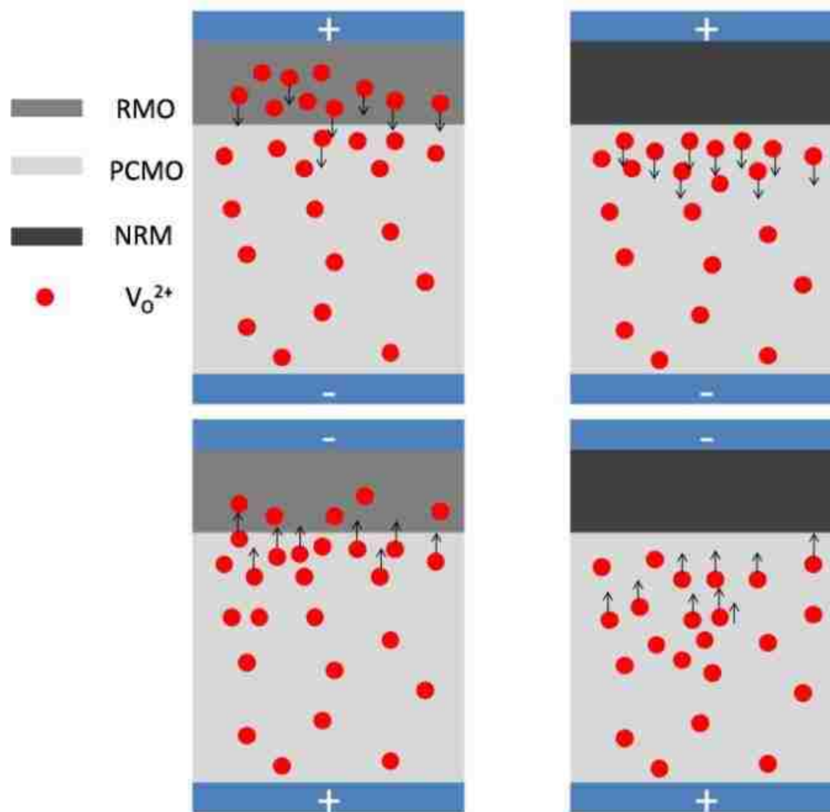

Figure 6-14: Scheme of mechanism of resistance switching in Electrode/PCMO junction. Left, oxygen migration induced interfacial oxidation/reduction. Right, oxygen pileup near non-reactive metal electrode under external electric field.

6.2.3 Self-limiting of Redox at Reactive-Metal/$Pr_{0.7}Ca_{0.3}MnO_3$ Junction

RM seems to enhance the RS in RM/PCMO/Pt devices. To reveal underlying physics, we investigated the electroforming and endurance behavior of Al/PCMO with Al served as typical RM. We used the same PCMO thin film as discussed in **6.2.1**. In order to prevent oxidization of Al TE, the Al film of ~ 3 nm deposited on the as-grown PCMO thin film was capped with 90 nm Pt by magnetron sputtering at room temperature. An array of 200 μm × 200 μm electrodes was subsequently patterned by a standard photolithography and reactive ion etching technique. All patterned devices were made to have the same thicknesses for the material stack. The electrical properties of the devices were characterized by means of *I-V* sweep using Keithley-2400 with Pt BE being grounded.

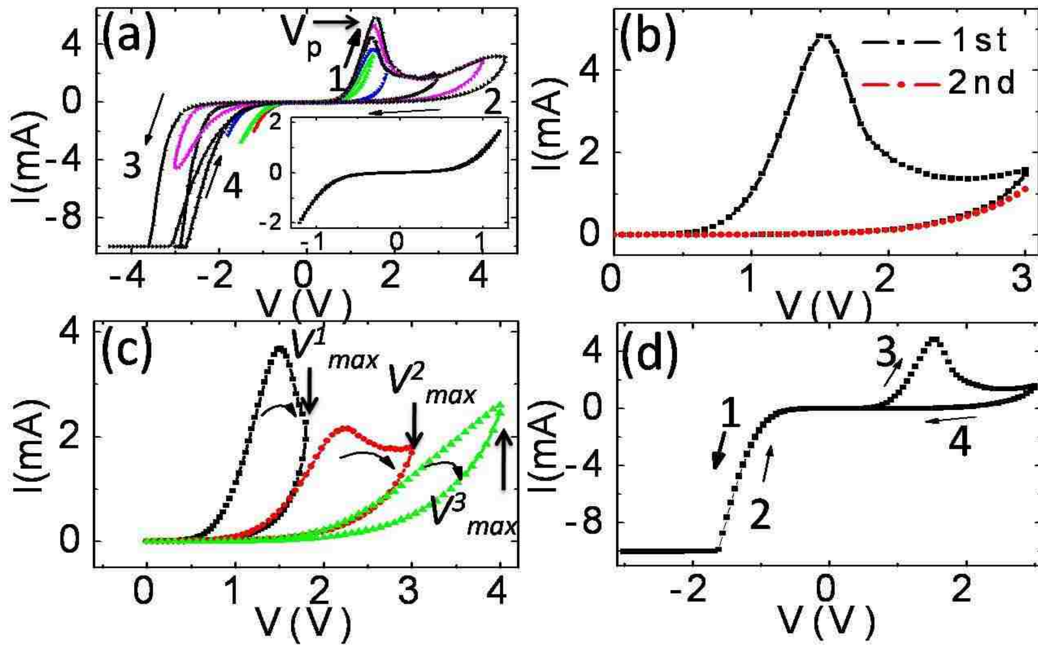

Figure 6-15: RS characteristics of the Al/PCMO/Pt memory devices: (a) The electroforming with different sweep voltages with the inset showing no hysteresis when $V < 1.5$ V; (b) Consecutive *I-V* sweep loops ($0 \rightarrow V_{max} \rightarrow 0$) $V_{max} = 3$ V; (c) Sequential I-V sweep loops ($0 \rightarrow V_{max} \rightarrow 0$) with $V_{max} = 1.8$ V (black), 3 V (red), 4 V (green); and (d) *I-V* sweep loop ($0 \rightarrow$ $-3V \rightarrow 3V \rightarrow 0$). Arrows and number indicate sweep direction and sequence.

Figure 6-15a presents the first electroforming (EF) *I-V* curves of different Al/PCMO/Pt devices with several maximum voltages, $0 \rightarrow +V_{max} \rightarrow -V_{max} \rightarrow 0$, respectively. The *I-V* curves exhibit hysteresis only when V_{max} reaches a threshold value. As shown in the inset of **Figure 6-15a**, no *I-V* hysteresis has been observed for $V_{max} \leq 1.2$V. Through the extrapolation of our data, this threshold voltage for effective EF is found to be ~ 1.5V which is directly related to the current peak position ($V_p = 1.5$ V) in the I-V loops [see **Figure 6-15a**], reflecting the presence of an activation barrier for EF. In order to gain more insight into the EF as well as RS behavior, we applied only positive sweep loops ($0 \rightarrow V_{max} \rightarrow 0$) successively with gradually increasing V_{max} for a given device. First we notice that after the initial EF at a V^1_{max}, subsequent positive voltage sweep loop does not exhibit hysteresis for $V_{max} \leq V^1_{max}$ (the red curve overlaying the return trace of the 1st I-V in black in **Figure 6-15b**).

However, hysteresis reappears when the V_{max} exceeds V^1_{max} and increases sequentially to V^2_{max} and V^3_{max} (see **Figure 6-15c**). Furthermore the threshold voltage of EF (V_p) increases with each additional cycle of voltage ramp at higher V_{max} than its previous cycle, indicating that the resistance state or RS barrier can be tuned with maximum EF voltage. On the other hand, for an as-fabricated device if the initial sweep voltage polarity is reversed to 0 → - 3V → 3V → 0, there is no I-V hysteresis at negative bias as shown in **Figure 6-15d**. When the negative applied voltage is increased further by removing the current compliance, a permanent breakdown due to large joule heating will occur. Therefore, we concluded that EF only occurs in the initial positive bias ramp for Al/PCMO/Pt devices.

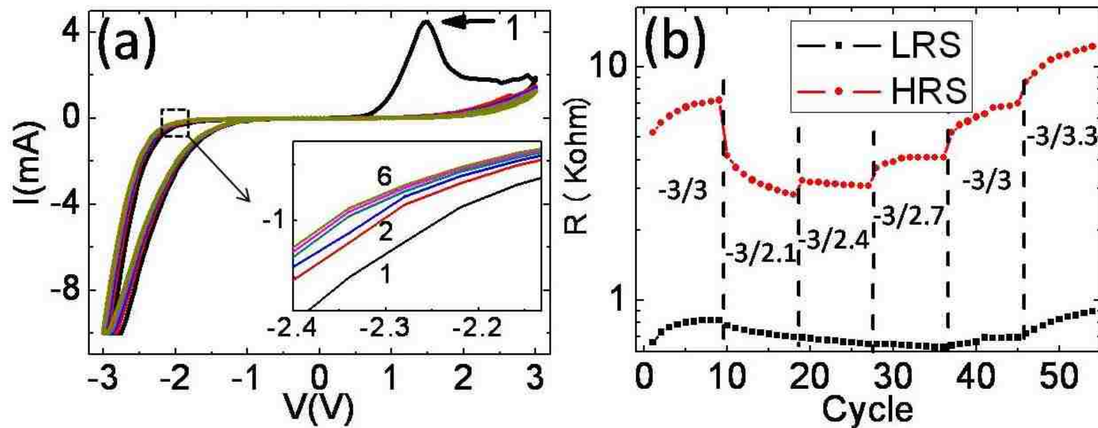

Figure 6-16: (a) Consecutive *I-V* sweeps after electroforming with V_{max} = 3.0 V. Inset shows the zoom-in of the marked region of *I-V* curves of 6-sequencial loops. Label-1 marks the first loop (EF). (b) 6 groups of HRS and LRS are distinguished by the vertical dash line and the corresponding sweep parameter $V^{(-)}_{max}/V^{(+)}_{max}$ is indicated for each group. Resistance state was read at V_r=- 2.1 V.

For a given device, RS behavior is uniquely determined by the EF process. As long as the switching voltage does not exceed the maximum EF voltage (V_{max}), the device can be cycled between SET (from a high resistance state (HRS) to a low resistance state (LRS)) and RESET (from LRS to HRS) (see **Figure 6-16a**). As shown in **Figure 6-16a** for a device with EF at V_{max} = 3.0 V, some degrees of fatigue are evident as the hysteresis loop changes during the

initial cycles, reflecting the imbalance between SET and RESET processes. However, after few initial cycles of SET/RESET, the *I-V* hysteresis loop becomes repeatable, clearly indicating that the device reaches a new balance between SET and RESET.

The above device characteristics that EF only happens in positive bias which RESET a device from a LRS to various HRS depending on the amplitude of the EF voltage and that a large negative bias can SET the device back to a LRS allow us to tune the HRS and LRS for multilevel RS simply by changing the SET voltage $V^{(-)}_{max}$ (at negative sweep, $0 \rightarrow V^{(-)}_{max} \rightarrow 0$) and RESET voltage $V^{(+)}_{max}$ (at positive sweep $0 \rightarrow V^{(+)}_{max} \rightarrow 0$). For example, we successively swept the device (i.e., $0 \rightarrow V^{(+)}_{max} \rightarrow V^{(-)}_{max} \rightarrow 0$) with different ratios of $V^{(-)}_{max}$ / $V^{(+)}_{max}$ after a single EF and then recorded the resistances of both HRS and LRS at a read voltage $V^{(-)}_{max} < V_r < 0$. **Figure 6-16b** shows the data for 6 sets of $V^{(-)}_{max}$/ $V^{(+)}_{max}$ with 9 sweeps carried out for each and the HRS and LRS recorded at V_r = - 2.1 V. The first sweep, -3 V/3 V is the initial EF. For each $V^{(-)}_{max}$/ $V^{(+)}_{max}$, the resistances settle to stable values after several cycles of voltage sweep, indicating that the device is able to quickly reestablish a balance after it being set to a new level. These results suggest that the working resistance states can be tuned sequentially and effectively for these devices.

As discussed in 6.2.1, the Al/PCMO interface dominates the RS characteristics. To reveal the nature of the interface, we have investigated the cross-section structure of Al/PCMO/Pt with high resolution transmission electron microscopy (HRTEM). Interestingly, HRTEM image reveals a ~ 4.7 nm thick amorphous layer [see **Figure 6-17a**] at the interface between Al and 125 nm thick PCMO film. We further examined a 19 nm thick PCMO film capped with the same thickness of Al layer and found no change in the thickness of amorphous layer

[see **Figure 6-17b**]. Comparing with the same thickness of PCMO film capped with a glue layer of **Figure 6-17c**, it is clear that a portion of the PCMO layer should become amorphous

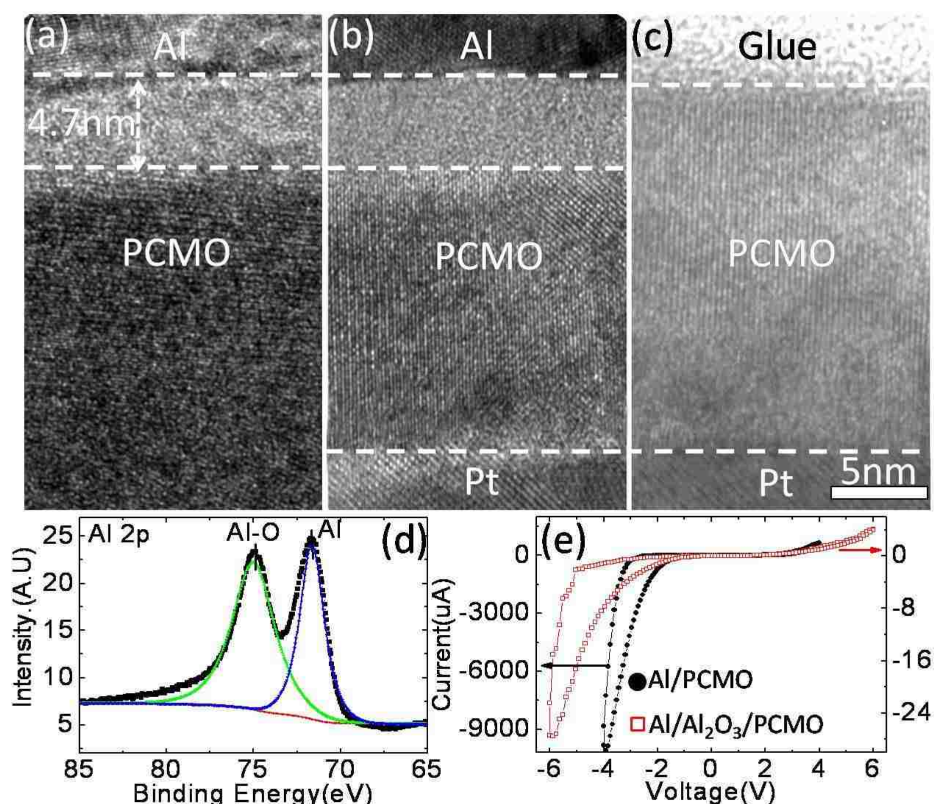

Figure 6-17: HRTEM images (with the same scale bar) of Al/PCMO/Pt device cross section: (a) 125 nm thick PCMO; (b) 19 nm thick PCMO. (c) HRTEM image of 19 nm thick PCMO without Al layer. (d) XPS spectra of Al 2p core level showing distinct oxidization state. (e) *I-V* characteristics for electroformed Al/PCMO/Pt (black curve) and as fabricated Al/Al_2O_3/PCMO/Pt (red curve).

(α-PCMO) after Al capping. In addition, X-ray photoelectron spectroscopy (XPS) of the Al 2p level taken near the Al electrode (**Figure 6-17d**) shows both metal Al 2p (at ~ 72 eV) and oxidized Al 2p (~ 75 eV) peaks, suggesting partial oxidization of Al electrode and formation of $Al_2O_{3-\delta}$ at the interface. Yasuhara *et al.* **[216]** also reported a similar observation and suggested that a ~1 nm thick $Al_2O_{3-\delta}$ layer was formed at the Al/PCMO interface. Thus the structure of our device is actually Al/$Al_2O_{3-\delta}$/α-PCMO/PCMO/Pt. It is suggested that the formation of the α-PCMO layer is the consequence of the loss of oxygen to the top reactive electrode **[199]**. From the relative thickness of 1 nm Al_2O_3 vs. 4nm α-PCMO, the oxygen

vacancies concentration in the α-PCMO is estimated to be ~34%. Therefore, the spontaneous formation of oxygen-deficient $Al_2O_{3-\delta}$ and α-PCMO at the interface is the essential aspect of this device.

The oxygen migration at the Al/PCMO interface and the redox reaction of the interface layer are thus critical for the RS in Al/PCMO/Pt devices. The *oxidation* (RESET) of the Al electrode, extraction of oxygen ions from PCMO under positive bias, and its *reduction* (SET), migration of oxygen ions from $Al_2O_{3-\delta}$ back to PCMO under negative bias, occur alternatively at the Al/PCMO junction forming the characteristic RS. The thickness of $Al_2O_{3-\delta}$ may change, but the secondary-ion mass spectrometry analyses indicate that oxygen migration mainly changes the relative oxygen content in $Al_2O_{3-\delta}$ **[217]**. In general, the SET and RESET should be asymmetric since oxidation is much easier in aluminum oxide than its reduction. However the resistance of $Al_2O_{3-\delta}$ will increase during RESET, such that more voltage drops across $Al_2O_{3-\delta}$ layer and less across PCMO.As a result it is harder for oxygen ions to migrate from PCMO to $Al_2O_{3-\delta}$,, and further oxidation in $Al_2O_{3-\delta}$ becomes limited **[218]**. On the other hand, during SET, the large initial voltage drop on in $Al_2O_{3-\delta}$ will facilitate oxygen migration from $Al_2O_{3-\delta}$ into PCMO, but reduction of $Al_2O_{3-\delta}$ becomes harder as the layer becomes more conductive with increasing oxygen vacancies. There is no quantitative data yet on the redox reaction kinetics of $Al_2O_{3-\delta}$/PCMO interface. However, for perovskite $SrTi_{1-x}Fe_xO_{3-\delta}$, Steinsvik et al. **[219]** found that the activation enthalpy for annihilation of oxygen vacancies decreases from 2.0 eV to - 0.2 eV with δ increasing from 0 to 0.4. In other words, it will be increasingly difficult to create oxygen vacancies (reduction) in a sample with a higher degree of oxygen deficiency. Likewise for $Al_2O_{3-\delta}$ the degree of

difficulty in oxidization (or, reduction) will decrease (or, increase) with increasing δ. Therefore, both the electric field distribution and the kinetics of the redox reaction at the interface naturally self–limit the process and create the balance between SET and RESET.

Based on the above scenario, the EF and the SET/RESET cycles can be qualitatively understood. To drive oxygen migration between PCMO and $Al_2O_{3-\delta}$ and cause reduction/oxidation, the electric field should overcome the kinetic barrier of interface reduction/oxidation. Initially, because of rich oxygen vacancies in the $Al_2O_{3-\delta}$ layer, oxygen ions incline to migrate to the $Al_2O_{3-\delta}$ from PCMO, thus EF occurs at positive bias. The activation barrier increases as the oxygen vacancies in the $Al_2O_{3-\delta}$ layer are depleted with successive EF, hence the current peak shifts to higher bias in **Figure 6-15c.** Furthermore, the SET/RESET balance will depend on the history of relative oxygen vacancy concentration between $Al_2O_{3-\delta}$ and PCMO. For each SET/RESET parameter, $V^{(-)}_{max}$/ $V^{(+)}_{max}$, the device can adjust the relative level of oxygen concentration by the self-limiting process at the interface through a few SET/RESET cycles and eventually reach a new balance as shown in **Figure 6-16b**.

To further test the above mechanism, we have deposited a 3 nm stoichiometric Al_2O_3 layer on the top of PCMO by atomic layer deposition at 250 ^oC. Indeed the as fabricated Al/Al_2O_3/PCMO/Pt devices can yield reproducible RS without EF as shown in **Figure 6-17e**. The Al/Al_2O_3/PCMO/Pt devices exhibit similar *I-V* hysteresis to that of electroformed Al/PCMO/Pt ones, but require larger negative bias to SET (reduce) Al_2O_3 due to more stable initial phase of Al oxide. The better insulation and fewer oxygen vacancies in the Al_2O_3 layer also result a much larger resistance of Al/Al_2O_3/PCMO/Pt than that of Al/PCMO/Pt device.

In summary, we have revealed important characteristics of the EF and RS of Al/PCMO/Pt devices. The redox reaction at the interface between reactive Al electrode and PCMO layer plays a key role in the EF and RS. In particular, a self-limited field-induced oxygen migration leads to a balance between oxidization/reduction during SET/RESET cycles. Our results demonstrate the advantage of using a reactive metal electrode for improving the functionality of the metal oxide based memory devices.

6.2.4 EPIR Performance in Reactive-Metal/$Pr_{0.7}Ca_{0.3}MnO_3$/Pt Devices

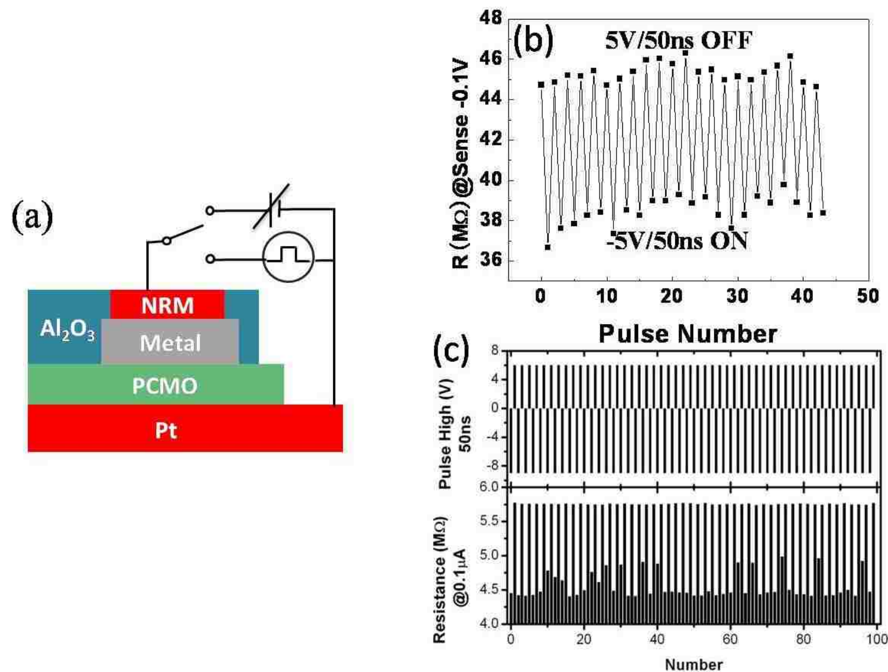

Figure 6-18: (a) Scheme of devices and measurement setup. (b) Resistance switching under pulsed cycles for (b)Ti/PCMO/Pt device and (c) Ta/PCMO/Pt devices

The reactive metal enhances the RS especially the endurance behavior. Our PCMO thin film with top reactive metal electrode exhibits good EPIR effect. To measure the EPIR effect, we use Agilent 8110A to provide variable voltage pulse and Keithley 2400 to measure resistance at low voltage or current in case that read process changes the resistance. A switching circuit is developed to switch between read and programming. A scheme of EIPR measurement is shown in **Figure 6-18a**. EPIR in Ti/PCMO/Pt and Ta/PCMO/Pt devices are

displayed in **Figure 6-18b and c respectively**. The pulse width is 50 ns and amplitude of the pulse is ~5 V. It guarantees the high speed of programming, indicating that RM/PCMO/Pt can be a promising candidate for RRAM.

6.2.5 Dynamic Visualization of Oxygen Migration and Diffusion with *in-situ* TEM

Both the interface oxidation/reduction and oxygen pileup require the motion of oxygen. The Direct imaging of oxygen migration and diffusion would be significant for understanding the motion of oxygen in metal oxide, and it will guide us to build up oxygen motion based next generation metal oxides multifunctional electronics with application ranging from sensors and memory to logic circuit. *In-situ* electrical field Transmission Electron Microscopy (TEM) can locally investigate structural and chemical information during resistance switching. We chose $Pr_{0.7}Ca_{0.3}MnO_3$ (PCMO) as a demonstration to use *in-situ* TEM technique to present evidence of dynamic oxygen vacancies migration and diffusion, and its coupling to resistance switching. Strong correlated PCMO is a typical resistance switching material in which many papers present evidence for the oxygen migration and diffusion **[66, 198-201, 213]**. However, microscopy real time view is absent. The oxygen vacancies content would vary mix of divalent (Mn^{4+}) and trivalent (Mn^{3+}) manganese ions, which is a key parameter in manganite materials. Here, we report a dynamic evolution of stripes during both applying electric field and after termination of electric field. These results indicate electric field induced migration and oxygen vacancies concentration gradient induced oxygen vacancies diffusion behavior. Our results provided a microscopic image of coupling of oxygen vacancies and physics properties and bring benefits to research of metal oxide based electronics.

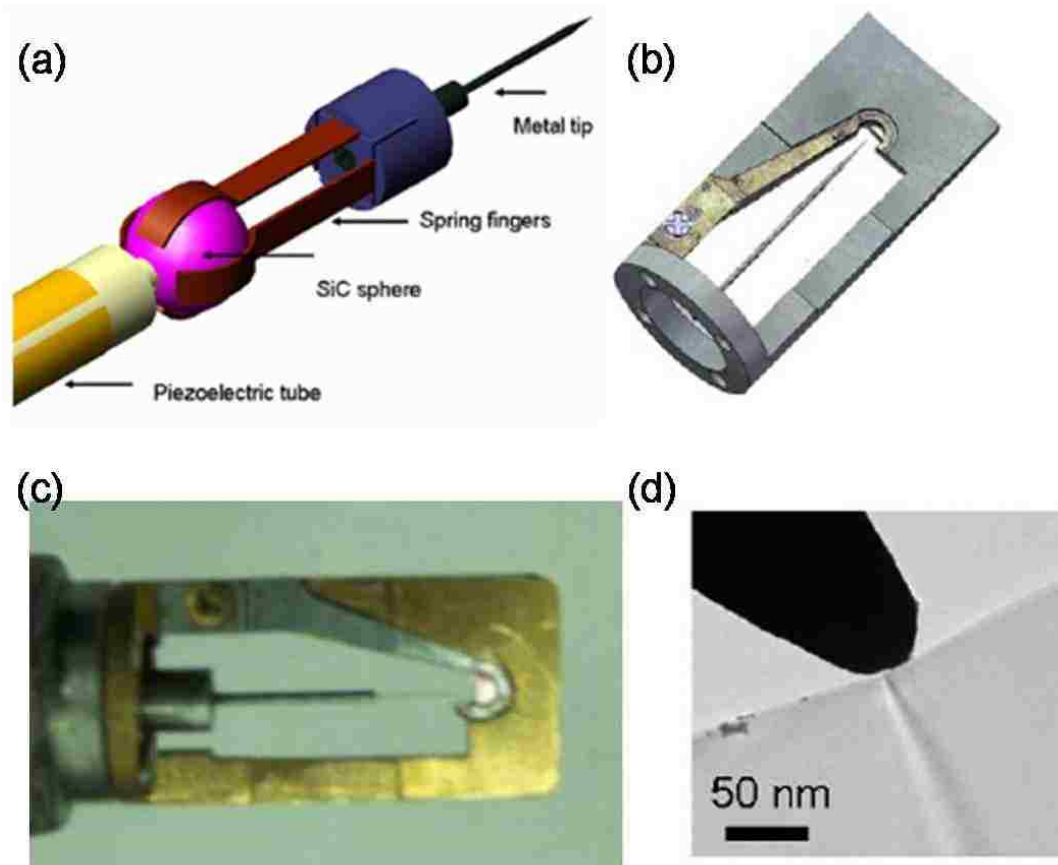

Figure 6-19: (a) Draft of SPM inside TEM, (b) TEM specimen holder, (c) Photo of the holder with SPM-tip and TEM specimen, (d) TEM image of Au-tip/Si contact.

A home-made integrated scanning probe microscopy (SPM)-TEM system was used to perform the *in-situ* measurement **[220]**. A 3D piezomotor as shown in **Figure 6-19a** was integrated into TEM sample holder. To *in-situ* measure thin film, a thin film TEM specimen head was designed (**Figure 6-19b**). The photo of specimen holder and TEM image of one in-situ device are shown in **Figure 6-19d**. A sharp tungsten-tip (W-tip) was used as SPM tip which can be finely approached to specific position of specimen with navigation of JOEL 2010F operating at 200 kV. To enable the W-tip to contact the PCMO, we chose the TEM specimen that has some parts of the PCMO without being covered with glue for tip contact. Furthermore, we cut off the copper grid in a way as shown in **Figure 6-20** schematically to allow the tip to approach the specimen. Then the setup with the PCMO sample was mounted

to the SPM-TEM sample holder and put into our TEM system. The bottom Pt layer was grounded through copper grid and the W-tip was used as the other electrode, so that the W-Tip/PCMO/Pt formed a two terminal device inside TEM. The I–V characteristics were measured with a Keithley 2400 sourcemeter. The constant voltage was also provided by Keithley 2400. The measurements with simultaneous TEM imaging were performed at room temperature.

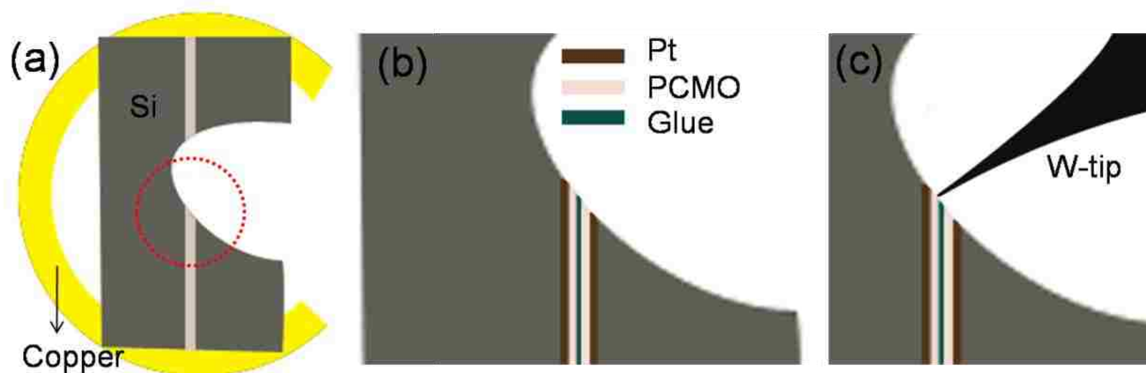

Figure 6-20: (a)Schematic figure of cross-section specimen. (b) enlarged picture of cross-section structure as indicated in (a). (c) Schematic diagram for W-tip/PCMO Contact.

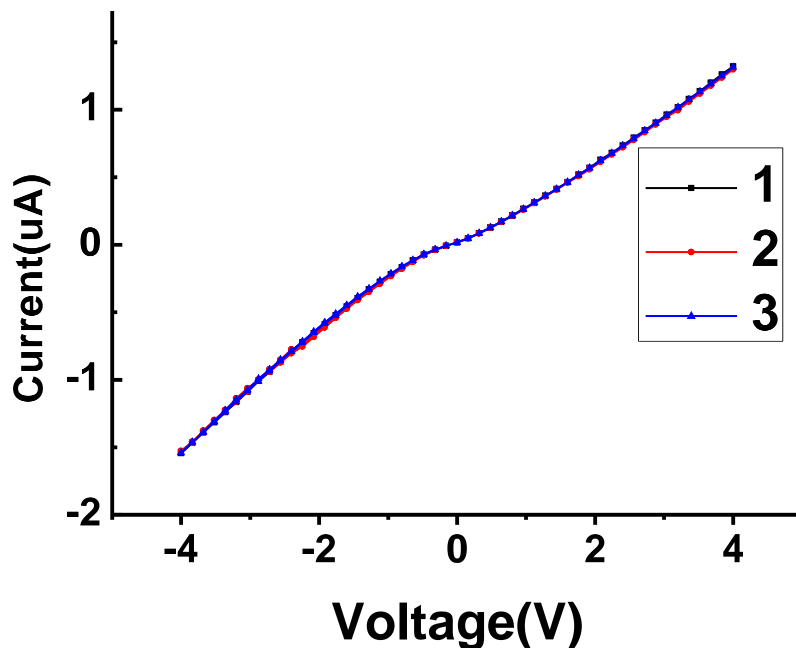

Figure 6-21: I-V characteristics for W-tip/Si/Pt device. Three I-V curves were taken every one minute. The I-V curves show a very excellent repeatability.

The cross-section TEM specimen of PCMO thin film was first prepared by mechanical grinding and dimpling to ~ 1 μm thick at the center; then mounted to copper grid by using silver epoxy connecting the Pt to copper grid; and finally milled with 4-5 keV argon ion beam to be thin enough for TEM investigation. The thinnest area of the TEM specimen was ~ 30-100 nm thick.

The mechanical stability of the SPM tip was tested first by using Au-tip/Si-film contact. We made the Au-tip contact Si film whose high-solution-TEM (HRTEM) image can be observed and performed current-voltage (I-V) sweep. Three I-V curves taken every one minute repeated very well (see **Figure 6-21**), indicating very good and stable Au-tip/Si contact and very stable mechanical stability of Au-tip.

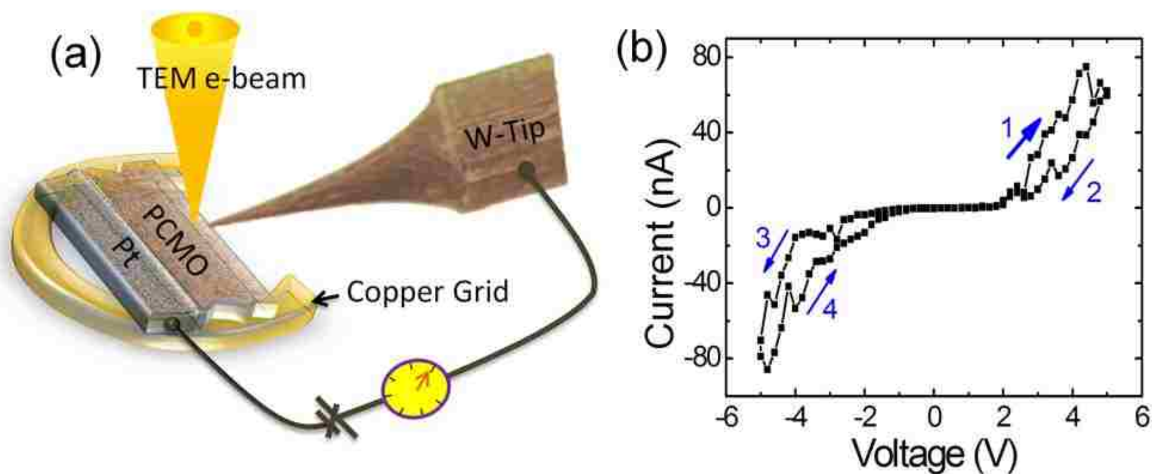

Figure 6-22: A schematic view of the *in-situ* TEM characterization setup. The W-tip is controlled by a 3D piezomotor and Pt electrode is grounded. The SiO_2/Si substrate is not shown. (b) An *I-V* sweep loop (0→5V→-5V→0) for W-tip/PCMO/Pt device measured inside TEM. The sweep sequence is 1→2→3→4.

With such a setup, we were able to perform simultaneously TEM characterization to investigate the electric-field-driven structural evolution of devices. **Figure 6-22** shows the characteristic I-V sweep loop of W-tip/PCMO/Pt setup, evident for the bipolar RS character. Under positive bias the system changes from low resistance to high resistance state. This is

also confirmed by our independent conductive Atomic Force Microscopy (AFM) measurement on similar implemented W-tip/PCMO/Pt setup as shown in **Figure 6-13**.

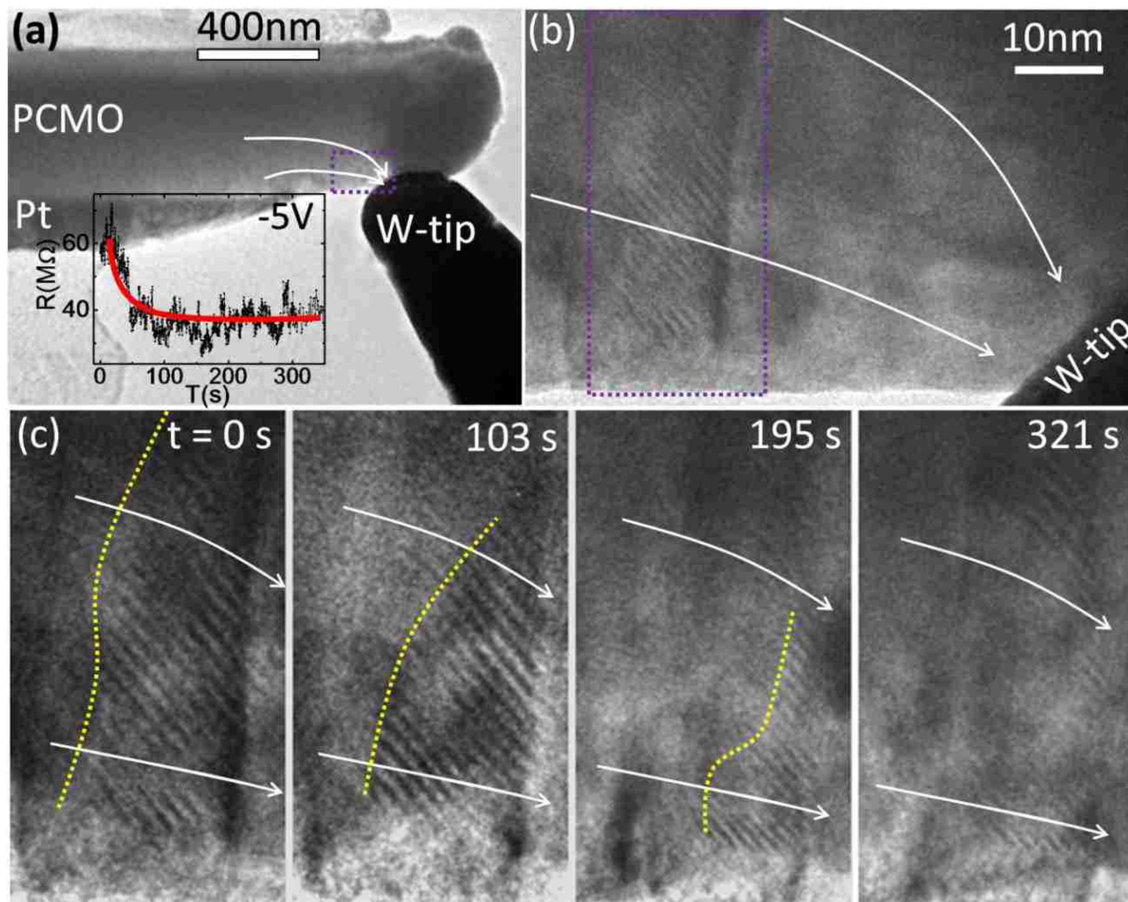

Figure 6-23: (a) A TEM image of W-tip/PCMO/Pt devices. Inset is the resistance of the device versus time under -5 V bias and the thick solid line curve is used to shows the trend. (b) A zoom-in image of the selected region of the PCMO film marked in (a). (c) A zoom-in and time-dependent image of selected region marked in (b) under the electric field applied through the W-tip. The field intensity is estimated ~ 9×10^6 V m^{-1}. The dot curves sketch the boundary of stripe domain. The white arrows indicate the electric field directions. An electron energy of 200 keV was used for TEM imaging.

The characteristic I-V hysteresis of W-tip/PCMO/Pt has been explained by the oxygen migration assisted interface oxidation/reduction of WO_x as discussed in section **6.2.2**. If the oxygen migration is the case to drive RS, it should cause a local structural distortion along the migration path. To monitor the structure evolution in real time, we applied a constant bias to W-tip and then took a TEM image every ~1.0 second. The TEM image of W-tip/PCMO/Pt is shown in **Figure 6-23a**. The thickness of PCMO along the TEM electron beam direction is

estimated to be less than 100 nm. The contact area between W-tip and PCMO is estimated about 100 × 100 nm^2 and the distance from W-tip to the nearest part of the bottom Pt electrode is about 550 nm. **Figure 6-23b** presents the zoom-in image of the region close to the W-tip before applying electric field. A stripe-ordered region with a spacing period of stripes of ~ $3\,d_{(001)_P}$ (P means primitive in pseudo cubic phase, so as to following text) is clearly revealed in the zoom-in image. We also observed similar stripe domains but with different stripe spacings. As we will discuss in the following, such a modulation stripe has been interpreted as an ordering of oxygen vacancies, where the stripe spacing depends on the local density of oxygen vacancies which exist in the film intrinsically **[221]**.

Interesting, both the structural modulation and the consequent electric transport can be tuned by applied external field. The resistance of the device versus time after applying a sample bias voltage of -5 V is shown in inset panel of **Figure 6-23a**. The large noise observed in R vs. T curve is due to instability at the in-situ mechanical contact between W-tip and the PCMO thin film. The electric field can be roughly estimated as E = ~ 9 × 10^6 V m^{-1}. The resistance decreased with time and started to saturate after ~ 50 s. A structure evolution near the tip was visualized simultaneously during applying the electric field. **Figure 6-23c** displays a series of time-dependent images of structural modulation after applying the bias voltage. The boundary of the striped area indicated by a dashed yellow line gradually moves along the electric field direction. The stripes moved close to the tip and gradually faded away with time. After about 321 seconds, the stripes were almost diminished. Therefore, we directly observed for the first time an electric-field-induced migration and evolution of stripes in PCMO film, which is correlated with the evolution of the device resistance.

In order to exclude the possible electron irradiation effect on the observed change of local structure, we monitored possible structure change of PCMO after half an hour of strong electron irradiation with a dose of ~ 2×10^{6} electrons $\cdot$Å^{-2} at a magnification of 500 k. We found no change of structure with such irradiation treatment. We also checked whether the structure change could be due to the stress from the W-tip contact. We found no change in structure in the TEM image with contacting W-tip but no applied bias. Thus we conclude that the observed structure evolution in PCMO film (see **Figure 6-23**) is solely due to the effect of the electric field.

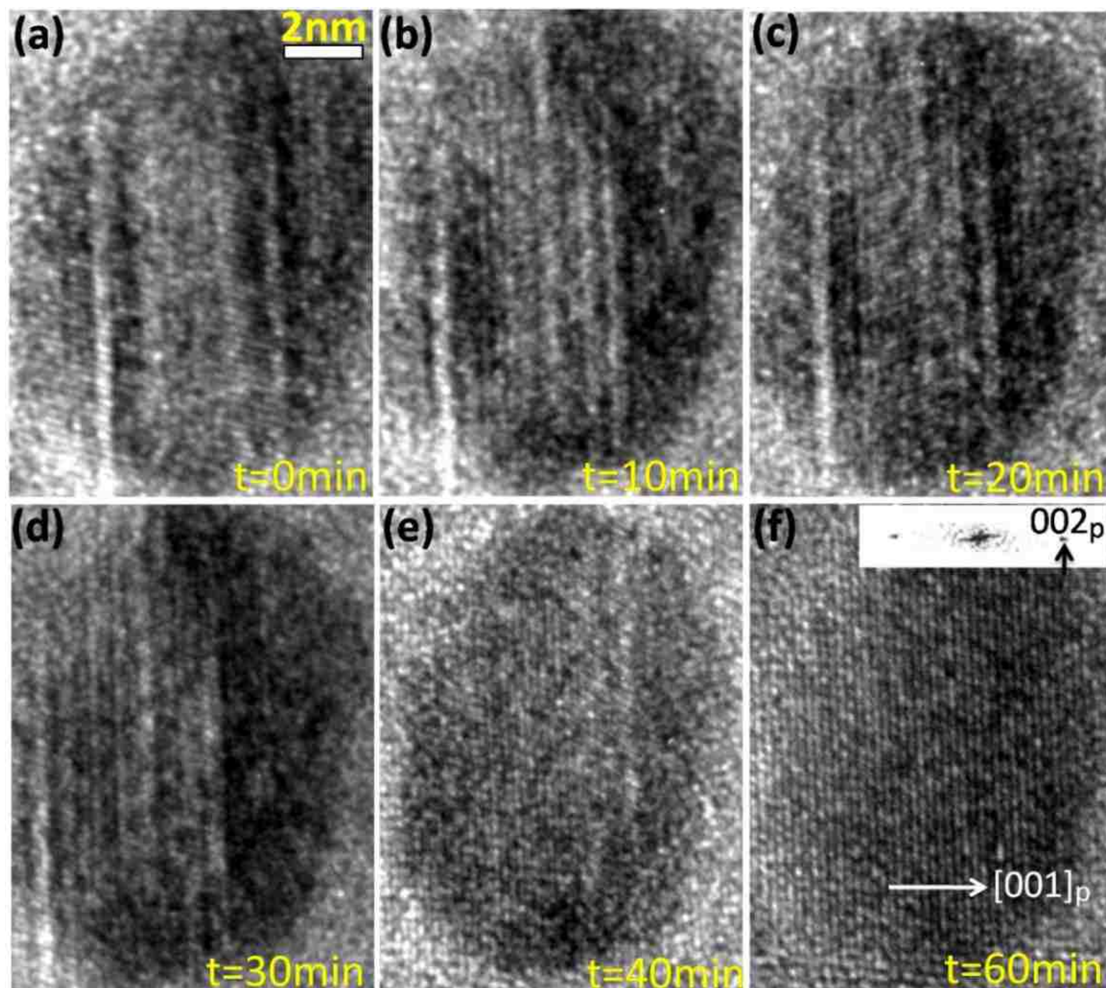

Figure 6-24: A series of TEM images for the decaying electric-field-induced stripes in a crystalline grain of PCMO film. The evolution started right after the applied electric field (~ 9×10^{6} V $\cdot$m^{-1}) was removed. The crystalline orientation of the imaged grain is marked in panel (f). The inset is the corresponding FFT pattern.

To gain further insight into the local lattice dynamics associated with such an electric-field-induced oxygen vacancy migration, we have performed in-situ measurements on the relaxation of electric-field-induced structural distortion/reconstruction. **Figure 6-24(a-f)** presents a series of time-dependent images on the relaxation of the electric-field-induced stripe structure in a single crystalline grain of PCMO film after removing the external electric field through W-tip bias. The electric-field-induced vertical stripes in the grain gradually fade away with time and finally the crystalline grain restores its primary structure with no observable superstructure.

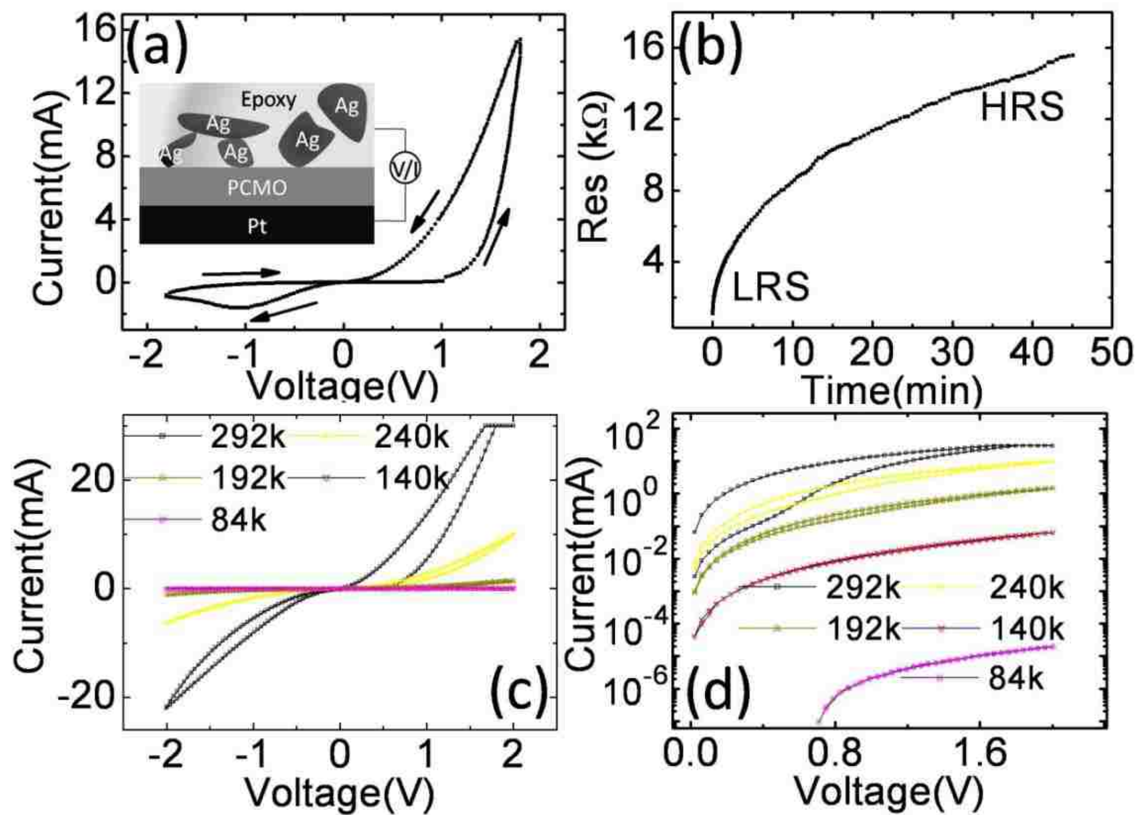

Figure 6-25: (a) *I-V* hysteresis of Ag-Paint/PCMO/Pt; (b) Resistance relaxation after applying only positive sweep loop; Temperature-dependent *I-V* hysteresis in (c) linear and (d) logarithmic scale

The relaxation time scale (referred as τ_s here and after) for the observed stripes is estimated on the order of 1 hour, profoundly longer than any simple electronic or structural

relaxation, such as the melting of charge **[222]** or polaron ordering**[188].** Such a slow relaxation should be related directly to the ion motion, i.e., oxygen vacancy diffusion. Based on the fact that when PCMO relaxes back to the thermal equilibrium state, the resistance should simultaneously become stable. The structure relaxation then should be responsible for the relaxation of the switched resistance. As shown in **Figure 6-25a**, an Ag-Paint/PCMO/Pt device with point contact between Ag nanoparticle and PCMO **[212]** exhibits the same characteristic resistance switching behavior as our Ag-tip/PCMO/Pt as shown in **Figure 6-13**. If only applying positive sweep loop, the resulted LRS then will slowly decay with relaxation time of 50 min [see **Figure 6-25b**], which is indeed very close to τ_s. Nian et al. has also reported the same order of resistance relaxation time (~ 10 min) in this material and the resistance relaxation is thought to result from oxygen diffusion **[66]**. The temperature-dependent resistance switching characteristics displayed in **Figure 6-25(c-d)** also imply that the field induced switching is related to ion migration. The I-V hysteresis became smaller with decreasing temperature and completely disappeared below 140K, even though a voltage sweep-loop with the maximum voltage of 10 V was applied (data not shown). Since the mobility of the oxygen ($\mu = \mu_0 e^{-E/(KT)}$) exponentially decays with increasing 1/T, the oxygen will be frozen at low temperature. For example, $\mu(140\ K)/\mu(300\ K)$ is equal to ~ 10^{-8} (here the activation energy (E) of 0.4 eV is used according to the result from **Ref. 66**). It can be interpreted that the freeze of oxygen causes the disappearance of RS. These results strongly suggest that both the electric field induced evolution of superstructure (**Figure 6-23**) and the relaxation of the stripes (**Figure 6-24**) are related to motion of oxygen vacancy in the system.

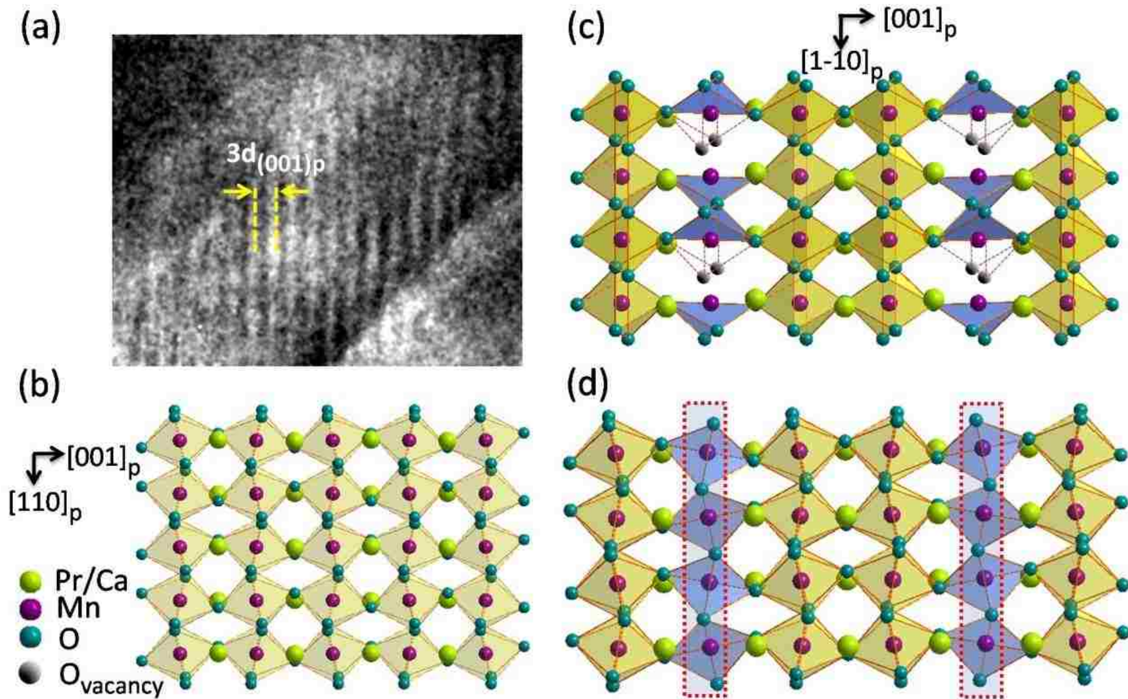

Figure 6-26: (a) Zoom-in image of stripes in **Figure 6-23c**, showing a $p(3\times1)$ stripe superstructure along [001] direction; (b) The structural model in $(1\text{-}10)_P$-plane view of primitive lattice in pseudo cubic perovskite (ABO_3) structure; A possible $A_3B_3O_8$ oxygen vacancy model in (c) $(110)_P$- and (d) $(1\text{-}10)_P$-plane view.

We now interpret the *in-situ* observed stripes as the superstructure associated with the local oxygen vacancy order and their formation and evolution induced by an applied electric field result in the change of transport properties, including RS. With sufficient density, oxygen vacancies can self-assemble into certain orders and result in lattice reconstructions in this class of perovskite materials **[221, 223-226]**, such as the observed stripe modulation. An external electric field induced oxygen vacancy migration can change the local vacancy density and affect their self-assembling, resulting in the electric-field-induced superstructure evolution. Back in 1976, Grenier *et al.*[**221]** proposed that oxygen vacancies in 3D cubic TMO perovskites [ABO_3, as shown in **Figure 6-26b**] could form $A_nB_nO_{3n-1}$-type structure where (n-1) octahedral planes alternate with one tetrahedral structure. According to the $A_nB_nO_{3n-1}$ model, oxygen vacancies prefer to locate on $\{001\}_P$ plane, and form strings along $<110>_P$ direction, forming a modulated stripes with period of $nd_{(001)_p}$. The n = 3 and n = 4

type reconstructions have been reported before.**[221, 224-226]** The high resolution image of the stripe in **Figure 6-24** shows that the field induced stripes locate in the (001) plane, consistent with the characteristic of oxygen vacancy order in perovskite materials. Although we do not have atomic-resolved images of stripes in **Figure 6-23**, the measured spacing of ~ $3d_{(001)_p}$ between stripes in PCMO (see **Figure 6-23** and **Figure 6-26a**) implies that stripes have a modulation as n = 3 case in the $A_nB_nO_{3n-1}$ model. A schematic model for these observed stripes is shown in **Figure 6-26(c-d)**. The oxygen vacancies in the $(001)_P$ plane form strings along $[110]_P$ direction. The planar view of reconstructed structure in the $(1\text{-}10)_P$ plane then gives rise to stripes with a period of $3d_{(001)_p}$. The local oxygen vacancy density should manipulate the evolution of stripes, including possible change of periodicity and even orientation. Under an external electric field which influences the local oxygen vacancy density, the stripes will migrate, change their shape and orientation, depending on the strength and direction of local electric field (see **Figure 6-23**). Without the external field, the field induced a gradient of the concentration of oxygen vacancies will cause the stripes to relax as shown in **Figure 6-24**. Yang *et al.* also reported similar phenomena in $SrTi_{0.2}Fe_{0.8}O_3$ **[224].**

The structure evolution under electric field allows estimating the oxygen vacancy mobility. The drift velocity of oxygen vacancies should approximately equal that of stripes. The stripe boundary marked by a dashed yellow line in **Figure 6-23c** moved ~ 14 nm in 321 s at an electric-field of ~ 9×10^6 V $\cdot$m^{-1}, so the oxygen vacancy mobility is estimated to be μ = 4.8×10^{-14} cm^2 $\cdot$V^{-1} $\cdot$s^{-1}. It is smaller than the reported value of 3.9×10^{-12} cm^2 $\cdot$V^{-1} $\cdot$s^{-1} in Ref. 110. The smaller mobility probably resulted from different oxygen vacancy concentrations **[66].** The sample in **Ref. 66** was grown to be oxygen deficient in oxygen free atmosphere and

the resistivity of the low resistance state was reported to be ~ 1.2×10^5 Ω·cm, three orders higher than that of our sample (~ 3.4×10^2 Ω·cm). The sample we have should have lower oxygen vacancy concentration, thus causing lower mobility as discussed in Ref. 66.

In summary, we present direct evidence for the dynamic migration and diffusion of oxygen vacancies in PCMO through in-situ structural imaging, thus provide a microscopic view for the nature of RS functionality in this class of oxide materials. The manipulation of oxygen vacancy with external electric field not only controls the local chemical stoichiometry but also the structure, resulting in the change of the physical properties of TMOs, typically resistivity for example. Although we use PCMO as a demonstration, the results should be general for other metal oxides and give insight into the development of oxide-based resistance random access memory.

6.3 Investigation of Resistance Switching in Single Crystalline CeO_2 Thin Film

6.3.1 Improve Resistance Switching Performance of CeO_2

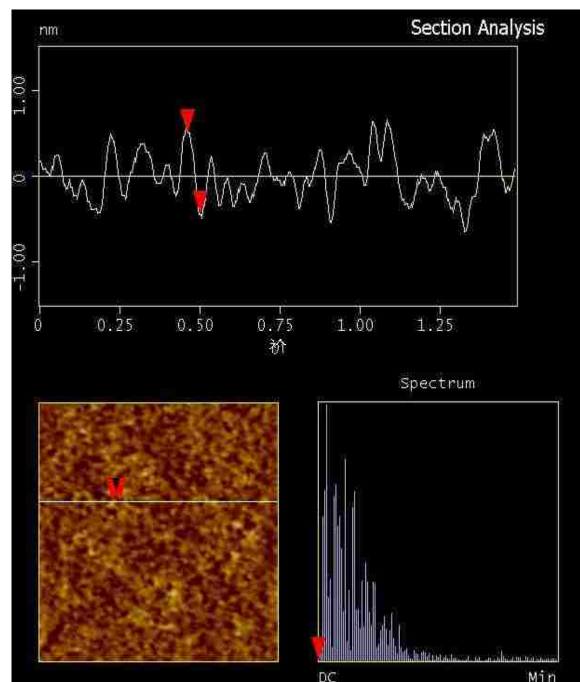

Figure 6-27: AFM image of CeO_2 surface.

CeO_2 single crystalline thin film was epitaxially grown on single crystal 0.7wt% (001) Nb-$SrTiO_3$ (NSTO) substrate by pulsed laser deposition (PLD) at 530 ^oC in oxygen ambient of 15 mTorr. The surface is very flat with roughness of ~1 nm as shown in **Figure 6-27**. XRD data shown in **Figure 6-28a** indicates the grown direction was [100]. The thickness was 175 nm (see **Figure 6-28b**). High resolution transmission electron microscopy (HRTEM) also confirmed that the film was well crystalline and homogeneous (see **Figure 6-28(c-d)**).

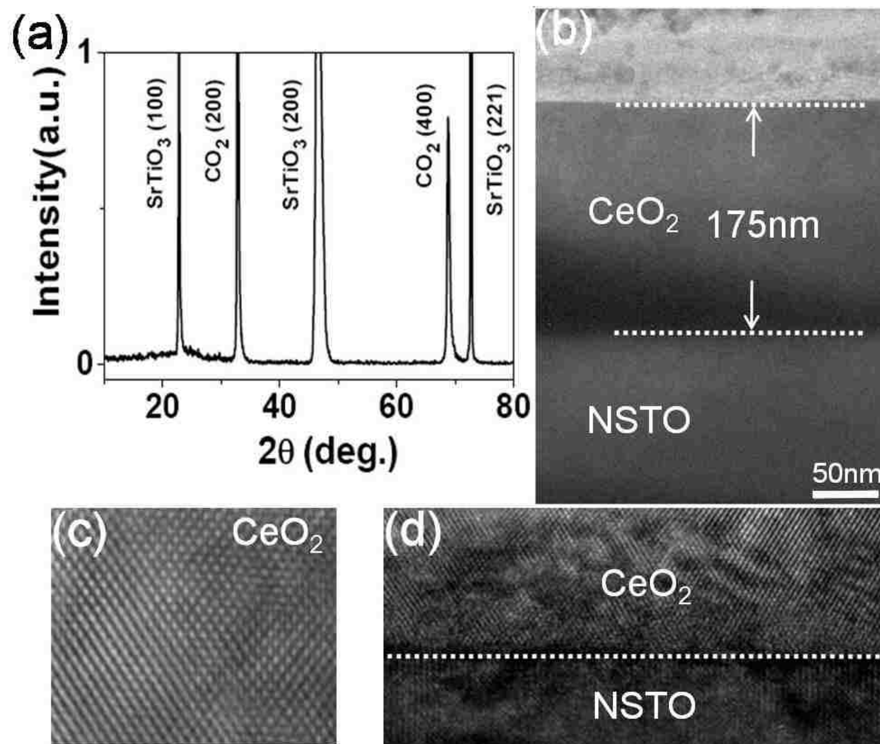

Figure 6-28: (a) XRD pattern of single crystalline CeO_2 thin film (b) TEM image of cross-section of CeO_2/NSTO (c) High resolution image of CeO_2 thin film (d) High resolution image of CeO_2/NSTO interface.

An array of 100 μm×100 μm electrodes, 30 nm thick and with 600 μm separation in both x&y directions, on top of the CeO_2 thin film by using the standard photolithographic technique was fabricated. The conductive NSTO substrate was always grounded as bottom electrode. Systematic current-voltage (I-V) sweep loops (*0→Vmax→-V'max→0*) were carried out with Keithley 2400. The electrodes with a number of materials were made by magnetron sputtering at room temperature.

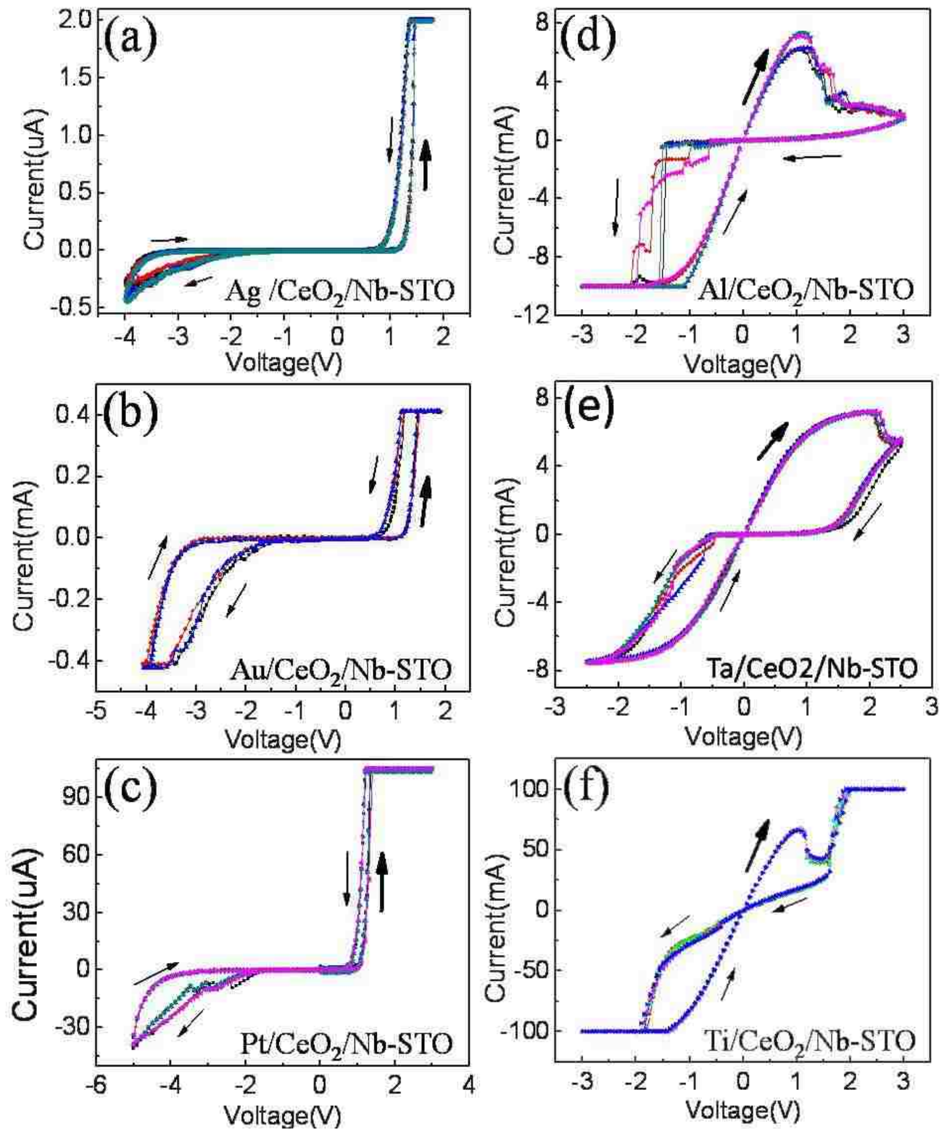

Figure 6-29: I-V sweep loops of Top-electrode/CeO_2/NSTO with different top-electrodes of Ag, Au, Pt, Al, Ta, Ti.

Figure 6-29 shows the I-V characteristics of six different devices with different types of metal electrodes on the top of the CeO_2/NSTO. We could obtain reproducible hysteresis for all kinds of top metal electrodes. Although all six sets of I−V curves exhibited hysteresis and bipolar resistive switching, the devices with NRM (Ag, Au, Pt) as the top electrodes show a different switching direction from that with RM (Al, Ta, Ti) as the top electrodes. As displayed in **Figure 6-29(a-c)**, In NRM (Ag, Au, Pt)/CeO_2/NSTO devices, resistance was switched from the high resistance state (HRS) to the low resistance state (LRS) when

applying positive bias and from LRS to HRS at negative bias, referenced as "Eightwise", while RM (Al, Ta, Ti)/CeO_2/NSTO did a reversed way which behaved like "Counter Eightwise". Therefore the choice of top electrode could be used to determine the resistance switching direction.

The retention behavior between NRM/CeO_2/NSTO and RM/CeO_2/NSTO displayed remarkable difference too. As shown in **Figure 6-30a**, we can take Ag/CeO_2/NSTO as an example, the consecutive (0→2V→0) sweep loops totally coincided. The time space between these two sweeps was ~1 s. During the sweep, the initial HRS was switched to LRS under positive bias and the LRS relaxed quickly back to HRS again when electric field was absent, thus subsequent same loop started from the same resistance state as previous sweep loop. The sweep loop at negative bias side also showed the same characteristic. In another word, RS in NRM/CeO_2/NSTO is volatile. The switched resistance by the external electric field could relax back to initial sate quickly. In contrast, RS in RM/CeO_2/NSTO is non-volatile. Take Al/CeO_2/NSTO as an example, both HRS and LRS in Al/CeO_2/NSTO devices maintained constant without any sign of decay as shown in **Figure 6-30b.** Therefore the reactive metal electrode should be used for practical application where long time retention is required.

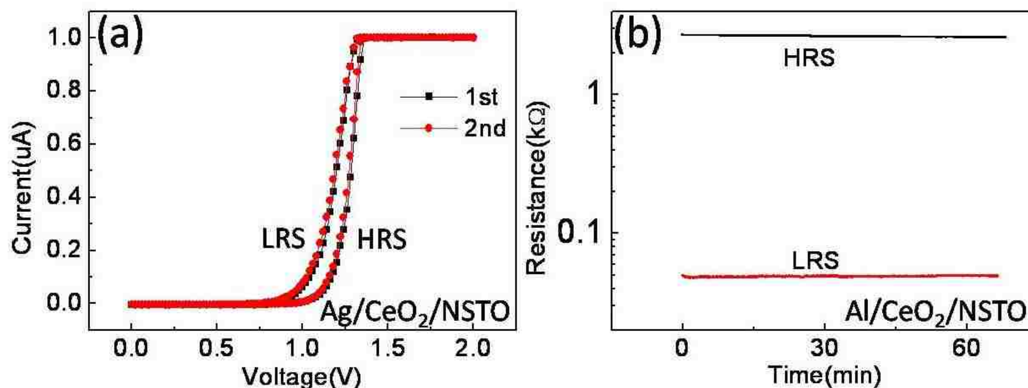

Figure 6-30: (a) Consecutive I-V (0→2V→0) sweep loops on Ag/CeO_2/NSTO, (b)Retention behavior of HRS and LRS of Al/CeO_2/NSTO. The resistance was read at 0.3V.

A strong rectification effect was observed in both HRS and LRS of NRM/CeO_2/NSTO devices (see **Figure 6-29(a-c)**). Quite different from NRM/CeO_2/NSTO devices, the I-V curves became linear or almost linear at LRS and rectification effect was distinct just at HRS (see **Figure 6-29(d-f))** in RM/CeO_2/NSTO. The rectification effect in NRM/CeO_2/NSTO devices could be attributed to presence of Schottky barrier at NRM/CeO_2 and CeO_2/NSTO junctions. Linear I-V curve observed in LRS state of RM/CeO_2/NSTO indicates a qualitative change of RM/CeO_2 and CeO_2/NSTO junction compared to those in NRM/CeO_2/NSTO. The rectification effect could affect the OFF/ON (equal to HRS/LRS) ratio. The HRS/LRS read at 0.24V for Ta, Al/CeO_2/NSTO were 770 and 165 respectively, much bigger than that of Ti/CeO_2/NSTO (HRS/LRS=4). The smaller ratio in Ti/CeO_2/NSTO may be induced by weak rectification effect in both LRS and HRS.

Based on discussion above and completely different behavior of RS characteristic and retention between NRM/CeO_2/NSTO and RM/CeO_2/NSTO, it is reasonable to say that the RS mechanism in these two different kinds of devices (NRM vs. RM) is completely different.

6.3.2 *In-situ* TEM Investigation of Resistance Switching in CeO_2 Thin Film

The method to measure CeO_2 thin film inside TEM is similar with that for PCMO as describe in **6.2.5.** The electron transparent cross-section samples were prepared by conventional mechanical polishing and argon ion milling to a thickness of around 30~60 nm at the center region of the samples. A sharp gold tip driven by piezo-controller moved forward to contact the ceria film of TEM-ready cross section sample which was loaded on a home-made specimen holder. Inset of **Figure 6-31** shows the *in-situ* TEM device-Au-tip/CeO_2/Nb-STO. The metallic Nb-STO had good electric conductivity and was

grounded. A loop of *in situ* *I-V* sweep, $0 \rightarrow +V_{max} \rightarrow 0 \rightarrow -V'_{max} \rightarrow 0$, was performed and displayed the resistance switching effect, as shown in **Figure 6-31**. The I-V loop characteristic is same with Au-film/CeO_2/Nb-STO devices as shown in **Figure 6-29**.

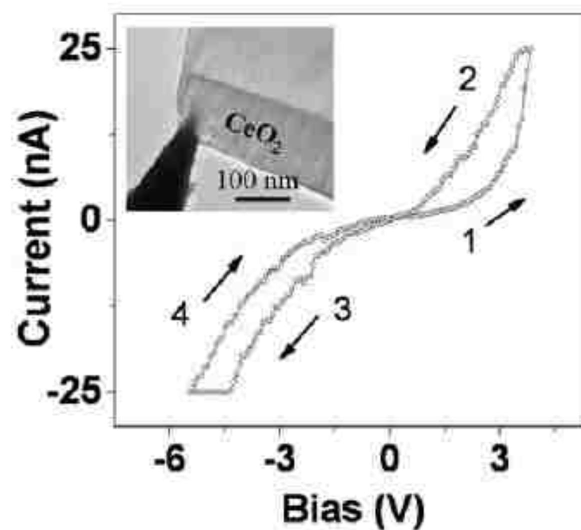

Figure 6-31: I-V loop of Au-tip/CeO_2/NSTO inside TEM. Inset is TEM image of Au-Tip/CeO_2/NSTO devices. Figure adapted from **[220]**.

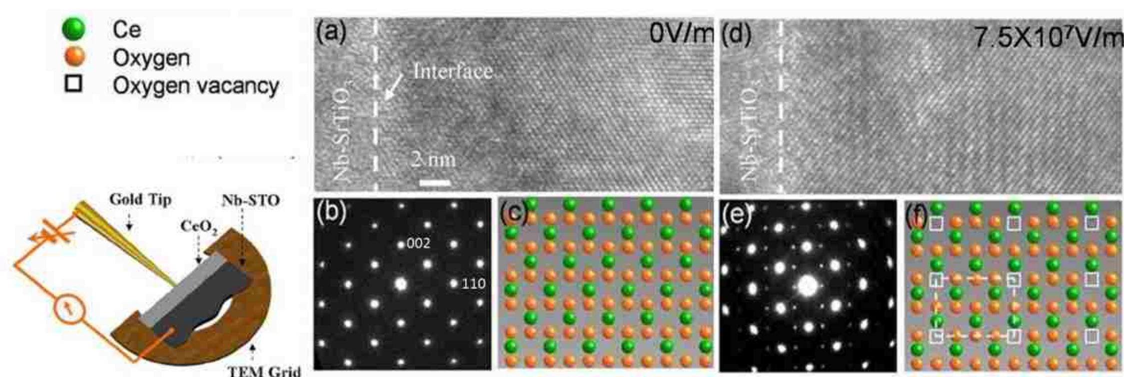

Figure 6-32: (a) High resolution image of CeO_2 film along <110> zone axis and its diffraction pattern and structure model shown in (b) and (c) respectively. After application of 5 V bias, superstructure appeared. The higher resolution image is shown in (d), the diffraction pattern and structure mode are shown in (e) and (f) respectively. Figures adapted from **[220]**.

Figure 6-32(a-b) show the atomic-level TEM image and electron diffraction pattern from <110> zone axis before applying the electric field. By applying a small bias 1 V to the junction for seconds (the threshold voltage is not overcome), no change was observed. When the bias was up to 10 V (electric field $E \sim 1.5 \times 10^8$ V/m and the device was at LRS), as shown

in **Figure 6-32d**, the structural transformations took place with the appearance of wave sweeping in high resolution TEM image. The extra diffraction spots were also observed from diffraction pattern [see **Figure 6-32e**], corresponding to the long periodicity of two-fold CeO_2 {200} and four-fold CeO_2 {110}. This superlattice reflection indicated that oxygen anions had been removed from the ceria and the introduced oxygen vacancies were ordered **[227-229]**.

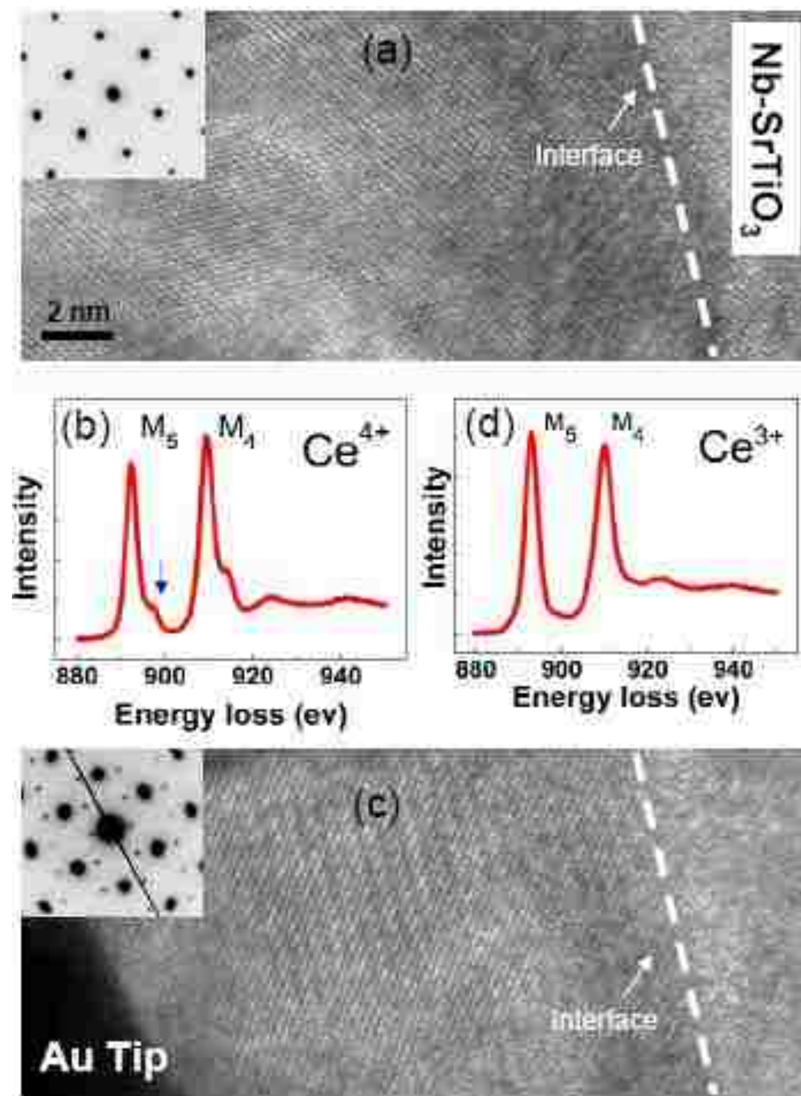

Figure 6-33: (a) Atomic-level TEM image of CeO_2 film alone <110> zone axis. Inset: corresponding electron diffraction pattern. (b) EELS a of Ce-M edge. (c) 10 V voltage was applied between the gold tip and NSTO. Gold tip was anode. Superlattice reflections and extra diffraction spots (inset) appeared. (d) A reversal in the intensity of Ce M_{45} was observed; and the shoulder indicated by arrow in (b) disappeared. Figure b and d adapted from **[220]**.

To gain further evidence of the phase transition, electron energy loss spectra (EELS) analysis that showed the chemical valence changing of Ce ions were performed. When applying bias of 10 V, a reversal in the intensity of Ce M_{45} was observed [**Figure 6-33b and d**], suggesting that Ce has undergone a transition from 4+ to 3+ oxidation state **[229, 230]**. The shoulder [indicated by arrowhead in **Figure 6-33b**] that suggested the strong covalence hybridization between Ce *4f* and O *2p* states **[231]**, disappeared in the electric field. Then we applied -10V (the device was back to the HRS), the EELS showed that the Ce oxidation state reverts to 4+; at the same time the superstructure reflection stripe disappeared from TEM image.

The oxygen vacancies stripes always prefer to appear at NSTO/CeO_2 interface. Under positive bias (NSTO was grounded), the stripes emerge from NSTO/CeO_2 interface and propagated through the thickness of the ceria to the gold electrode. Reverse bias then melts the stripes starting from gold electrode. As the diffraction pattern and EELS showing, the stripes are due to the ordering of oxygen vacancies, thus should arise from generation of more and more oxygen vacancies. To understand the behavior of stripes under field, it should be noticed that communications between oxygen anions and oxygen gas could occur **[74]**. Szot *et al.* discovered that the gas bubbles had developed under the anode when the electric field was applied to single crystalline $SrTiO_3$ **[73]**. From measuring the fatigue behavior of $Ag/La_{0.7}Ca_{0.3}MnO_3/Pt$ heterostructure, Shang *et al.* proposed that oxygen gas could infuse into the electrode/film interface and oxygen anions could diffuse out to the environment when different biases are applied **[232]**. More recently, Yoshida *et al*. demonstrated that the oxygen gas could penetrate into the non-stoichiometric nickel oxide film by using ^{18}O tracer

gas atmosphere **[233]**. For fluorite structure, oxygen is more easily released and absorbed by cerium oxide, that is why this material is widely used as oxygen storage capacity in catalysis **[234, 235]**. Therefore, the top interface of Au/CeO_2 is exposed to oxygen atmosphere while the NSTO/CeO_2 is buried under CeO_2 thin film, which gives rise to the broken symmetry of interface. Under positive bias, oxygen anions move to top Au/CeO_2 interface and then formed O_2 which is released into atmosphere. At the same time the removal of oxygen anions leaves oxygen vacancies and since $SrTiO_3$ could not compensate oxygen anions, more and more oxygen vacancies are created starting from $SrTiO_3$/CeO_2 interface. That is why that the stripes start from $SrTiO_3$/CeO_2 interface and propagate to gold electrode. The negative bias will convert O_2 into oxygen anions and then migration into inert CeO_2 crystal, then melting the stripes.

6.3.3. Resistive Switching Mechanism in CeO_2 Thin Film Device

In-situ TEM experiment indicates that oxygen could easily move into CeO_2 and CeO_2 could communicate with oxygen gas. In the case that the top electrode is non-reactive metal, NRM/CeO_2/NSTO, the oxidation of NRM could not occur. As discussed in **6.3.2**, positive bias will cause oxygen vacancies to move across the CeO_2 thin film and negative bias will remove oxygen vacancies. For stoichiometric CeO_2, every oxygen atom is situated at the center of tetrahedron, surrounded by four Ce atoms. The oxygen *p* band has two extra electrons provided by Ce atom while there is a narrow empty Ce *f* band in the gap between the valence and conducting bands **[236]**. When an oxygen atom is leaving its lattice position, the two electrons may occupy the lowest possible empty state which is the *f* band of nearest Ce atoms, tuning Ce^{4+} to Ce^{3+} and enhancing the electron conductivity of the cerium oxide

[237]. Perfect CeO_2 is an insulator (band gap 6 eV), corresponding to the HRS **[238]**. The presence of oxygen vacancies lowered the local electron resistivity. So positive bias results in LRS and negative bias will give rise to HRS. Generally CeO_2 is a stable phase while CeO_{2-x} can only be stable at high temperature and/or ultralow pressure. For example, a stable Ce_2O_3 phase occurs only at the pressure lower than10^{-95} atm at room temperature **[239]**. In the absence of electrical field, the CeO_{2-x} conductive path will be melted due to the infusion of the oxygen into film even in the vacuum of ~ 10^{-10} atm (as discussed in 6.3.2). In this study, our NRM/CeO_2/NSTO devices were measured at ~1 atm. It is much easier for the conductive Ce_2O_3 to recover back to the insulating CeO_2 phase, resulting in a volatile RS.

Unlike NRM, the RM can easily react with the oxygen to form metal oxide. It is reported in some RM/Metal-oxide interface that the electric field induced oxygen migration can cause redox at interface and interface redox at RM/MO is suggested to be the main reason that causes RS. Under the electric field, oxygen will migrate between top electrode (or top electrode oxide) and metal oxide. The remarkable difference between NRM/CeO_2/NSTO and RM/CeO_2/NSTO indicates similar interface properties with Metal/PCMO/Pt devices. Under positive bias with respect to the bottom NSTO, oxygen will migrate into top RM to oxidize it (resulting in HRS) while negative bias can reduce the RM top electrode oxide (resulting in LRS), as a result RS is "Counter Eightwise". In contrast to oxygen diffusion in RM/CeO_2/NSTO, such kind of electrochemical reaction at interface requires not only the migration of oxygen across interface but also resultant oxidation/reduction. The change of interface chemical component induced by electrochemical redox will be more stable **[194]**, hence the oxidation/reduction of the RM (Al, Ta, Ti) is stable against thermal fluctuation, and

so RM/CeO_2/NSTO has an excellent retention. The linear I-V behavior in LRS of RM/CeO_2/NSTO may be related to relative oxygen concentration level between CeO_2 and top RM electrodes. In the future we will try to reveal the role of interface junction in I-V rectification, RS and microscopic mechanism of interface redox process.

Metal oxide with mobile oxygen will be a good candidate for RS but may have bad retention due to diffusion. Resistance relaxation is also reported in Ag/$Pr_{0.7}Ca_{0.3}MnO_3$/Pt devices where in some specific physics state the pileup of oxygen proximity to electrode can diffuse, leading to volatile behavior **[66]**. The diffusion will kill the retention. Redox based RS in the RM/Metal-oxide could be used to improve the retention. The interface current rectification effect is another approach that enables us to adjust the OFF/ON ratio.

In summary, we demonstrated that RS performance in TE/CeO_2/NSTO sandwiched devices strongly depends on the activity of top electrodes. The NRM/CeO_2/NSTO devices display "Eightwise" bipolar RS, but are all volatile with a stable HRS. The RM/CeO_2/NSTO devices show "Counter Eightwise" RS direction and are non-volatile with no sign of decay or relaxation. Between RM/CeO_2/NSTO, Ta/CeO_2/NSTO showed a bigger OFF/ON ratio. Therefore we can engineer electrode to improve devices performance, which will enlighten the way to improve performance of resistance random access memory.

6.4 Investigation of Resistance Switching in Metal Oxide Heterojunction

The current technology that based on charge storage, such as flash memory, has become increasingly limited as the cell size decreases. Developing non-volatile high speed memory based on solid state system that can exist in two or more stable states is one key technological step to extend the functional equivalent of Moore's law.**[240]** Phase-change random access

memory (PCRAM),**[241]** magnetoresistive random access memories (MRAM),**[242]** etc., are candidates for future non-volatile, high speed, high density memories. Yet another class of promising non-volatile, high performance memory is resistance random access memory (RRAM) which is based on resistance switching (RS) effect. The RS behavior, as a common feature of metal oxide thin film based sandwich devices is thought in most cases to be strongly related to oxygen and its defects (typically the oxygen vacancy). More specifically, either the field induced redox or oxygen migration plays a central role in RS. In another word, the RS phenomenon benefits much from strong coupling between oxygen atom/defects and properties of the metal oxides. The external electric field can move the oxygen ions or vacancies so the local density of oxygen ion/vacancy will change, thus changing the resistance.

Although a great effort has been paid to develop reliable and stable devices for practical application, it still requires a lot work to solve such as uniformity, endurance and retention issues to finally make it commercialized. Most of the structures of RRAM devices are the M/MO/M, and actually the metal electrode not only performs as an electrode but also provides an M/MO interface. The M/MO contact could be a pure electronic contact such as Schottky barrier or a chemical contact where a redox may occur depending on the Gibbs free energy of oxidation of metal electrode. For the latter case, a new electrode oxide will be formed, hence the actual structure should be M_1/M_1-Oxide/M_2-Oxide/M_3. For example, the Al/$Pr_{0.7}Ca_{0.3}MnO_3$(PCMO)/Pt device in fact is Al/AlO_x/PCMO/Pt and the field induced redox at AlO_x/PCMO heterostructure causes the RS. The M/MO/M structure is not essential for RS. Some of the metal-oxide heterostructure (MOH) forming from two metal-oxides coupling

together can have better endurance due to self-limiting effect. Although the performance of the MOH arising from the oxidation of metal electrode could have a good RS, but it is strongly limited by the nature of the metal electrode and that just a few active metals could be used. To fabricate a MOH as shown in **Figure 6-34** on purpose will be a more flexible way allowing us to improve device performance by choosing proper oxides.

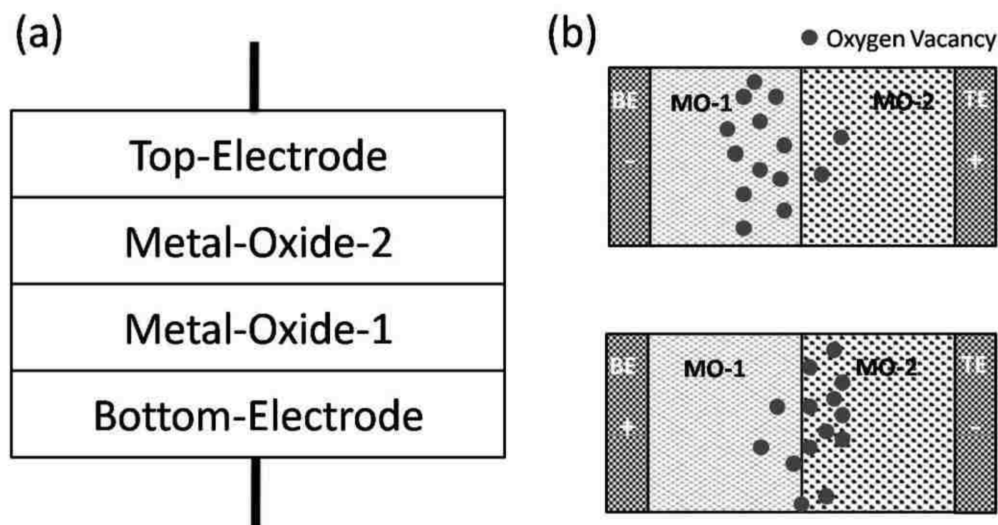

Figure 6-34: (a) Structure of a MOH RRAM device. (b) Schematic diagram of working mechanism.

Oxygen vacancy will strongly affect the properties of metal oxides as discuss in **Chapter 1**. A specific property of a metal oxide could be a function of its oxygen vacancy concentration.

$$\varphi = \varphi(n_{V_o}) \qquad (1)$$

Here φ is a specific property of a metal oxide and n_{V_o} is its oxygen vacancy concentration. Change of the oxygen vacancy concentration will change the properties. Concerning the RS phenomenon specifically, the resistivity as a function of oxygen vacancies will be discussed. For convenience, using n to represent the concentration of oxygen vacancy (so as the following text), then we have

$$R(n_0 + \Delta n) = R_0 + \alpha \Delta n + \beta \Delta n^2 + \cdots \qquad (2)$$

In the case of the MOH, an electric field induced migration of oxygen vacancies from one MO to the other MO (see schematic picture in **Figure 6-34b**) will then change the oxygen vacancy concentration of both metal oxides. Take **Figure 6-34b** as an example, a positive bias (bottom electrode is grounded as reference) will move the oxygen vacancies from MO-2 into MO-1, thus changing both vacancy concentrations and causing change of the both resistances. Neglecting the interface rectifying effect and the high order items of more than 3 in equation (2) since in most cases the Δn will be very small and then the change of resistance (ΔR) of MOH will be

$$\Delta R = \Delta R_1 + \Delta R_2 = \alpha_1 \Delta n_1 + \beta_1 \Delta n_1{}^2 + \alpha_2 \Delta n_2 + \beta_2 \Delta n_2{}^2 \qquad (3)$$

The change of the concentration (Δn) is proportional to the change of the amount of oxygen vacancies (ΔN), $\Delta n = k\Delta N$, then we have

$$\Delta R = (\alpha_1 k_1 - \alpha_2 k_2)\Delta N + (\beta_1 k_1{}^2 + \beta_2 k_2{}^2)\Delta N^2 \qquad (4)$$

The relative change of resistance is determined by the followed item

$$\frac{\Delta R}{R} = \frac{(\alpha_1 k_1 - \alpha_2 k_2)\Delta N + (\beta_1 k_1{}^2 + \beta_2 k_2{}^2)\Delta N^2}{R_0} \qquad (5)$$

Under external electric field

$$\Delta N \propto \int j(V(t))dt \propto \int n\mu(V(t))Edt \qquad (6)$$

ΔN is determined by the interface oxygen flux and the duration time. Here μ is the oxygen mobility and a function of external bias $V(t)$. It is evident that the field induced migration can change the oxygen content to induce a resistive switching in MOH. In other words, a real time control of the resistance of MOH can be realized. To maximize the speed of the switching, either a strong electric field or high mobility of oxygen is required. Generally the

mobility of the oxides is very small at low electric field as shown in **Table 1-1**, but the it can be greatly enhanced at high electric field, so it is still possible to provide nanosecond scale switching speed in MOH.

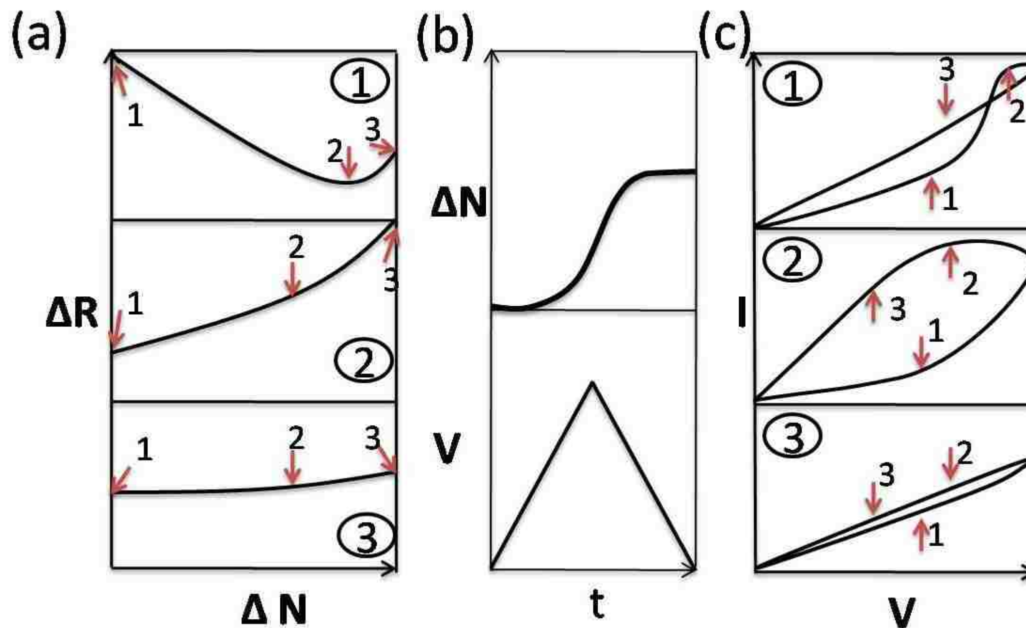

Figure 6-35: (a) three types of relation between change of resistance (ΔR) and number of oxygen (ΔN) moving across the MOH interface. (b) Applied bias versus time and corresponding ΔN versus time. (c) Correspond I-V curves for three types of MOH in (a).

Under the external electric field, the characteristic hysteresis will be strongly affected by relative resistivity behavior of the metal oxides. Since the introduction of oxygen vacancies can either enhance or decrease the conductivity, the coefficient α and β could be positive or negative. The ΔR as a function of ΔN could have three types as shown in **Figure 6-35a**. Under a positive sweep loop ($0 \rightarrow V_{max} \rightarrow 0$) (bottom panel in **Figure 6-35b**), the oxygen will start moving at above certain critical electric field intensity, and a schematic change of ΔN correspondingly as a function of time is shown in the top panel of **Figure 6-35b**. The coefficient ($\alpha_1 k_1$- $\alpha_2 k_2$) and ($\beta_1 K_1^2+\beta_2 k_2^2$) could be of different sign which then gives rise to type-1 as shown in top panel of **Figure 6-35a**; of same sign then giving rise to type-2. If ($\alpha_1 k_1$- $\alpha_2 k_2$) is close to zero and ($\beta_1 K_1^2+\beta_2 k_2^2$) is also very small, then we will have type-3.

The I-V characteristics corresponding to each case are shown in **Figure 6-35c**. . For each type, the ΔN at the point marked by an arrow labeled by a number *n* (= 1, 2, 3) in the I-V curve corresponds to the point in **Figure 6-35a** with same number. With applying bias, the oxygen will move across the MOH interface, and then ΔR will vary along the ΔR Vs. ΔN curve. In the case of type-1 MOH, the resistance will keep decreasing before ΔN running across peak valley (point 2). However the resistance will start to increase after ΔN going through peak valley, therefore, a "8"-type I-V hysteresis will be observed as shown in panel-1 in **Figure 6-35c**. For the type-2 MOH, since the resistance will keep increasing with increasing ΔN, a nice hysteresis without intersection point could be obtained. If the resistance is not sensitive to oxygen (type-3 for example), the I-V hysteresis will become very weak (see panel 3 of **Figure 6-35c** as an example).

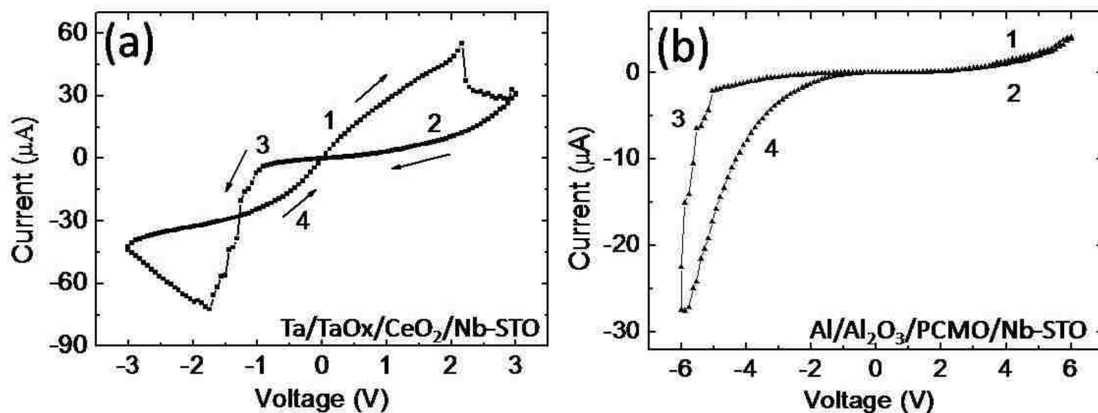

Figure 6-36: I-V sweep loop (1→2→3→4) of (a) $Ta/TaO_x/CeO_2$/Nb-STO; (b) Al/Al_2O_3/PCMO/Pt.

According to the above discussion, how the resistance depends on the oxygen distribution between the two metal oxides swill strongly affect the resultant performance of the MOH based RRAM devices. **Figure 6-36** shows the I-V hysteresis for Ta/CeO_2/Nb-$SrTiO_3$ (NSTO) and Al/Al_2O_3/PCMO/Pt (for details of the devices please see **6.3.1** and **6.2.3** respectively). The Ta/CeO_2/NSTO actually will be $Ta/TaO_x/CeO_2$/NSTO due

to interfacial oxidation. The Nb-$SrTiO_3$ is used as a bottom electrode. The oxygen vacancies in both TaO_x **[243]** and CeO_2 behave as dopants, so the α_1 and α_2 have the same sign, and so at some specific condition, e.g., specific relative oxygen vacancy concentration, the TaO_x/CeO_2 can become a type-1 MOH. In our Ta/CeO_2/NSTO devices, a "8" type hysteresis was indeed observed after some forming process as shown in **Figure 6-36a**. Although we could not observe the same behavior at positive sweep loop, this could be attributed to different rectification effect which may turn this heterostructure into type-2 at positive bias. The observed unusual "8" type hysteresis in In/$La_{0.7}Sr_{0.3}MnO_3$/In **[244]** could be attributed to the equivalent type-1 MOH. As proposed by Ref. **[244]**, the In could be oxidized then resulting in the forming of InO_x/LSMO/InO_x heterostructure with two InO_x/LSMO interfaces. When oxygen vacancies migrate in one direction, resistance of one interface increases while the another one decreases, thus the overall change of resistance could become type-1 in some specific condition. For the Al/Al_2O_3/PCMO/Pt devices, the oxygen vacancies will enhance the conductivity of Al_2O_3, but will make PCMO more insulating. The oxygen vacancies moving from Al_2O_3 to PCMO will increase both the resistance of Al_2O_3 and PCMO, hence Al_2O_3/PCMO heterostructure is type-2 and it shows a bipolar RS (see **Figure 6-36b**) without "8" type hysteresis.

For a RRAM device, several parameters need to be improved, for example, endurance, OFF/ON (= HRS/LRS) ratio, switching speed, uniformity. The active-metal-oxide/PCMO/Pt devices show very good endurance due to self-limiting effect in the process of interfacial redox. Considering the OFF/ON ratio, if MO-1 and MO-2 both have bigger/smaller resistance with increasing oxygen vacancies, the OFF/ON ratio will be suppressed due to their overall

cancelling effect. For example, oxygen vacancies moving from MO-1 into MO-2 will then make resistance of MO-1 decrease/increase while resistance of MO-2 increase/decrease. In another way, if MO-1 have bigger/smaller resistance with increasing oxygen vacancies while the MO-2 does a reverse way, the change of the resistance should be enhanced. The MOH made of such oxides is called complemental MOH (CMOH).

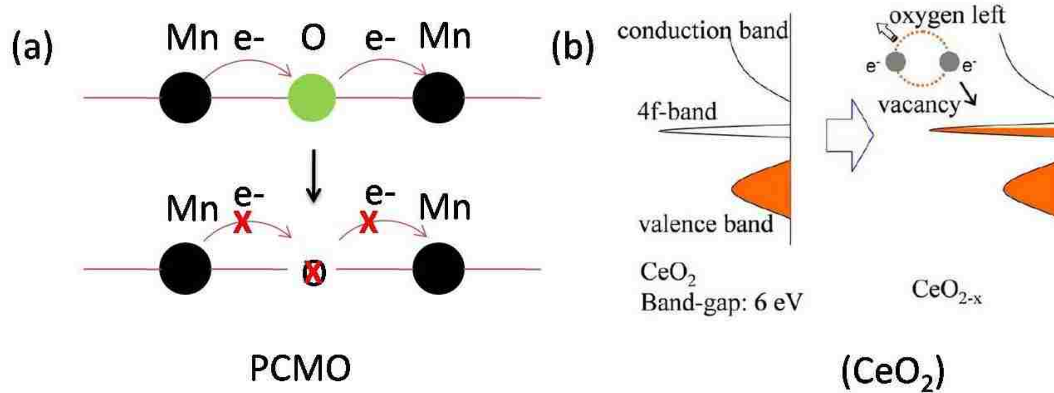

Figure 6-37: (a): Electron moves via Mn-O-Mn chain and is blocked after that the oxygen ion is removed. (b) Band structures of CeO_2 without oxygen vacancies and with oxygen vacancies.

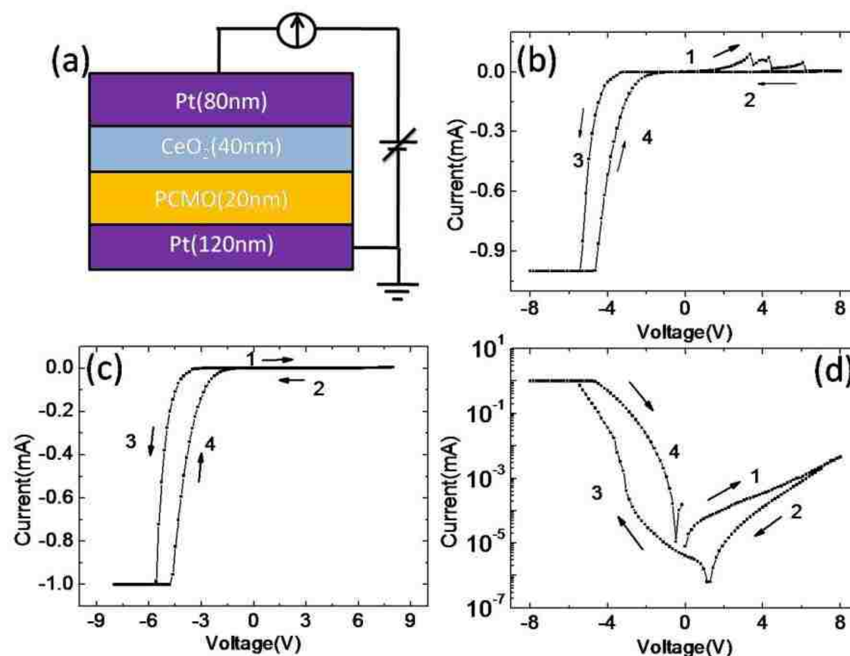

Figure 6-38: (a) Schematic cross-section structure of Pt/CeO_2/PCMO/Pt MOH device. (b) First I-V sweep loop (forming process). Reproducible I-V hysteresis in linear scale (c) and in logarithm scale (d).

To realize an enhanced RS in MOH, we notices that oxygen vacancies in PCMO will induce a rupture of Mn-O-Mn channel chain thus decreasing the conductivity while in CeO_2 can dope electrons which can then occupy empty 4f band and enhance conductivity as shown in **Figure 6-37**. Our *in-situ* TEM experimental results indicate that the PCMO and CeO_2 are oxygen mobile systems, such that combining PCMO and CeO_2 together may help us get an improved RS performance. An CeO_2/PCMO heterostructure device with Pt used as electrodes to remove oxidation of electrode effect was fabricated (see **Figure 6-38a**). After a forming process as shown in **Figure 6-38b**, the devices exhibited reproducible resistive switching effect (see **Figure 6-38(c-d)**). Under positive bias, the devices were switched from low resistance state (LRS) to high resistance state (HRS) and from HRS to LRS at negative bias. Since oxygen vacancies moving from CeO_2 to PCMO will increase both of their resistance, so the positive bias should induce a resistance switched from LRS to HRS, so do the analysis for negative bias. Further, due to the enhanced switching ratio, the HRS/LRS ratio (read at -1.5V) can reach 350. The p-n junction like I-V curve will arise from the n-type nature of oxygen deficient CeO_2 and p-type behavior of PCMO. The I-V characteristic is consistent with our analysis, further supporting the oxygen migration model.

In summary, MOH based devices can be one of the promising structure for RRAM devices. The MOH benefits a lot from the strong coupling between oxygen and properties of metal oxide and enhanced oxygen mobility at strong electric field. The field induced oxygen migration across interface change both of the resistivity of the metal oxides, hence changes the overall resistance of MOH device. The performance of the MOH devices strongly depend on the relation between oxygen vacancies concentration and the resistivity. The mutually

CMOH based RRAM such as Pt/CeO_2/PCMO/Pt device could enhance the OFF/ON ratio. CMOH can be easily grown and there are a lot of candidates for us to choose from to combine them together to explore better CMOH for RRAM.

References

[1] J. G. Bednorz, K. A. Müller, Z. Phys. B-Condensed Matter **64**,189 (1986).

[2] Nicola A. Spaldin, S. –W. Cheong, Physics Today **63**, 38 (2010).

[3] B. C. H. Steele, A. Heinzel, Nature **414**, 345 (2001).

[4] A. P. Ramirez, J. Phys.: Condens. Matter **9**, 8171 (1997).

[5] The April 21st Issue of Science, 288 (2000) was dedicated to Correlated Electron Systems.

[6] The October 2007 issue of Materials Today [http://www.sciencedirect.com/science/journal/13697021] was dedicated to "Complexity and Diversity: The Wonderful World of Oxides" with review articles.

[7] C. H. Ahn, *et al.*, Rev. Mod. Phys. **78,** 1185 (2006), and references there in.

[8] Y. Tokura, N. Nagaosa, Science **288**, 462 (2000).

[9] E. Dagotto, Science **309**, 257 (2005).

[10] A. Moreo, S. Yunoki, E. Dagotto, Science **283**, 2034 (1999).

[11] V. B. Shenoy, D. D. Sarma, C. N. R. Rao, Chemphyschem **7**, 2053 (2006).

[12] R. P. Feynman, Caltech Engineering and Science **23(5)**, 22 (1960).

[13] M. Haruta, Catal. Today **36**, 153 (1997).

[14] A. J. Cox, J. G. Louderback, L. A. Bloomfield, Phys. Rev. Lett. **71**, 923 (1993); A. J. Cox, J. G. Louderback, S. E. Apsel, L. A. Bloomfield, Phys. Rev. B **49**, 12295 (1994).

[15] K. Wildberger, *et al.*, Phys. Rev. Lett. **75**, 509 (1995).

[16] A. V. Boris, *et al.*, Science **332**, 937 (2011).

[17] K. Yoshimatsu, *et al.*, Science **333**, 319 (2011).

[18] R. T. Senger, K. K. Bajaj, Phys. Rev. B **68**, 045313 (2003).

[19] J. Tao, *et al.*, Phys. Rev. Lett. **103**, 097202 (2009).

[20] L.W. Zhang, *et al.*, Science **298**, 805 (2002).

[21] Ai L Efros, A L Efros, Soviet Physics Semiconductors USSR 16, 772 (1982).

[22] S. R. Mehrotra; G. Klimeck (2010), http://nanohub.org/resources/8805.

[23] C. W. Chu, *et al.*, Nature **365**, 323 (1993).

[24] H. Y. Hwang, *et al.*, Nate. Mater. **11**, 103(2012).

[25] Jinbo Cao, Junqiao Wu, Materials Science and Engineering R **71**, 35 (2011).

[26] H. P. Sun, *et al.*, Appl. Phys. Lett. **84**, 3298 (2004).

[27] H. Guo, *et al.*, Appl. Phys. Lett. **89**, 022509 (2006).

[28] A. Ohtomo, H. Y. Hwang, Nature **427**, 423 (2004).

[29] N. Reyren, *et al.*, Science **317**, 1196 (2007).

[30] A. Gozar, G. Logvenov, L. Fitting Kourkoutis, A. T. Bollinger, L. A. Giannuzzi, D. A. Muller, I. Bozovic, Nature **455**, 782 (2008).

[31] O. Yuli, *et al.*, Phys. Rev. Lett. **101**, 057005 (2008).

[32] K. Ueda, H. Tabata, T. Kawai, Science **280**, 1064 (1998).

[33] P. W. Anderson, Phys. Rev. **79**, 350 (1950).

[34] J. B. Goodenough, Phys. Rev. **100**, 564 (1955).

[35] Junsoo Shin, V. B. Nascimento, A. Y. Borisevich, E. W. Plummer, S. V. Kalinin, A. P. Baddorf, Phys. Rev. B **77**, 245437 (2008).

[36] Junsoo Shin, V. B. Nascimento, G. Geneste, J. Rundgren,E. W. Plummer, B. Dkhil, S. V. Kalinin, A. P. Baddorf, Nano Lett. **9**, 3720 (2009).

[37] K. Yoshimatsu,T. Okabe, H. Kumigashira, S. Okamoto, S. Aizaki, A. Fujimori, M. Oshima, Phys. Rev. Lett. **104**, 147601 (2010)

[38] S. Liang, J. R. Sun, J. Wang, B. G. Shen, S. Liang, J. R. Sun, J. Wang, B. G. She, Appl. Phys. Lett. **95**, 182509 (2009).

[39] J. Z. Sun, D. W. Abraham, R. A. Rao, C. B. Eom, Appl. Phys. Lett. **74**, 3017 (1999).

[40] R. P. Borges, W. Guichard, J. G. Lunney, J. M. D. Coey, F. Ott, J. Appl. Phys. **89**,3868 (2001).

[41] A. Biswas, *et al.*, Phys. Rev. B **63**, 184424 (2001).

[42] M. Izumia, *et al.*, Appl. Phys. Lett. **73**, 2497 (1998).

[43] Y. X. Han, W. B. Wu, G. S. Jiang, C. F. Zhu, J. Appl. Phys. **111**, 066104 (2012).

[44] V. N. Varyukhina, *et al.*, Technical Physics Letters **35**. 937 (2009).

[45] J.-M. Liu, Q. Huang, J. Li, C. K. Ong, Z. C. Wu, Z. G. Liu, Y. W. Du, Phys. Rev. B **62**, 8976 (2000).

[46] H. Yamada, Y. Ogawa, Y. Ishii, H. Sato, M. Kawasaki, H. Akoh, Y. Tokura, Science **305**, 646(2004).

[47] M. Uehara, S. Mori, C. H. Chen, S.-W. Cheong, Nature (London) **399**, 560 (1999).

[48] K. H. Kim, M. Uehara, V. Kiryukhin, S.-W. Cheong, Colossal Magnetoresistive Manganites, edited by T. Chatterji, Kluwer Academic, New York, 2002.

[49] H. -Y. Zhai, J. X. Ma, D. T. Gillaspie, X. G. Zhang, E. W. Plummer, J. Shen, Phys. Rev. Lett. **97**, 167201 (2006).

[50] T. Z. Ward, S. H. Liang, K. Fuchigami, L. F. Yin, E. Daggotto, E. W. Plummer, J. Shen, Phys. Rev. Lett. **100**, 247204 (2008).

[51] R. E. Cohen, H. Krakauer, Phys. Rev. B **42**, 6416 (1990).

[52] C. Zener, Phys. Rev. **81**, 440 (1951).

[53] V. B Shenoy, C. N. R. Rao, Phil. Trans. R. Soc. A. **366**, 63 (2008).

[54] L. Robinson, Science **236**, 1063 (1987).

[55] A. Zawadowski, solid state communications **70**, 439 (1989).

[56] J. M. Tarascon, L. H. Greene, W. R. McKinnon, G. W. Hull, J. H. Geballe, Science **235**, 1373 (1987).

[57] H. J. Kang, P. Dai, B. J. Campbell, P. J. Chupas, S. Rosenkranz, P. L. Lee, Q. Huang, S. Li, S. Komiya, Y. Ando, Nat. Mater. **6**, 224 (2007).

[58] Y. Kitanaka, Y. Noguchih, M. Miyayama, Phys. Rev. B **81**, 094114 (2010).

[59] P. F. Xing, Y. X. Chen, S. S. Yan, G. L. Liu, L. M. Mei, Z. Zhang, J. Appl. Phys. **106**, 043909 (2009).

[60] J. R. Sun, H. W. Yeung, H. Li, K. Zhao, H. N. Chan, H. K. Wong, J. Appl. Phys. **90**, 2831 (2001).

[61] M. Jourdan, N. Blümer, H. Adrian, Eur. Phys. J. B **33**, 25-30 (2003).

[62] J. Mannhart, D. G. Schlom, Nature **430**, 620 (2004).

[63] D. Kan *et al.*, Nature Mater. **4**, 816 (2005).

[64] H. Y. Hwang, Nature Mater. **4** ,803 (2005).

[65] E. A. Kotomin, V. Alexandrov, D. Gryaznov, R. A. Evarestov, J. Maier, Phys. Chem. Chem. Phhs. **13**, 923 (2011).

[66] Y. B. Nian, J. Strozier, N. J. Wu, X. Chen, A. Ignatiev, Phys. Rev. Lett. **98**, 146403 (2007).

[67] W. Jiang, M. Noman, Y. M. Lu, J. A. Bain, P. A Salvador, M. Skowronski, J. Appl. Phys. **110**, 034509 (2011).

[68] H.-I. Yoo, M.-W. Chang, T.-S. Oh, C.-E. Lee, K. D. Becker, J. Appl. Phys. **102**, 093701 (2007).

[69] D.-K. Lee, H.-I. Yoo, Solid State Ionics **177**, 1 (2006).

[70] D. S. Jeong, H. Schroeder, R. Waser, Phys. Rev. B **79**, 195317 (2009).

[71] Electrical properties of silicon, Ioffe Institute Database

[72] C. Cen, S. Thiel, G. Hammerl, C. W. Schneider, K. E. Andersen, C. S. Hellberg, J. Mannhart, J. Levy, nature materials **7**, 298 (2008).

[73] K. Szot, W. Speier, G. Bihlmayer, R. Waser, Nature Mater. **5**, 312–320 (2006).

[74] R. Waser, M. Aono, Nature Materials **6**, 833 (2007).

[75] A. Sawa, Materials Today **11**, 28 (2008).

[76] T. W. Hickmott, J. Appl. Phys. **33**, 2669 (1962).

[77] C. L. Jia, M. Lentzen, K. Urban, *et al.*, Science **299**, 870 (2003).

[78] M. Nagashima, D. Schmidt, US Patent 6962648 B2 (2005).

[79] J. E. Bonevich, L. D. Marks, J. Mater. Res. **7(6)**, 1489 (1992).

[80] M. Kusunoki, K. Yonemitsu, Y. sasaki, Y. Kubo, J. Am. Ceram. Soc. **76(3)**, 763 (1993).

[81] Y. M. Zhu, A. R. Moodenbaugh, Z. X. Cai, J. Tafto, M. Suenaga, D. O. Welch, Phys. Rev. Lett. **73,** 3026 (1994).

[82] F. M. Ross, R. Hull, D. Bahnck, J. C. Bean, L. J. Peticolas, R. A. Hamm, H. A. Huggins, Journal of Vacuum Science & Technology B **10**, 2008 (1992).

[83] Z. L. Wang, P. Poncharal, W. A. de Heer, Nanomeasurements of individual carbon nanotubes by *in situ* TEM, Hong Kong, Peoples R China, Jul 14-18; Int Union Pure Applied Chemistry: Hong Kong, Peoples R China, 1999; pp 209-219.

[84] X. D. Bai, E. G. Wang, P. X. Gao, Z. L. Wang, Nano Letters **3 (8)**, 1147 (2003).

[85] Z. Xu, X. D. Bai, E. G. Wang, Appl. Phys. Lett. **88**, 133107 (2006).

[86] Z. L. Wang, Advanced Materials **15**, 1497 (2003).

[87] Z. Xu, Ph. D thesis, Institute of Physics, Chinese Academy of Sciences, 2008

[88] Z. Z. Wang, Ph. D thesis, Institute of Physics, Chinese Academy of Sciences, 2009.

[89] J. Tersoff, D. R. Hamann, Phys. Rev. B **31**, 805 (1985).

[90] L. C. Feldman, J. W. Mayer, Fundamentals of Surface and Thin Film Analysis, Elsevier Science, New York, 1986.

[91] J. B. Pendry, J. Phys. C **13**, 937 (1980).

[92] T. Z. Ward, *et al.*, Phys. Rev. Lett. **102**, 087201 (2009).

[93] A. Singh, S. Mukhopadhyay, A. Ghosh, Phys. Rev. Lett.**105**, 067206 (2010).

[94] V. Podzorov, M. E. Gershenson, M. Uehara, S. -W. Chong, Phys. Rev. B **64**, 115113 (2001).

[95] J. G. Mavroides, J. A. Kafalas, D. F. Kolesar, Appl. Phys. Lett. **28**, 241 (1976).

[96] B. Cord, R. Courths, Surf. Sci. **162**, 34 (1985).

[97] A. F. Santander-Syro, *et al.*, Nature **469**, 189 (2011).

[98] W. Meevasana, *et al.*, Nature Materials **10**, 114 (2011).

[99] S. Kimura , M. Tsukada, Applied Surface Science **121/122**, 195 (1997).

[100] T. Ohnishi, K. Shibuya, M. Lippmaa, D. Kobayashi, H. Kumigashira, M. Oshima, H. Koinuma, Appl. Phys. Lett. **85**, 272 (2004).

[101] R. Bachelet, *et al.*, Appl. Phys. Lett. **95,** 141915 (2009).

[102] M. Radovic, *et al.*, Appl. Phys. Lett. **94**, 022901 (2009).

[103] N. Erdman, L. D. Marks, Surface Science **526**, 107001 (2003).

[104] Martin R. Castell, Surface Science **505**, 1 (2002).

[105] Martin R. Castell, Surface Science **516**, 33 (2002).

[106] N. Erdman, K. R. Poeppelmeier, M. Asta, O. Warschkow, D. E. Ellis, L. D. Marks, Nature London **419**, 55 (2002).

[107] N. Erdman, O. Warschkow, M. Asta, K. R. Poeppelmeier, D. E.Ellis, L. D. Marks, J. Am. Chem. Soc. **12**5, 10050 (2003).

[108] C. H. Lanier, *et al.*, Phys. Rev. B **76**, 045421 (2007).

[109] S. H. Phark, Y. J. Chang, T. W. Noh, Appl. Phys. Lett. **98**, 161908 (2011).

[110] J. Cheng, P. Regreny , L. Largeau, G. Patriarche, O. Mauguin, K. Naji, G. Hollinger, G. Saint-Girons, Journal of Crystal Growth **311**, 1042 (2009).

[111] J. Biscaras, N. Bergeal, A. Kushwaha, T. Wolf, A. Rastogi, R. C. Budhani, J. Lesueur, Nature Communications **1**, 89.

[112] B. Zheng, N. Binggeli, Phys. Rev. B **82**, 245311 (2010).

[113] Y. Hikita, M. Nishikawa, T. Yajima, H. Y. Hwang, Phys. Rev. B **79**, 073101 (2009).

[114] Y. Liang, D. A. Bonnell, Surf. Sci. **310**, 12894 (1994).

[115] Y. Liang, D. Bonnell,J. Am. Ceram. Soc. **78**, 2633 (1995).

[116] A. Hirata, A. Ando, K. Saiki, A. Koma, Surf. Sci. **310**, 89 (1994).

[117] John J. Barton, Phys. Rev. Lett. **61**, 1356 (1988).

[118] T. Kimura, Y. Tokura, Annu. Rev. Mater. Sci. **30**, 45(2000).

[119] A. Urushibara, *et al.*, Phys. Rev. B **51**, 14103(1995).

[120] C. D. Potter, *et al.*, J. D. Jorgensen, Phys. Rev. B **57**, 72 (1998).

[121] J.-H. Park, E. Vescovo, H.-J. Kim, C. Kwon, R. Ramesh, T. Venkatesan, Nature **392**, 794 (1998).

[122] A. Fert, *et al.*, Materials Science and Engineering B **84**, 1 (2001)

[123] V. Garcia, *et al.*, Science **327**, 1106 (2010).

[124] D. Pantel, S. Goetze, D. Hesse, M. Alexe, Nature Materials **11**, 289 (2012).

[125] M. Huijben, *et al.*, Phys. Rev. B **78**, 094413 (2008)

[126] M. Angeloni, G. Balestrino, N. G. Boggio, P. G. Medaglia, P. Orgiani, A. Tebano, J. Appl. Phys. **96**, 6387(2004).

[127] A. Tebano, *et al.*, Phys. Rev. B **74**, 245116 (2006).

[128] B. Kim, D. Kwon, T.Yajima, C. Bell, Y. Hikita, Bog G. Kim, H. Y. Hwang, Appl. Phys. Lett. **99**, 092513 (2011).

[129] A. Tebano, *et al.*, Phys. Rev. Lett. **100**, 137401 (2008).

[130] M. B. Lepetit, B. Mercey, C. Simon, Phys. Rev. Lett. **108**, 087202 (2012).

[131] P. G. Radaelli, *et al.*, Phys. Rev. B **56**, 8265 (1997).

[132] R. Herger, *et al.*, Phys. Rev. B **77**, 085401 (2008).

[133] J. R. Sun, *et al.*, Eur. Phys. J. B **35**, 481 (2003).

[134] F. W. Lytle, J. Appl. Phys. **35**, 2212 (1964).

[135] K. Hirota, J. P. Hill, S. M. Shapiro, G. Shirane, Y. Fujii, Phys. Rev. B **52**, 13195 (1995).

[136] R. Loetzsch, *et al.*, Appl. Phys. Lett. **96**, 071901 (2010).

[137] R. K. Zheng, Y. Wang, H. L. W. Chan, C. L. Choy, H. S. Luo, Phys. Rev. B **75**, 212102 (2007).

[138] L. M. Wang, Jing-Kae Lin, Jong-Pyng Shyu, Phys. Rev. B **74**, 184412 (2006).

[139] S. J. Zhu, *et al.*, Appl. Phys. Lett. **91**, 012505 (2007).

[140] F.Y. Bruno, *et al.*, Phys. Rev. Lett. **106**, 147205 (2011).

[141] J. Garcia-Barriocanal, *et al.*, Nature Communications **1**, 82 (2010).

[142] T. Taniuchi, Surface Science **601**, 4690 (2007).

[143] I. C. Infante, *et al.*, Adv. Funct. Mater. **20**, 2035 (2010).

[144] Judith L. MacManus-Driscoll, Adv. Funct. Mater. 20, 2035 (2010).

[145] S. Kang, *et al.*, Science **311**, 1911 (2006).

[146] H. Zheng, *et al.*, Science **303**, 661 (2004).

[147] E. Weal, S. Patnaik, Z. Bi, H. Wang, T. Fix, A. Kursumovic, J. L. MacManus Driscoll, Appl. Phys. Lett. **97**, 153121 (2010).

[148] H. Yang, H. Y. Wang, J. Yoon, Y. Q. Wang, M. K. Jain, David M. Feldmann, P. C. Dowden, Judith L. MacManus-Driscoll, Quanxi Jia, Adv. Mater. **21**, 3794 (2009).

[149] Yi Zhang, *et al.*, Appl. Phys. Lett. **98**, 042509 (2011).

[150] O. I. Lebedev, *et al.*, Phys. Rev. B **66**, 104421 (2002).

[151] M. Fäth, *et al.*, Science 285, 1540 (1999).

[152] Elbio Dagotto, Nanoscale Phase Separation and Colossal Magnetoresistance, Springer, (2002).

[153] H. Yang, H. Y Wang, J. Yoon, Y. Q. Wang, M. k. Jain, D. M. Feldmann, P. C. Dowden, J. L. MacManus-Driscoll, Q. X. Jia, Adv. Mater. **21**, 3794 (2009).

[154] B. S. Allimi, S. P. Alpay, C. K. Xie, B. O. Wells, J. I. Budnick, D. M. Pease, Appl. Phys. Lett. **92**, 202105 (2008).

[155] S. Miyasaka, T. Okuda, Y. Tokura, Phys. Rev. Lett. **85**, 5388 (2000).

[156] J. F. Gibbons, W. E. Beadle, Solid State Electron. **7**, 785 (1964).

[157] J. G. Simmons, R. R. Verderber, Proc. Roy. Soc. A. **30**1, 77 (1967).

[158] G. Dearnaley, A.M. Stonehamand D. V.Morgan, Rep. Prog. Phys. **33**, 1129 (1970).

[159] S. Q. Liu, N. J. Wu, A. Ignatiev, Appl. Phys. Lett. **76**, 2749 (2000).

[160] Y. Watanabe, *et al.*, Appl. Phys. Lett. **78**, 3738 (2001).

[161] C. Rossel, G. I. Meijer, D. Brémaud, D. Widmer, J. Appl. Phys. **90**, 2892 (2001).

[162] W. W. Zhuang, *et al.*, in IEDM Tech. Dig., 193 (2002).

[163] J. R. Contreras, *et al.*, Appl. Phys. Lett. **83**, 4595 (2003).

[164] S. Seo, *et al.*, Appl. Phys. Lett. **85**, 5655 (2004).

[165] B. J. Choi, *et al.*, J. Appl. Phys. **98**, 033715 (2005).

[166] T. L. Chen, X. M. Li, R. Dong, Q. Wang, L. D. Chen, Thin Solid Films **488**, 98 (2005).

[167] M. Hamaguchi, K. Aoyama, S. Asanuma, Y. Uesu, T. Katsufuji, Appl. Phys. Lett. **88**, 142508 (2006).

[168] C.-Y. Lin, C.-Y. Wu, C.-Y. Wu, T.-Y. Tseng, C. Hu, J. Appl. Phys. **102**, 094101 (2007).

[169] T. Sakamoto, K. Lister, N. Banno, T. Hasegawa, K. Terabe, M. Aono, Appl. Phys. Lett. **91**, 092110 (2007).

[170] C. Schindler, S. C. P. Thermadam, R. Waser, M. N. Kozicki, IEEE T. Electron Dev. **54**, 2762 (2007).

[171] I. H. Inoue, S. Yasuda, H. Akinaga, H. Takagi, Phys. Rev. B **77**, 035105 (2008).

[172] S. Lee, W. G. Kim, S. W. Rhee, K. Yong , Journal of The Electrochemical Society **155**, (2) H92-H96 (2008).

[173] W. Shen, R. Dittmann, U. Breuer, R. Waser, Appl. Phys. Lett. **93**, 222102 (2008).

[174] C.-Y. Lin , D. -Y. Lee, S.-Y. Wang , C.-C. Lin , T.-Y. Tseng, Surface & Coatings Technology **203**, 480(2008).

[175] H. Shima, F. Takano, H. Muramatsu, H. Akinaga, Y. Tamai, I. H. Inque, H. Takagi, Appl. Phys. Lett. **93**, 113504 (2008).

[176] N. Xu, L. F. Liu, X. Sun, C. Chen, Y. Wang, D. D. Han, X. Y. Liu, R. Q. Han, J. F. Kang, B. Yu, Semiconductor Science and Technology **23**, 075019(2008).

[177] C. Kugeler, R. Rosezin, R. Weng, R. Waser, S. Menzel, B. Klopstra, U. Bottger, Fast resistive switching in WO_3 thin films for non-volatile memory applications, IEEE-NANO 9th IEEE Conference, 900 (2009).

[178] M. K. Yang, J. -W. Park, T. K. Ko, J. K. Lee, Appl. Phys. Lett. **95**, 042105(2009)**.**

[179] C.-H. Yang, *et al.*, *Nature Materials* **8**, 485 (2009).

[180] K. Okimura, N. Ezreena, Y. Sasakawa, J. Sakai, Jpn. J. Appl. Phys. **48**, 065003 (2009).

[181] H. H. Huang, W. C. Shih, C. H. Lai, Appl. Phys. Lett. **96**, 193505 (2010).

[182] S. C. Chen, T. C. Chang, S. Y. Chen, C. W. Chen, S. C. Chen, S. M. Sze, M.-J Tsai, M.-J. Kao, F.-S Yeh Huang, Solid-State Electronics 62, 40 (2011).

[183] S.-Y. Huang, T.-C. Chang, M.-C. Chen, S.-C. Chen, H.-P. Lo, H.-C. Huang, D.-S. Gan, S. M. Sze, M.-J. Tsai, Solid-State Electronics **63**, 189 (2011).

[184] A. Moradpour, *et al.*, Adv. Mater. 23, 4141 (2011).

[185] A. Sawa, T. Fujii, M. Kawasaki, Y. Tokura, Appl. Phys. Lett. **85**, 4073 (2004).

[186] R. Fors, S. I. Khartsev, A. M. Grishin, Phys. Rev. B **71**, 045305 (2005).

[187] D. S. Shang, Q. Wang,L. D. Chen, R. Dong,X. M. Li, W. Q. Zhang, Phys. Rev. B **73**, 245427 (2006).

[188] C. Jooss, L. Wu, T. Beetz, R. F. Klie, M. Beleggia, M. A. Schofield, S. Schramm, J. Hoffmann, Y. Zhu, Proc. Natl. Acad. Sci. U. S. A. **104**, 13597 (2007).

[189] M. Janousch, G. Ingmar Meijer, U. Staub, B. Delley, S. F. Karg, B. P. Andreasson, Adv. Mater. 19, 2232 (2007).

[190] A. Baikalov, Y. Q. Wang, B. Shen, B. Lorenz, S. Tsui, Y. Y. Sun, Y. Y. Xue, C. W. Chu, Appl. Phys. Lett. **83**, 957 (2003).

[191] S. Tsui, A. Baikalov, J. Cmaidalka, Y. Y. Sun, Y. Q. Wang, Y. Y. Xue, C. W. Chu, L. Chen, A. J. Jacobson., Appl. Phys. Lett. **85**, 317 (2004).

[192] D. J. Seong, M. Jo, D. S. Lee, H. S. Hwang, Electrochem. Solid-State Lett. **10**, H168 (2007).

[193] S. H. Jeon, *et al.*, Appl. Phys. Lett. **89**, 042904 (2006).

[194] R. Waser, R. Dittmann, G. Staikov, K. Szot, Adv. Mater. **21**, 2632 (2009).

[195] M. J. Rozenberg, I. H. Inoue, M. J. Sánchez, Phys. Rev. Lett. **92**, 178302 (2004).

[196] C. B. Lee, B. S. Kang, A. Benayad, M. J. Lee, S.-E. Ahn, K. H. Kim, G. Stefanovich, Y. Park, I. K. Yoo, Appl. Phys. Lett. **93**, 042115 (2008).

[197] Ch. Jooss, J. Hoffmann, J. Fladerer, M. Ehrhardt, T. Beetz, L. Wu, Y. Zhu, Phys. Rev. B **77**, 132409 (2008).

[198] K. Tsubouchi, I. Ohkubo, H. Kumigashira, M. Oshima, Y. Matsumoto, K.Itaka, T. Ohnishi, M. Lippmaa, H. Koinuma, Adv. Mater. (Weinheim, Ger) **19**, 1711 (2007).

[199] H. Kawano, K. Shono, T. Yokota, M. Gomi, Appl. Phys. Express **1**, 101901 (2008).

[200] K. Shono, H. Kawano, T. Yokota, M. Gomi, Appl. Phys. Express **1**,055002 (2008).

[201] M. Hasan, R. Dong, H. J. Choi, D. S. Lee, D.-J. Seong, H. Hwang, Appl. Phys. Lett. **93**, 052908 (2008).

[202] D. S. Jeong, H. Schroeder, R. Waser, Electrochem. Solid-State Lett. **10**, G51 (2007).

[203] R. Meyer, L. Schloss, J. Brewer, R. Lambertson, W. Kinney, J. Sanchez, D. Rinerson, "Oxide dual-layer memory element for scalable nonvolatile cross-point memory technology," in Proc. Non-Volatile Memory Technol. Symp., Nov. 2008, pp. 1–5.

[204] H. B. Lv, *et al.*, Appl. Phys. Lett. **94**, 213502 (2009).

[205] R. Yang, X. M. Li, Phys. Status Solidi A **208**, 1041-1046 (2011).

[206] D. W. Reagor, S. Y. Lee, Y. Li, Q. X. Jia, J. Appl. Phys. **95**, 7971 (2004).

[207] H.-G. Lee, Chemical Thermodynamics for Metals and Materials (ImperialCollege, London, 1999), pp. 127–130.

[208] G. V. Samsonov, The Oxide Handbook, 2nd ed. (IFI/Plenum, New York, (1982), pp. 44–48.

[209] S. Shirasaki, H. Yamamura, H. Haneda, K. Kakegawa, J. Moori, J. Chem. Phys. **73**, 4640 (1980).

[210]A. Odagawa, H. Sato, I. H. Inoue, H. Akoh, M. Kawasaki, Y. Tokura, T.Kanno, H. Adachi, Phys. Rev. B **70**, 224403 (2004).

[211] D. S. Kim, Y. H. Kim, C. E. Lee, Y. T. Kim, Phys. Rev. B **74**, 174430 (2006).

[212] M. Fujimoto, H. Koyama, Y. Nishi, T. Suzuki, Appl. Phys. Lett. **9**, 223504 (2007).

[213] F. Gomez-Marlasca, P. Levy, J.of Physics: Conference Series **167**, 012036 (2009).

[214] Y. Tomioka, A. Asamitsu, H. Kuwahara, Y. Moritomo, Y. Tokura, Phys. Rev. B **53**, R1689 (1996).

[215] P. Knauth, H. L. Tuller, J. Appl. Phys. **85**, 897 (1999).

[216] R. Yasuhara, T. Yamamoto, I. Ohkubo, H. Kumigashira, M. Oshima, Appl. Phys. Lett. **97**, 132111 (2010).

[217] D. J. Seong, M. Hassan, H. J. Choi, J. Y. Lee, J. S. Yoon, J. B. Park, W. T. Lee, M. S. Oh, H. S. Hwang, IEEE Electron Device Lett. **30**, 919 (2009).

[218] S. K. R. S. Sankaranarayanan, E. Kaxiras, S. Ramanathan, Phys. Rev. Lett. **102**, 095504 (2009).

[219] S. Steinsvik, R. Bugge, J. Gjønnes, J. Taftø, T. Norby, J. Phys. Chem. Solids **58**, 969 (1997).

[220] P. Gao, *et al.*, Journal of Micron **41**, 301(2009).

[221] J. C. Grenier, J. Darriet, M. Pouchard, P. Hagenmuller, Mater. Res. Bull. **11**, 1219 (1976).

[222] K. Miyano, T. Tanaka, Y. Tomioka, Y. Tokura, Phys. Rev. Lett. **78**, 4257 (1997).

[223] A. G. Khachaturyan, Theory of Structural Transformations in Solids, Wiley, New York, 1983, 511-523.

[224] Y. G. Wang, S. Steinsvik, R. Høier, T. Norby, J. Mater. Sci. Lett. **14**, 1027 (1995).

[225] J. M. González-callbet, M. Vallet-Regí, J. Solid St. Chem. **68**, 266 (1987).

[226] J. -C. Grenier, *et al.*, J. Solid St. Chem. **20**, 365 (1977).

[227] Z. L. Wang, Z. C. Kang, Functianl and smart materials: structural evolution and structure analysis. Plenum Press, New York: 1998.

[228] T. Akita, *et al.*, Catal. Today **117**, 62 (2006).

[229] R. Sharma, *et al.*, Philosophical Magazine **84**, 2731 (2004).

[230] Garvie, L. A. J.; Buseck, P. R. J. Phys. Chem. Solids **60**, 1943 (1999).

[231] M. Finazzi, *et al.*, J. Electron Spectroscopy and Related Phenomena **78**, 221 (1996).

[232] D. S. Shang, *et al.*, J. Phys. D-Appl. Phys. **40**, 5373 (2007).

[233] C. Yoshida, K. Kinoshita, T. Yamasaki, Y. Sugiyama, Appl. Phys. Lett. 93, 3 (2008).

[234] D. J. M. Bevan, J. Kordis, Journal of Inorganic & Nuclear Chemistry **26**, 1509 (1964).

[235] A. Trovarelli, Catal. Rev.-Sci. Eng. **38**, (4), 439 (1996).

[236] D. D. Koelling, A. M. Boring, J. H. Wood, Solid State Commun. **47**, 227 (1983).

[237] N. V. Skorodumova, *et al.*, Phys. Rev. Lett. **89**, 4 (2002).

[238] F. Esch, *et al.*, Science **309**, 752 (2005).

[239] G. Adachi, N. Imanaka, Chem. Rev. **98**, 1479 (1998).

[240] G. E. Moore , Electronics **38**, 114 (1965).

[241] R. Neale, D. Nelson, Gordon Moore, Electronics, pp **56-60**, Sep. 30(1970).

[242] M. N. Babich, *et al.*, Phys. Rev. Lett. **61**, 2472 (1988).

[243] R. Ramprasad, J. Appl. Phys. **94**, 5609 (2003).

[244] Z. T. Xu, *et al.*, Applied Physics A **105**, 149 (2011).

Appendix A: Software Interfaces and Codes

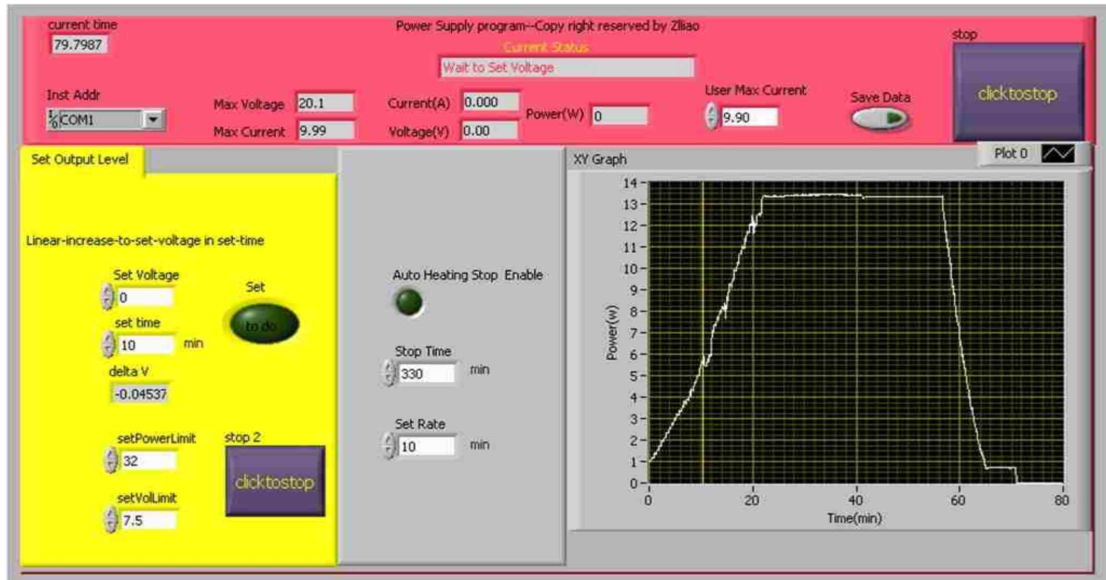

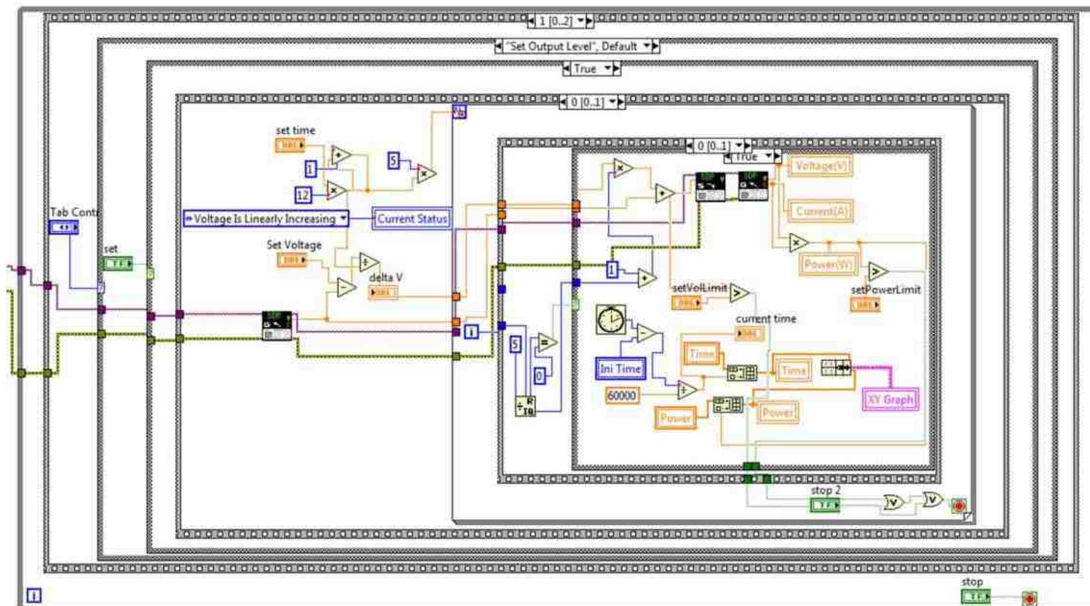

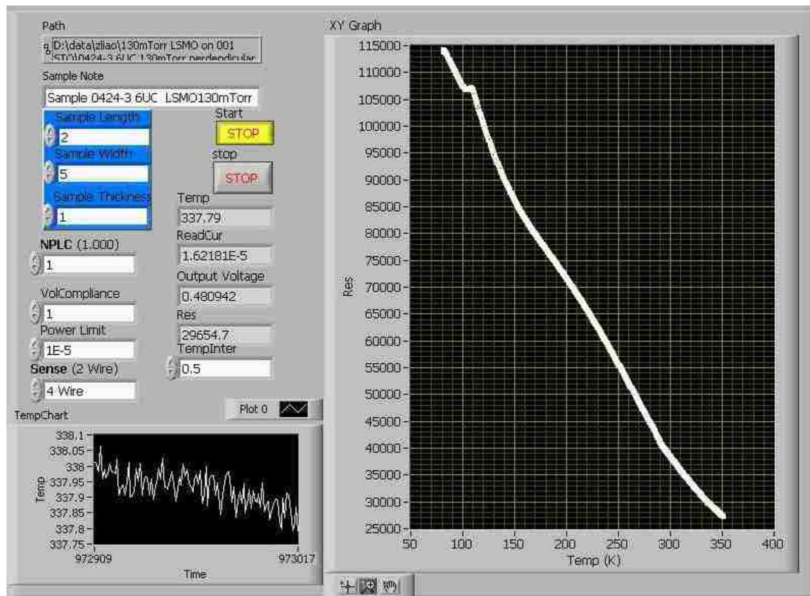
Path
Sample Note
Sample 0424-3 6UC LSMO130mTorr
Sample Length
2
Sample Width
5
Sample Thickness
1
Start
STOP
stop
STOP
Temp
337.79
ReadCur
1.62181E-5
Output Voltage
0.480942
Res
29654.7
TempInter
0.5
NPLC (1.000)
1
VolCompliance
1
Power Limit
1E-5
Sense (2 Wire)
4 Wire
TempChart
Plot 0
Temp
Time
XY Graph
Res
Temp (K)

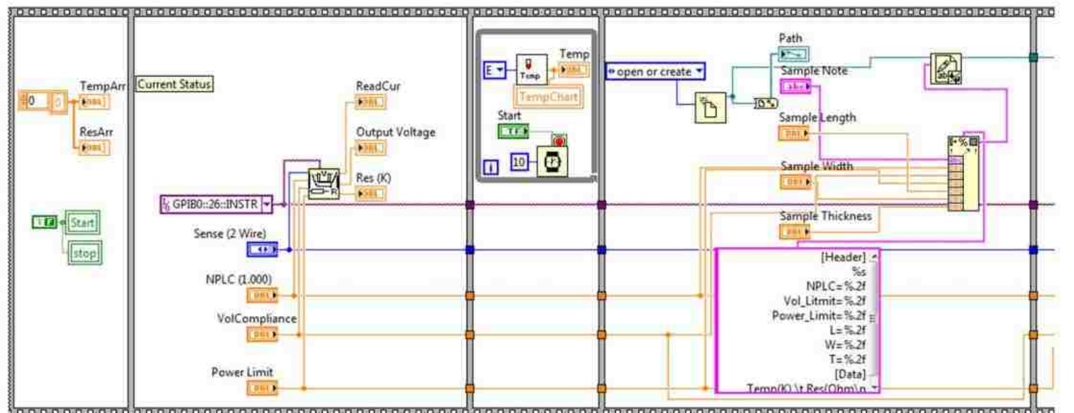
TempArr
ResArr
Start
stop
Current Status
ReadCur
Output Voltage
Res (K)
GPIB0::26::INSTR
Sense (2 Wire)
NPLC (1.000)
VolCompliance
Power Limit
Temp
TempChart
Start
10
open or create
Path
Sample Note
Sample Length
Sample Width
Sample Thickness
[Header]
%s
NPLC=%.2f
Vol_Litmit=%.2f
Power_Limit=%.2f
L=%.2f
W=%.2f
T=%.2f
[Data]

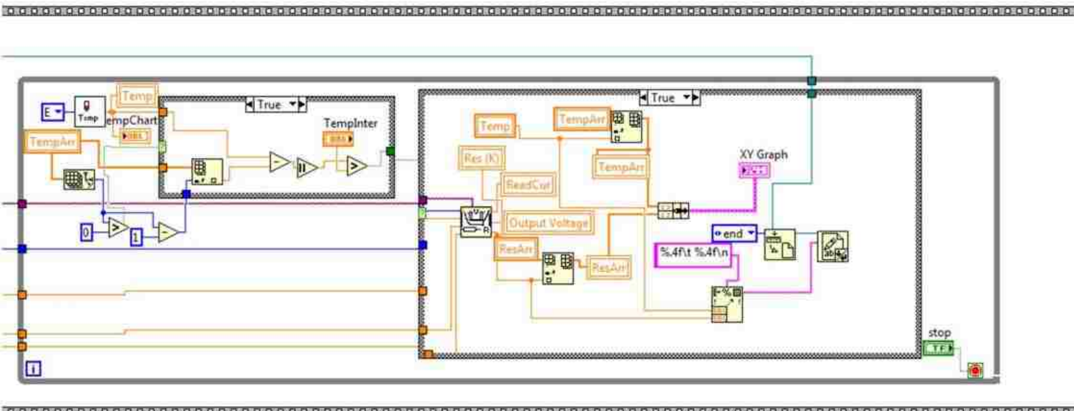
Temp
TempChart
TempArr
True
TempInter
0
1
Temp
TempArr
Res (K)
ReadCur
Output Voltage
ResArr
TempArr
ResArr
XY Graph
end
%.4f\t %.4f\n
stop

Bmp
Log
Status
Image Inf
Read Image
Contrast
Auto
Manual
ZOOM In Image
UpdateZM
stop
STOP
Line ZOOM-IN
Point ZOOM-IN
3D mode
3D Graph
ZOOM-IN
Backward Manual Forward
File NO
Tab Control 2
UpdateFactor
CurE
Cur Factor
Cursor 1
Cursor 2
Cursor 0
Intensity(A.U)
X(A.U)

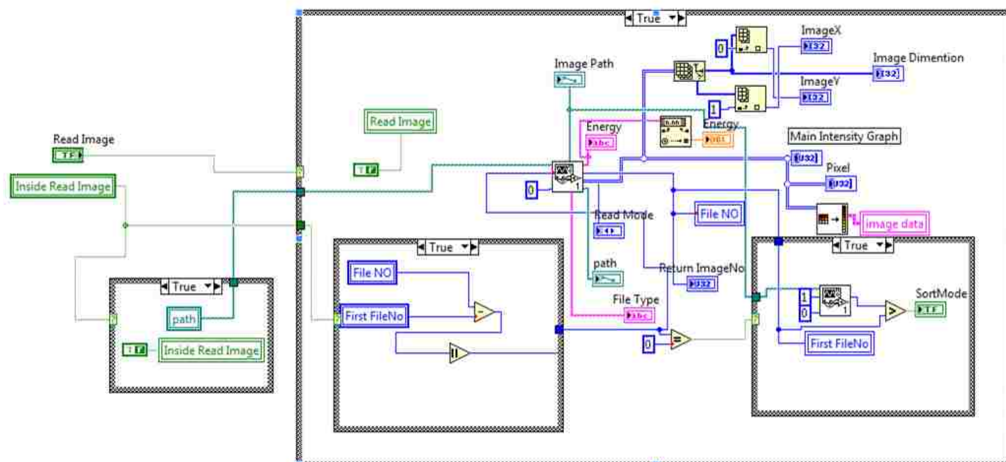
Read Image
Inside Read Image
True
path
Image Path
ImageX
ImageY
Image Dimention
Energy
Main Intensity Graph
Pixel
image data
Read Mode
File NO
Return ImageNo
File Type
First FileNo
SortMode

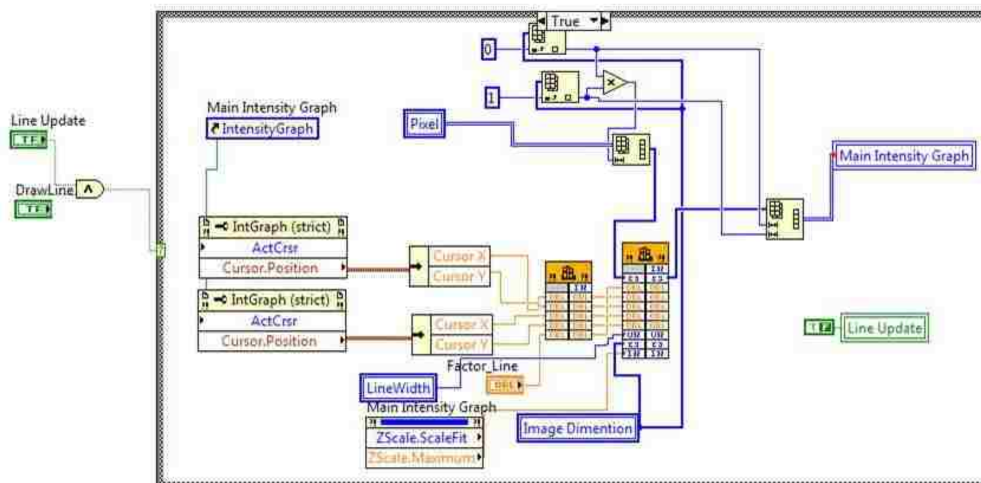
True
Line Update
DrawLine
Main Intensity Graph
IntensityGraph
Pixel
IntGraph (strict)
ActCrsr
Cursor.Position
Cursor X
Cursor Y
Factor_Line
LineWidth
ZScale.ScaleFit
ZScale.Maximum
Image Dimention

Appendix B: Letters of Permission

This is a License Agreement between zhaoliang liao ("You") and Elsevier ("Elsevier") provided by Copyright Clearance Center ("CCC"). The license consists of your order details, the terms and conditions provided by Elsevier, and the payment terms and conditions.

All payments must be made in full to CCC. For payment instructions, please see information listed at the bottom of this form.

Supplier	Elsevier Limited The Boulevard,Langford Lane Kidlington,Oxford,OX5 1GB,UK
Registered Company Number	1982084
Customer name	zhaoliang liao
Customer address	LSU Dept. of Physics & Astronomy Baton Rouge, LA 70803
License number	3020290454473
License date	Nov 01, 2012
Licensed content publisher	Elsevier
Licensed content publication	Solid-State Electronics
Licensed content title	Electrode engineering for improving resistive switching performance in single crystalline CeO2thin films
Licensed content author	Zhaoliang Liao,Peng Gao,Yang Meng,Wangyang Fu,Xuedong Bai,Hongwu Zhao,Dongmin Chen
Licensed content date	June 2012
Licensed content volume number	72
Licensed content issue number	None
Number of pages	4
Start Page	4
End Page	7
Type of Use	reuse in a thesis/dissertation
Portion	full article
Format	both print and electronic
Are you the author of this Elsevier article?	Yes
Will you be translating?	No
Order reference number	None
Title of your thesis/dissertation	THE EFFECTS OF SPATIAL CONFINEMENT AND OXYGEN STOICHIOMETRY ON COMPLEX METAL OXIDES
Expected completion date	Dec 2012
Estimated size (number of pages)	200
Elsevier VAT number	GB 494 6272 12

This is a License Agreement between zhaoliang liao ("You") and Elsevier ("Elsevier") provided by Copyright Clearance Center ("CCC"). The license consists of your order details, the terms and conditions provided by Elsevier, and the payment terms and conditions.

All payments must be made in full to CCC. For payment instructions, please see information listed at the bottom of this form.

Supplier	Elsevier Limited The Boulevard,Langford Lane Kidlington,Oxford,OX5 1GB,UK
Registered Company Number	1982084
Customer name	zhaoliang liao
Customer address	LSU Dept. of Physics & Astronomy Baton Rouge, LA 70803
License number	3020291280280
License date	Nov 01, 2012
Licensed content publisher	Elsevier
Licensed content publication	Micron
Licensed content title	*In situ*TEM studies of oxygen vacancy migration for electrically induced resistance change effect in cerium oxides
Licensed content author	Peng Gao,Zhenzhong Wang,Wangyang Fu,Zhaoliang Liao,Kaihui Liu,Wenlong Wang,Xuedong Bai,Enge Wang
Licensed content date	June 2010
Licensed content volume number	41
Licensed content issue number	4
Number of pages	5
Start Page	301
End Page	305
Type of Use	reuse in a thesis/dissertation
Intended publisher of new work	other
Portion	full article
Format	both print and electronic
Are you the author of this Elsevier article?	Yes
Will you be translating?	No
Order reference number	None
Title of your thesis/dissertation	THE EFFECTS OF SPATIAL CONFINEMENT AND OXYGEN STOICHIOMETRY ON COMPLEX METAL OXIDES
Expected completion date	Dec 2012
Estimated size	200

License Number	3020290909322
Order Date	Nov 01, 2012
Publisher	American Institute of Physics
Publication	Applied Physics Letters
Article Title	Categorization of resistive switching of metal-Pr0.7Ca0.3MnO3-metal devices
Author	Z. L. Liao, Z. Z. Wang, Y. Meng, Z. Y. Liu, et al.
Online Publication Date	Jun 24, 2009
Volume number	94
Issue number	25
Type of Use	Thesis/Dissertation
Requestor type	Author (original article)
Format	Print and electronic
Portion	Figure/Table
Number of figures/tables	4
Title of your thesis / dissertation	THE EFFECTS OF SPATIAL CONFINEMENT AND OXYGEN STOICHIOMETRY ON COMPLEX METAL OXIDES
Expected completion date	Dec 2012
Estimated size (number of pages)	200
License Number	3020290948526
Order Date	Nov 01, 2012
Publisher	American Institute of Physics
Publication	Applied Physics Letters
Article Title	Categorization of resistive switching of metal-Pr0.7Ca0.3MnO3-metal devices
Author	Z. L. Liao, Z. Z. Wang, Y. Meng, Z. Y. Liu, et al.
Online Publication Date	Jun 24, 2009
Volume number	94
Issue number	25
Type of Use	Thesis/Dissertation
Requestor type	Author (original article)
Format	Print and electronic
Portion	Excerpt (> 800 words)
Will you be translating?	No
Title of your thesis / dissertation	THE EFFECTS OF SPATIAL CONFINEMENT AND OXYGEN STOICHIOMETRY ON COMPLEX METAL OXIDES
Expected completion date	Dec 2012
Estimated size (number of pages)	200

All payments must be made in full to CCC. For payment instructions, please see information listed at the bottom of this form.

License Number	3020290845634
Order Date	Nov 01, 2012
Publisher	American Institute of Physics
Publication	Applied Physics Letters
Article Title	Electroforming and endurance behavior of Al/Pr0.7Ca0.3MnO3/Pt devices
Author	Zhaoliang Liao, Peng Gao, Yang Meng, Hongwu Zhao, et al.
Online Publication Date	Sep 13, 2011
Volume number	99
Issue number	11
Type of Use	Thesis/Dissertation
Requestor type	Author (original article)
Format	Print and electronic
Portion	Figure/Table
Number of figures/tables	3
Title of your thesis / dissertation	THE EFFECTS OF SPATIAL CONFINEMENT AND OXYGEN STOICHIOMETRY ON COMPLEX METAL OXIDES
Expected completion date	Dec 2012
Estimated size (number of pages)	200

License Number	3020291138372
Order Date	Nov 01, 2012
Publisher	American Institute of Physics
Publication	Applied Physics Letters
Article Title	Electroforming and endurance behavior of Al/Pr0.7Ca0.3MnO3/Pt devices
Author	Zhaoliang Liao, Peng Gao, Yang Meng, Hongwu Zhao, et al.
Online Publication Date	Sep 13, 2011
Volume number	99
Issue number	11
Type of Use	Thesis/Dissertation
Requestor type	Author (original article)
Format	Print and electronic
Portion	Excerpt (> 800 words)
Will you be translating?	No
Title of your thesis / dissertation	THE EFFECTS OF SPATIAL CONFINEMENT AND OXYGEN STOICHIOMETRY ON COMPLEX METAL OXIDES
Expected completion date	Dec 2012
Estimated size (number of pages)	200

License Number	3020290581678
Order Date	Nov 01, 2012
Publisher	American Institute of Physics
Publication	Journal of Applied Physics
Article Title	Evidence for electric-field-driven migration and diffusion of oxygen vacancies in Pr0.7Ca0.3MnO3
Author	Zhaoliang Liao, Peng Gao, Xuedong Bai, Dongmin Chen, et al.
Online Publication Date	Jun 5, 2012
Volume number	111
Issue number	11
Type of Use	Thesis/Dissertation
Requestor type	Author (original article)
Format	Print and electronic
Portion	Figure/Table
Number of figures/tables	5
Title of your thesis / dissertation	THE EFFECTS OF SPATIAL CONFINEMENT AND OXYGEN STOICHIOMETRY ON COMPLEX METAL OXIDES
Expected completion date	Dec 2012
Estimated size (number of pages)	200

License Number	3020290632835
Order Date	Nov 01, 2012
Publisher	American Institute of Physics
Publication	Journal of Applied Physics
Article Title	Evidence for electric-field-driven migration and diffusion of oxygen vacancies in Pr0.7Ca0.3MnO3
Author	Zhaoliang Liao, Peng Gao, Xuedong Bai, Dongmin Chen, et al.
Online Publication Date	Jun 5, 2012
Volume number	111
Issue number	11
Type of Use	Thesis/Dissertation
Requestor type	Author (original article)
Format	Print and electronic
Portion	Excerpt (> 800 words)
Will you be translating?	No
Title of your thesis / dissertation	THE EFFECTS OF SPATIAL CONFINEMENT AND OXYGEN STOICHIOMETRY ON COMPLEX METAL OXIDES
Expected completion date	Dec 2012
Estimated size (number of pages)	200

Vita

Zhaoliang Liao was born in 1984, in Luocheng, Guang Xi province, China. He graduated from University of Science and Technology of China, with a Bachelor of Science Degree in Physics in July 2006. He received his first Ph.D degree in Physics from Institute of Physics, Chinese Academy of Sciences, Beijing, China, in November 2011. He came to U.S. in January 2010 as a dual degree student and started his graduate study in the Department of Physics and Astronomy in The Louisiana State University, Baton Rouge, Louisiana. He expects to receive his Doctor of Philosophy degree in December, 2012.